



NATIONAL ADVISORY COMMITTEE FOR AERONAUTICS

TECHNICAL NOTE 3691

ANALYSIS AND COMPARISON WITH THEORY OF FLOW-FIELD
MEASUREMENTS NEAR A LIFTING ROTOR IN
THE LANGLEY FULL-SCALE TUNNEL

By Harry H. Heyson

Langley Aeronautical Laboratory
Langley Field, Va.



Washington
April 1956

AFM-4
TECHNICAL



0066365

TECHNICAL NOTE 3691

ANALYSIS AND COMPARISON WITH THEORY OF FLOW-FIELD

MEASUREMENTS NEAR A LIFTING ROTOR IN

THE LANGLEY FULL-SCALE TUNNEL

By Harry H. Heyson

SUMMARY

Results of an investigation in the Langley full-scale tunnel of the induced flow near a lifting rotor are given. Measurements of stream angles and velocities were made in several transverse planes along and behind the rotor in four different conditions representative of the cruising and high-speed ranges of flight. These measurements indicate that available theory may be used to calculate with reasonable accuracy the induced flow over the forward three-quarters of the disk for these flight conditions provided that a realistic nonuniform rotor disk-load distribution is assumed. Rearward of the three-quarter-diameter point, calculations of the induced velocity are increasingly inaccurate due to the rolling up of the trailing-vortex system. Farther rearward, well behind the rotor, the flow may be represented more accurately by the flow behind a uniformly loaded wing.

INTRODUCTION

A detailed knowledge of the induced velocity in and near the rotor is required for a complete helicopter analysis. Fortunately, very superficial estimates are usually adequate for isolated rotor performance or stability calculations. Recently, however, the emphasis on rotor-blade vibration problems and the advent of the compound helicopter and convertiplane have highlighted the need for more complete information.

Rotor-blade vibration analyses, in general, require a knowledge of the instantaneous induced velocity acting on the rotor blades at any particular moment. Some experimental evidence (ref. 1) is available which indicates that the fluctuating component of the flow may be so large that there is little apparent relation between the instantaneous and the time-averaged induced velocities. Such instantaneous velocities have not been calculated theoretically and are not discussed in this paper.

Although performance calculations for a compound helicopter or convertiplane do not require as detailed a knowledge of the flow as do vibration analyses, they do require a more elaborate analysis than is needed for an isolated rotor. A knowledge of the time-averaged induced velocity at locations in the vicinity of the rotor should be adequate to predict the effect of the rotor on the wings and tail surfaces of these machines. The time-averaged flows are considerably simpler to deal with theoretically than are the instantaneous flows, and the results of several theoretical analyses are available (refs. 2 to 6, for example). These analyses are limited by the restricted number of locations for which the calculations were made and also by the fact that the side-to-side asymmetries caused by a finite tip-speed ratio are usually neglected.

Several previous experimental investigations (see ref. 7 for a bibliography) have provided some qualitative information on the subject by the use of smoke in flight and in wind tunnels. However, quantitative measurements (refs. 8 to 10) are extremely scarce and, in general, are inadequate either to define the nature of the flow or to check the accuracy of the theoretical calculations.

This investigation was undertaken in an attempt to provide such information. Stream angle and velocity measurements were made in several transverse planes along and behind a lifting rotor in the Langley full-scale tunnel. The simulated flight conditions cover tip-speed ratios between 0.095 and 0.232 and calculated wake skew angles between 75.0° and 85.8° . Substantially all the basic data are presented in order to provide the designer with the maximum amount of information. At those locations for which theoretical calculations are available, the measured data are compared with theory in order to determine the extent to which the calculations are valid and also to determine the general nature of the flow field.

SYMBOLS

C_L	rotor lift coefficient, $\frac{L}{\frac{\rho V^2}{2} \pi R^2}$
C_T	rotor thrust coefficient, $\frac{T}{\rho (\Omega R)^2 \pi R^2}$
f	equivalent flat-plate area representing parasite drag, based on unit drag coefficient, $\frac{\text{Helicopter parasite drag}}{\frac{\rho V^2}{2}}$, sq ft

i	complement of skew angle (used in ref. 4 as angle of attack of rotor tip-path plane), deg
L	lift, lb
q	dynamic pressure, lb/sq ft
q ₀	free-stream dynamic pressure, lb/sq ft
R	blade radius, ft
s	semispan of wing, ft
T	rotor thrust, lb
V	forward speed of rotor, ft/sec
v	normal component of induced velocity, positive downward, ft/sec
v ₀	average or momentum value of the normal component of induced velocity, positive downward, ft/sec
X	distance parallel to longitudinal rotor tip-path-plane axis, measured positive rearward from center of rotor, ft (fig. 1)
Y	distance parallel to lateral rotor tip-path-plane axis, measured positive on advancing side of disk from center of rotor, ft (fig. 1)
Z	distance parallel to axis perpendicular to rotor tip-path plane, measured positive above rotor from center of rotor, ft (fig. 1)
α	rotor control-axis angle of attack, radians
Γ	circulation, sq ft/sec
γ	vorticity, radians/sec
μ	tip-speed ratio, $\frac{V \cos \alpha}{\Omega R}$
ρ	mass density of air, slugs/cu ft
χ	rotor wake skew angle, angle between Z-axis of tip-path plane and axis of skewed wake, positive rearward from Z-axis, deg (fig. 1)
Ω	rotor angular velocity, radians/sec

Note that the definitions of X, Y, and Z, together with the direction of rotation of the rotor in this investigation, result in a left-handed axis system.

APPARATUS AND TESTS

The surveys were conducted in the Langley full-scale tunnel which is described in reference 11. The experimental apparatus used in these tests is shown in figure 2(a).

The rotor was of the teetering or seesaw type and had untapered, untwisted blades (fig. 2(b)) with NACA 0012 airfoil section. The rotor radius was 7.5 feet and its solidity was 0.0543. The rotor tip speed was 500 feet per second for all tests except that at $\mu = 0.232$. For this test, the rotor was operated at 450 feet per second.

Two different survey rakes were used in the tests (fig. 2(c)). A calibrated five-tube survey rake was used to measure the stream pitch and yaw angles and dynamic pressures for most of the tests (fig. 2(d)). This rake is fully described in reference 12. In order to obtain data closer to the plane of the rotor, a calibrated pitch head (fig. 2(e)) was used to survey points in the longitudinal plane of symmetry for one flight condition.

The procedure used in the tests was as follows: The rotor was first set approximately at a predetermined flight condition. Then, the area above, below, and behind the rotor was surveyed with the rakes. At intervals during the surveying, readings were taken of rotor thrust and drag, blade flapping and feathering motions, and tunnel dynamic pressure.

CORRECTIONS

A floor was installed in the tunnel test section for all the tests, and for this configuration the Langley full-scale tunnel has no appreciable jet-boundary correction (ref. 13).

In order to correct the measured dynamic pressures and stream angles for the flow about the supporting mechanism and for tunnel stream angle, data were taken twice at each point in space — once with and once without the rotor blades installed. The difference is considered to be characteristic of the isolated rotor. It should be noted, however, that this procedure is not adequate in regions immediately behind the rotor. (See

figs. 3 to 5.) Measurements made in these regions have little accuracy because of the effect of the rotor on the flow about the tower. The angle of attack of the rotor was corrected for tunnel stream angle.

PRECISION

The accuracy of the two rakes is essentially the same. Both measure dynamic pressure within 2 percent and stream angles within $1/2^\circ$. These figures take into account the unsteadiness of the flow and the high vibration level of the rake mount. At the lowest tip-speed ratio, additional inaccuracy is caused by the difficulty in reading the small changes of liquid height in the manometer tubes. Overall accuracy in terms of the average value of the normal component of induced velocity will be a function of the rotor lift coefficient. For ease of reference, the following table gives the estimated overall accuracy for each of the flight conditions covered in this investigation:

Tip-speed ratio, μ	Accuracy, percent v_0
0.095	± 15
.139	± 10
.140	± 10
.232	± 25

The rakes used were incapable of measuring instantaneous variations of induced velocity such as might be desired for a refined blade-vibration analysis. Therefore, all data are time-averaged values. The experimental results of reference 8 indicate that instantaneous values may differ greatly from the mean values measured in these tests.

During the tests, the rotor tip speed was held constant to within 1 percent. The thrust coefficient was measured within 1 percent. The skew angle, which was computed by using the measured values of C_T and the measured blade motions in equation (29) of reference 2, should be accurate to within 1° .

The position of the rake with respect to the hub was known within 0.3 percent R. Because the rotor was of the teetering type, the only coning was due to the deflection of the blades. The tip deflection was estimated visually to be between 2 and 3 percent of the radius. The

data are presented with reference to a plane parallel to the tip-path plane and passing through the teetering pin.

RESULTS AND DISCUSSION

Basic Data

Because of the present lack of information, both theoretical and experimental, on the induced velocities in many areas near the rotor, substantially all the basic data obtained in the investigation are presented. In each case the rotor flight condition is identified on the figure by the skew angle χ and the tip-speed ratio μ . Table I identifies the various flight conditions more completely.

Figures 3 to 5 show the measured stream angles in the flow; figures 6 to 8 show contours of dynamic-pressure ratio; and figures 9 to 29 give the measured values of induced-velocity ratio. The fairings of the measured data, shown in figures 9 to 29, are used for the subsequent analysis.

The basic-data curves are not discussed as such in this paper since the more significant phenomena have already been pointed out in reference 10.

Discussion of Applicable Theory

In reference 2, Castles and De Leeuw present calculated values of the normal component of induced velocity in the longitudinal plane of symmetry and along the principal (X,Y,Z) axes of a rotor with a uniform disk loading. Reference 3 uses the flow field of reference 2 to calculate the flow field for rotors having nonuniform but circularly symmetrical disk loadings (the specific cases calculated being rotors with a triangular disk loading and with a typical measured mean disk loading).

Additional theoretical calculations by Mangler and Squire (ref. 4) give induced-velocity information in the entire rotor disk and also for a transverse plane in the far wake. A later section discusses a method of transforming these results to correspond with the results of references 2 and 3 except for the specific disk loadings considered.

Drees (ref. 5) discusses some of the effects of a finite tip-speed ratio and presents calculations of some of these effects at selected

points on the rotor disk. It should be noted that the calculated curves presented with the data are not modified for the asymmetries discussed in this reference.

Comparison of Measured Data With Calculated

Values of References 2 and 3

Longitudinal plane of symmetry.- Figures 30 to 33 present the measured values of induced velocity in the longitudinal plane of symmetry as compared with the calculated values from references 2 and 3.

For the four flight conditions, the measured data near the forward portions of the rotor fall close to the flow calculated for the rotors with zero load in the center. The existence of essentially zero induced velocity at the center of the rotor and of regions of upwash behind the center are clearly shown. Further rearward in the flow, just behind the trailing edge of the rotor ($X/R = 1.07$), there is no longer any pronounced correlation between the measured and the calculated flow, regardless of the lift distribution assumed to exist on the rotor disk. At greater distances behind the rotor ($X/R = 2.07$ and 3.14), there seems to be no correlation. The physical reasons for this lack of correlation are discussed subsequently.

Longitudinal axis.- If curves are faired through the data in figures 30 to 33 and the values at $Z/R = 0$ are taken from these curves, it is possible to obtain an idea of the variation of induced velocity along the longitudinal axis of the rotor. The results, plotted in figure 34, show clearly the good correlation of the nonuniformly loaded rotor calculations in the flow over the forward three-quarters of the rotor and the deviation behind that point.

Figure 35 compares the measured points of figures 34(c) and 34(d): These two flight conditions have very small differences in skew angles. There is, however, an appreciable difference in tip-speed ratio and lift coefficient. Actually, the calculated induced-velocity ratios for these two skew angles are virtually identical. It may be seen that, experimentally, there is very little difference between the induced velocities along the longitudinal axis for the two tip-speed ratios. This fact is as assumed in references 2 and 5.

Lateral axis.- The basic data may be cross-plotted in the same manner to obtain the induced-velocity distribution along the lateral (Y) axis. The results of these cross plots are shown in figure 36 and are compared with the calculated distributions of references 2 and 3. The calculated flow is symmetrical since no account is taken of dissymmetries due to the finite tip-speed ratio.

A word of caution is necessary at this point. Because of the necessity of maintaining a clearance between the survey rake and the rotor, it was not possible to obtain data much closer than 20 percent R above the rotor. (See figs. 30, 32, and 33.) The theory predicts rather large gradients of induced velocity at locations closer to the rotor than this point. In the longitudinal plane of symmetry it is possible to cross-plot the data with some confidence by comparing the trends shown well above the rotor by the theory and by the measured points. At other locations, without the theory as a guide, the accuracy of cross plots is problematical. Therefore, the following discussion of the induced-velocity distribution on the Y -axis should be regarded as being on a less firm basis than the discussion in the preceding sections.

Figure 36 indicates that the rotor does have zero induced velocity at its center. This is in agreement with the assumption that the rotor carries zero load at its center and further indicates that this fact must be used if the flow is to be calculated with any degree of accuracy.

Figure 36 also shows that the induced-velocity peak on the retreating side is higher and further outboard than the peak on the advancing side. This result is logical when the difference in loading on the two sides of the rotor are compared. The resultant velocities at the inner portion of the blades on the retreating side are very low or even negative, whereas the corresponding velocities on the advancing side are much higher. Therefore, the loading on the inner portion of the retreating side of the disk must be less than that on the advancing side. The outer portion of the retreating side must then carry a greater loading in order that the blade thrust moment remain essentially constant around the disk. Thus, the loading on the retreating side will peak farther outboard and at a higher value than the loading on the advancing side of the disk. This is the same trend shown by the measured induced velocities and is indicative of the very close relation between the induced velocities and the loading along this axis.

Comparison of Measured Data With Calculated Values of Reference 4

Modification of calculations for finite lift coefficient.— Mangler and Squire, in reference 4, compute the induced velocities in the rotor disk and in a transverse plane in the far wake. Their calculated results are limited to vanishingly small lift coefficients in that the trailing-vortex system leaves the rotor in the same direction and with the same velocity as the free stream.

The assumption of a finite lift coefficient alters this picture in two ways: First, the trailing-vortex system must now cross the free-stream flow and, second, there will be a change in the vortex density.

The results of reference 4 are easily modified to account for these changes and, when so modified, will correspond with the results of references 2 and 3 except for the specific disk loadings considered. The first modification is merely a rotation of the field to account for the inclination of the wake. The incidence angle i is then the complement of the skew angle χ . The change in vortex density, although affecting the absolute induced velocity v , will have no effect upon the induced-velocity ratio $\frac{v}{v_0} = 4 \left(\frac{v}{VC_L} \right)$. Therefore, the new value of v may be found by using the value of v/v_0 from reference 4 and by calculating v_0 from an equation which considers the finite lift coefficient (such as eq. (32) of ref. 2).

For the purpose of comparison with the measured data of this paper, all the induced velocities of reference 4 have been modified to correspond with reference 2 in regard to both skew angle and vortex density.

Plane of the rotor.— Values of induced-velocity ratio in the plane of the rotor obtained by cross-plotting the measured data are compared with the corrected calculated values from reference 4 in figures 37 to 43. These figures are discussed only in general, since they indicate the same results as the previous comparison with references 2 and 3. This result might be expected since the calculated results should be comparable if the same load distributions are assumed. The resemblance between the typical loading of reference 3 and pressure distribution III of reference 4 is evident.

In general, the same extent of agreement is noticeable (see especially fig. 37(b)); that is, the calculated flow field is close to the measured field only over the forward three-quarters of the disk.

Each figure (figs. 37 to 43) shows that the induced-velocity field for pressure distribution III (labeled P.D. III) is closer to the measured field on both sides of the disk than that for pressure distribution I (labeled P.D. I). Since pressure distribution III represents a disk loading with zero load in the center and the other distribution does not, this result is as expected.

This result does not agree with that of reference 9, which indicates that pressure distribution I should be used for calculating the induced velocities over the advancing side and pressure distribution III, over the retreating side of the rotor. This result (ref. 9) arose from measurements made at $X/R = 1.5$ and, as such, is subject to error because of the discrepancy between theory and the measured data in this region. The present result is considered to be more accurate.

The values at $X/R = 0.5$ (fig. 43) seem to indicate that, at this location, the error is generally somewhat larger near the outer edges

of the disk. This result might be expected since the roll-up of the trailing-vortex system would be expected to affect the outer edges of the disk sooner than the center.

Far wake.— Reference 4 also computes the induced-velocity distribution in the far wake. The computed contours of induced-velocity ratio for both pressure distributions in the far wake are compared in figures 44 to 49 with measured contours of induced velocity at $X/R = 2.07$ and $X/R = 3.14$ for three different flight conditions. (Notice that the rotation of the calculated flow field required to obtain correspondence with references 2 and 3 results in a vertical displacement of the computed induced velocities.)

In general, the measured induced velocities are of the same order of magnitude as the calculated values. This result would be expected, regardless of the flow pattern assumed for the calculations, since a given amount of downward momentum must be imparted to the air to obtain a given lift. The distribution of induced velocity is, however, rather different from the calculated values, particularly in the central portion of the wake. In some cases, the calculated induced-velocity field in the usual location of short-span tail surfaces could be incorrect by as much as $1.5v/v_0$.

Nature of the Flow

At this point the reason for the rather severe discrepancies between the calculated and the measured induced velocities in the rearward portion of the flow is considered. Reference 10 has already noted the rolling up of the vortex sheet behind the rotor. Figures 50 to 52 examine this phenomenon more thoroughly for three different flight conditions. These figures are contour maps of the measured local mean vorticity behind the rotor. The intersection of the outermost edge of the assumed wake (refs. 2, 3, 4, and 6) with the survey plane is shown in each case by the dashed-line ellipse. If the assumed wake vortex pattern is correct, the contours of vorticity should be along this wake edge (or within it, depending upon the disk load distribution).

In general, this is not true since the dominant feature in each case is the vorticity associated with the well-developed, rolled-up vortices behind the rotor tips. It should be noted that these vortices have only been displaced vertically about half as far as the center of the wake. The lower half of the elliptical sheet is essentially completely rolled up at the trailing edge (figs. 50, 51(a), and 52). The upper half of the elliptical sheet (originating from the rear of the disk) is still visible at $X/R = 1.07$, but it also is completely rolled up shortly after that point (figs. 51(b) and 51(c)).

The similarity between the flow behind the rotor and that behind a low-aspect-ratio wing is very close and it is possible to draw a somewhat more quantitative analogy.

Reference 14 examines the rolling up of the trailing-vortex system behind a low-aspect-ratio wing. For lift coefficients of the order of several tenths, the roll-up is essentially complete in a very short distance. Figure 9 of reference 14 shows that, for an untwisted, rectangular wing of aspect ratio $4/\pi$ (the same aspect ratio as a rotor), and for the lift coefficients used herein (0.720, 0.373, and 0.122), the roll-up distances should be 0.33, 0.64, and 1.97 times the chord length, respectively. It is more difficult to determine the rate of roll-up for something as complex as a rotor, but figures 50 to 52 indicate qualitatively that it is also extremely rapid.

These observations are further substantiated by the induced-velocity measurements previously examined in figures 30 and 32. The measured data in these figures show a marked discontinuity (which would be expected at the edge of the wake) only in the vicinity of the upper wake edge at $X/R = 1.07$. Farther behind the rotor ($X/R = 2.07$ and 3.14), there is no pronounced discontinuity; this condition indicates the absence of a strong vortex sheet in this region.

Figures 33(f) and 33(g) seem to show a discontinuity somewhat above the upper edge of the assumed wake. The previous analogy with low-aspect-ratio wings indicates the possibility that the roll-up would not be as rapid in this case because of the low rotor lift coefficient ($C_L = 0.122$). The difference between the calculated and the measured flow fields may be explained on this basis. In the forward portions of the flow, the elliptical wake has not rolled up, and it therefore resembles the wake-vortex model used in the calculations. The wake here, has, of course, the greatest effect on the induced velocities in the forward portions of the flow and essentially determines their magnitude. Consequently, in this part of the flow, calculations give a reasonable picture of the actual induced velocity.

Farther rearward, however, the distorted portion of the wake has a greater effect in determining the actual induced velocity. The calculated flow field, therefore, is increasingly more inaccurate as its distance downstream increases.

A short distance behind the rotor, it should be possible to assume that the flow will be the same as that for an equivalent wing. The minimum distance behind the rotor at which this procedure will be valid is a function of the lift coefficient.

From reference 15 the induced velocity in the plane of symmetry of a uniformly loaded rectangular wing is

$$v = \frac{s\Gamma}{2\pi} \left[\frac{X}{\sqrt{s^2 + X^2 + Z^2}} \left(\frac{1}{X^2 + Z^2} + \frac{1}{s^2 + Z^2} \right) + \frac{1}{s^2 + Z^2} \right] \quad (1)$$

If it is assumed that the quarter chord of the equivalent wing and the lateral center line of the rotor coincide and also that $s = 0.85R$ (the approximate center of gravity of the vortex system),

$$v = \frac{0.85R\Gamma}{2\pi} \left\{ \frac{X}{\sqrt{(0.85R)^2 + X^2 + Z^2}} \left[\frac{1}{X^2 + Z^2} + \frac{1}{(0.85R)^2 + Z^2} \right] + \frac{1}{(0.85R)^2 + Z^2} \right\} \quad (2)$$

If nondimensionalized, equation (2) becomes

$$\frac{2\pi Rv}{\Gamma} = 0.85 \left\{ \frac{(X/R)^2}{\sqrt{0.723 + \left(\frac{X}{R}\right)^2 + \left(\frac{Z}{R}\right)^2}} \left[\frac{1}{\left(\frac{X}{R}\right)^2 + \left(\frac{Z}{R}\right)^2} + \frac{1}{0.723 + \left(\frac{Z}{R}\right)^2} \right] + \frac{1}{0.723 + \left(\frac{Z}{R}\right)^2} \right\} \quad (3)$$

Now

$$\Gamma = \frac{L}{2\rho VR} \quad (4)$$

and, for skew angles near 90° ,

$$v_0 = \frac{L}{2\rho V\pi R^2} \quad (5)$$

Substituting equation (4) into equation (3) and dividing both sides of the resulting equation by equation (5) gives

$$\frac{v}{v_0} = 0.425 \left\{ \frac{\frac{X}{R}}{\sqrt{0.723 + \left(\frac{X}{R}\right)^2 + \left(\frac{Z}{R}\right)^2}} \left[\frac{1}{\left(\frac{X}{R}\right)^2 + \left(\frac{Z}{R}\right)^2} + \frac{1}{0.723 + \left(\frac{Z}{R}\right)^2} \right] + \frac{1}{0.723 + \left(\frac{Z}{R}\right)^2} \right\} \quad (6)$$

The flow calculated by this equation is symmetrical about $Z/R = 0$; that is, it does not allow for the vertical displacement of the wake. As pointed out previously, the centers of the vortices are displaced downward an amount

$$\Delta \frac{Z}{R} = \frac{1}{2} \frac{X}{R} \cot \chi \quad (7)$$

The induced velocity for this assumed wing has been calculated from equations (6) and (7) and is compared with the flow measured at $X/R = 2.07$ and 3.14 (for $\mu = 0.140$ and $\chi = 82.3^\circ$) in figure 53. As expected in these rearward planes, it is a closer approximation to the actual flow than are the flows calculated on the basis of a skewed cylindrical wake (fig. 32, for example).

Another point is worth noting here. It has, upon occasion, been assumed that the rotor wake must have more vorticity behind the retreating side of the disk than behind the advancing side of the disk, since the unequal blade velocities on the two sides require the retreating blade to have a greater value of circulation. This would be true only at the trailing edge of the blade to an observer riding around with it. However, to an observer immediately behind the rotor disk (as in these surveys), the summation of vorticity behind the disk must be equal on each side, since vorticity can not end in space. More complete contours of local mean vorticity than those given in figures 50 to 52 indicate that this is essentially true.

CONCLUSIONS

The results of this wind-tunnel investigation of the induced flow near a single rotor in simulated cruising and high-speed flight are as follows:

1. As far rearward as three-quarters of a diameter behind the leading edge of the rotor disk, the normal component of induced velocity of a lifting rotor may be calculated with good accuracy by available theory provided that a realistic nonuniform disk loading is assumed.
2. Rearward of this three-quarter diameter point, calculation of the induced velocity becomes increasingly inaccurate because the trailing-vortex system rolls up very rapidly, and the wake vortex pattern behind the rotor is altered from that assumed as a basis for the calculations.
3. At locations well behind the rotor, the induced flow may be calculated more accurately by assuming the rotor to be a uniformly loaded

rectangular wing, provided that the rotor lift coefficient is sufficiently high.

4. There is little effect of the assymmetries associated with tip-speed ratio on the induced flow along the longitudinal axis of the rotor.

5. The induced-velocity calculations of Mangler and Squire can be modified to account for the wake crossing the flow because of the finite lift coefficient.

Langley Aeronautical Laboratory,
National Advisory Committee for Aeronautics,
Langley Field, Va., February 23, 1956.

REFERENCES

1. Falabella, Gaetano, Jr., and Meyer, John R., Jr.: Determination of Inflow Distributions From Experimental Aerodynamic Loading and Blade-Motion Data on a Model Helicopter Rotor in Hovering and Forward Flight. NACA TN 3492, 1955.
2. Castles, Walter, Jr., and De Leeuw, Jacob Henri: The Normal Component of the Induced Velocity in the Vicinity of a Lifting Rotor and Some Examples of Its Application. NACA Rep. 1184, 1954. (Supersedes NACA TN 2912.)
3. Heyson, Harry H., and Katzoff, S.: The Normal Component of Induced Velocity in the Vicinity of a Lifting Rotor with a Nonuniform Disk Loading. NACA TN 3690, 1956.
4. Mangler, K. W., and Squire, H. B.: The Induced Velocity Field of a Rotor. R. & M. No. 2642, British A.R.C., May 1950.
5. Drees, J. Meijer: A Theory of Airflow Through Rotors and Its Application to Some Helicopter Problems. Jour. Helicopter Assoc. of Great Britain, vol. 3, no. 2, July-Aug.-Sept. 1949, pp. 79-104.
6. Coleman, Robert P., Feingold, Arnold M., and Stempin, Carl W.: Evaluation of the Induced-Velocity Field of an Idealized Helicopter Rotor. NACA WR L-126, 1945. (Formerly NACA ARR L5E10.)
7. Gessow, Alfred: Review of Information on Induced Flow of a Lifting Rotor. NACA TN 3238, 1954.
8. Ross, Robert S.: An Investigation of the Airflow Underneath Helicopter Rotors. Jour. Aero. Sci., vol. 13, no. 12, Dec. 1946, pp. 665-677.
9. Fail, R. A., and Eyre, R. C. W.: Downwash Measurements Behind a 12-Ft Diameter Helicopter Rotor in the 24-Ft Wind Tunnel. R. & M. No. 2810, British A.R.C., Sept. 1949.
10. Heyson, Harry H.: Preliminary Results From Flow-Field Measurements Around Single and Tandem Rotors in the Langley Full-Scale Tunnel. NACA TN 3242, 1954.
11. DeFrance, Smith J.: The N.A.C.A. Full-Scale Wind Tunnel. NACA Rep. 459, 1933.
12. Lange, Roy H., and Fink, Marvin P.: Studies of the Flow Field Behind a Large-Scale 47.5° Sweptback Wing Having Circular-Arc Airfoil Sections and Equipped With Drooped-Nose and Plain Flaps. NACA RM L51L12, 1952.

13. Silverstein, Abe, and Katzoff, S.: Experimental Investigation of Wind-Tunnel Interference on the Downwash Behind an Airfoil. NACA Rep. 609, 1937.
14. Spreiter, John R., and Sacks, Alvin H.: The Rolling Up of the Trailing Vortex Sheet and Its Effect on the Downwash Behind Wings. Jour. Aero. Sci., vol. 18, no. 1, Jan. 1951, pp. 21-32, 72.
15. Silverstein, Abe, Katzoff, S., and Bullivant, W. Kenneth: Downwash and Wake Behind Plain and Flapped Airfoils. NACA Rep. 651, 1939.

TABLE I.- FLIGHT CONDITIONS

Tip-speed ratio, μ	Rotor wake skew angle, χ , deg	C_L	C_T	ΩR , ft/sec	Disk loading, lb/sq ft	Equivalent flat- plate area, f , sq ft	Angle of attack, α , deg
0.095	75.0	0.720	0.00320	500	1.91	2.77	-9.2
.139	85.8	^a 0.386	^a 0.00373	500	^a 2.18	2.34	-1.1
.140	82.3	^a 0.373	^a 0.00371	500	^a 2.21	2.79	-5.3
.232	83.9	.122	.00321	450	1.55	1.35	-9.5

^aThe seeming inconsistency between the values of rotor lift coefficient and thrust coefficient on one hand and the values of average disk load on the other was caused by a slight difference in the density of air at the different times during which the tests were run.

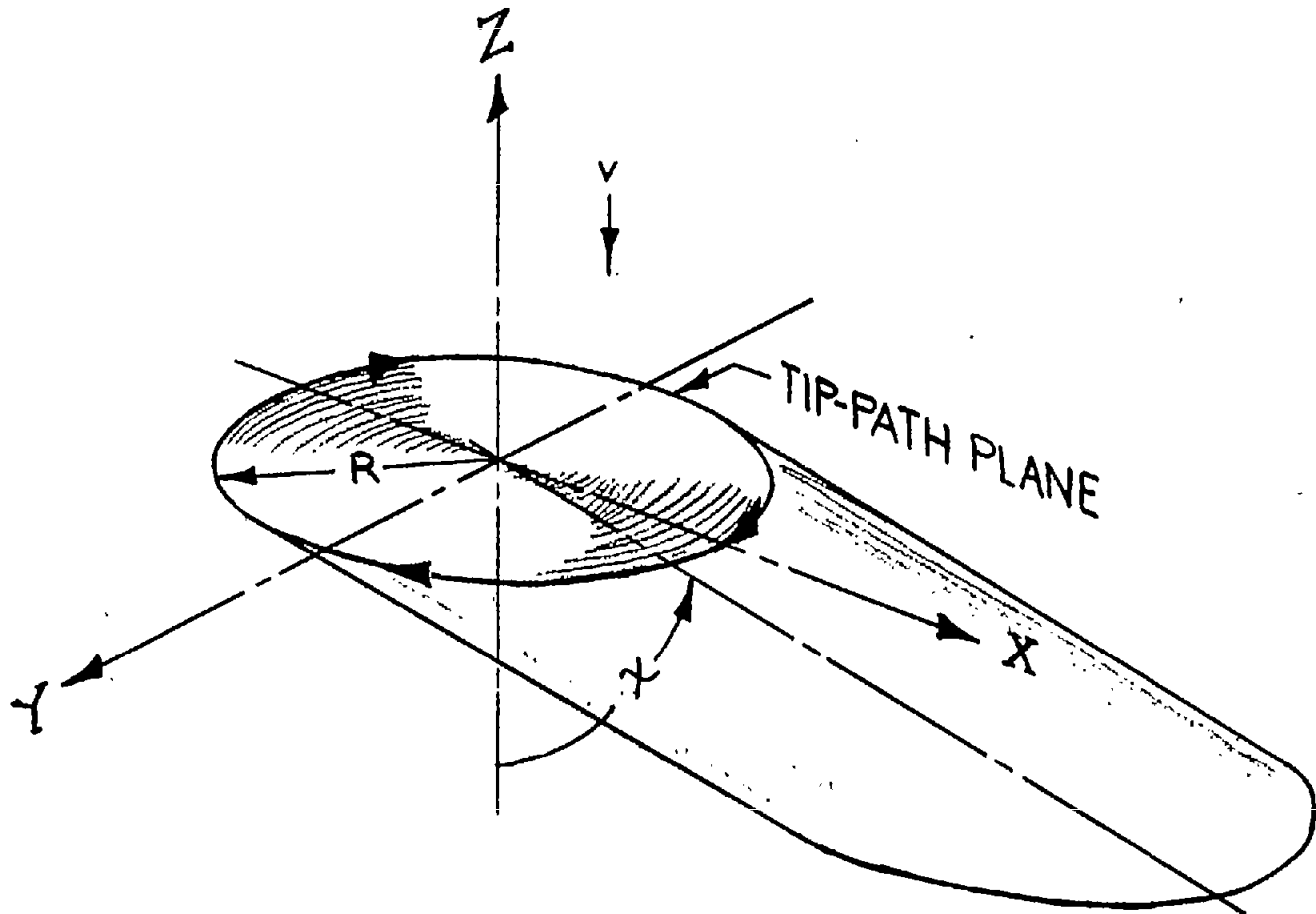
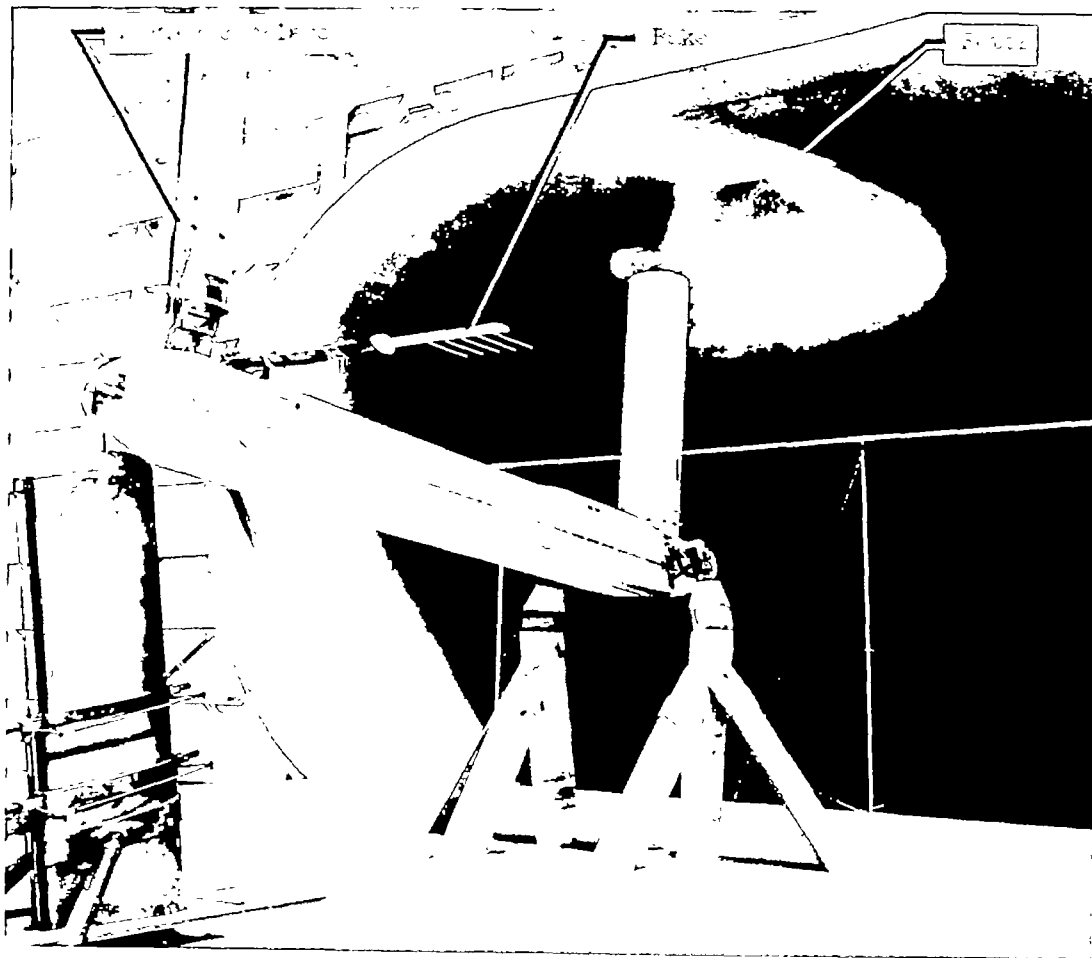
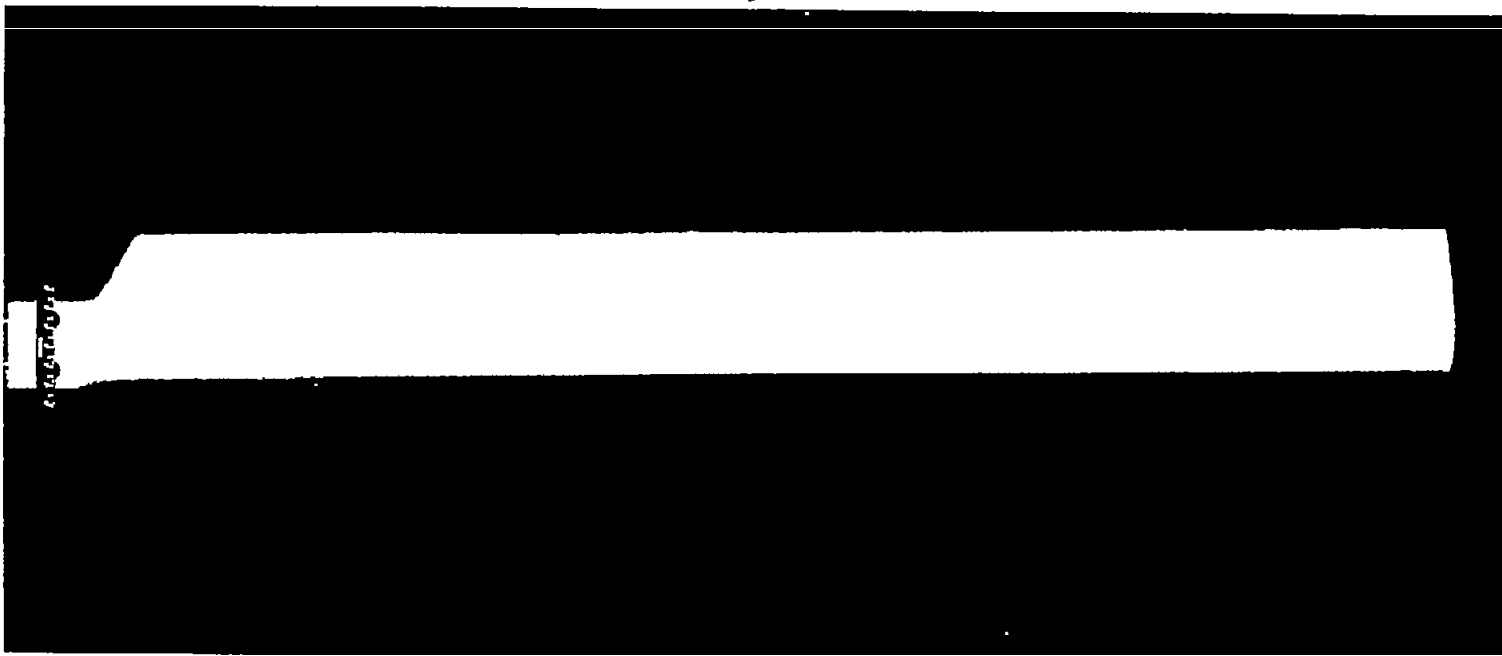


Figure 1.- Coordinate system of rotor and wake. Arrows indicate positive directions.



(a) Test setup looking into entrance cone of tunnel. L-83264.1

Figure 2.- Equipment used in surveys.



(b) Rotor blade.

L-91957

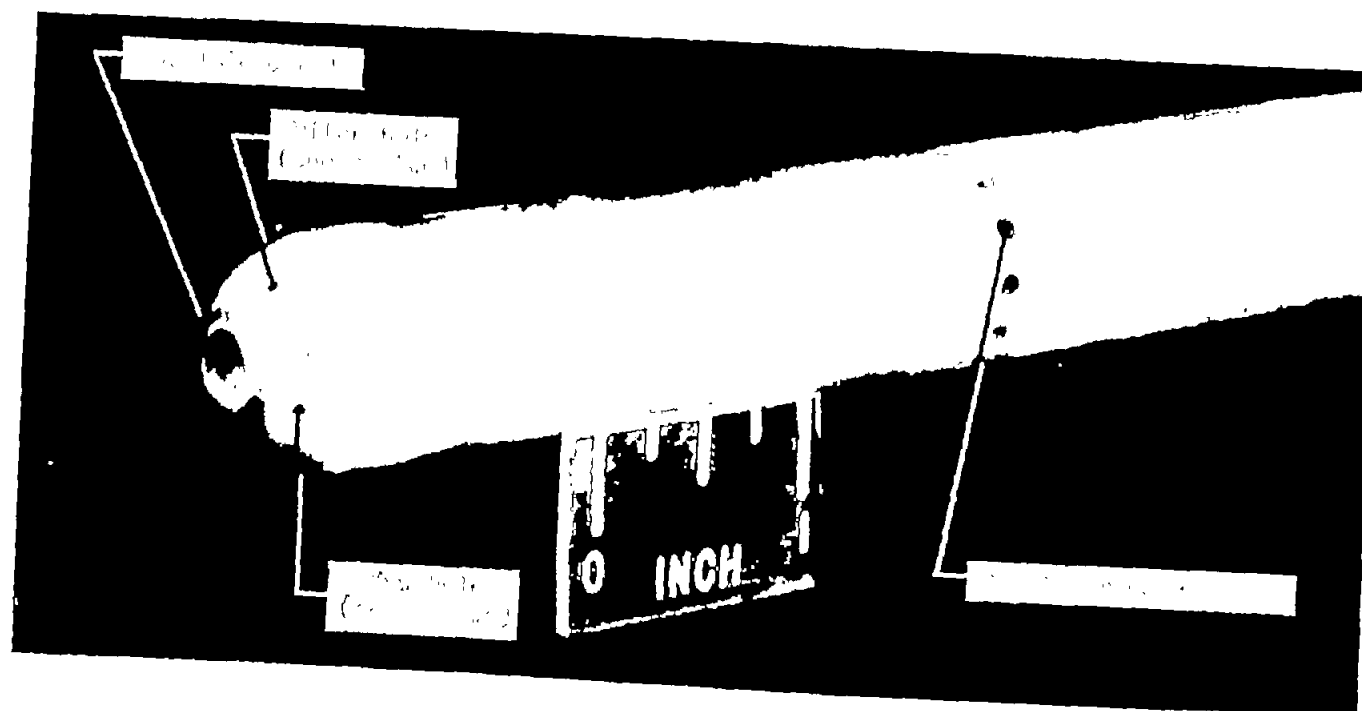
Figure 2.- Continued.



(c) Rakes as mounted on survey-carriage ram.

L-87200.1

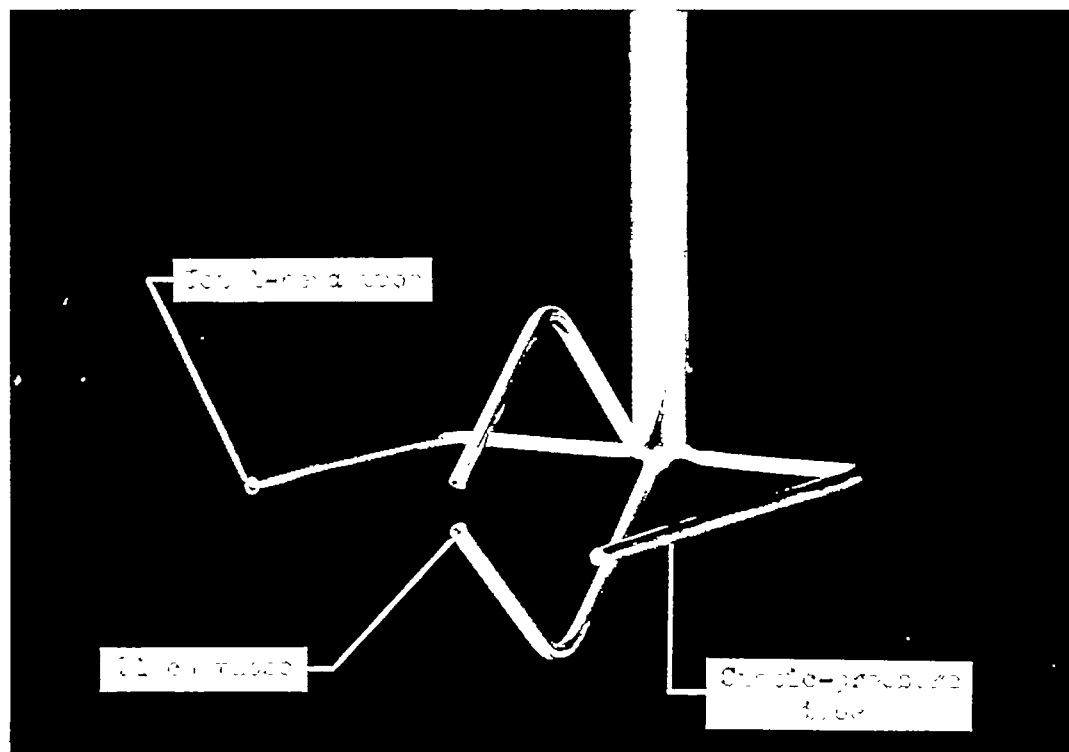
Figure 2.- Continued.



(d) End of one tube of five-tube rake.

L-91956.1

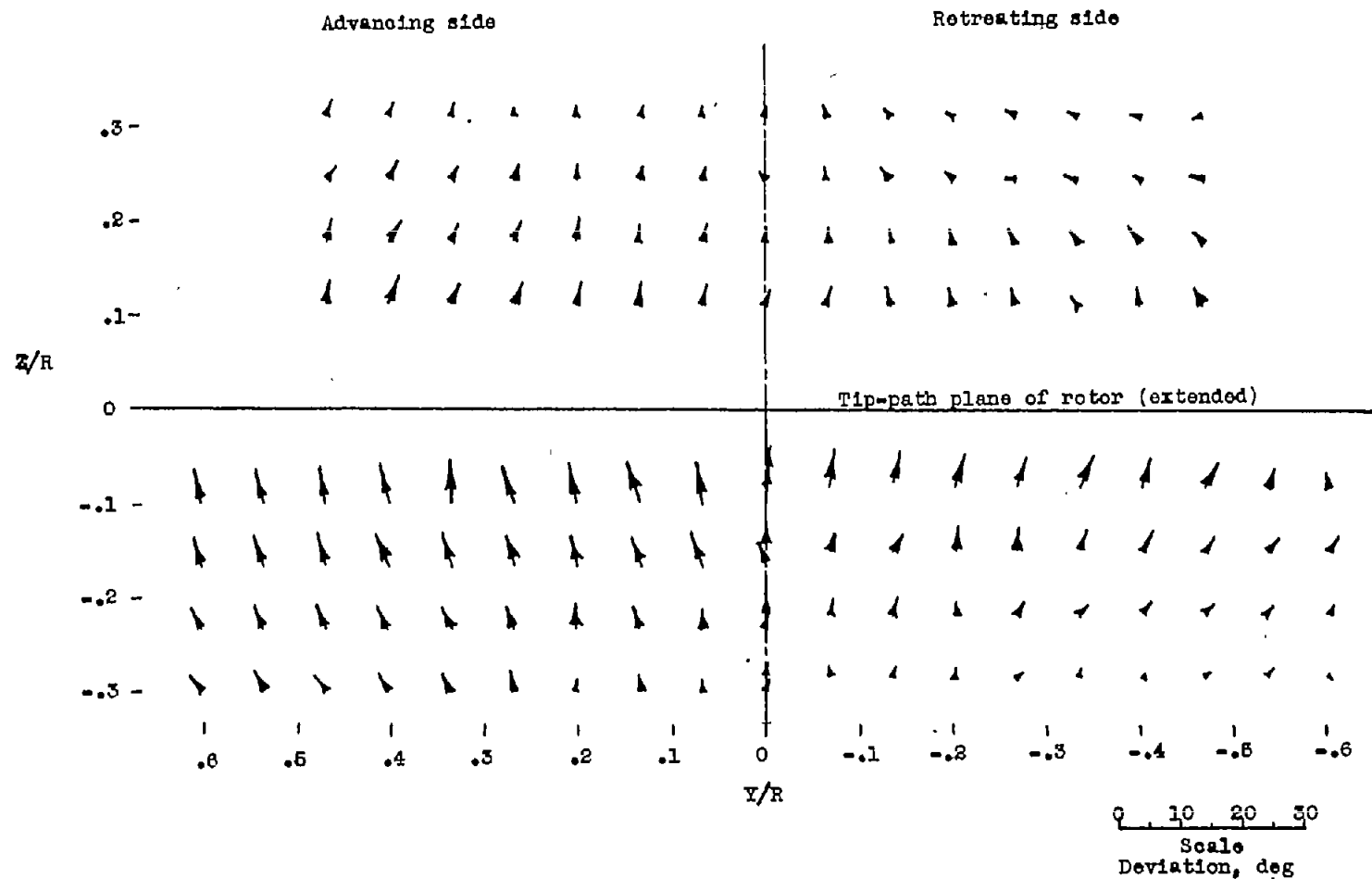
Figure 2.- Continued.



(e) Small pitch head.

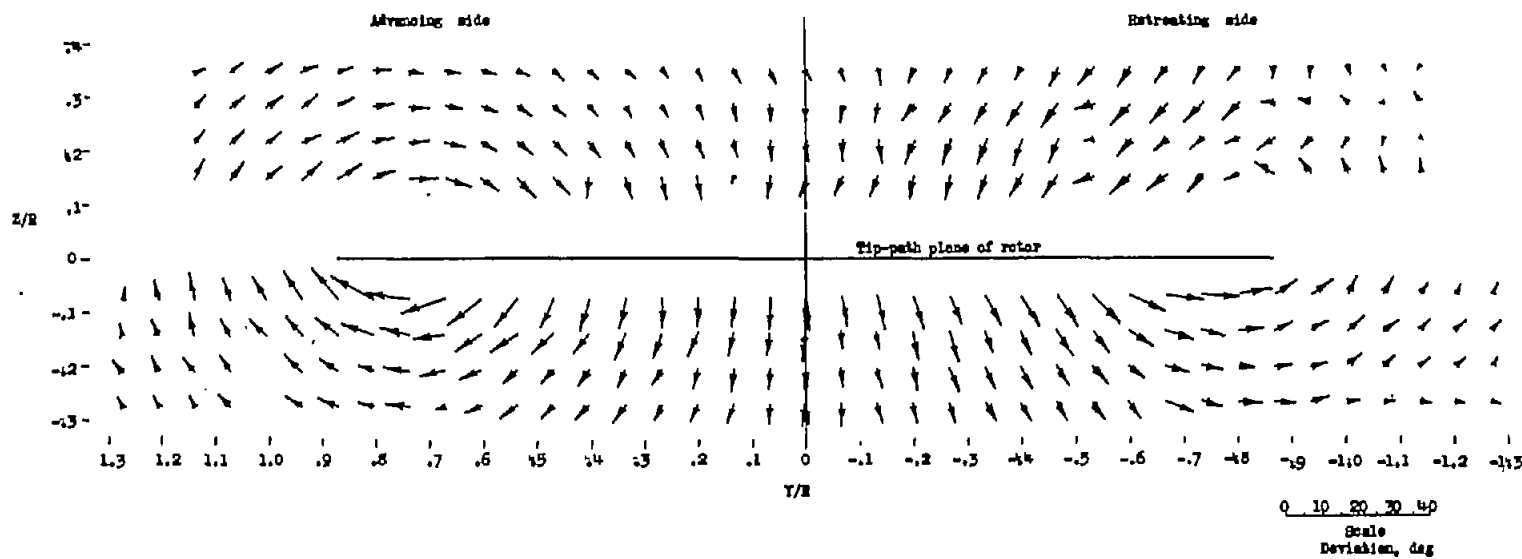
L-87202.1

Figure 2.- Concluded.



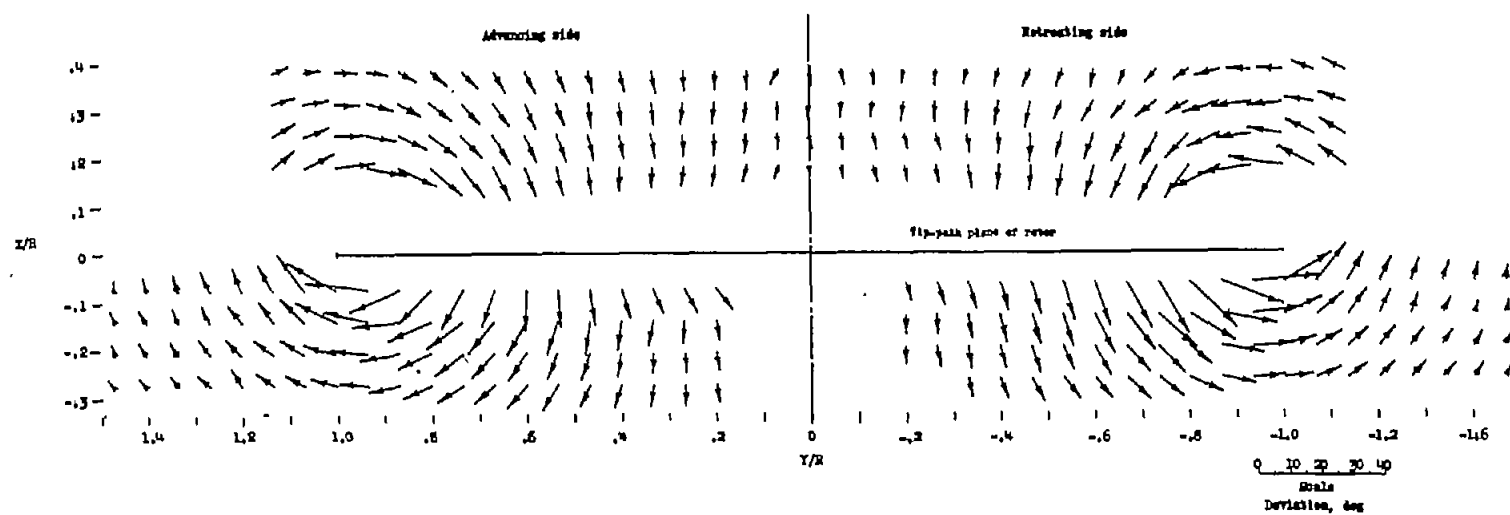
(a) $X/R = -1.0$.

Figure 3.- Measured stream angles in vicinity of rotor. Horizontal and vertical components of vectors represent yaw and pitch angles. Base of vector is at point of measurement. $\alpha = 75.0^\circ$; $\mu = 0.095$.



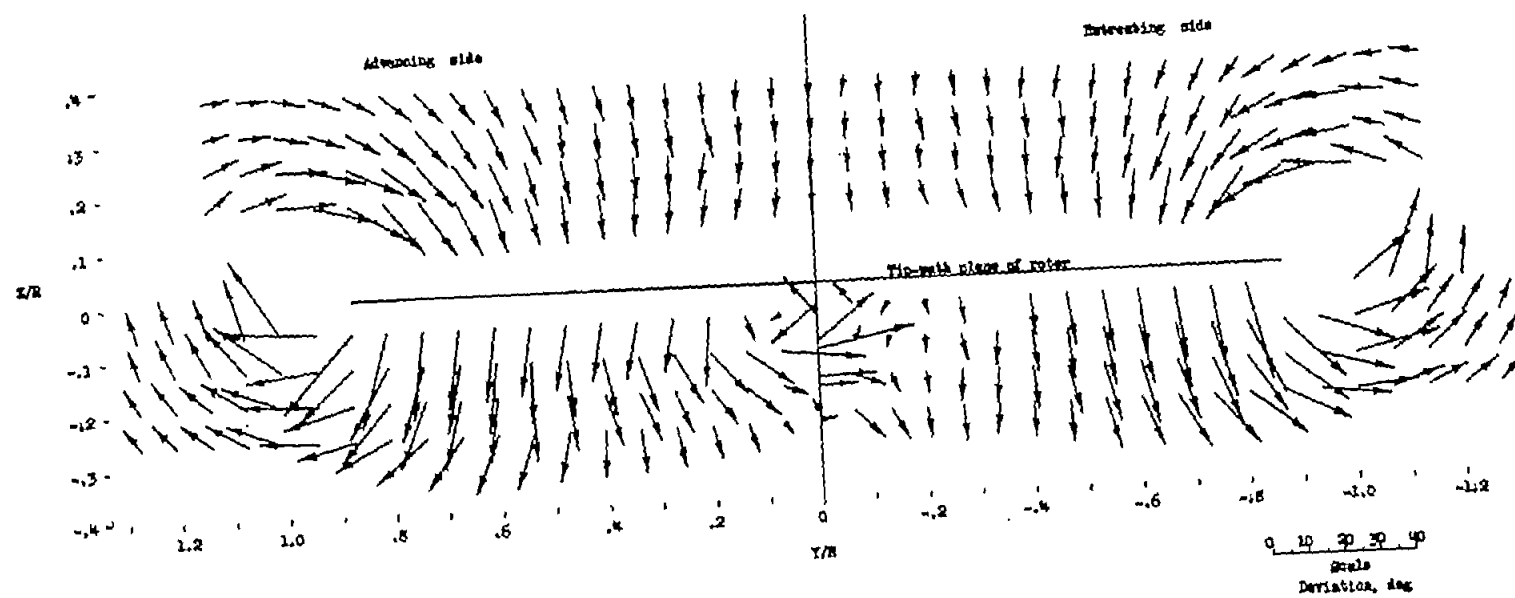
(b) $X/R = -0.5$.

Figure 3.- Continued.



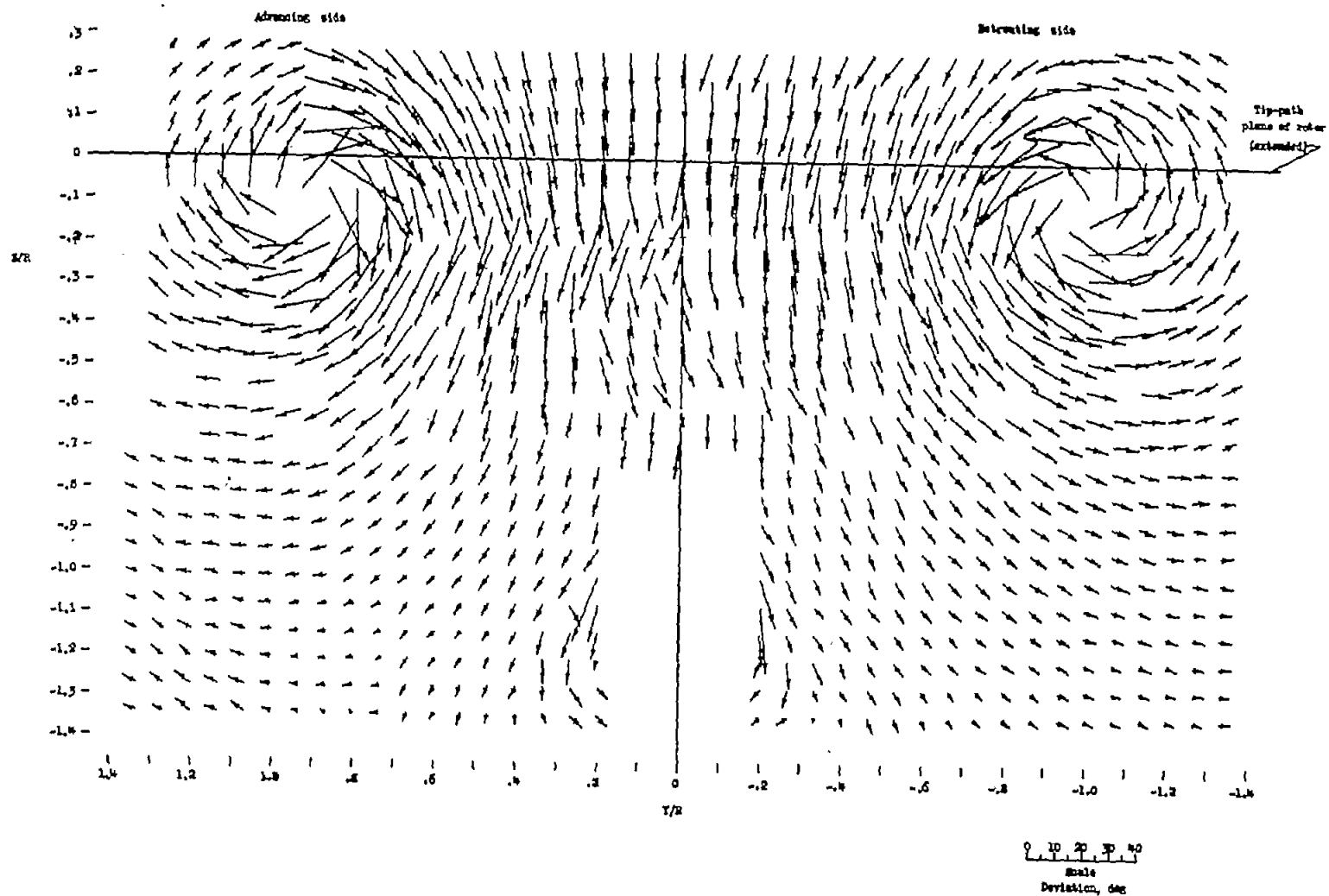
(c) $X/R = 0$.

Figure 3.- Continued.



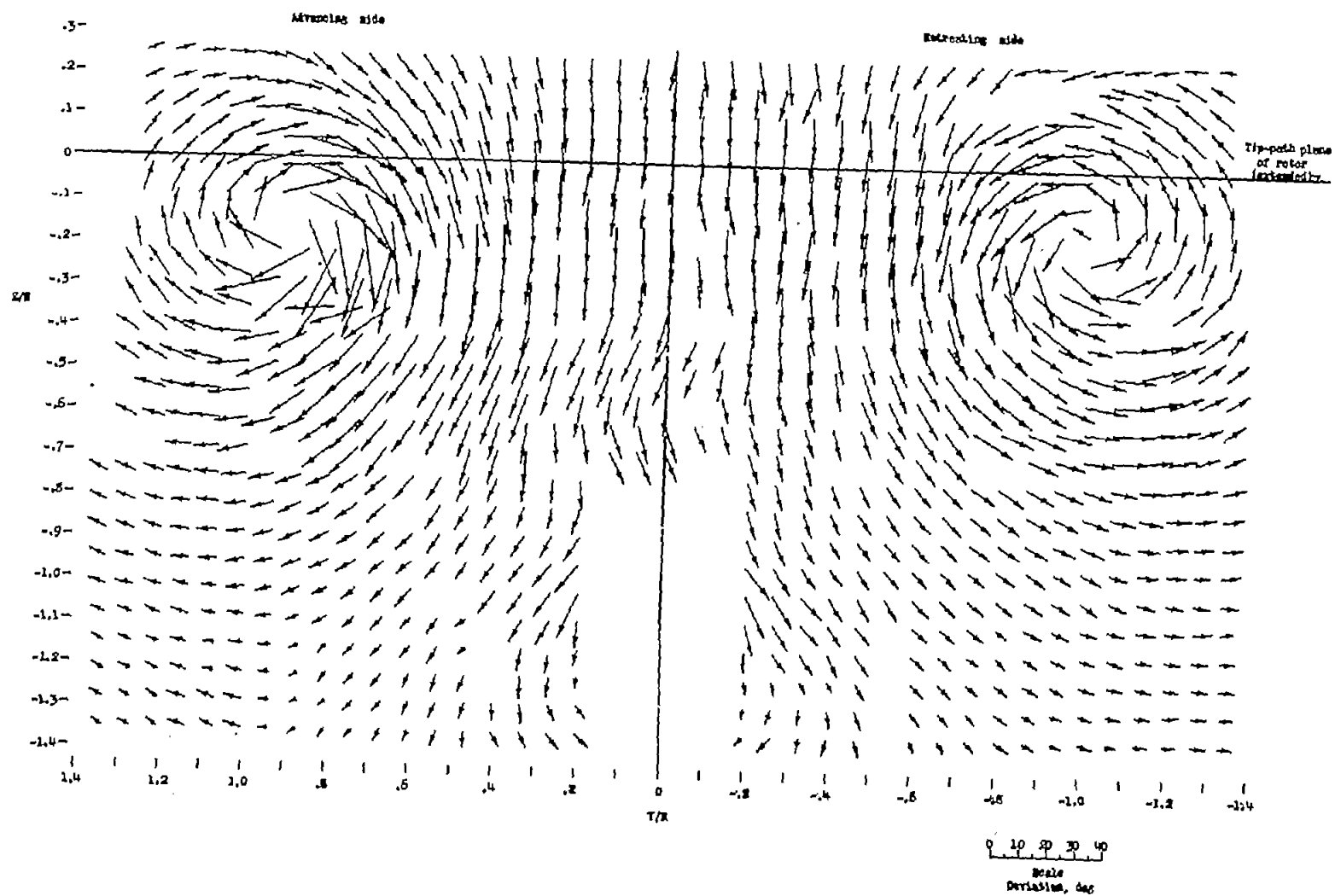
(d) $X/R = 0.5$.

Figure 3.- Continued.



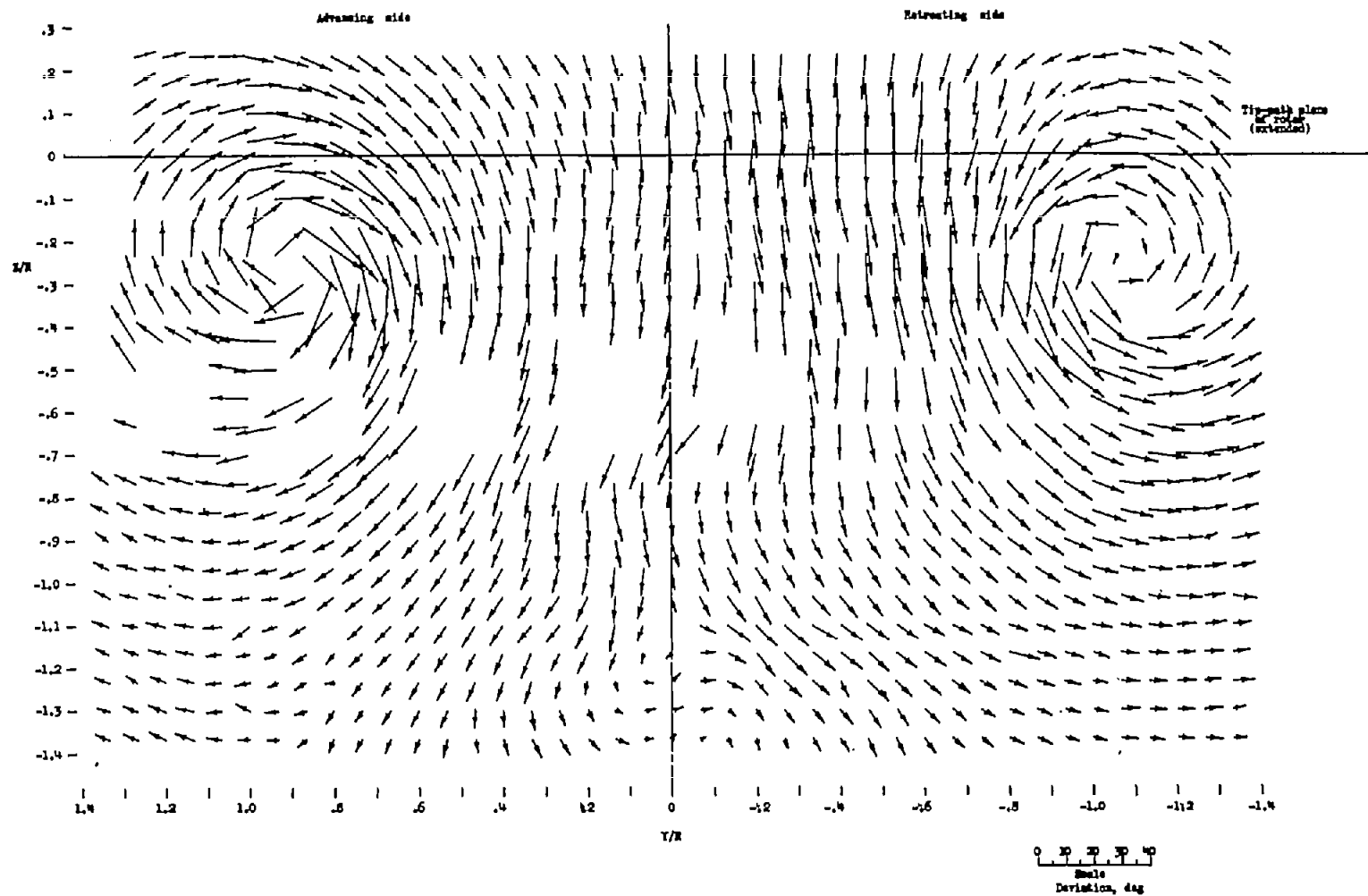
(e) $X/R = 1.07$.

Figure 3.- Continued.



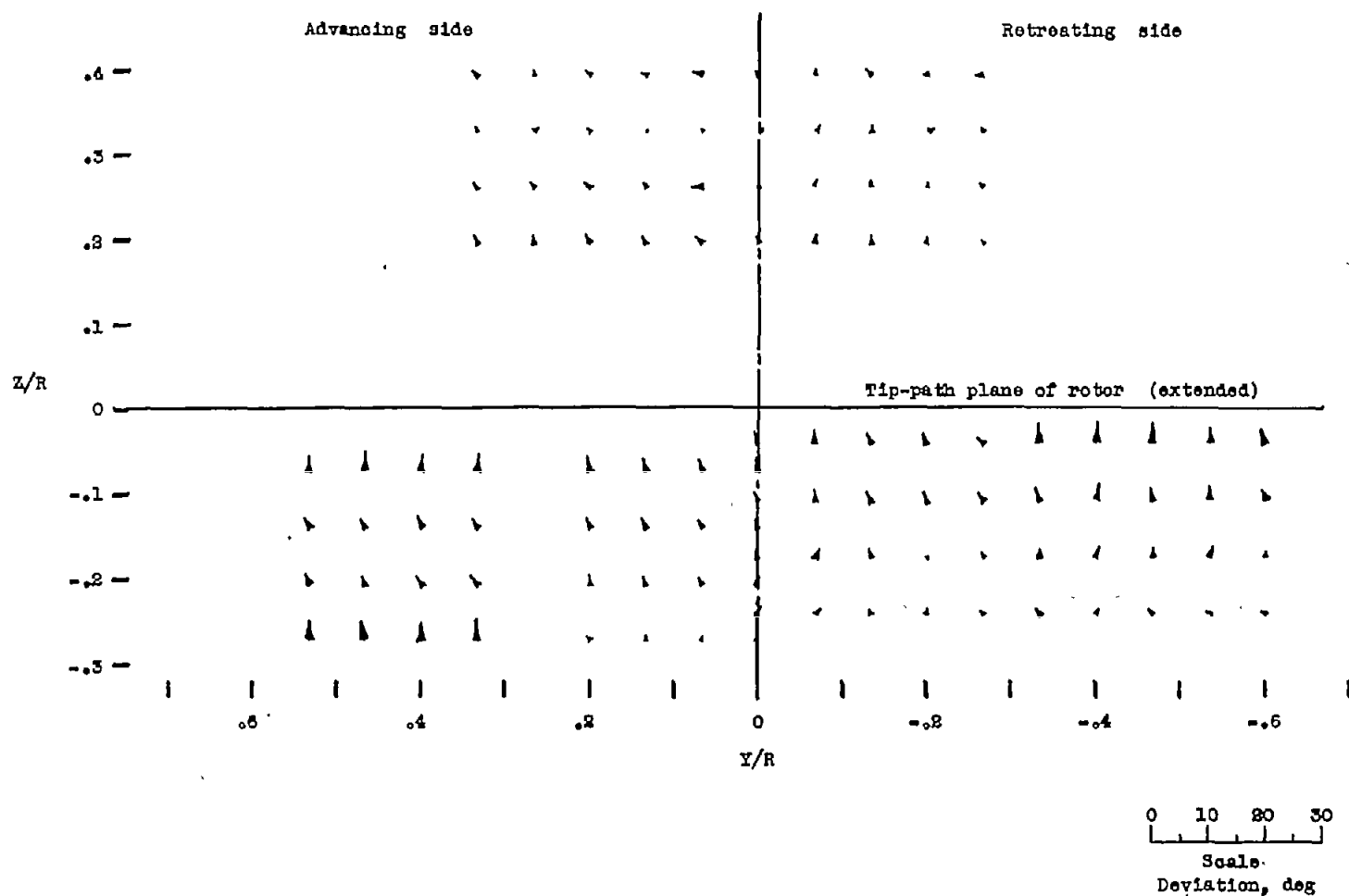
(f) $X/R = 2.07$.

Figure 3.- Continued.



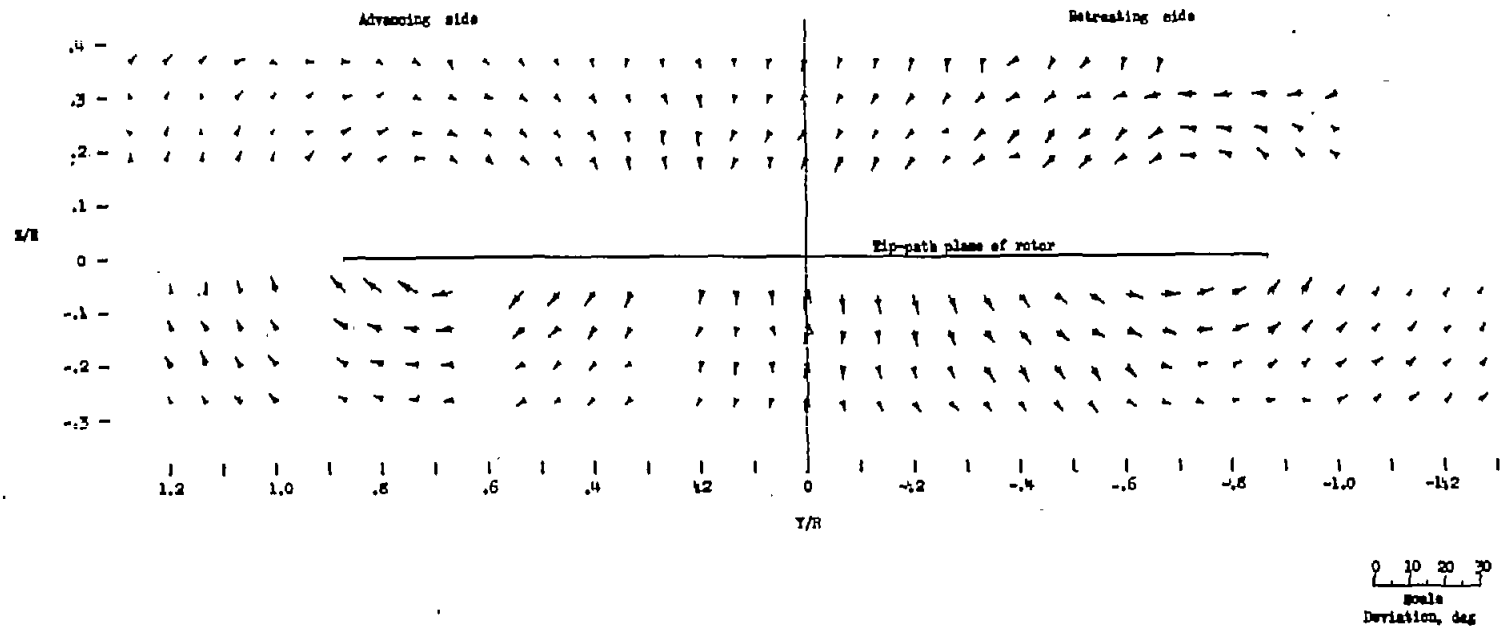
(g) $X/R = 3.14$.

Figure 3.- Concluded.



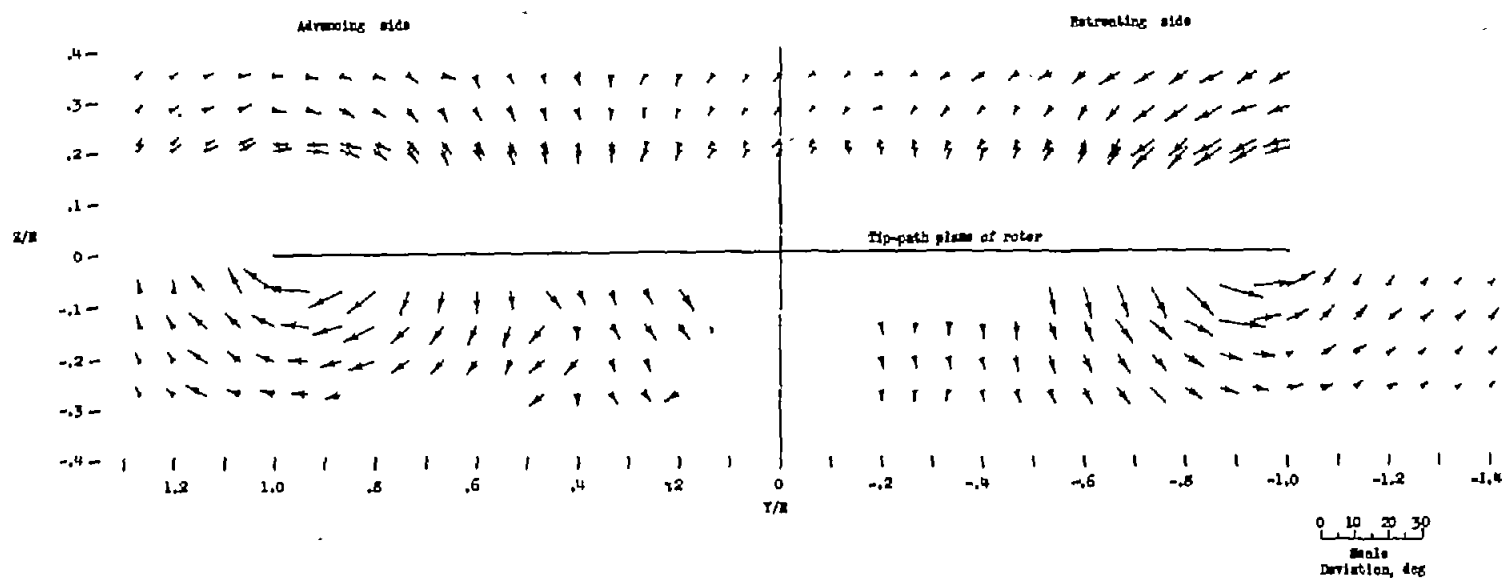
(a) $X/R = -1.0$.

Figure 4.- Measured stream angles in vicinity of rotor. Horizontal and vertical components of vectors represent yaw and pitch angles. Base of vector is at point of measurement. $\chi = 82.3^\circ$; $\mu = 0.140$.



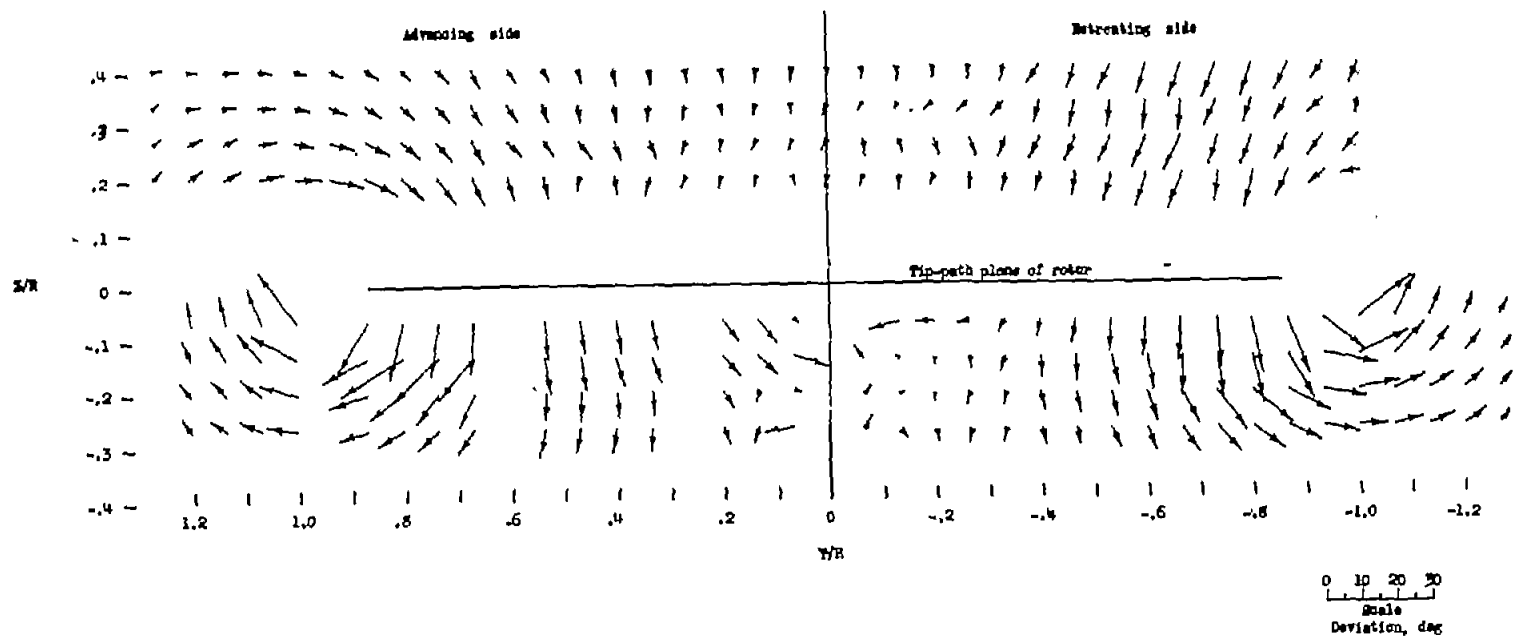
(b) $X/R = -0.5$.

Figure 4.- Continued.



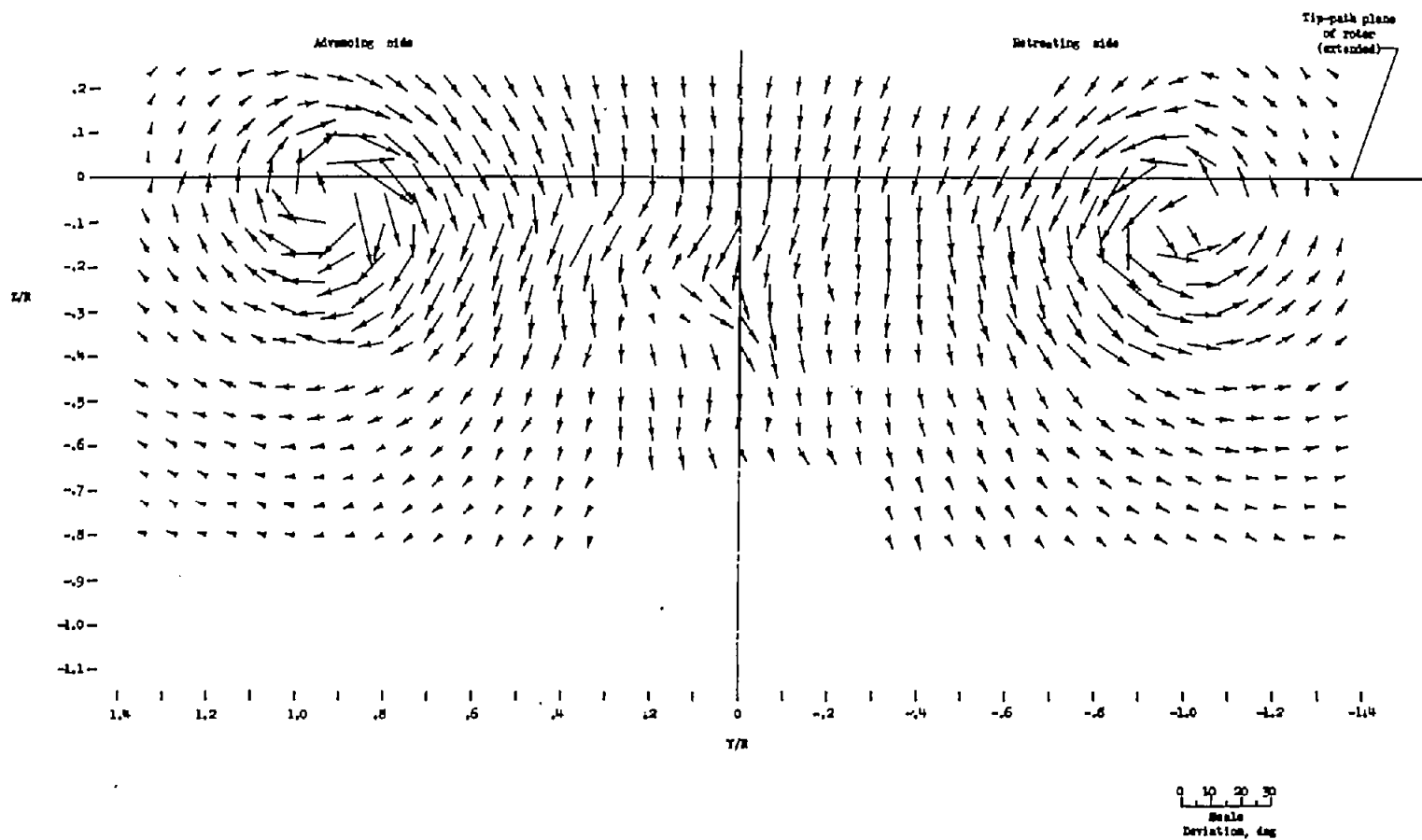
(c) $X/R = 0$.

Figure 4.- Continued.



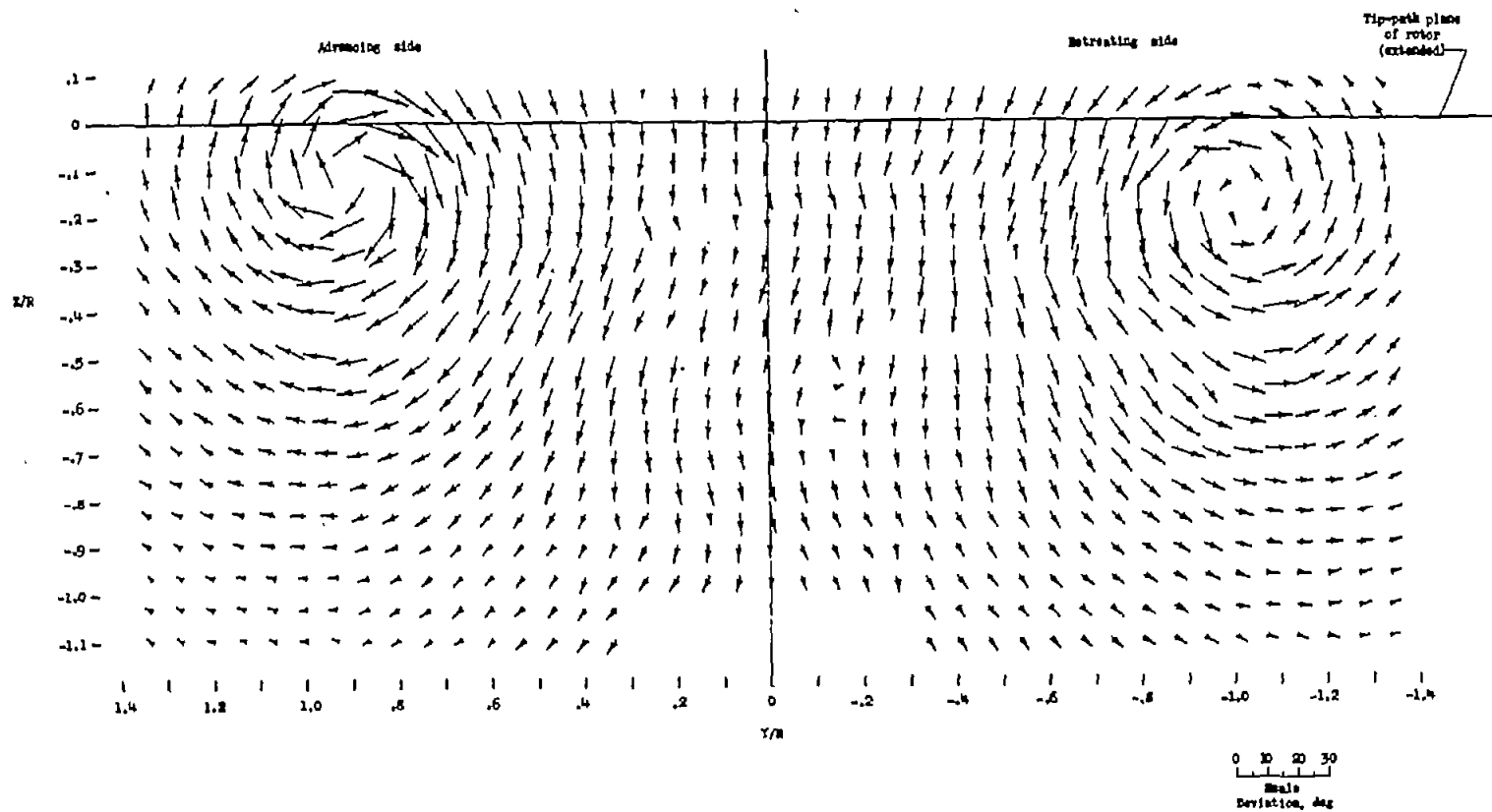
(d) $X/R = 0.5$.

Figure 4.- Continued.



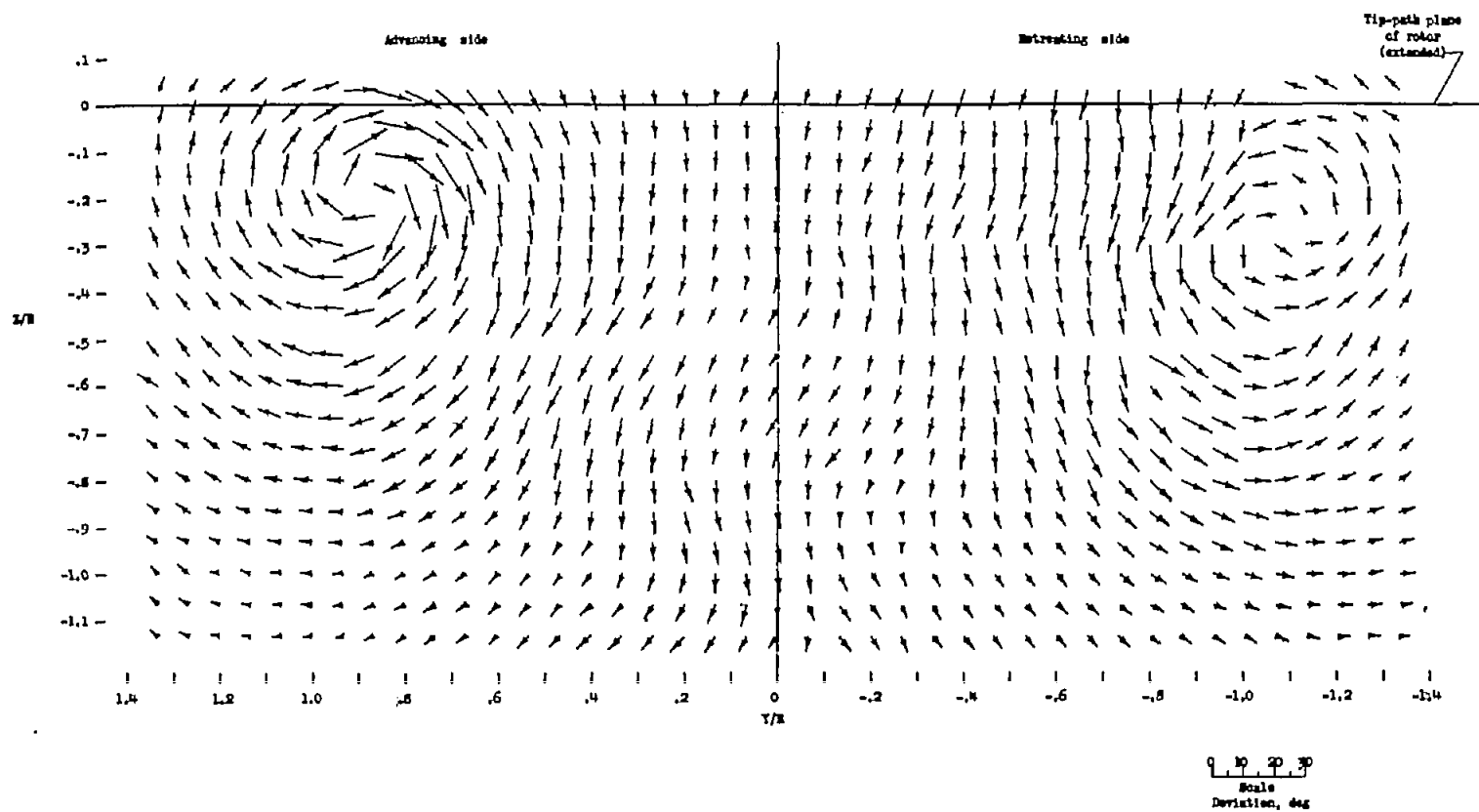
(e) $X/R = 1.07$.

Figure 4.- Continued.



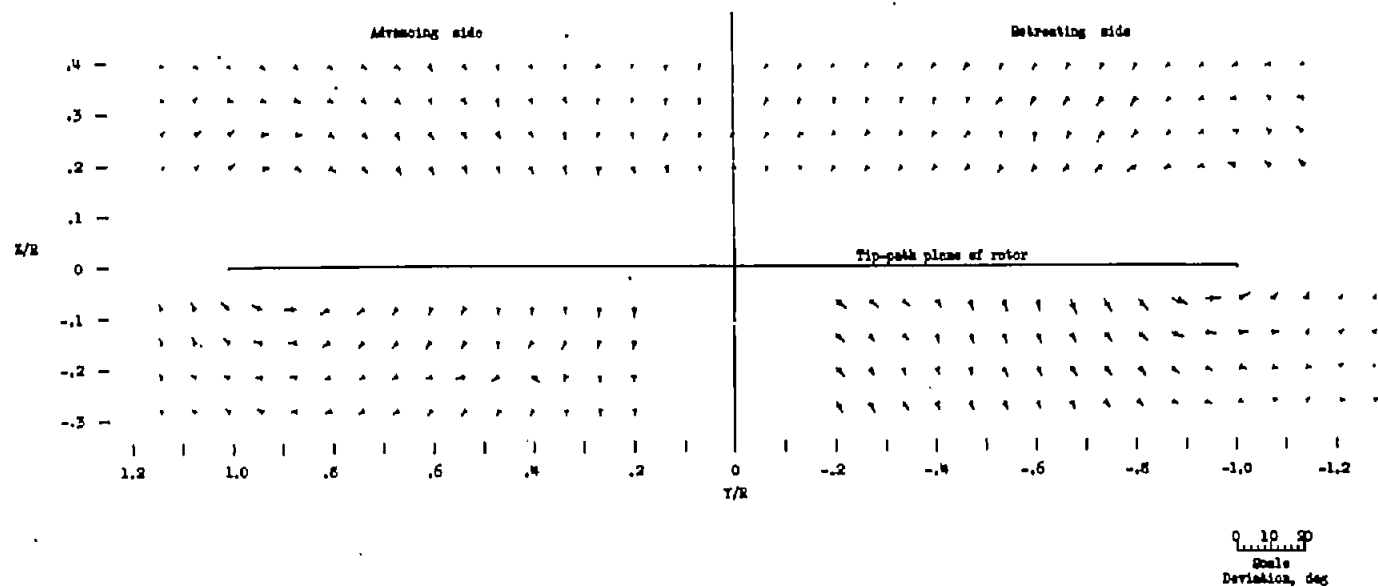
(f) $X/R = 2.07$.

Figure 4.- Continued.



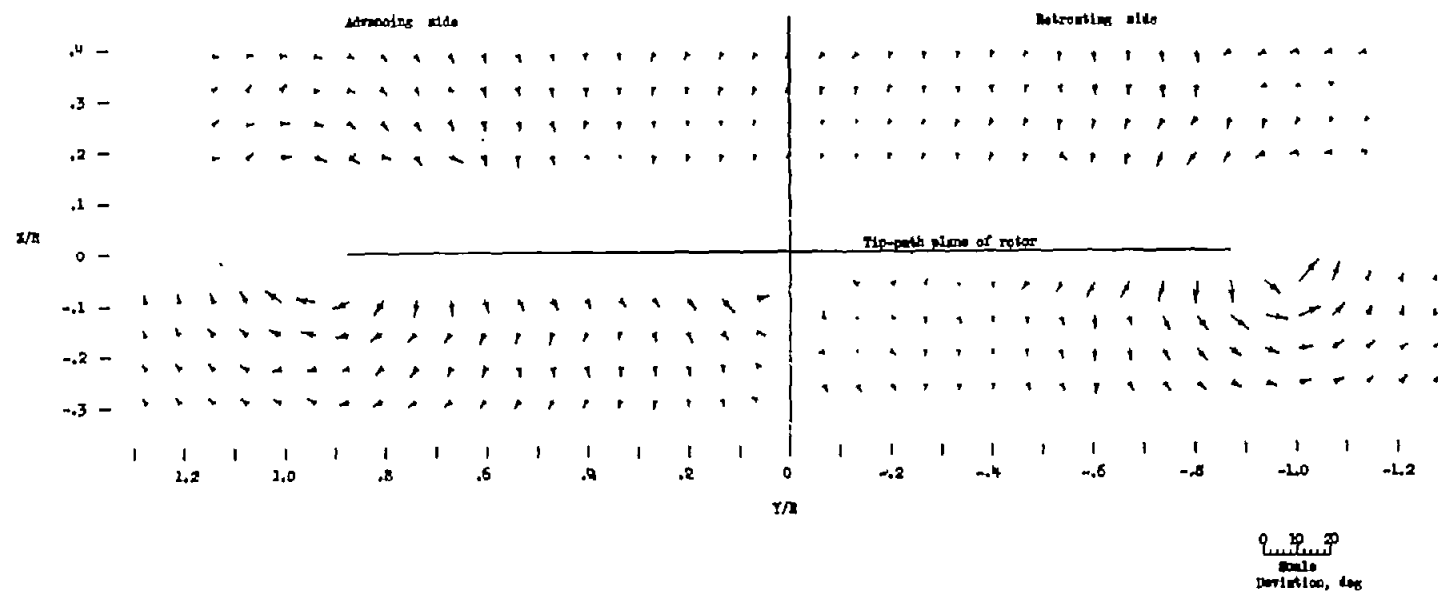
(g) $X/R = 3.14$.

Figure 4.- Concluded.



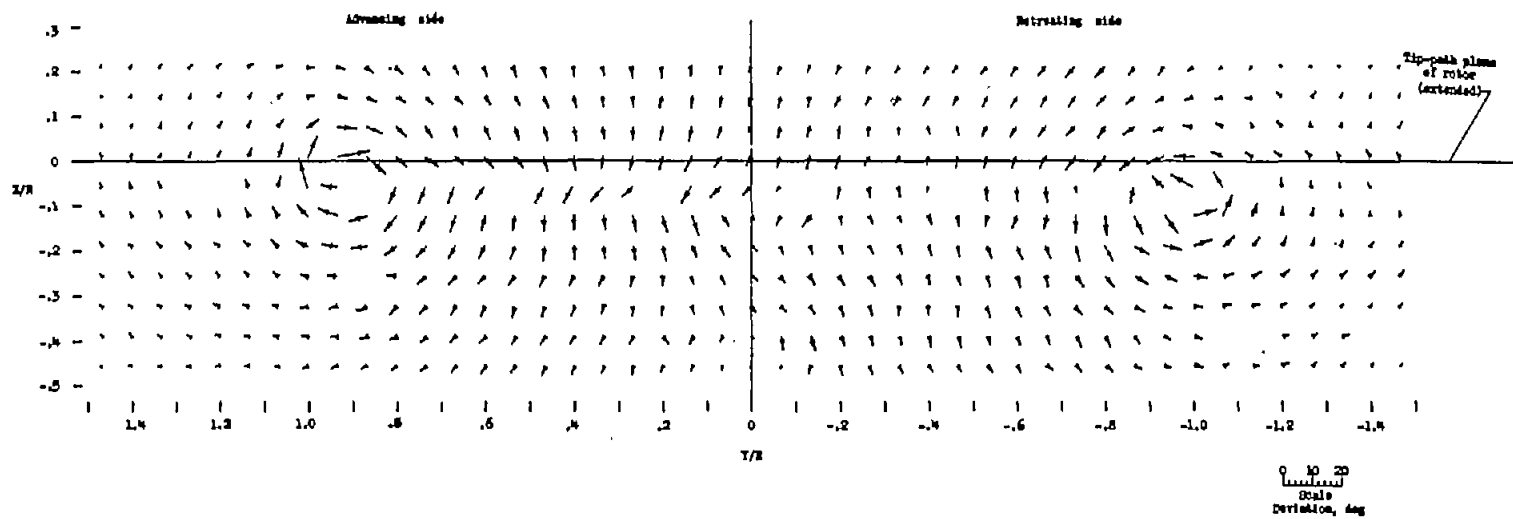
(a) $X/R = 0$.

Figure 5.- Measured stream angles in vicinity of rotor. Horizontal and vertical components represent yaw and pitch angles. Base of vector is at point of measurement. $\chi = 83.9^\circ$; $\mu = 0.232$.



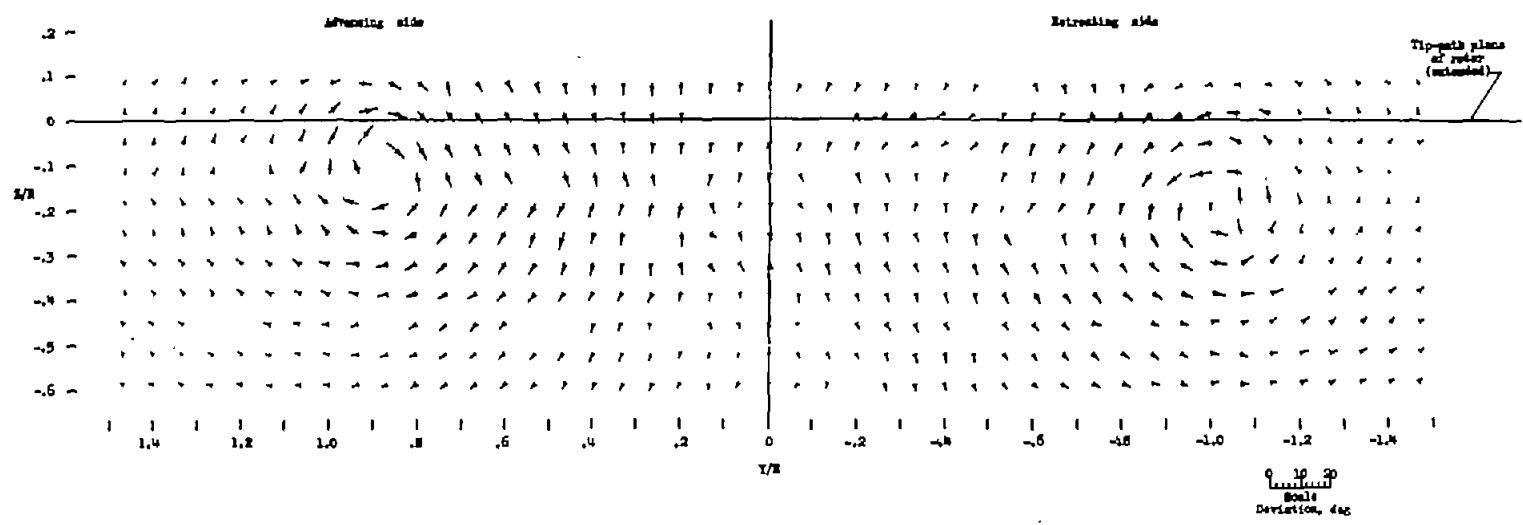
(b) $X/R = 0.5$.

Figure 5.- Continued.



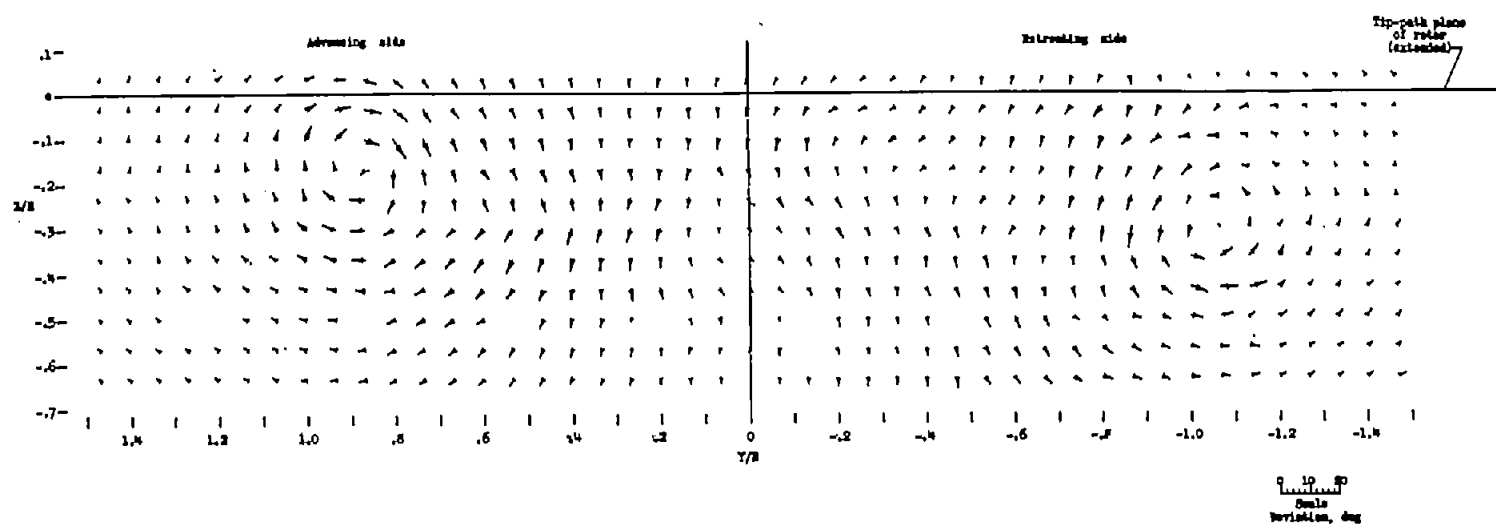
(c) $X/R = 1.07$.

Figure 5.- Continued.



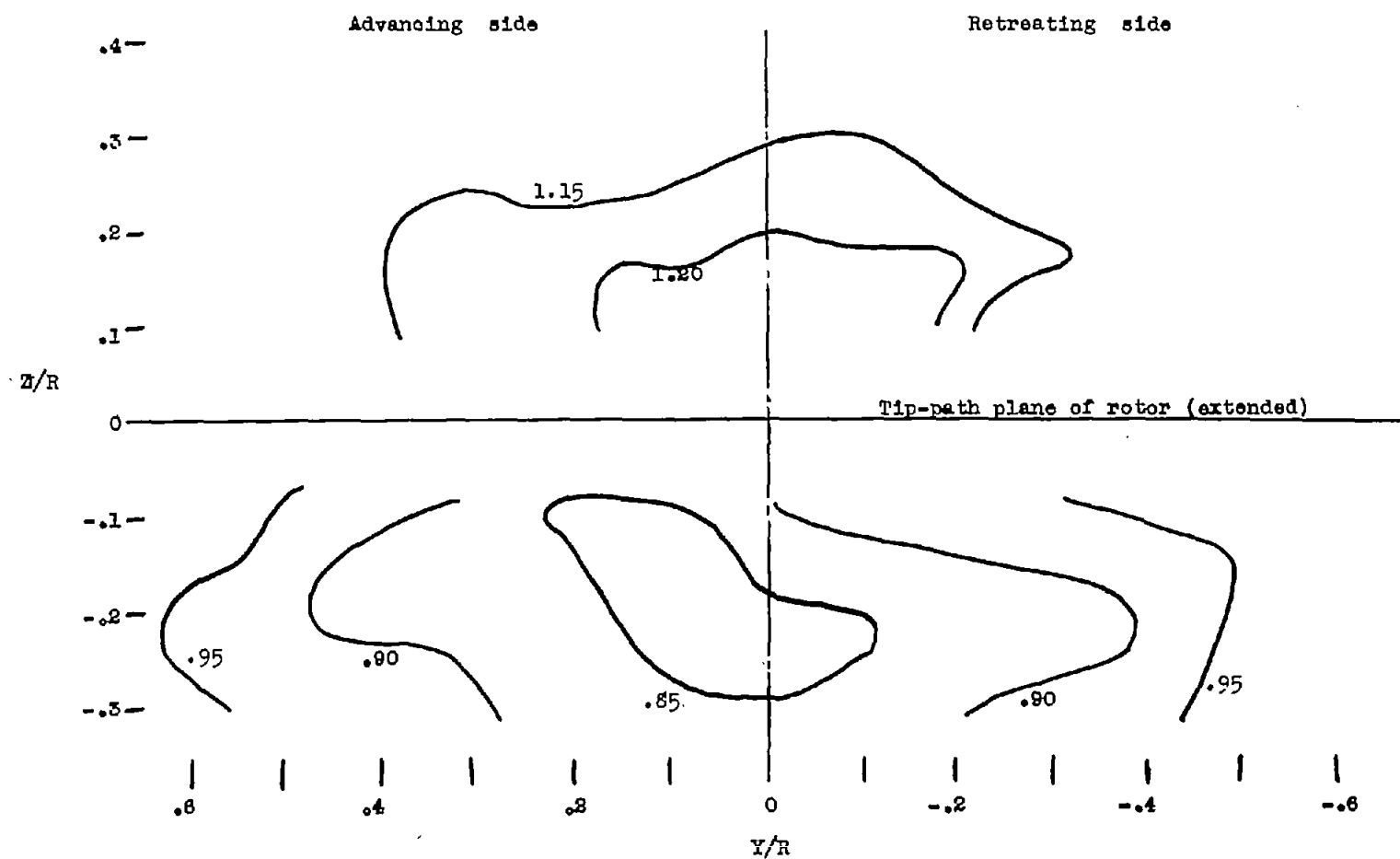
(d) $X/R = 2.07$.

Figure 5.- Continued.



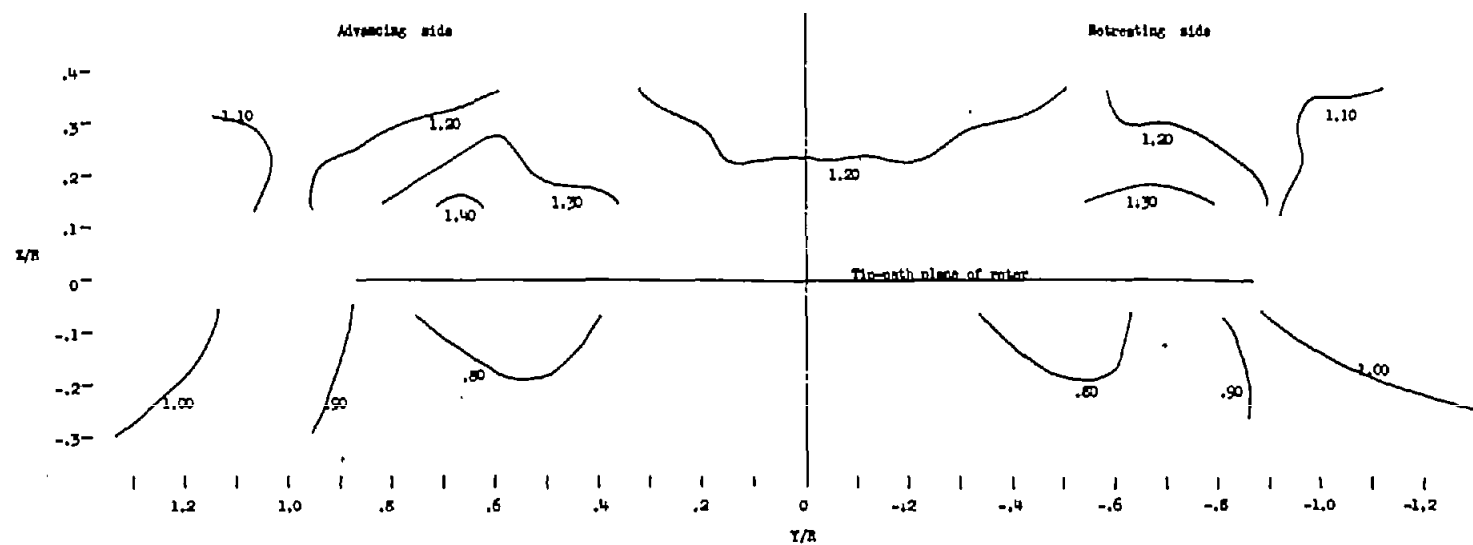
(e) $X/R = 3.14$.

Figure 5.- Concluded.



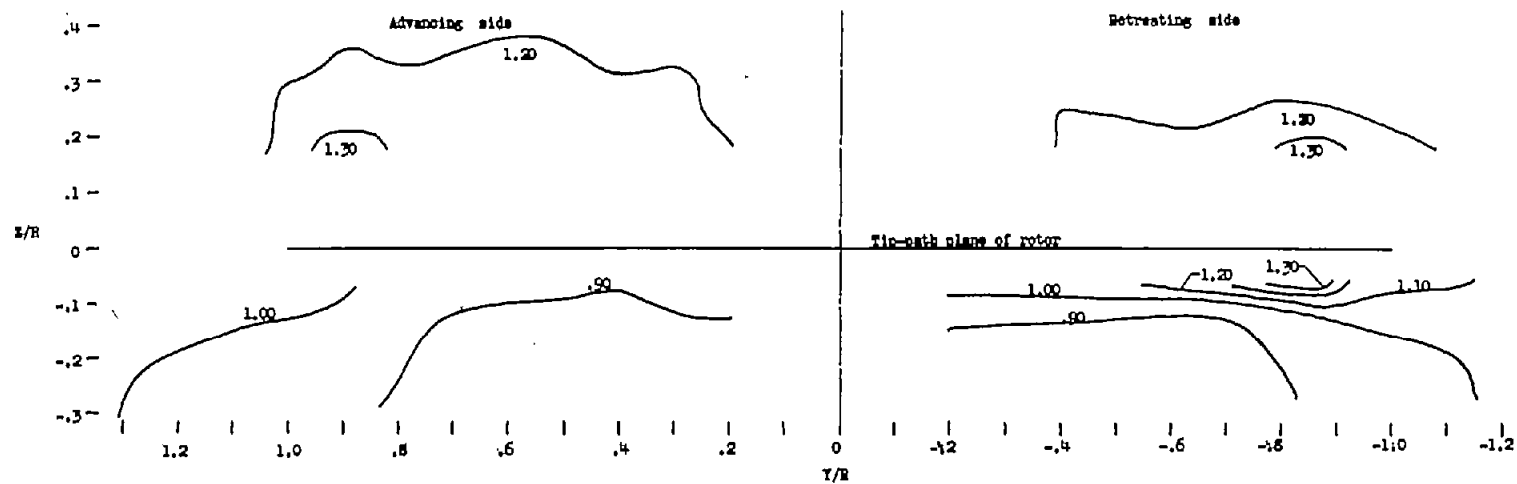
(a) $X/R = -1.0$.

Figure 6.- Contours of dynamic pressure q/q_0 in the vicinity of the rotor. $\chi = 75.0^\circ$; $\mu = 0.095$.



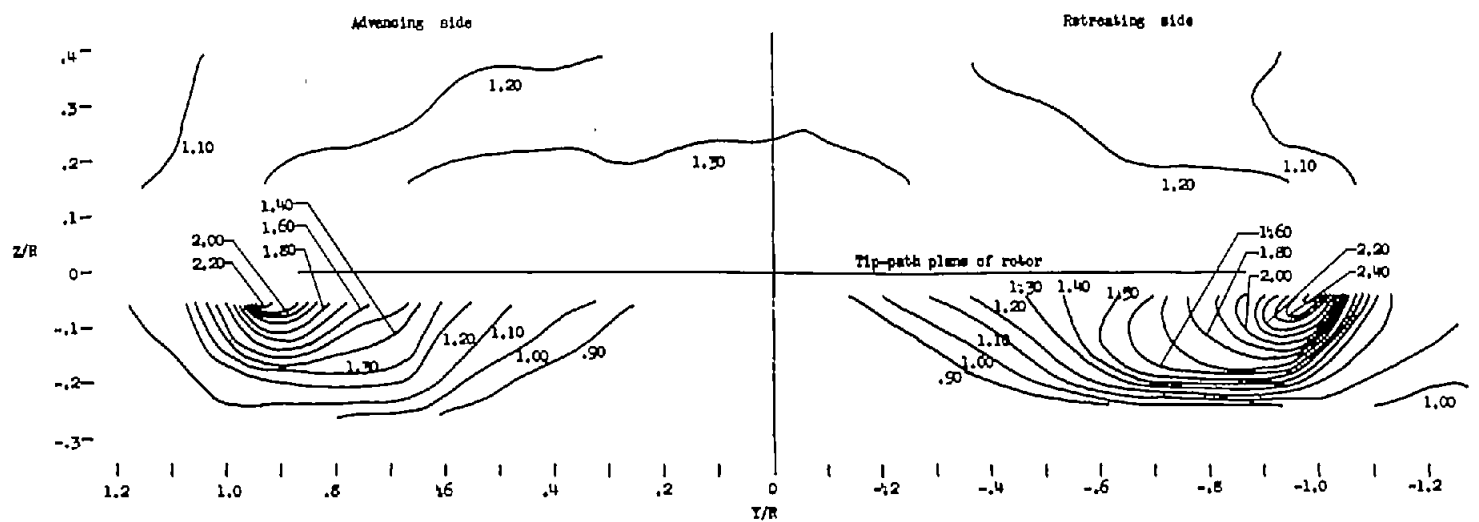
(b) $X/R = -0.50$.

Figure 6.- Continued.



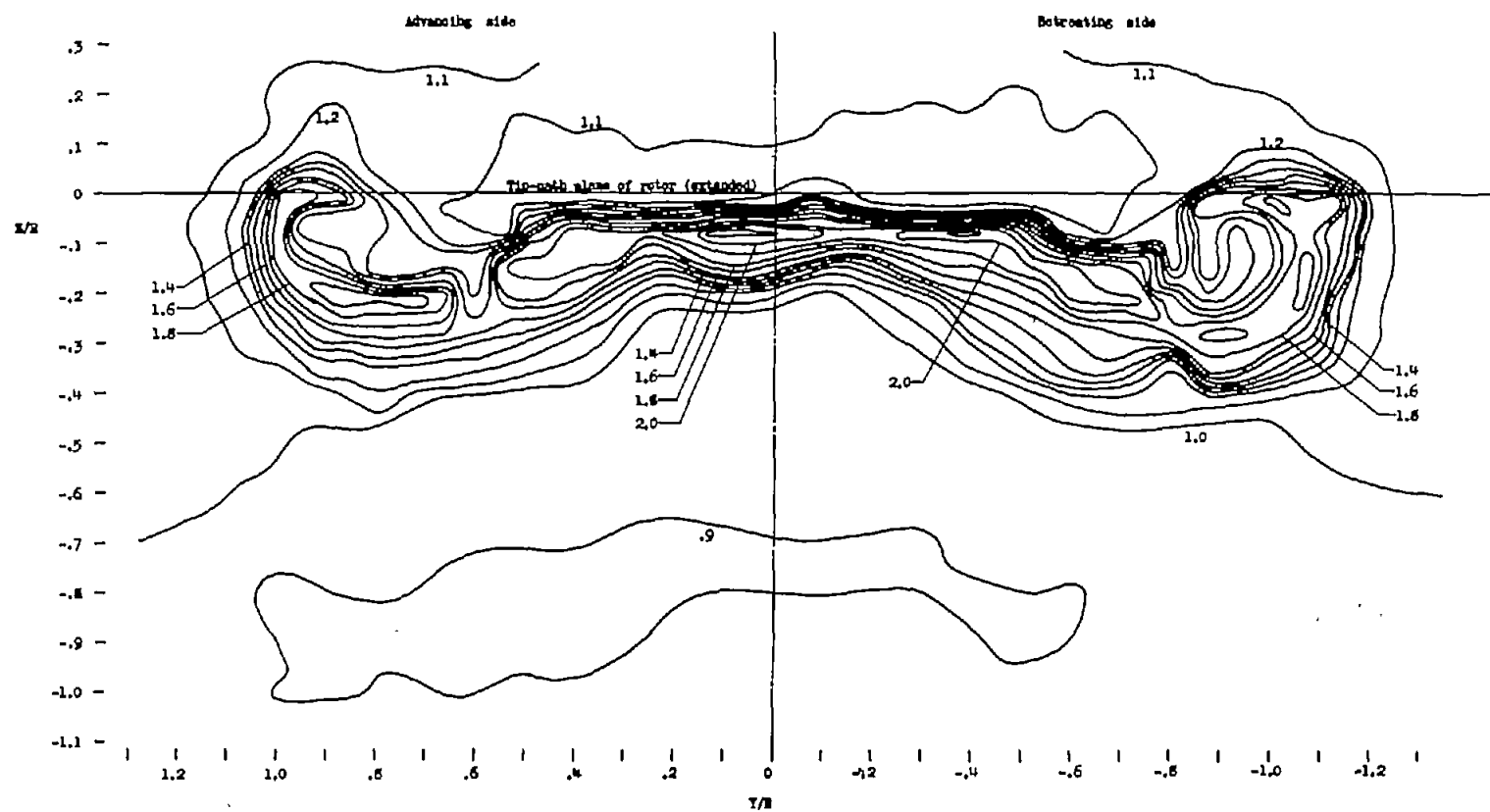
(c) $X/R = 0$.

Figure 6.- Continued.



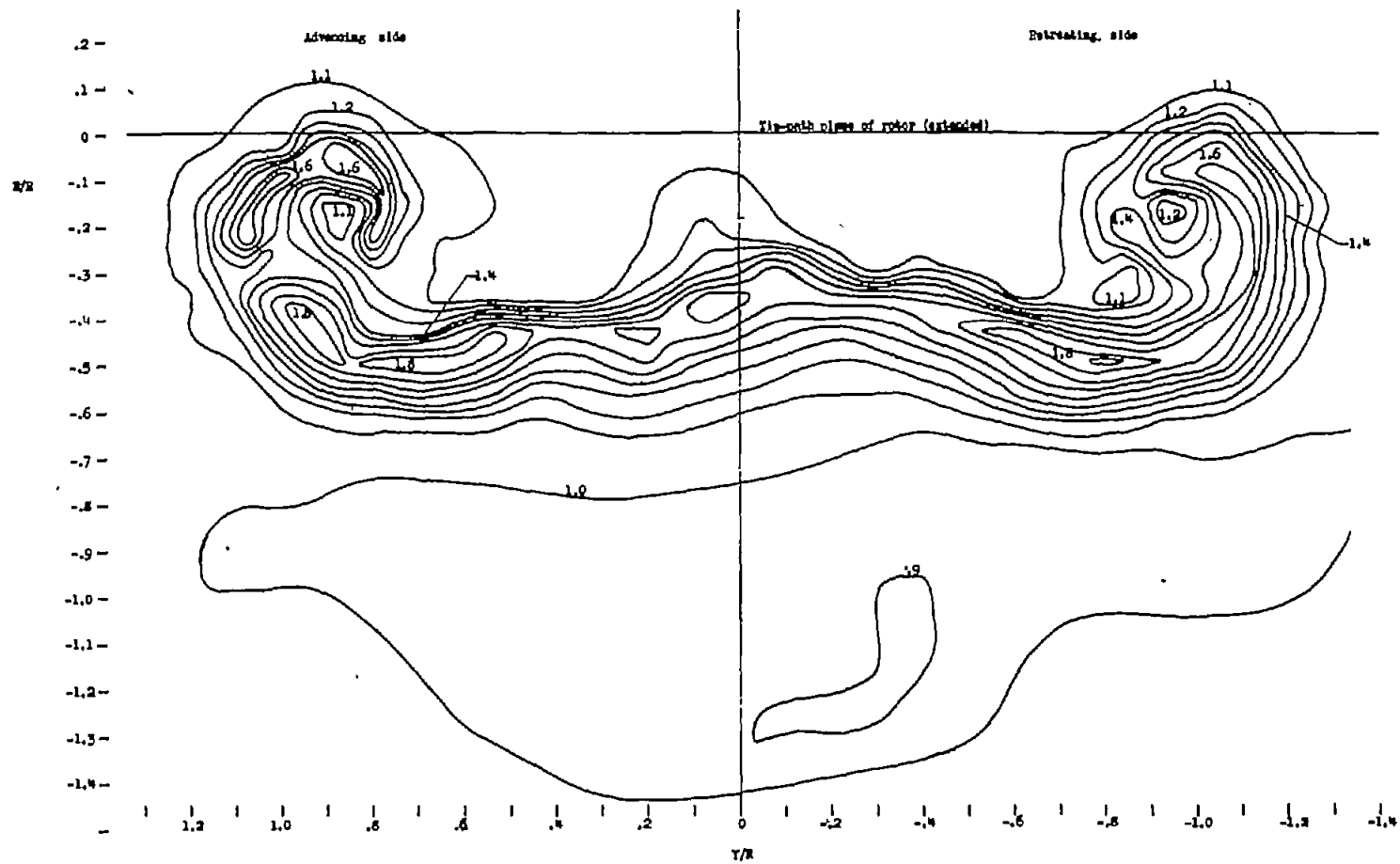
(d) $X/R = 0.5$.

Figure 6.- Continued.



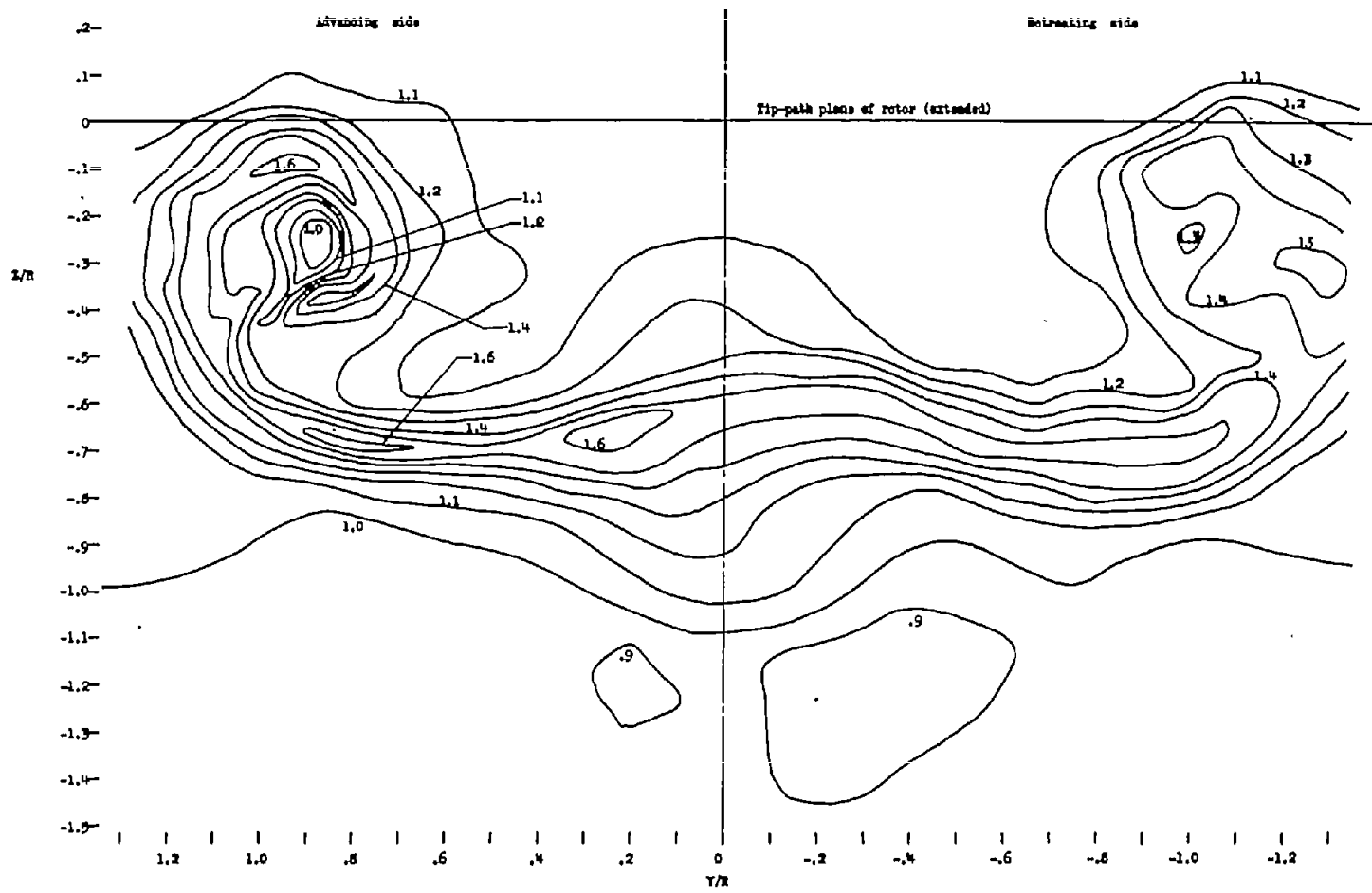
(e) $X/R = 1.07$.

Figure 6.- Continued.



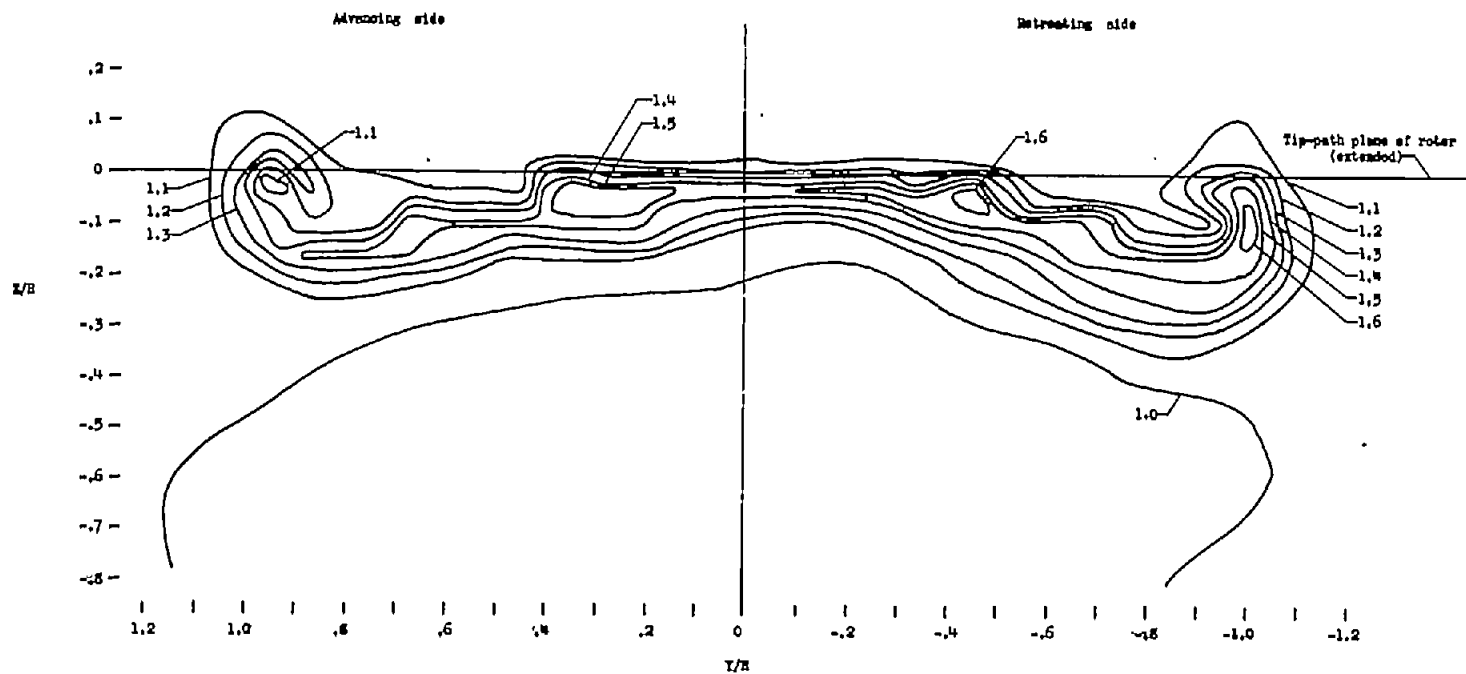
(f) $X/R = 2.07$.

Figure 6.- Continued.



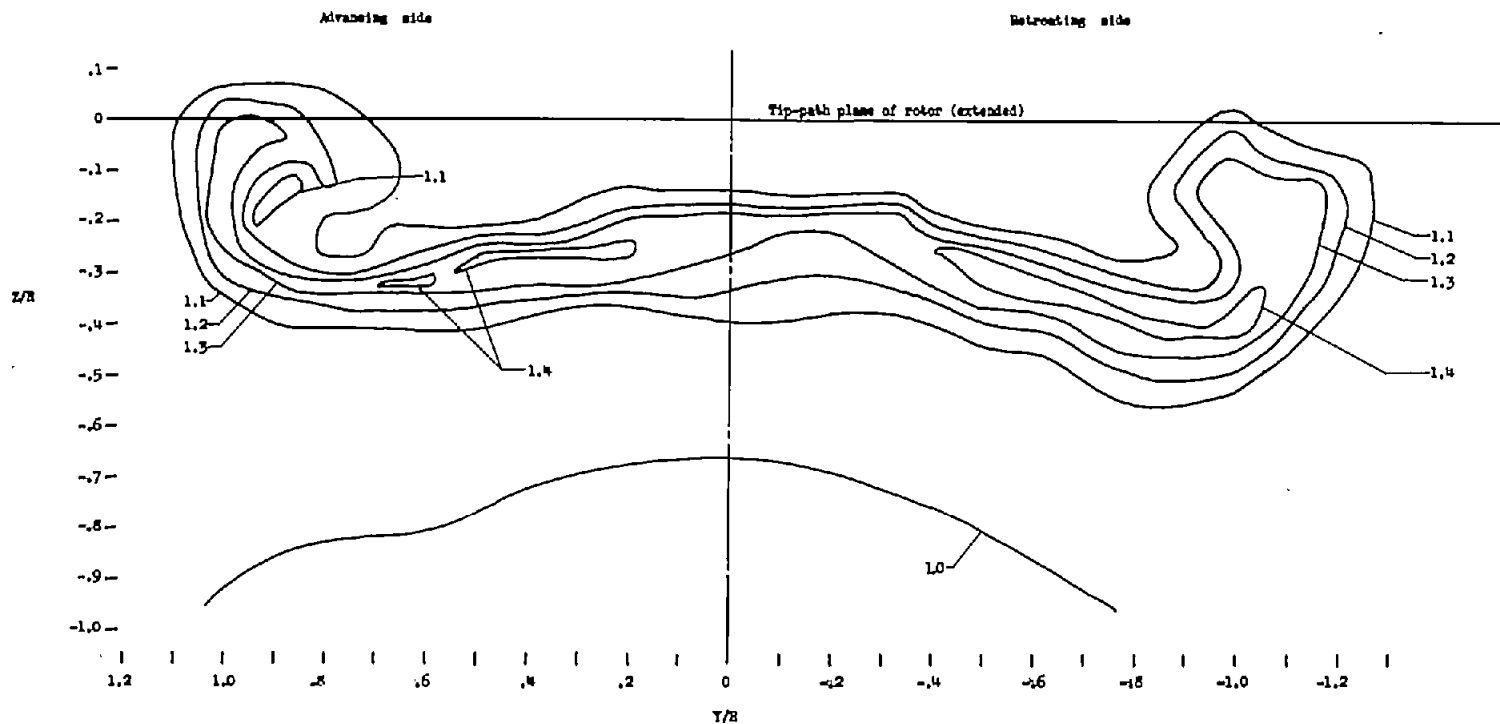
(g) $X/R = 3.14$.

Figure 6.- Concluded.



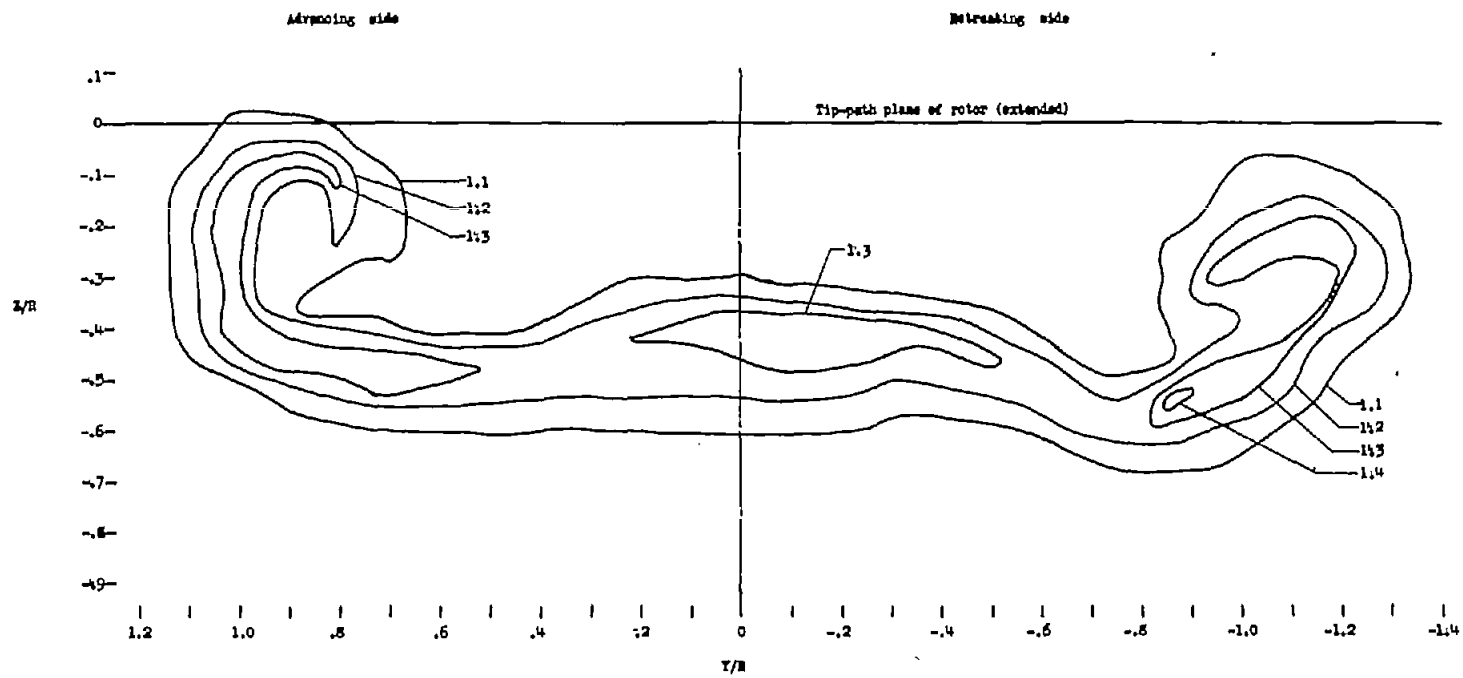
(a) $X/R = 1.07$.

Figure 7.- Contours of dynamic pressure q/q_0 in the vicinity of rotor. $\alpha = 82.3^\circ$; $\mu = 0.140$.



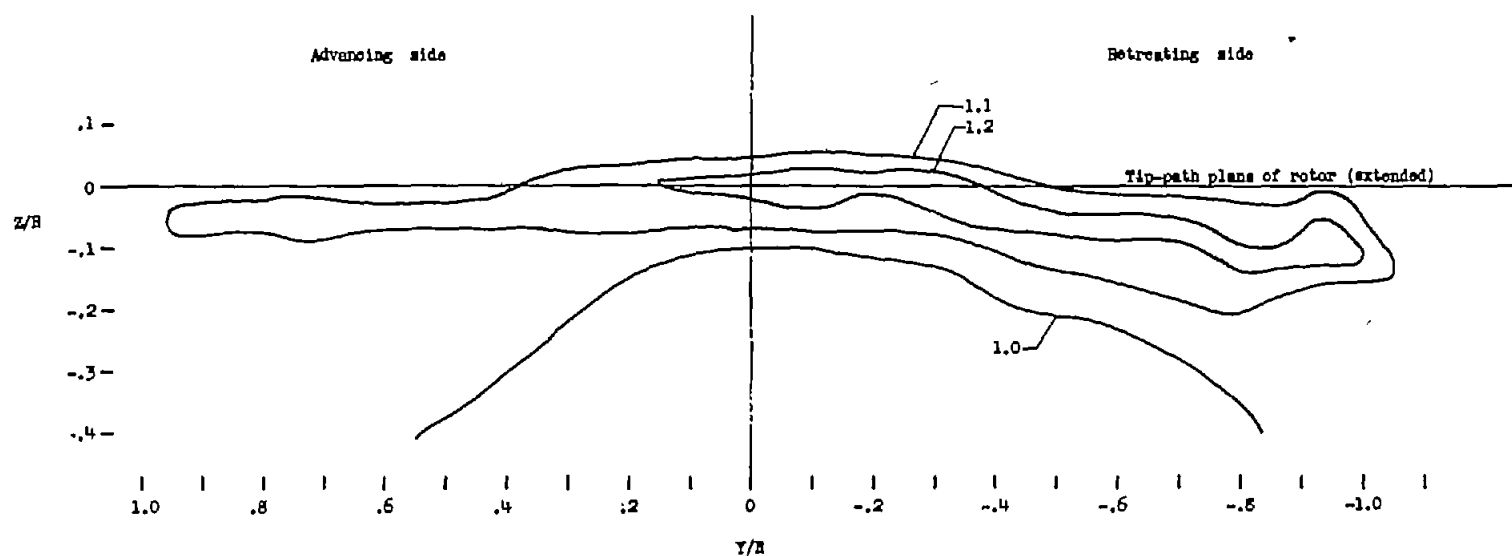
(b) $X/R = 2.07$.

Figure 7.- Continued.



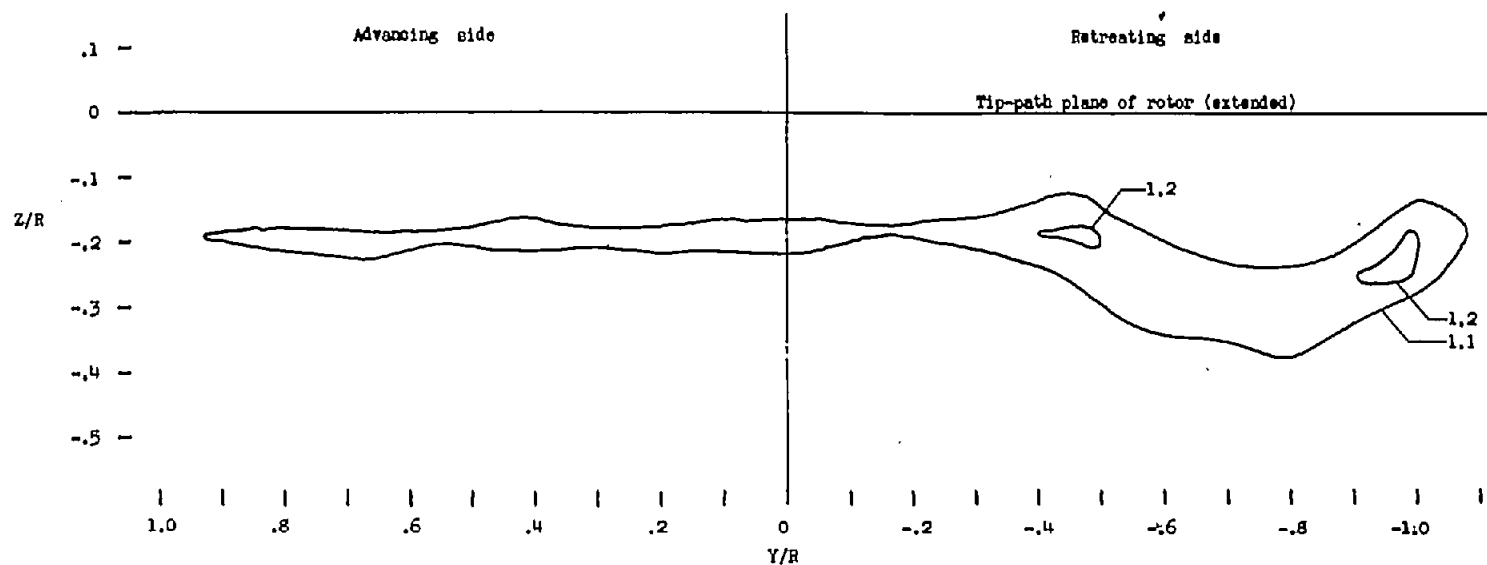
(c) $X/R = 3.14$.

Figure 7.- Concluded.



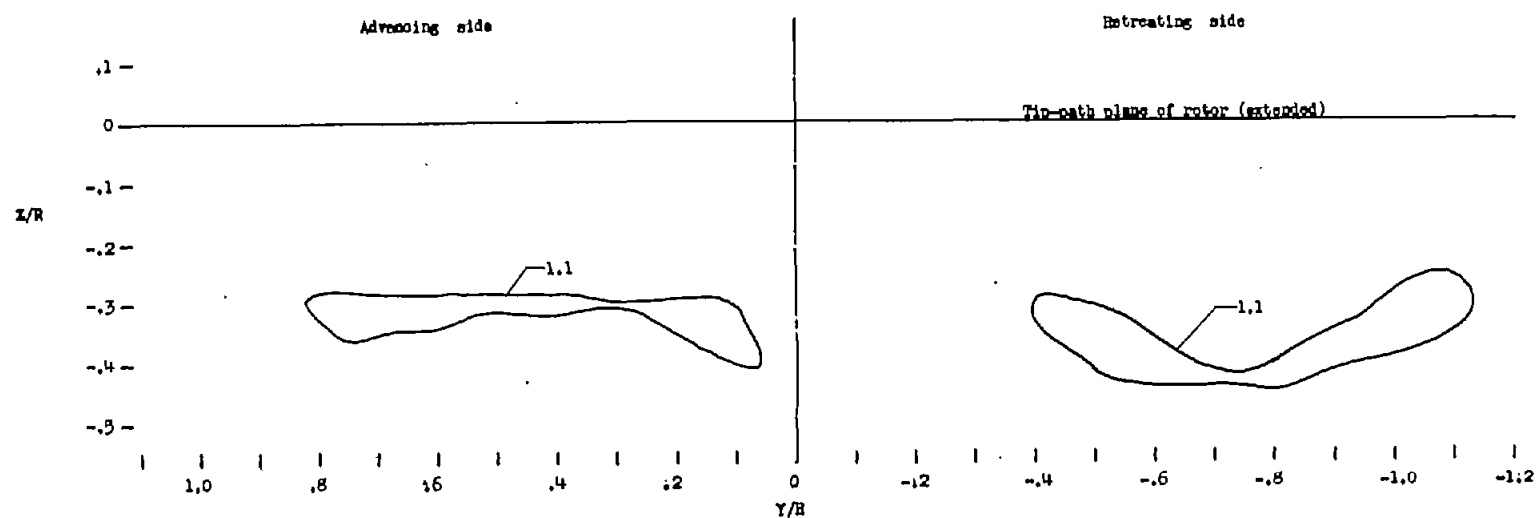
(a) $X/R = 1.07$.

Figure 8.- Contours of dynamic pressure q/q_0 in the vicinity of the rotor. $\alpha = 83.9^\circ$;
 $\mu = 0.232$.



(b) $X/R = 2.07$.

Figure 8.- Continued.



(c) $X/R = 3.14$.

Figure 8.- Concluded.

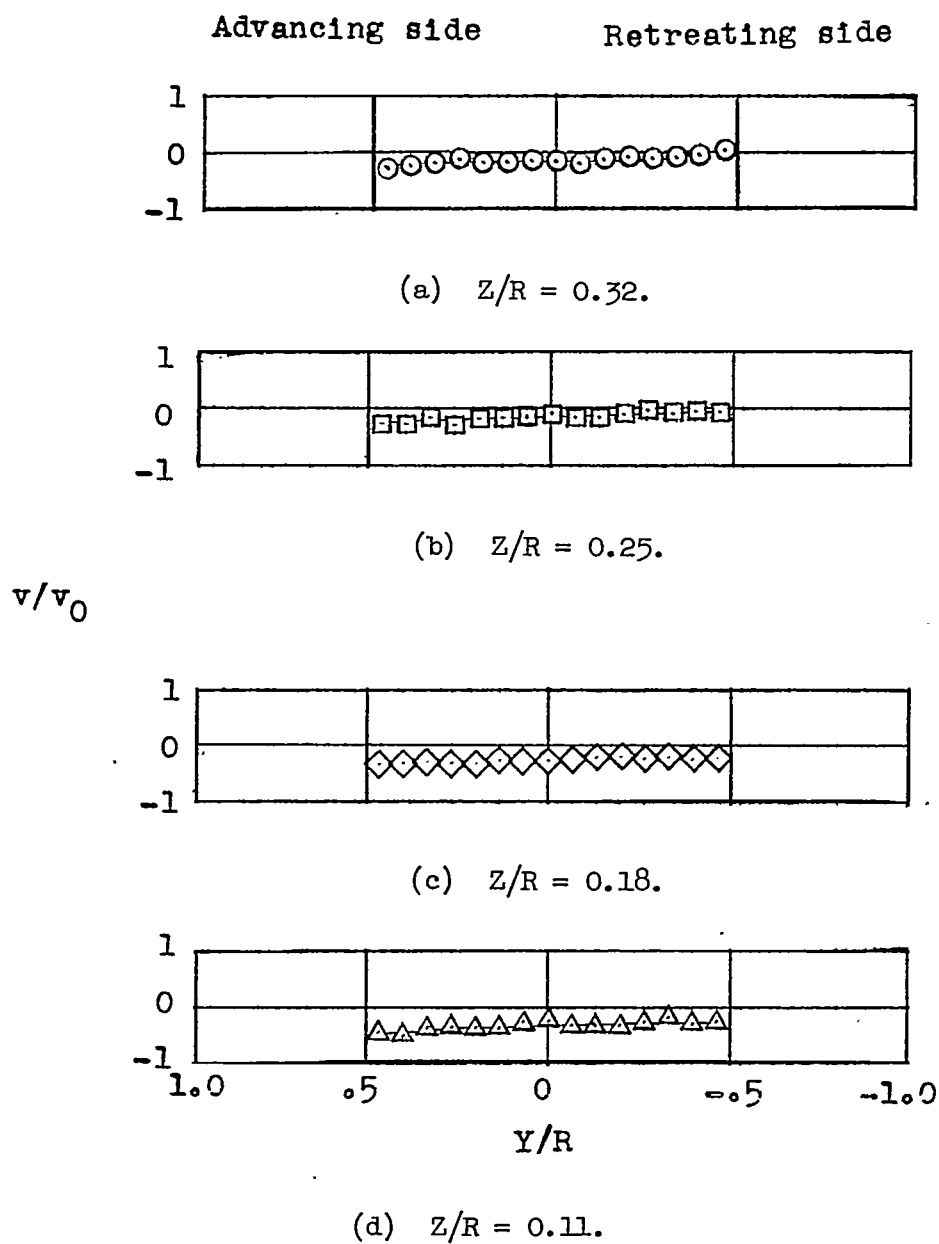


Figure 9.- Measured values of induced-velocity ratio v/v_0 . $X/R = -1.0$;
 $\chi = 75.0^\circ$; $\mu = 0.095$.

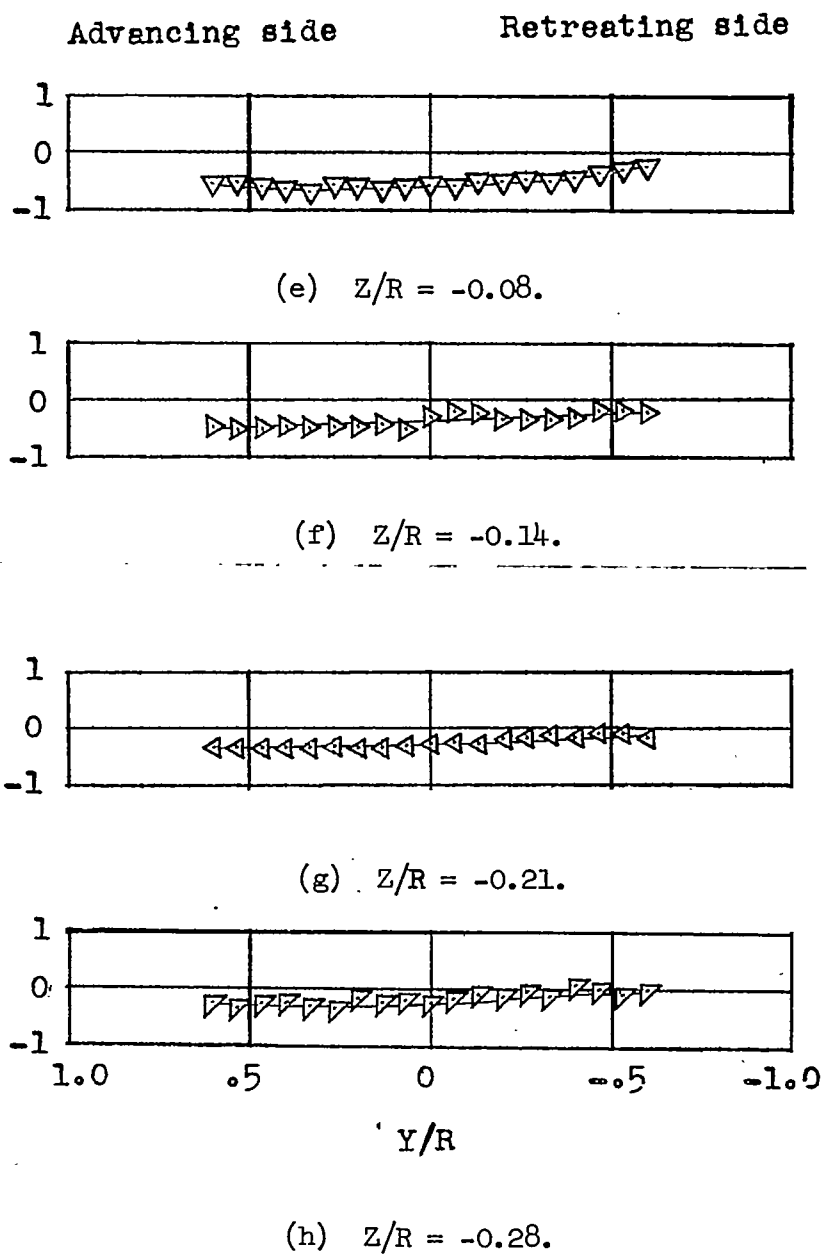


Figure 9.- Concluded.

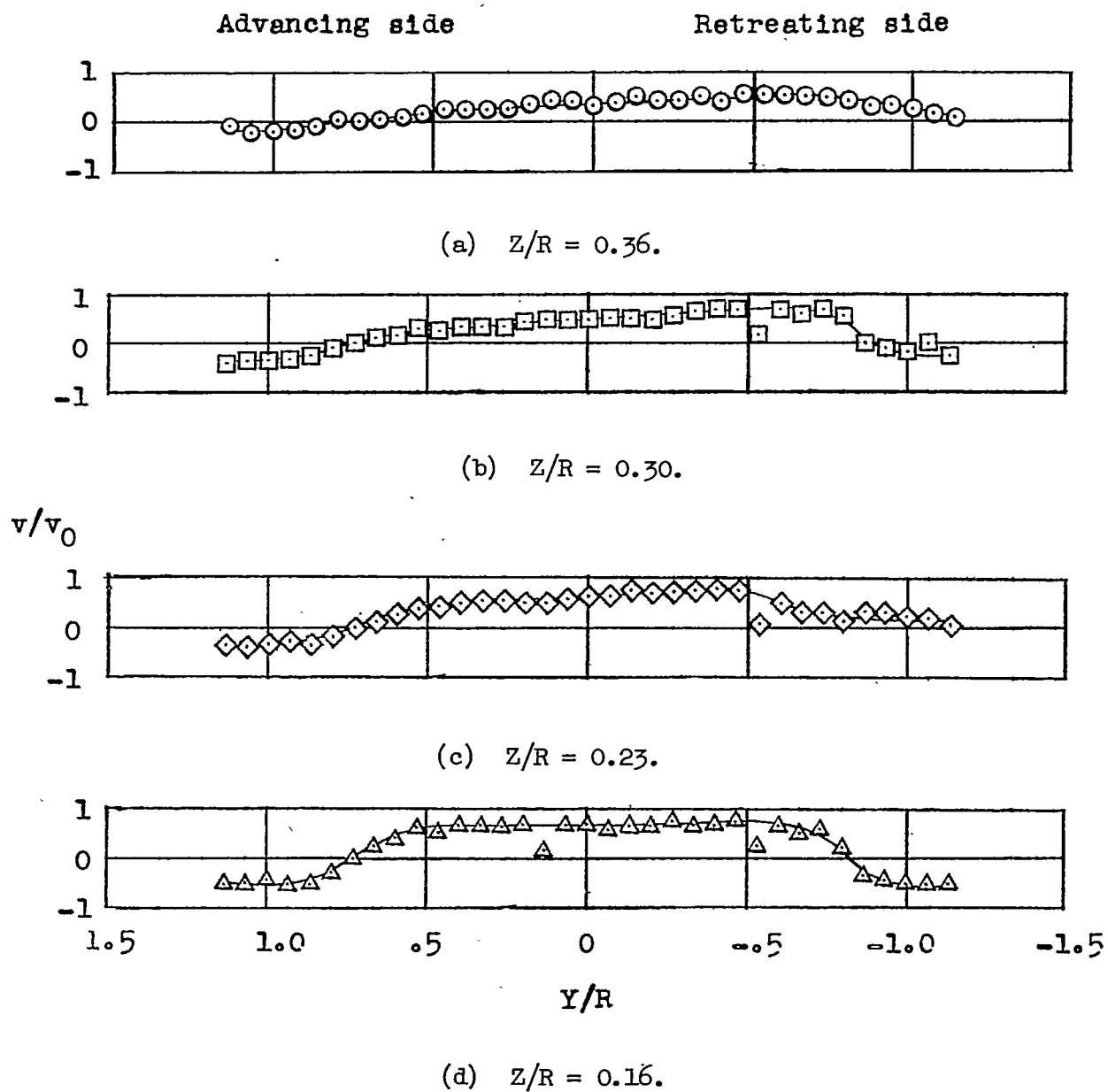


Figure 10.- Measured values of induced-velocity ratio v/v_0 . $X/R = -0.5$;
 $\alpha = 75.0^\circ$; $\mu = 0.095$.

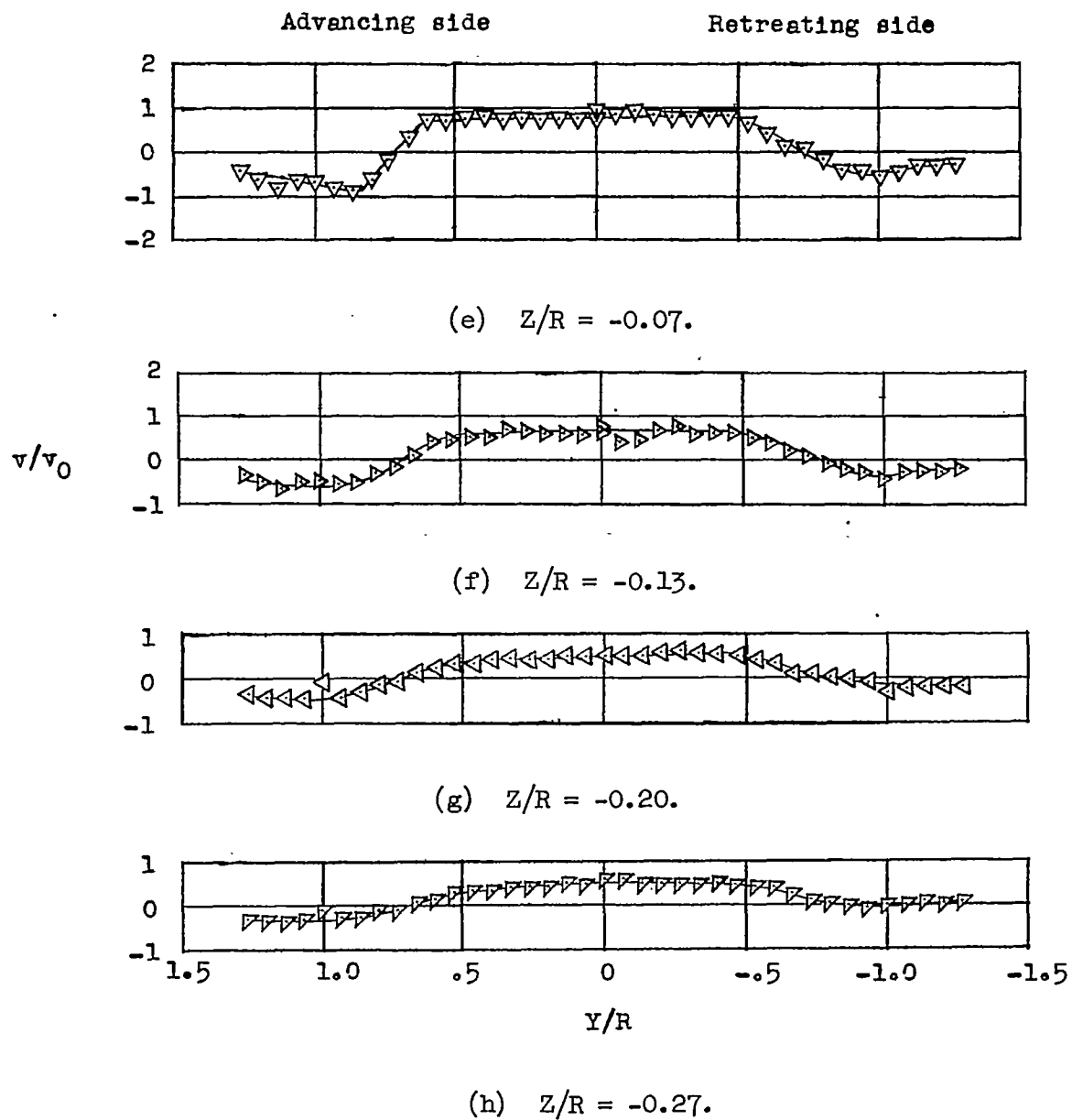


Figure 10.- Concluded.

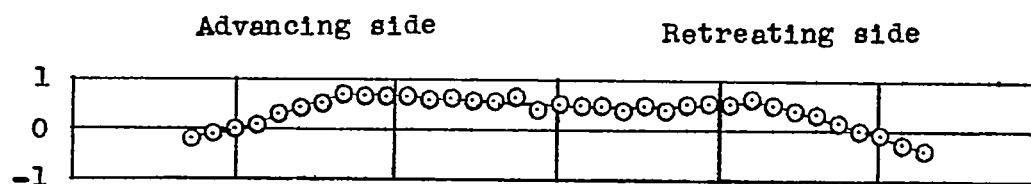
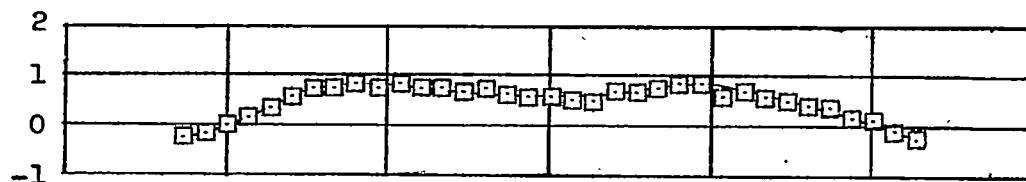
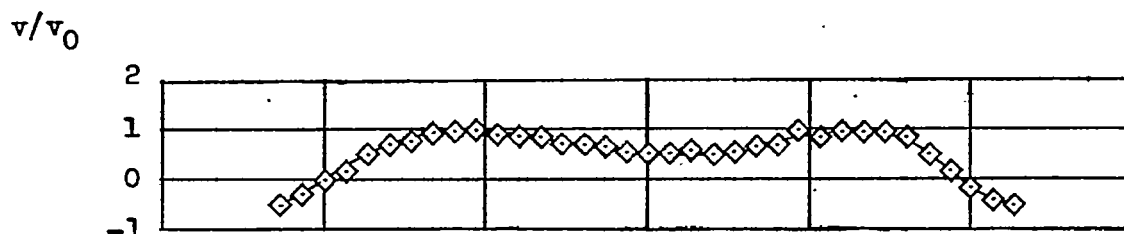
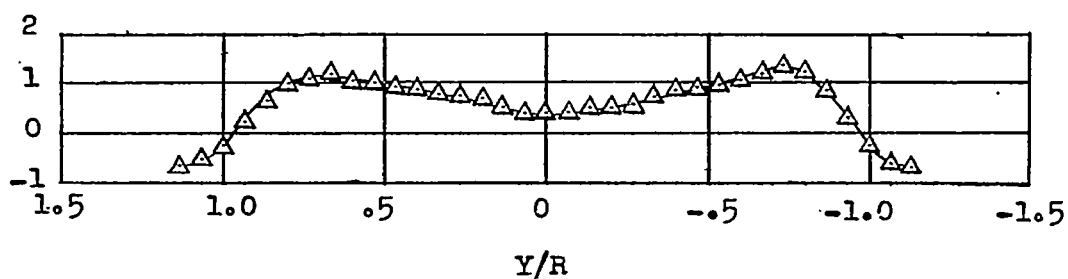
(a) $Z/R = 0.38$.(b) $Z/R = 0.31$.(c) $Z/R = 0.25$.(d) $Z/R = 0.18$.

Figure 11.- Measured values of induced-velocity ratio v/v_0 . $X/R = 0$;
 $\chi = 75.0^\circ$; $\mu = 0.095$.

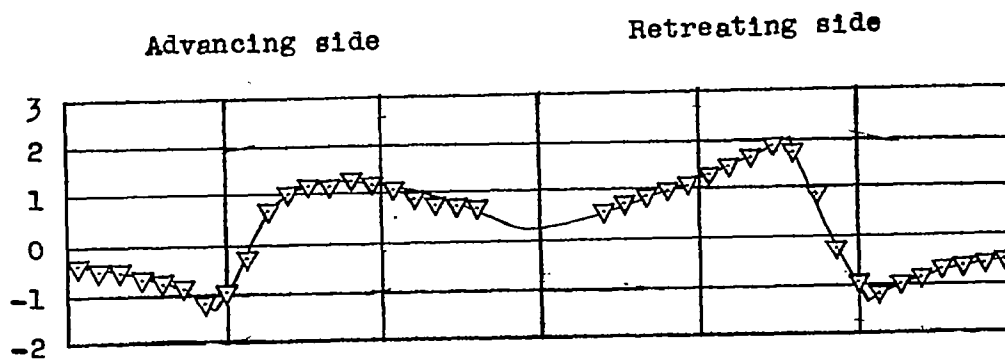
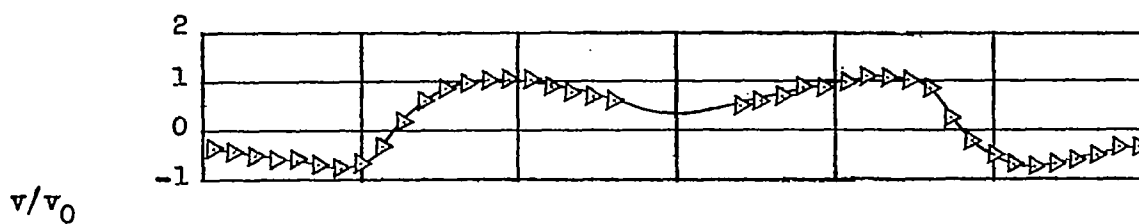
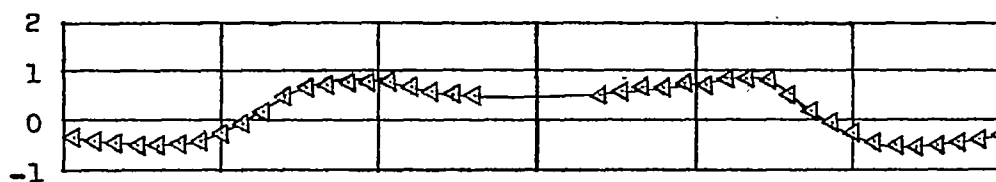
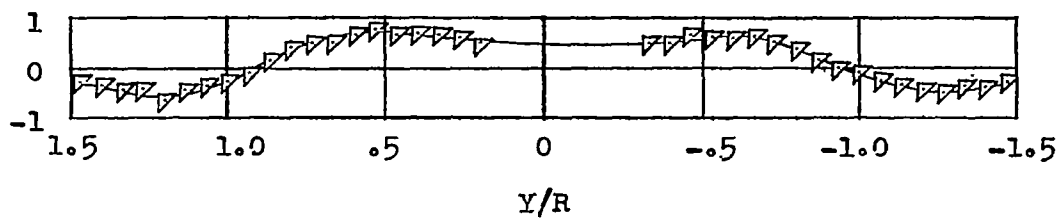
(e) $Z/R = -0.07$.(f) $Z/R = -0.14$.(g) $Z/R = -0.20$.(h) $Z/R = -0.27$.

Figure 11.- Concluded.

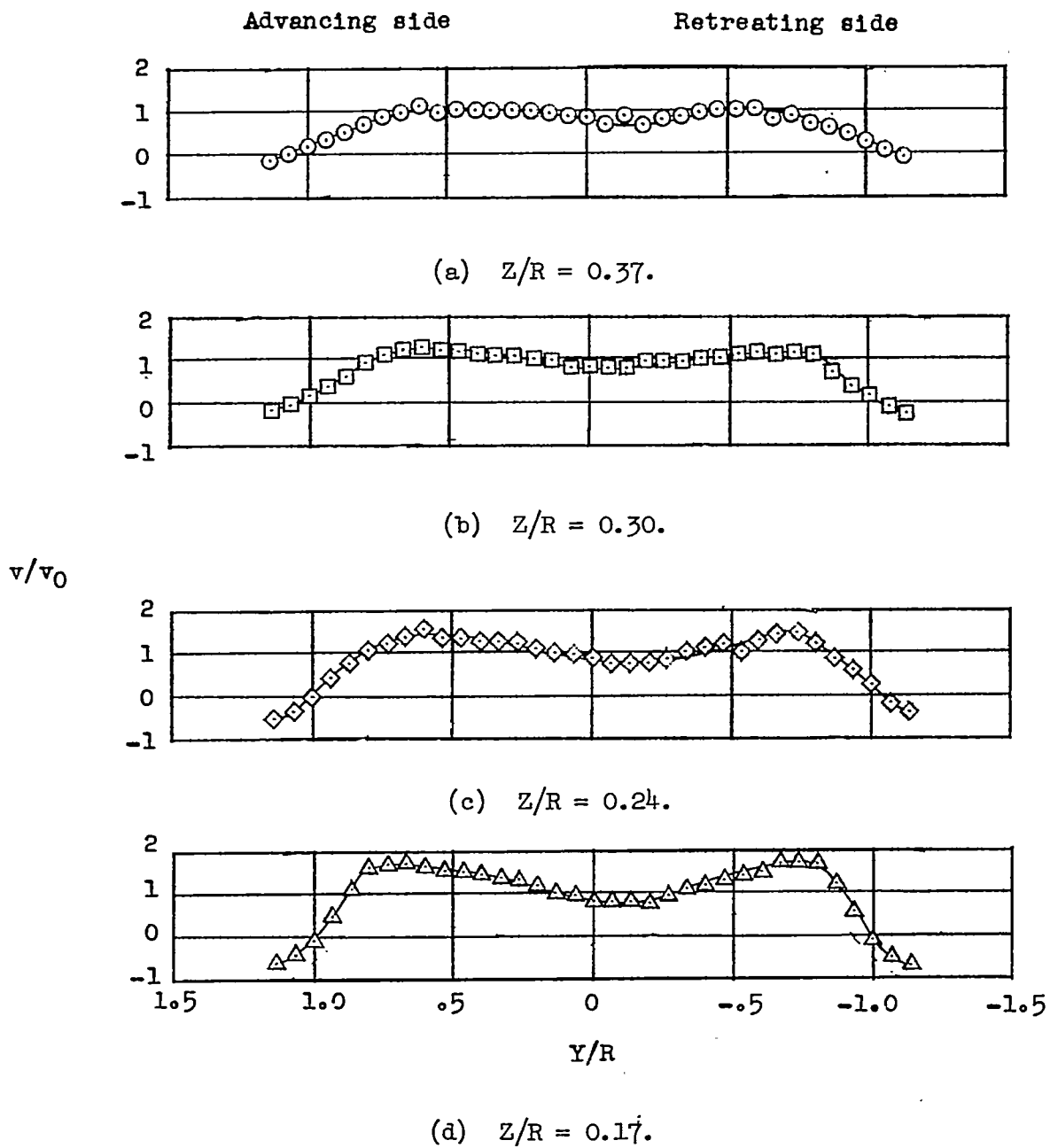


Figure 12.- Measured values of induced-velocity ratio v/v_0 . $X/R = -0.5$;
 $\alpha = 75.0^\circ$; $\mu = 0.095$.

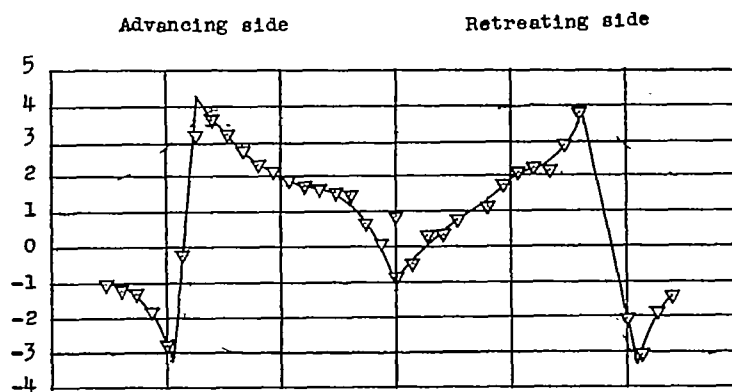
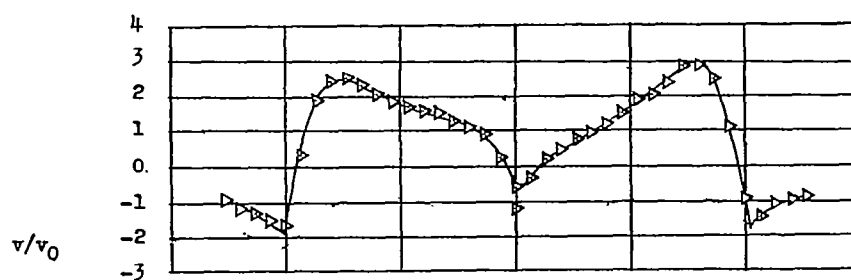
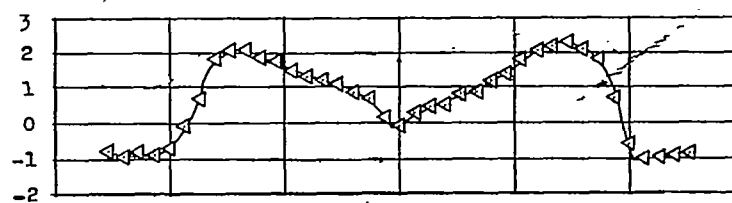
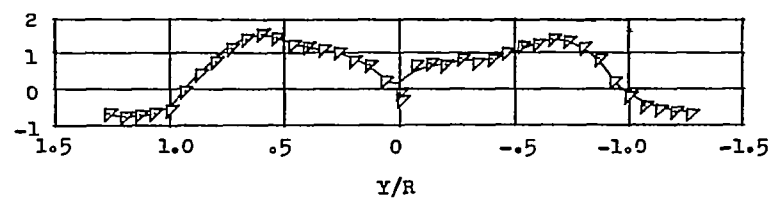
(e) $Z/R = -0.05$.(f) $Z/R = -0.12$.(g) $Z/R = -0.19$.(h) $Z/R = -0.25$.

Figure 12.- Concluded.

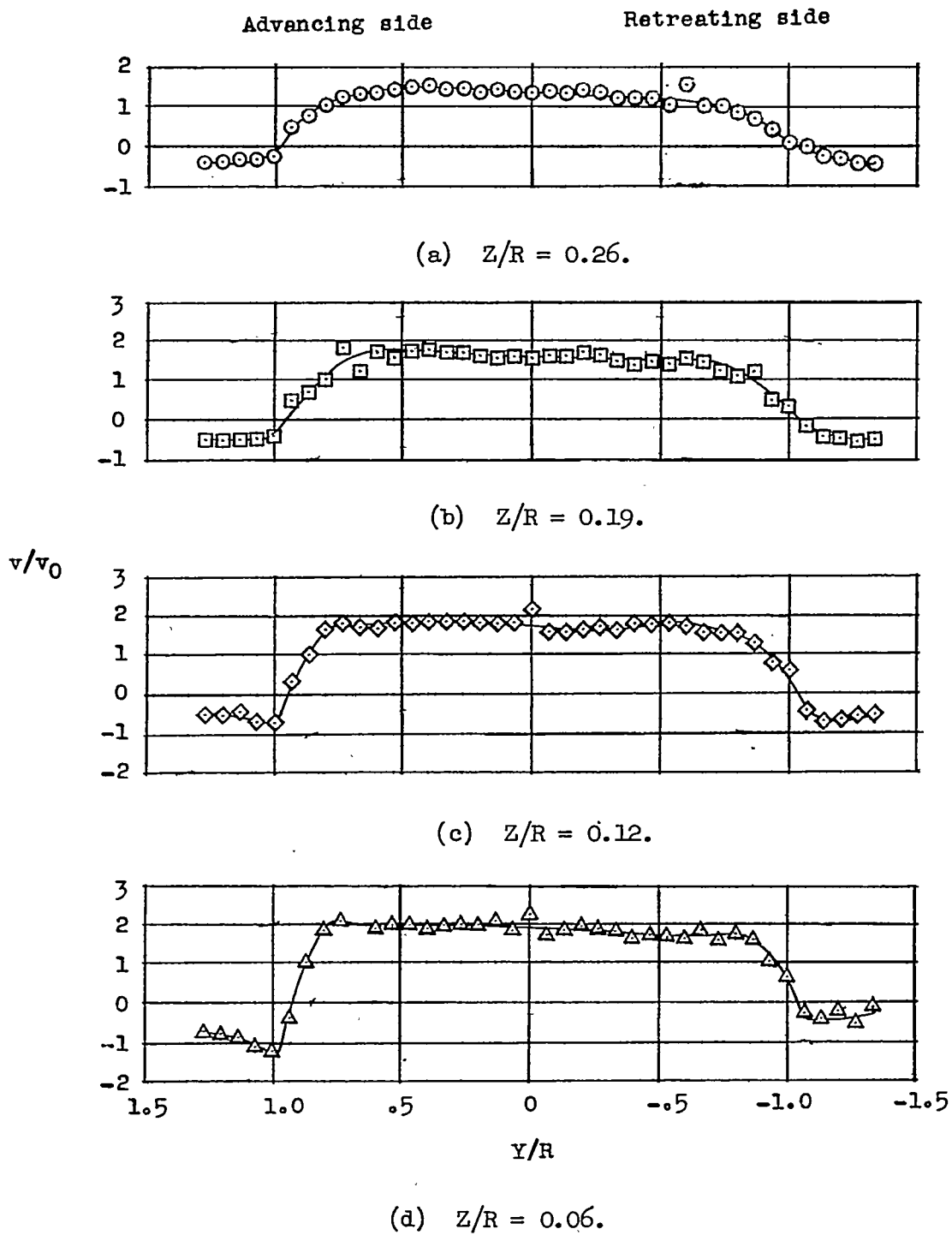


Figure 13.- Measured values of induced-velocity ratio v/v_0 . $X/R = 1.07$.
 $\chi = 75.0^\circ$; $\mu = 0.095$.

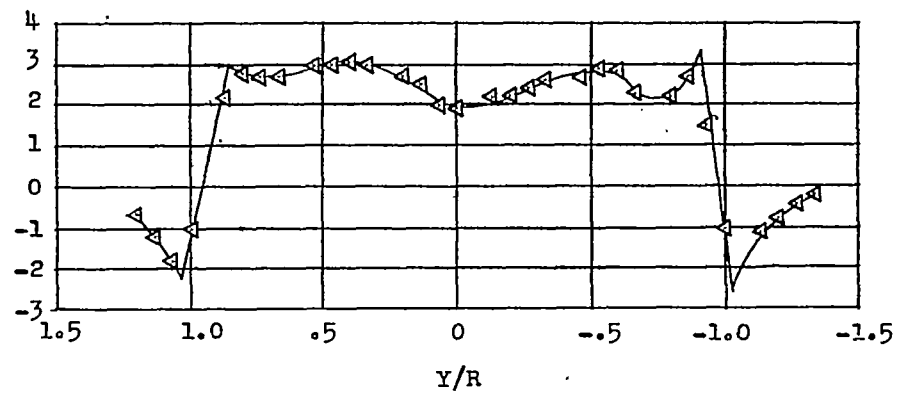
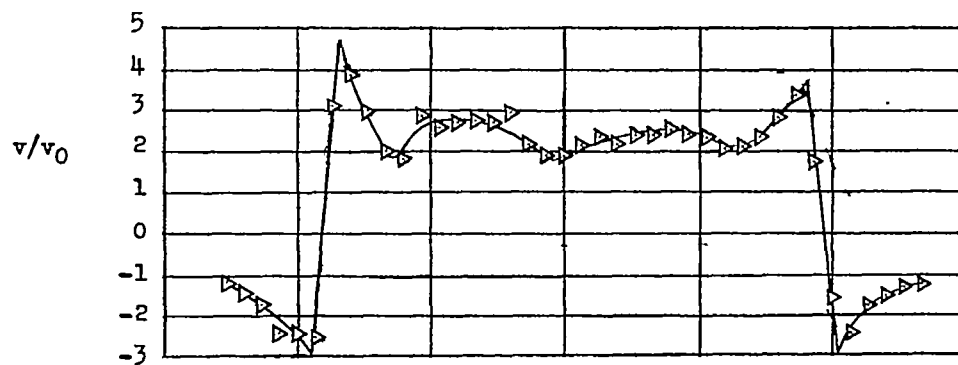
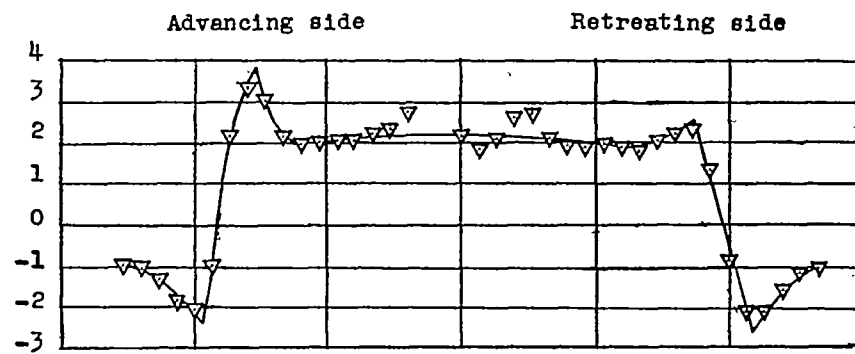


Figure 13.- Continued.

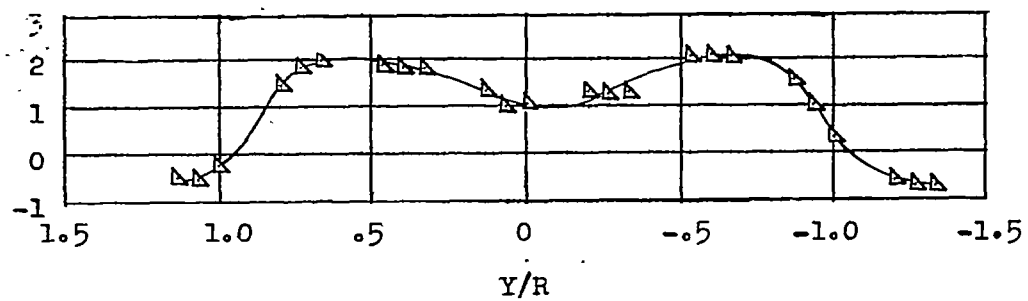
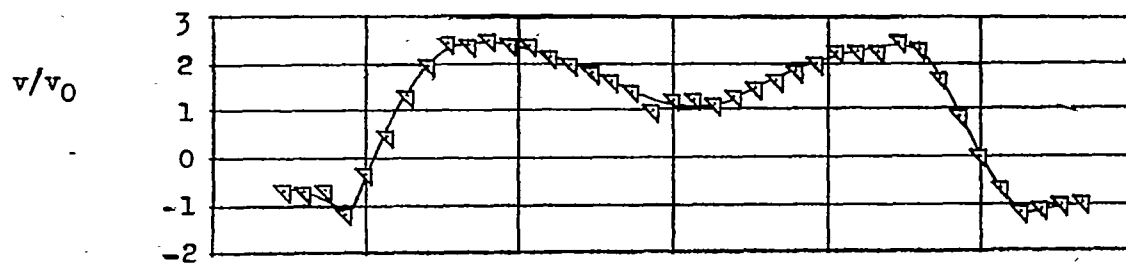
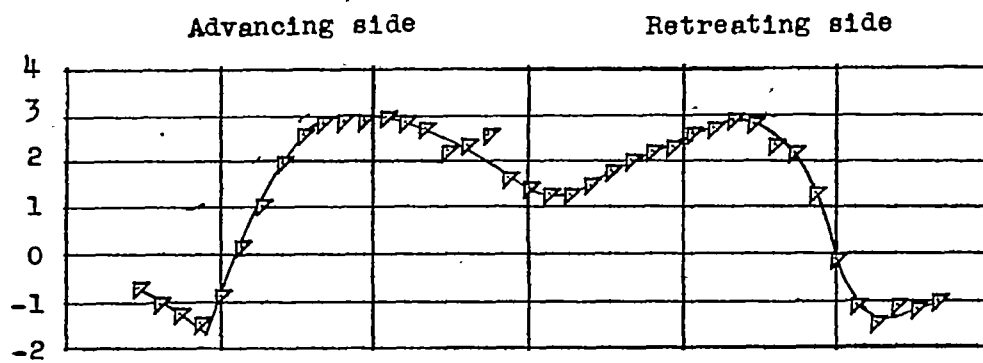


Figure 13.- Continued.

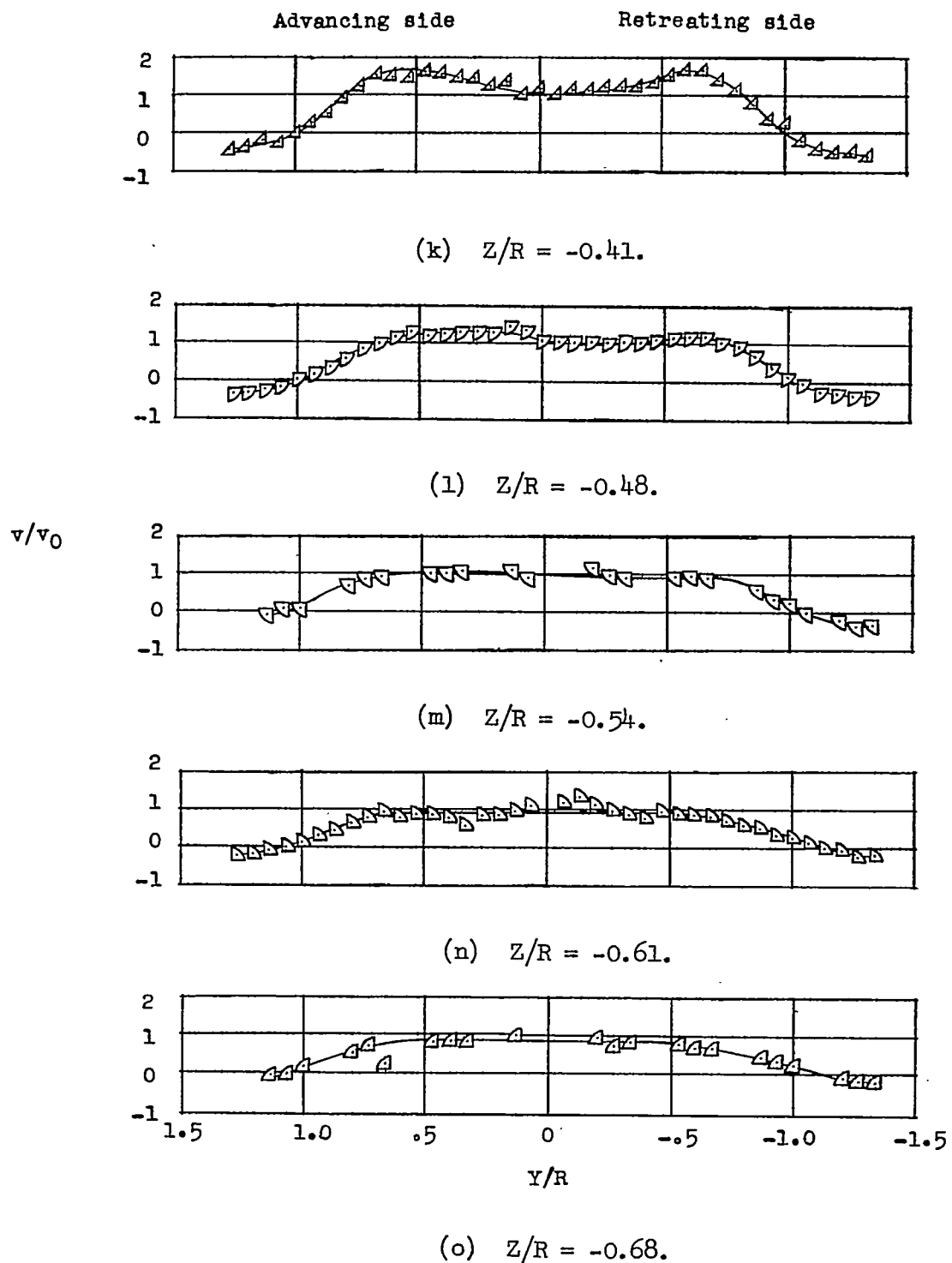


Figure 13.- Continued.

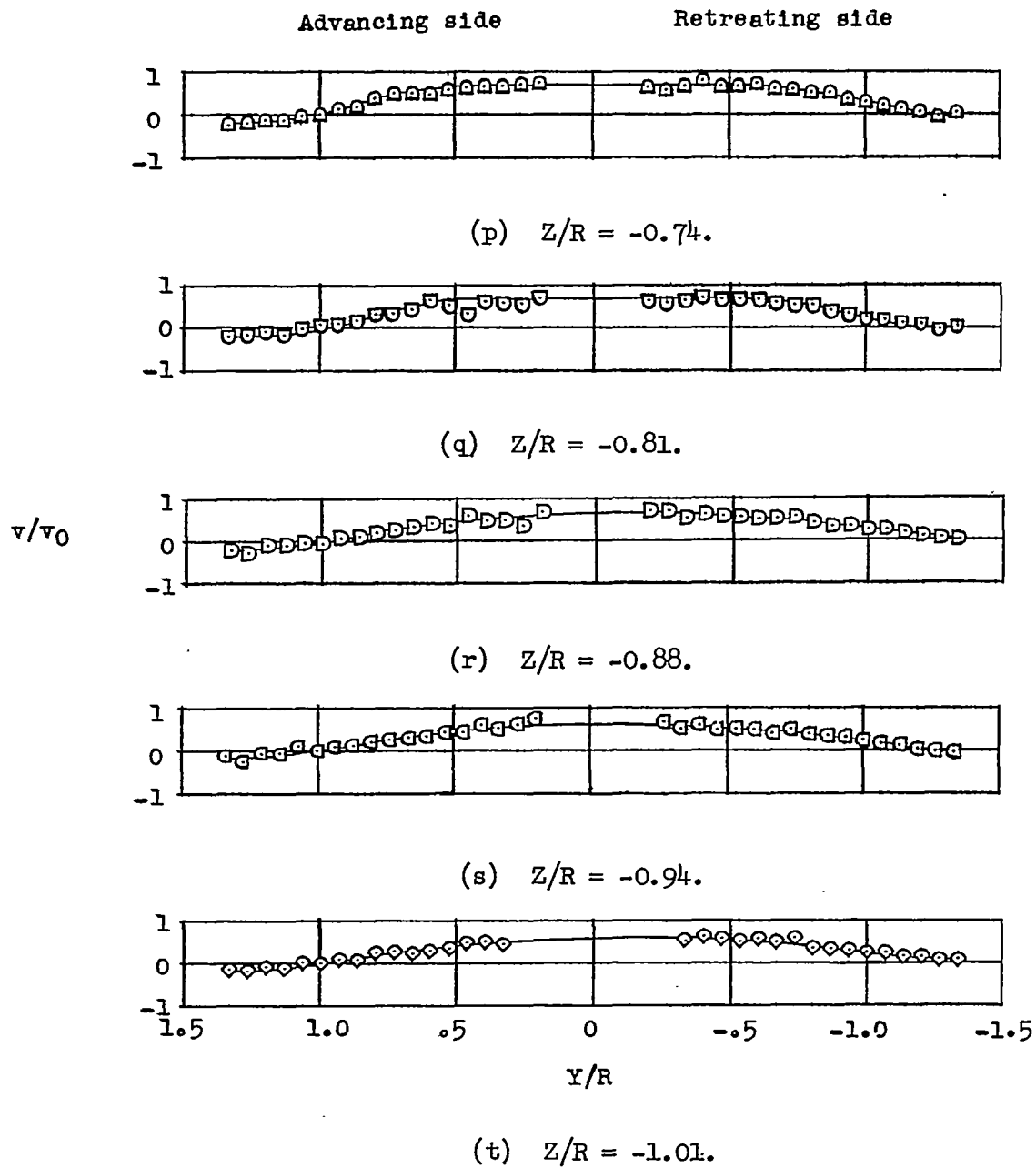


Figure 13.- Concluded.

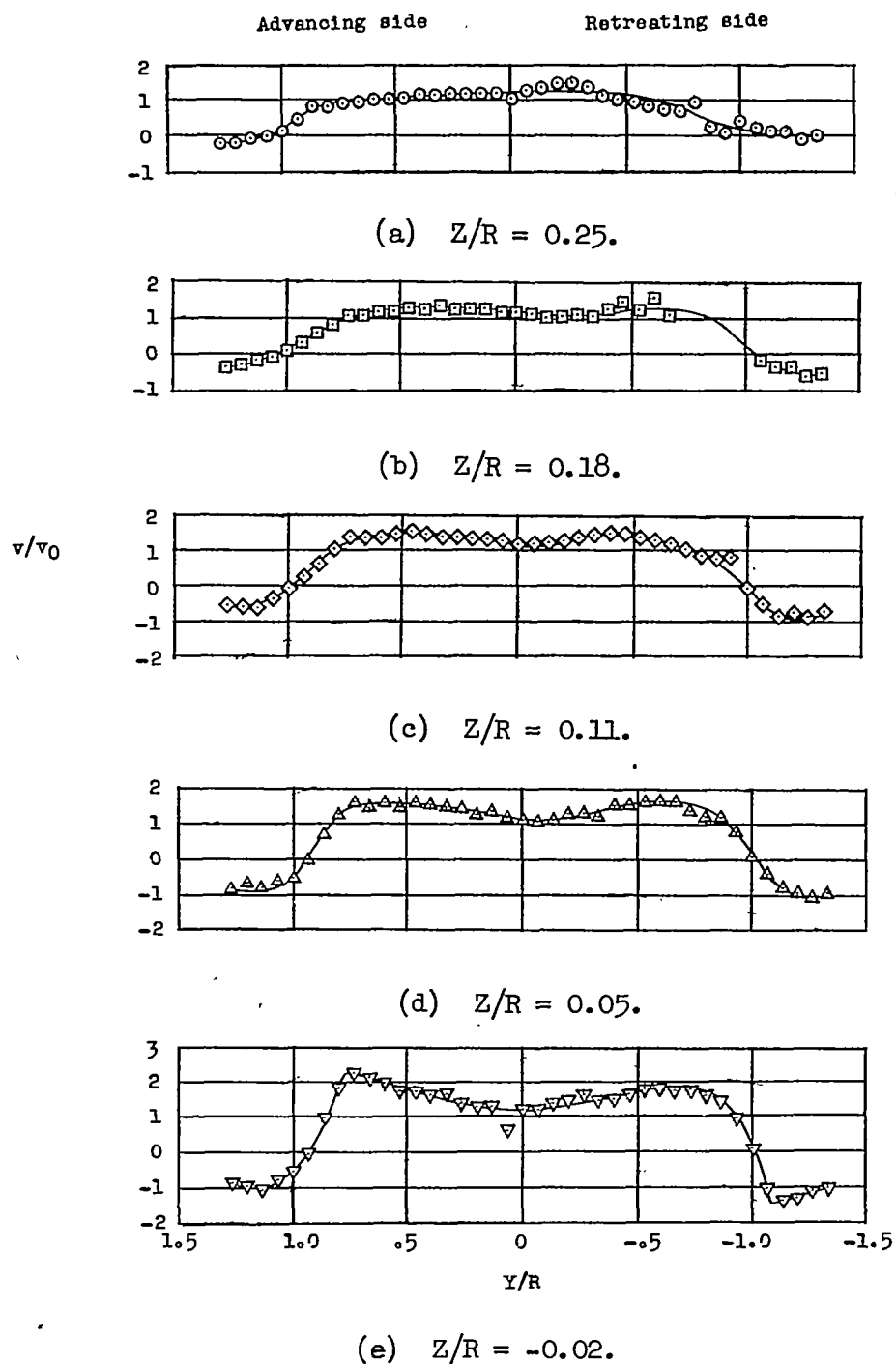


Figure 14.- Measured values of induced-velocity ratio v/v_0 . $X/R = 2.07$;
 $\chi = 75.0^\circ$; $\mu = 0.095$.

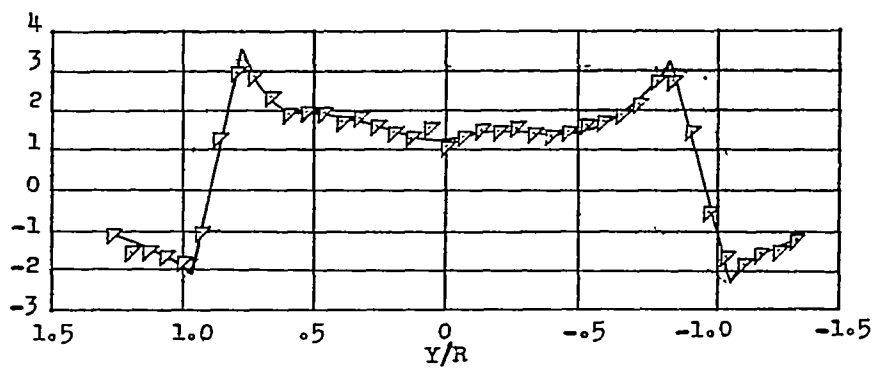
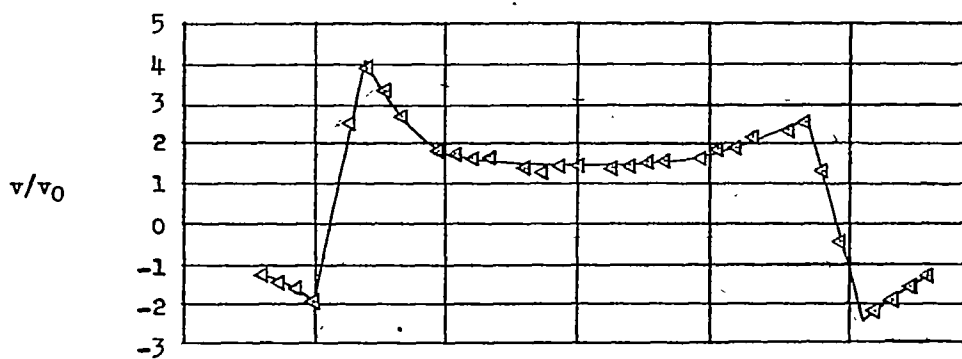
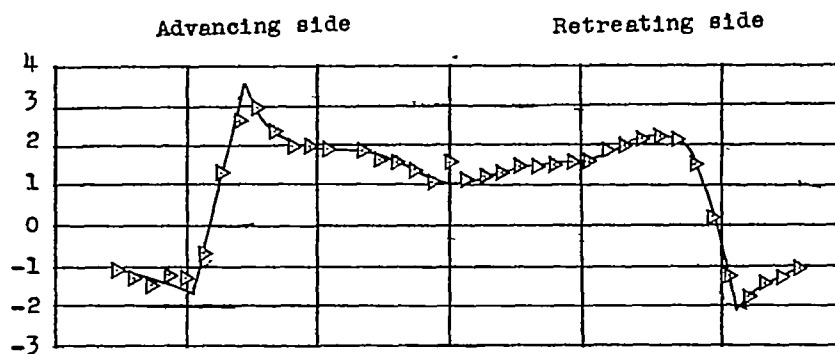


Figure 14.- Continued.

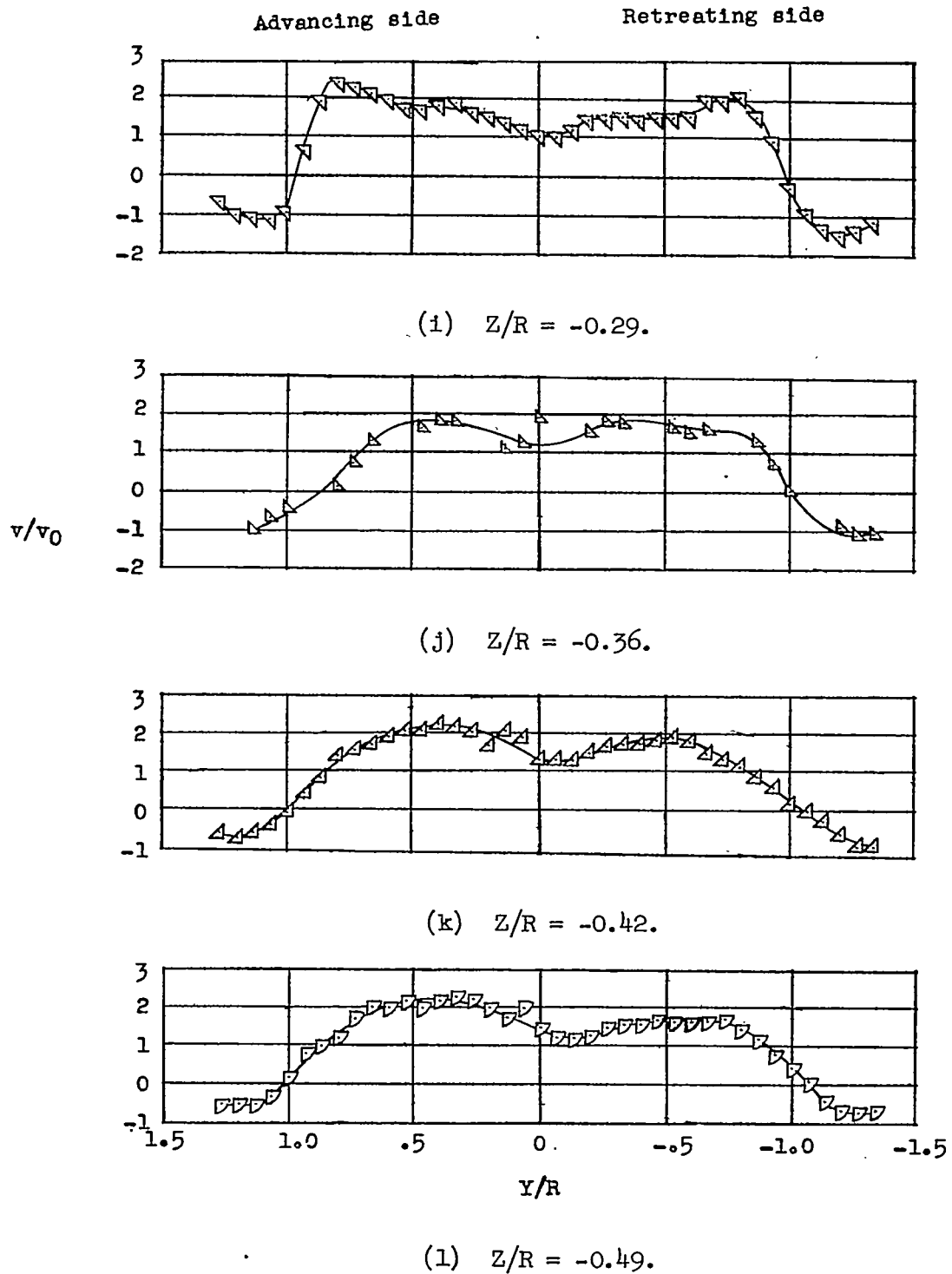
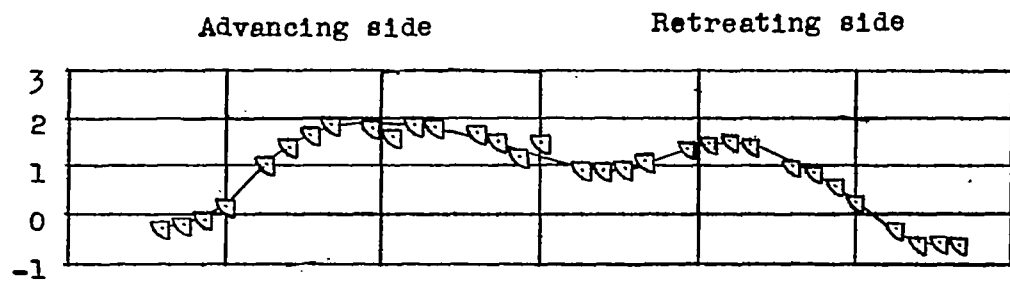
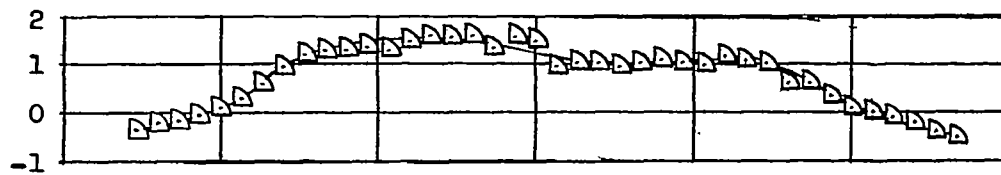


Figure 14.- Continued.

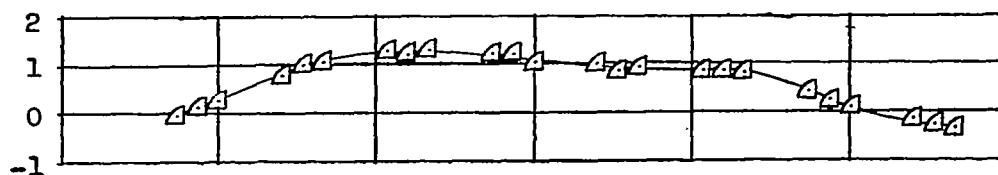


(m) $Z/R = -0.56.$

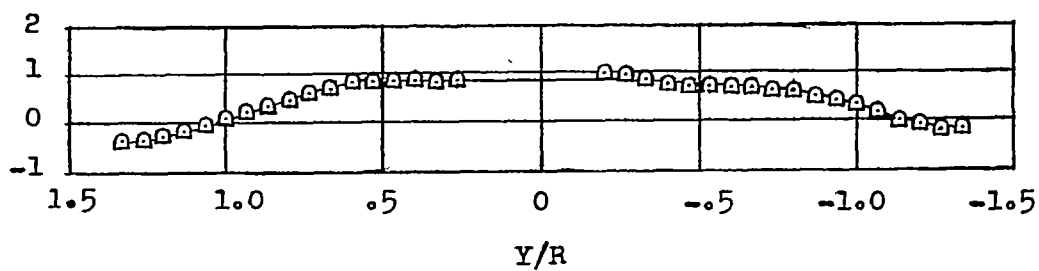


(n) $Z/R = -0.62.$

v/v_0

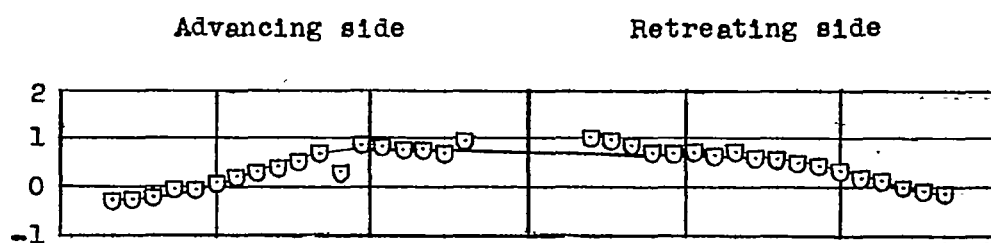


(o) $Z/R = -0.69.$

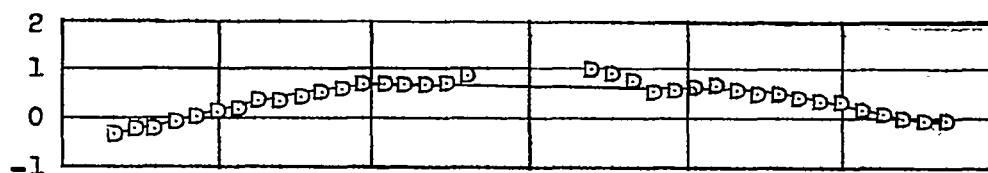


(p) $Z/R = -0.76.$

Figure 14.- Continued.

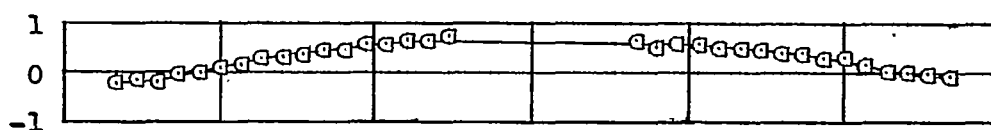


(q) $Z/R = -0.82$.

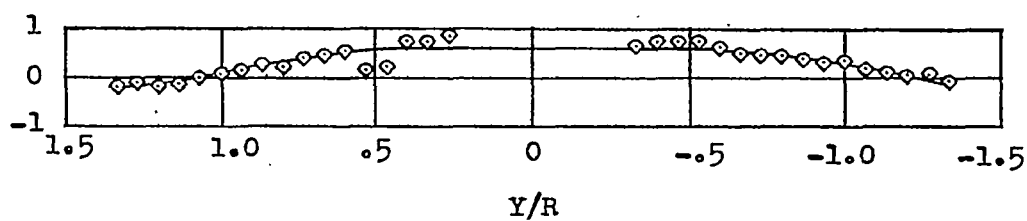


(r) $Z/R = 0.89$.

v/v_0



(s) $Z/R = -0.96$.



(t) $Z/R = -1.02$.

Figure 14.- Concluded.

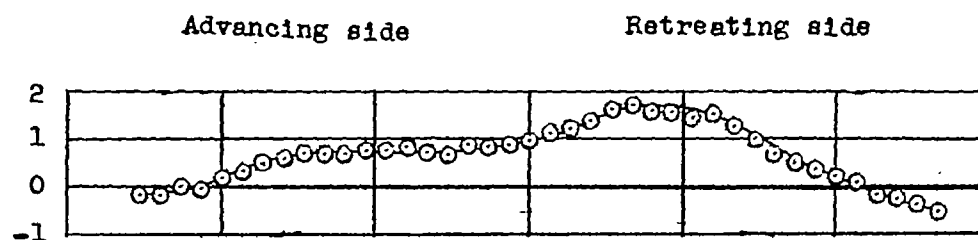
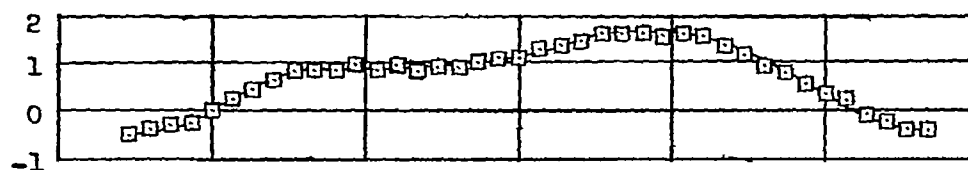
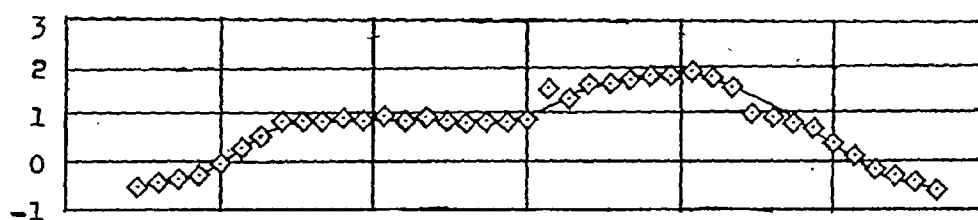
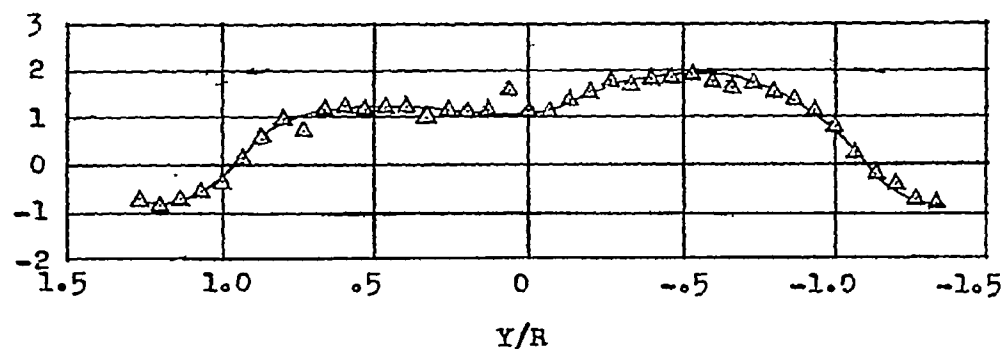
(a) $Z/R = 0.23$.(b) $Z/R = 0.17$. v/v_0 (c) $Z/R = 0.10$.(d) $Z/R = 0.03$.

Figure 15.- Measured values of induced-velocity ratio v/v_0 . $X/R = 3.14$.
 $\chi = 75.0^\circ$; $\mu = 0.095$.

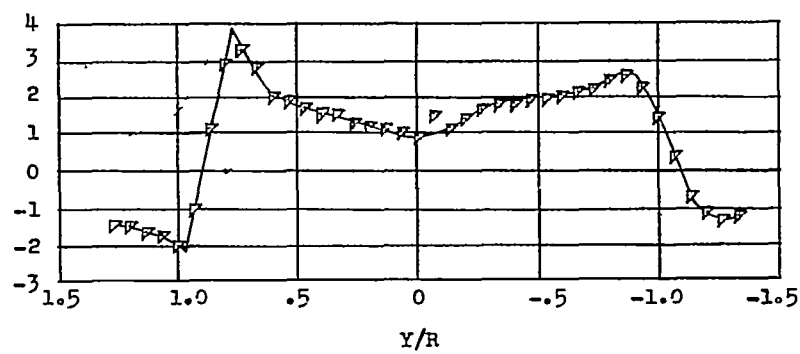
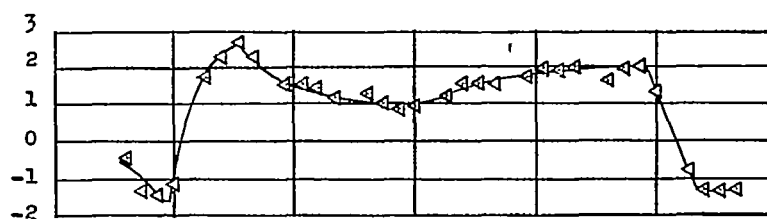
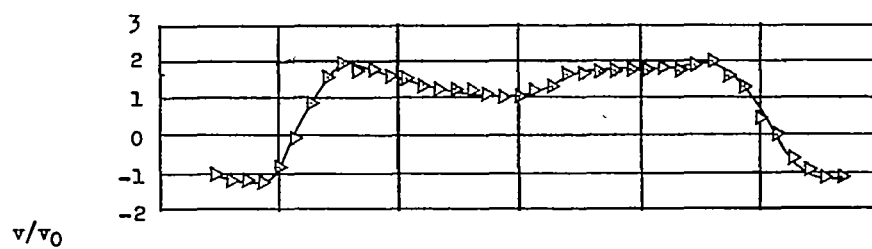
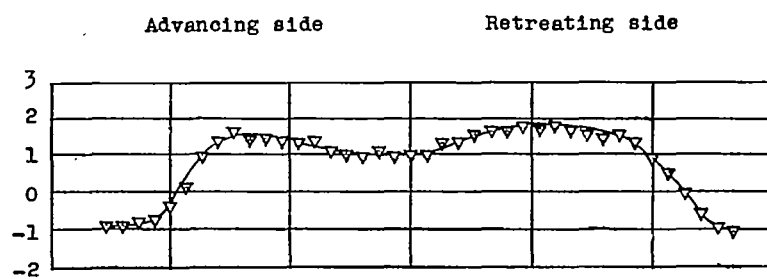


Figure 15.- Continued.

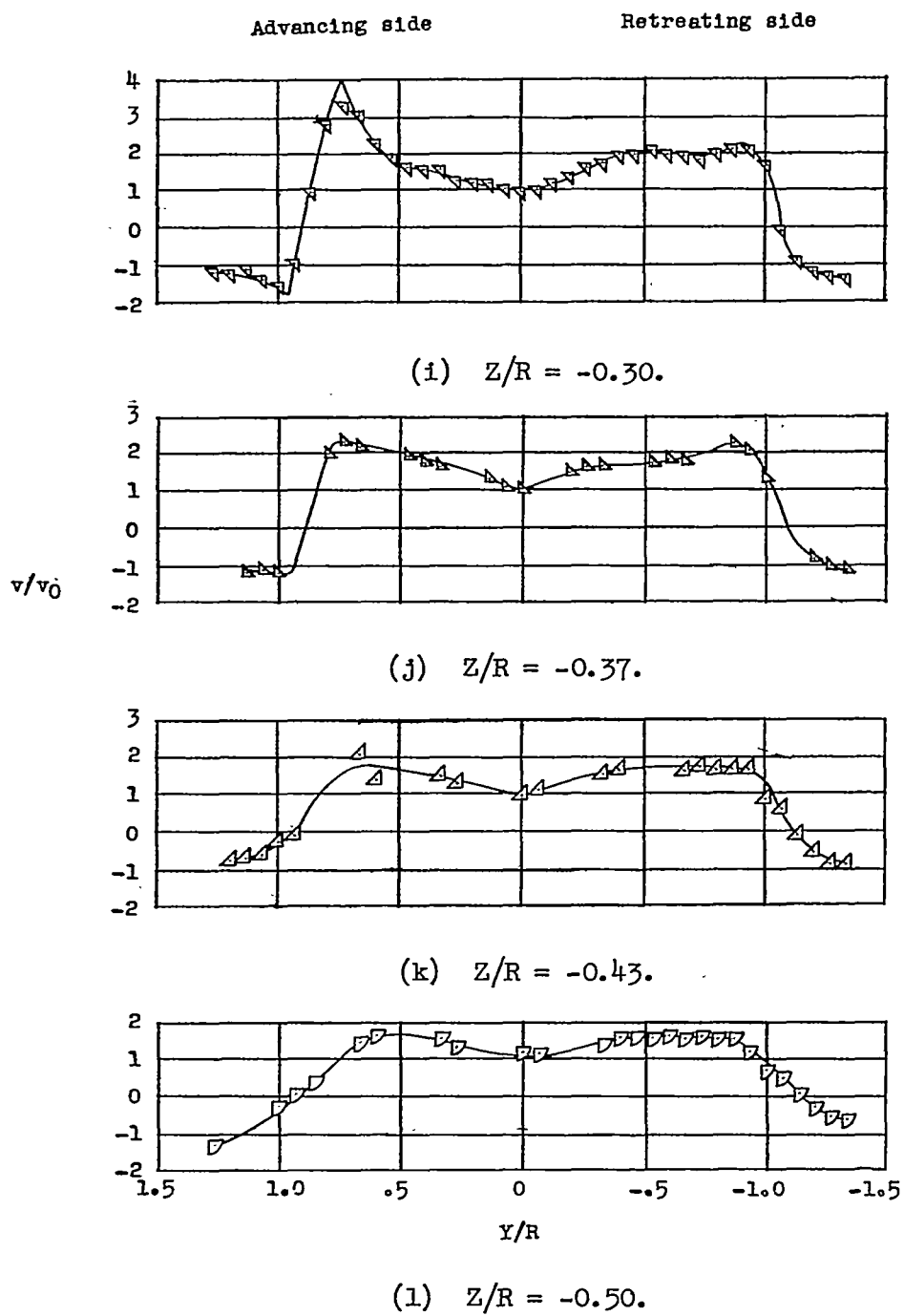


Figure 15.- Continued.

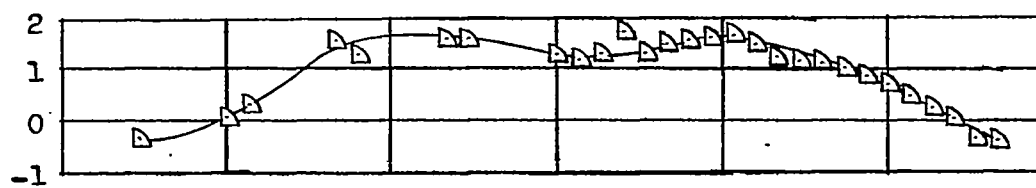
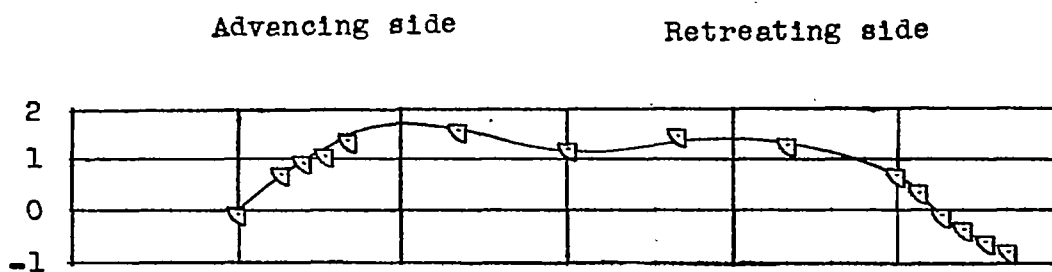
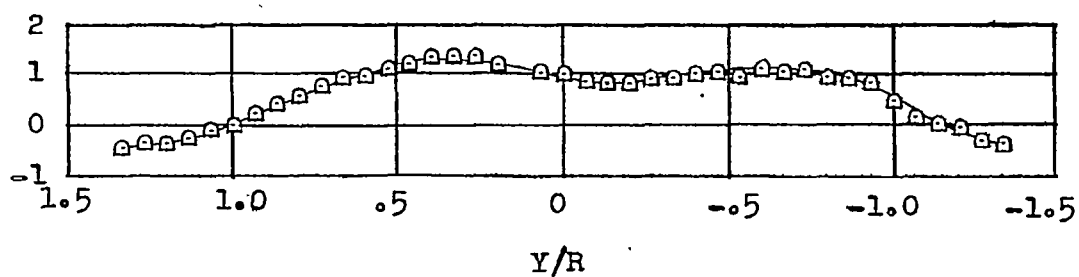
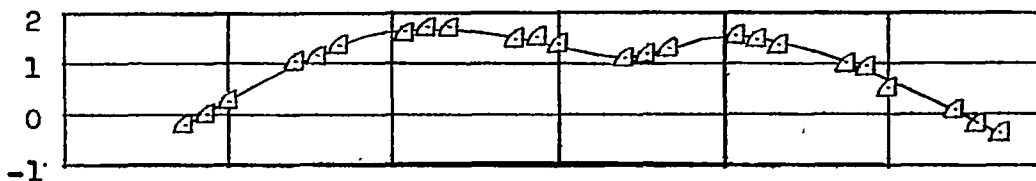
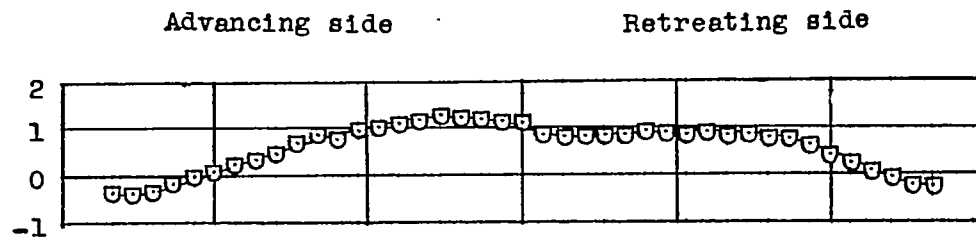
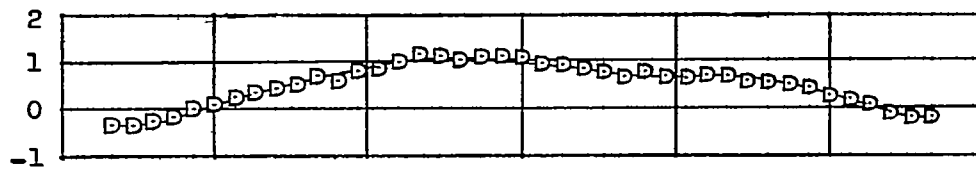
 v/v_0 

Figure 15.- Continued.

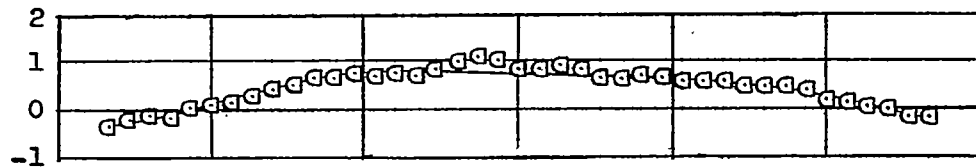


(q) $Z/R = -0.83$.

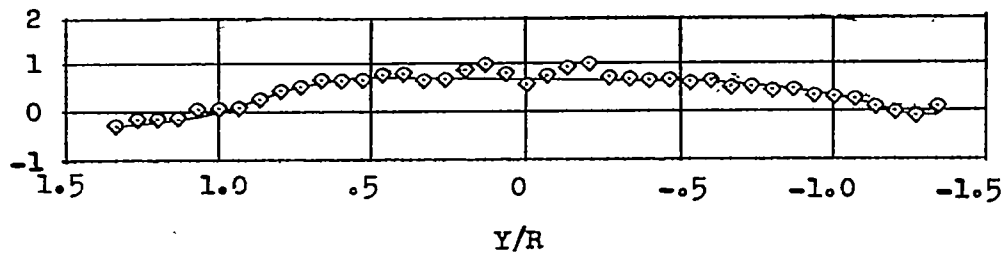


(r) $Z/R = -0.90$.

v/v_0



(s) $Z/R = -0.97$.



(t) $Z/R = -1.03$.

Figure 15.- Concluded.

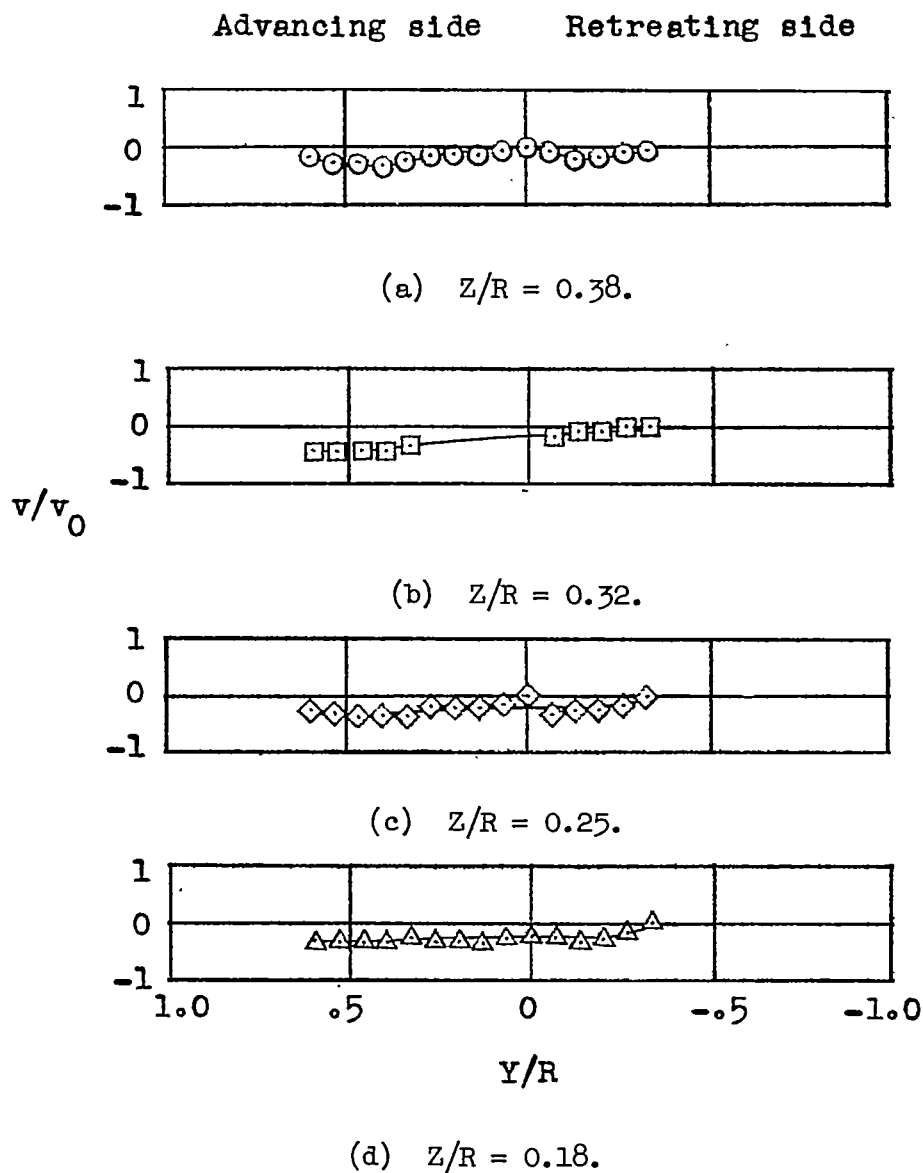


Figure 16.- Measured values of induced-velocity ratio v/v_0 . $X/R = -1.0$;
 $\alpha = 82.3^\circ$; $\mu = 0.140$.

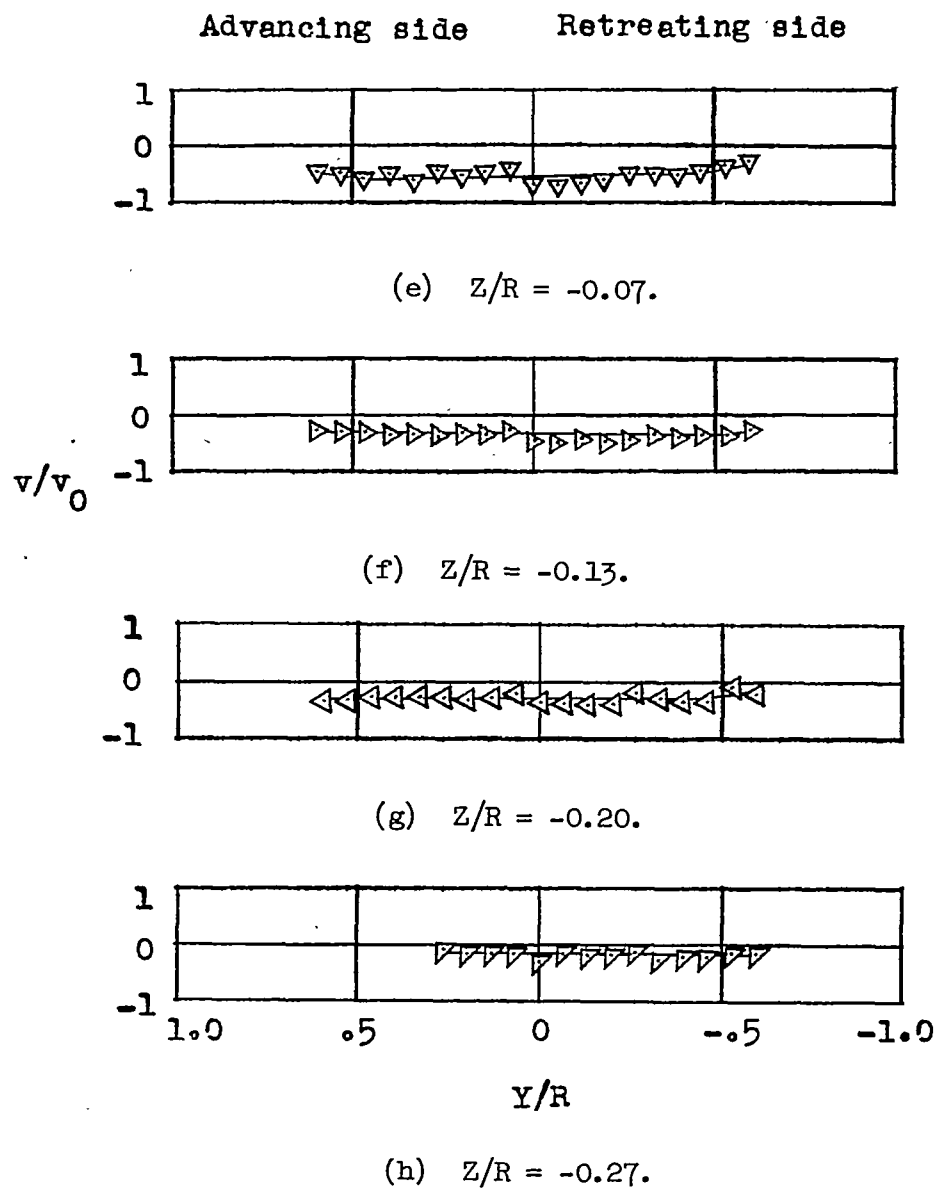


Figure 16.- Concluded.

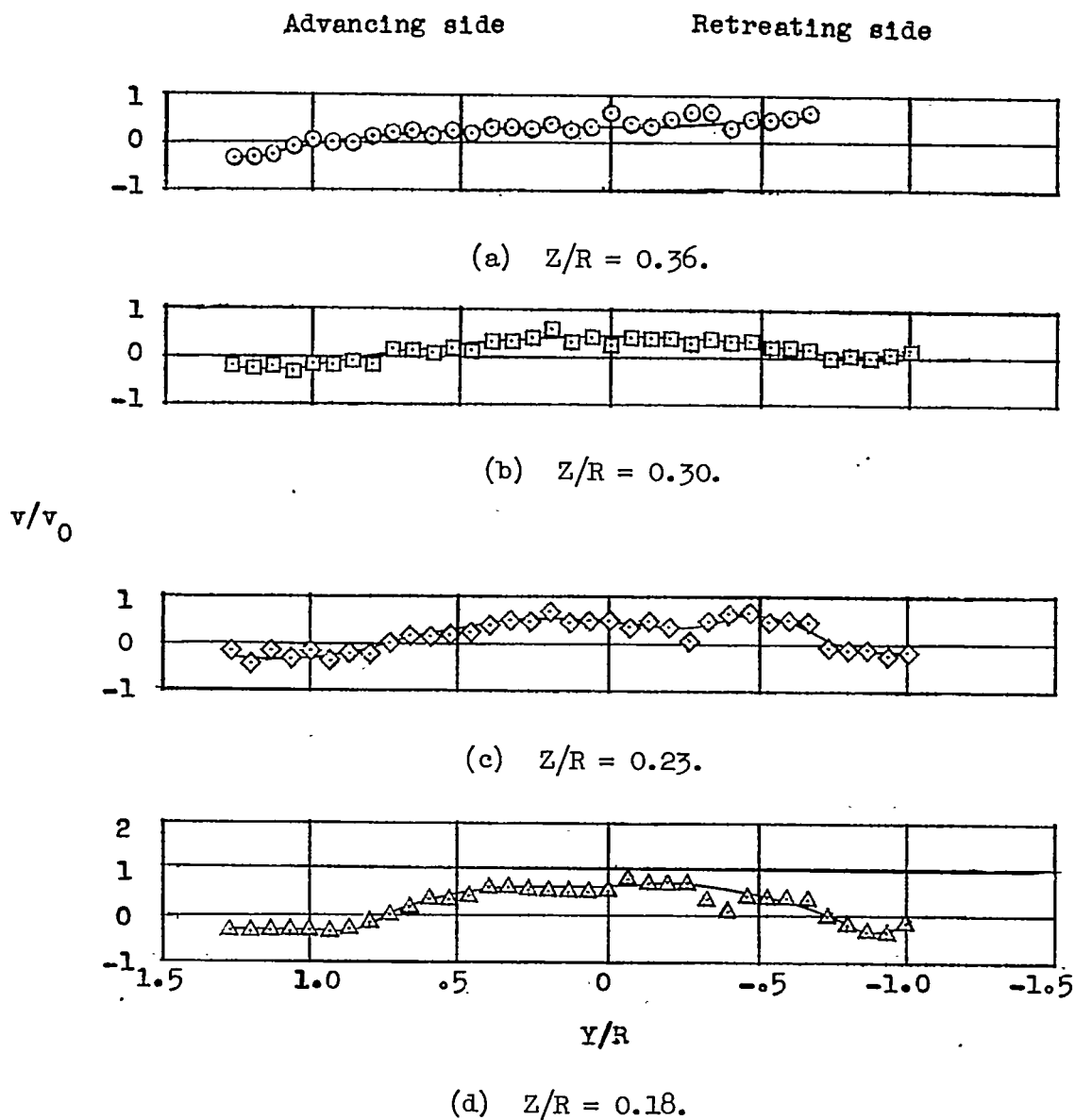


Figure 17.- Measured values of induced-velocity ratio v/v_0 . $X/R = -0.5$;
 $\alpha = 82.3^\circ$; $\mu = 0.140$.

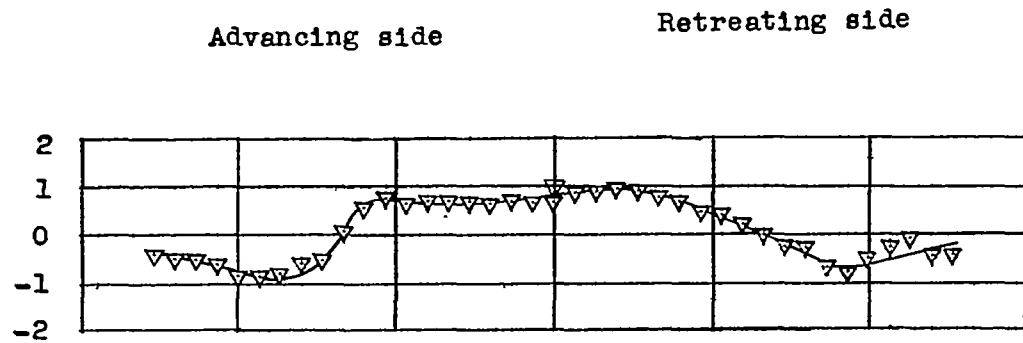
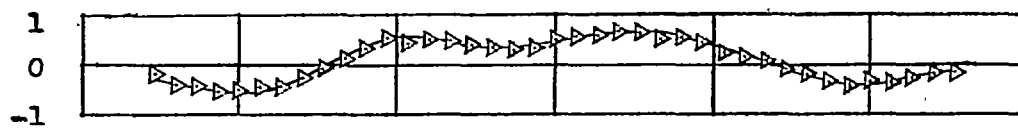
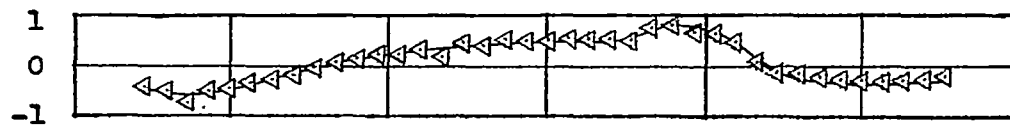
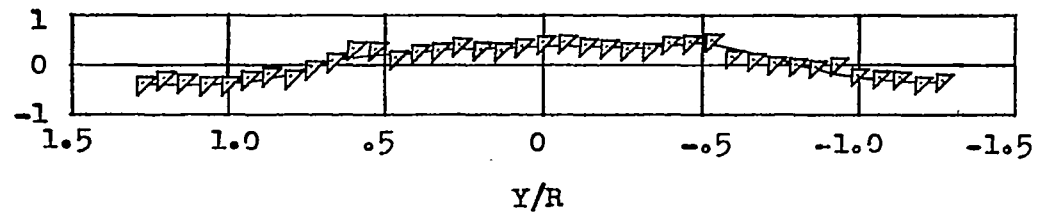
(e) $Z/R = -0.07.$ (f) $Z/R = -0.14.$ v/v_0 (g) $Z/R = -0.20.$ (h) $Z/R = -0.27.$

Figure 17.- Concluded.

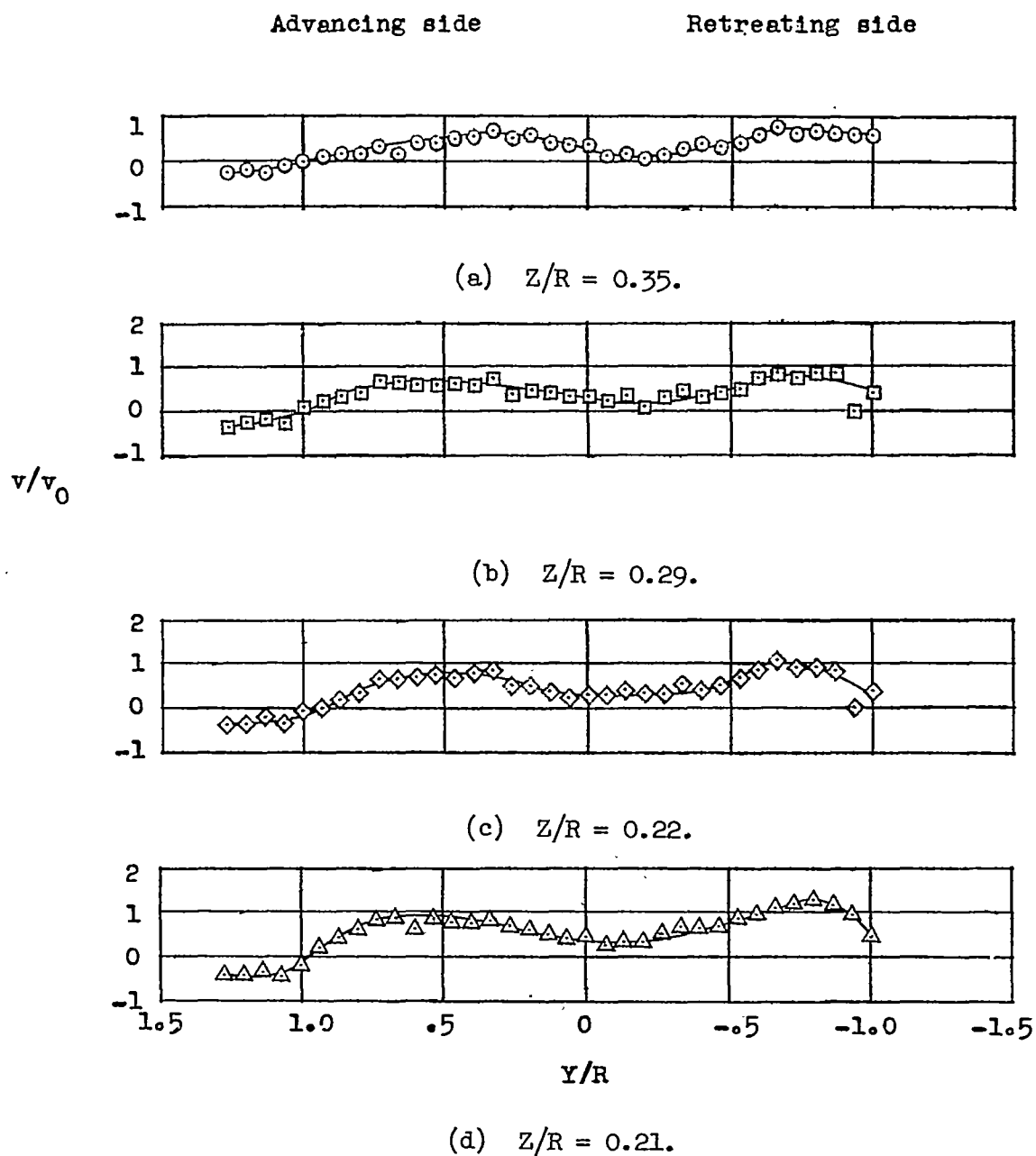


Figure 18.- Measured values of induced-velocity ratio v/v_0 . $X/R = 0$;
 $\alpha = 82.3^\circ$; $\mu = 0.140$.

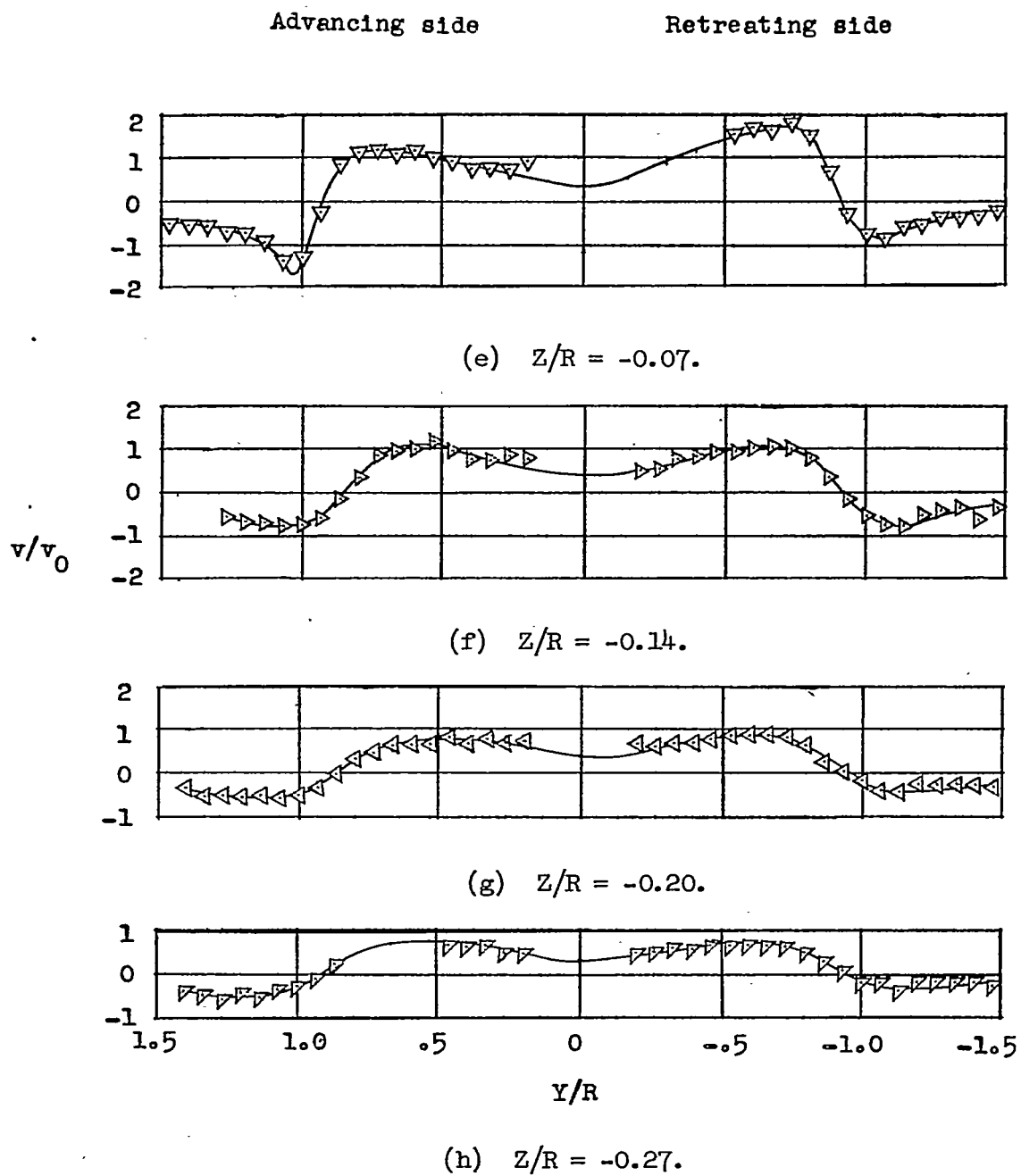


Figure 18.- Concluded.

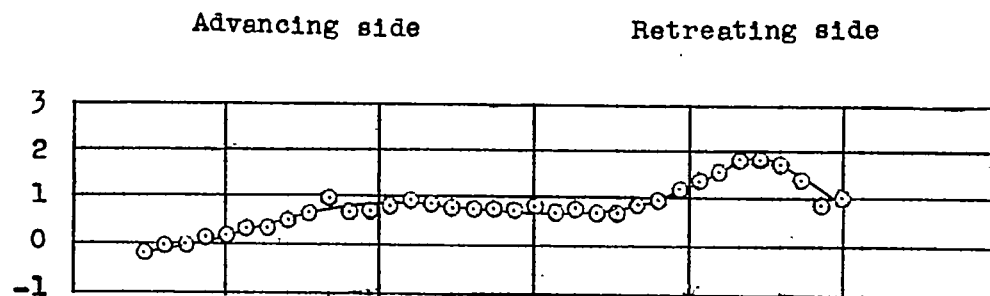
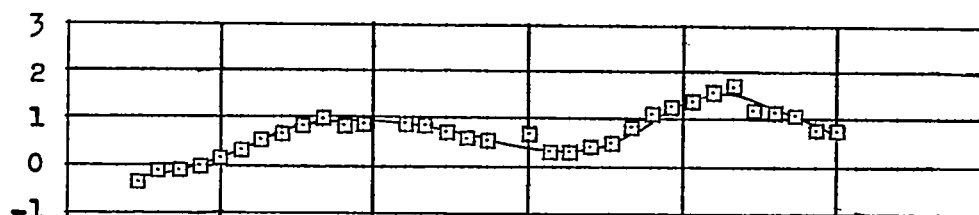
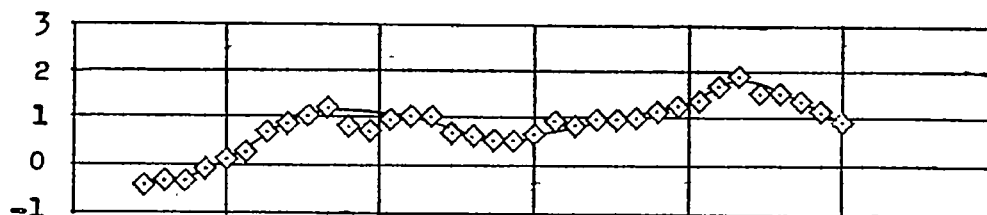
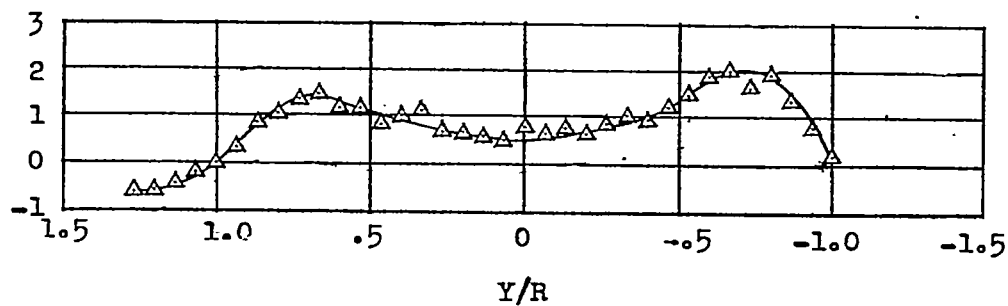
(a) $Z/R = 0.40$.(b) $Z/R = 0.34$. v/v_0 (c) $Z/R = 0.27$.(d) $Z/R = 0.20$.

Figure 19.- Measured values of induced-velocity ratio v/v_0 . $X/R = 0.5$;
 $\chi = 82.3^\circ$; $\mu = 0.140$.

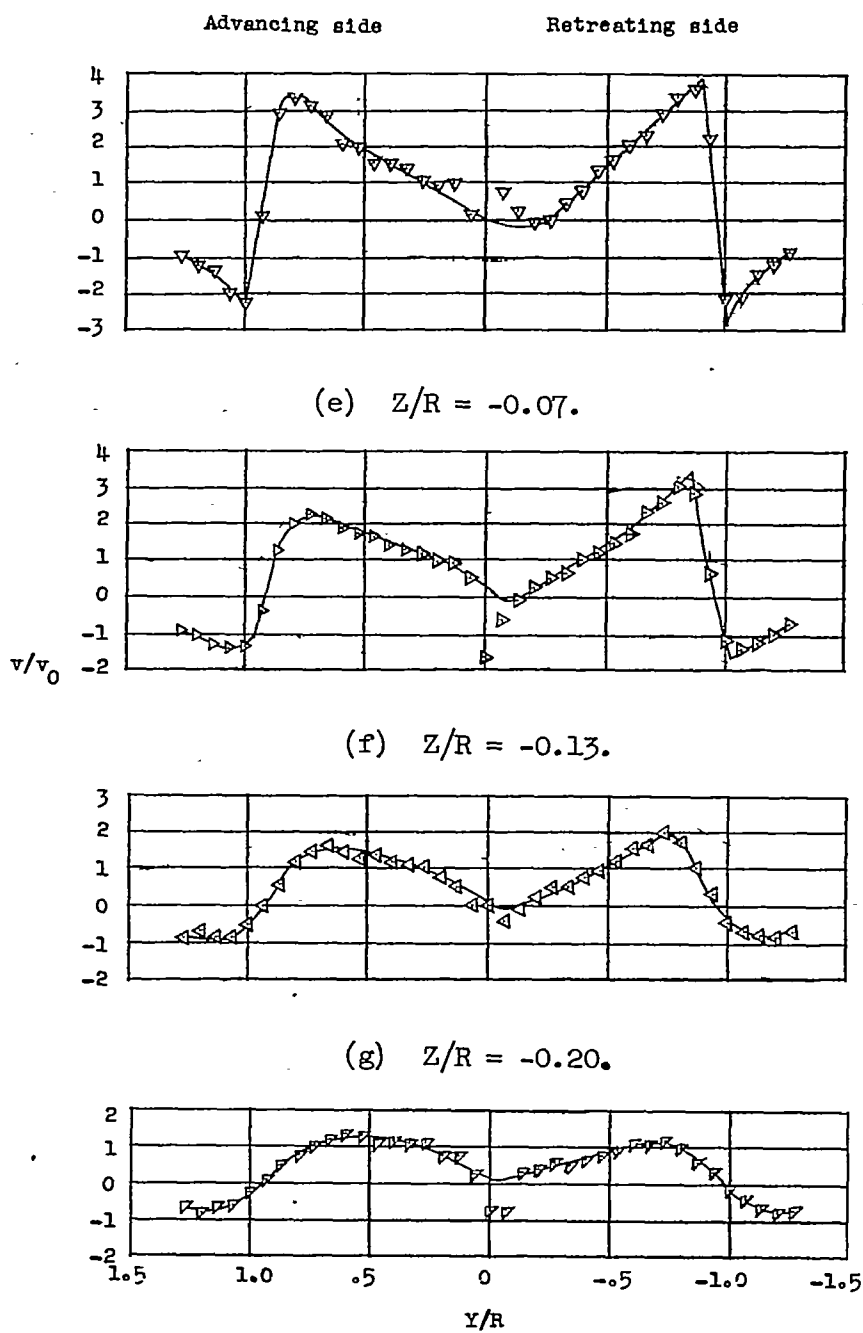


Figure 19.- Concluded.

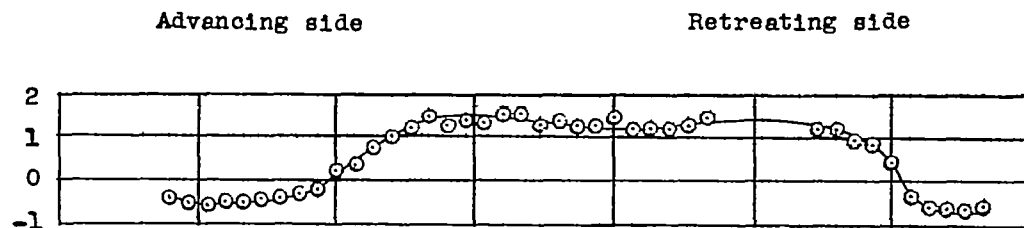
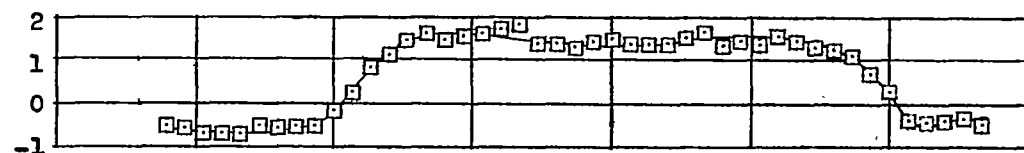
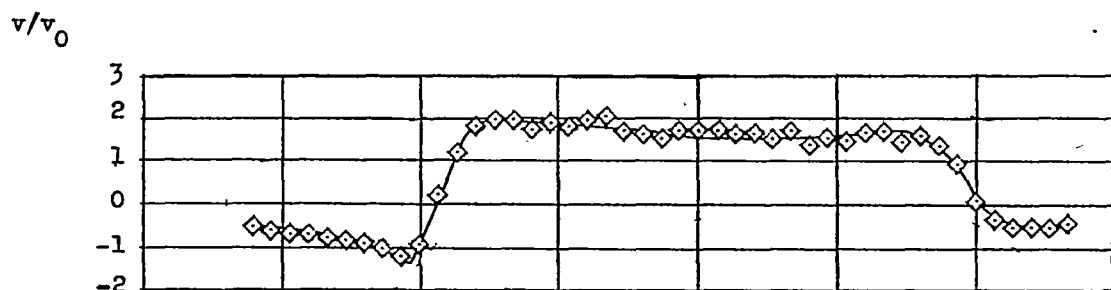
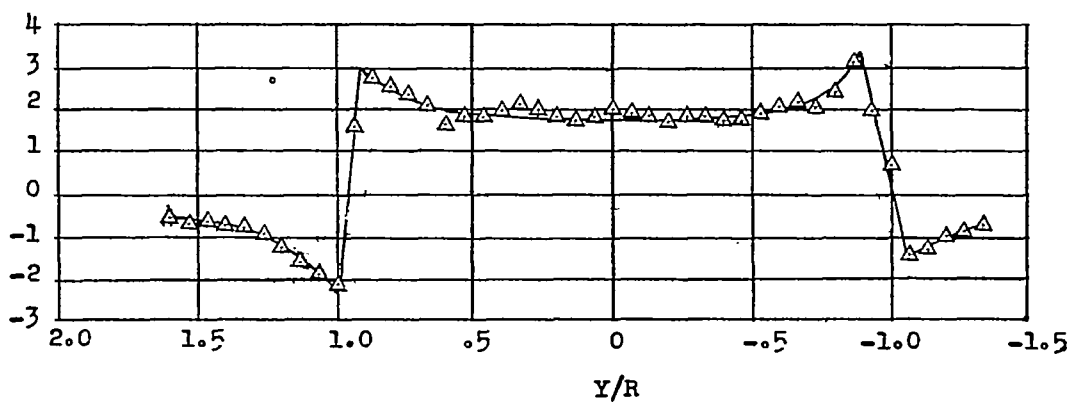
(a) $Z/R = 0.23$.(b) $Z/R = 0.17$.(c) $Z/R = 0.10$.(d) $Z/R = 0.03$.

Figure 20.- Measured values of induced-velocity ratio v/v_0 . $X/R = 1.07$;
 $\alpha = 82.3^\circ$; $\mu = 0.140$.

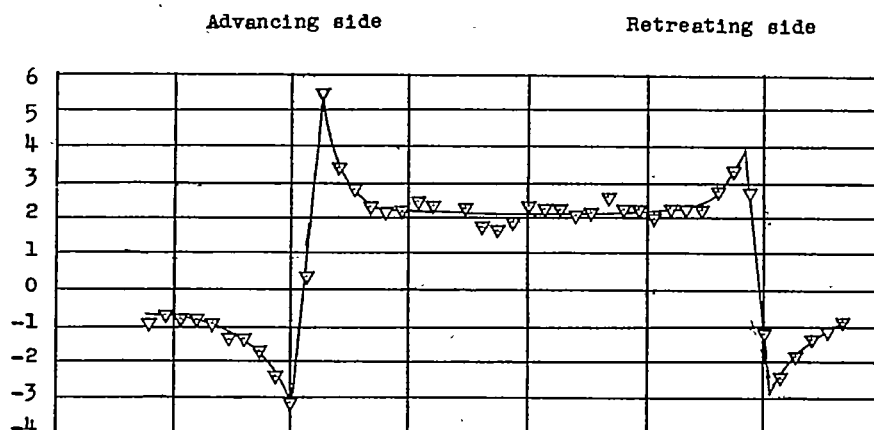
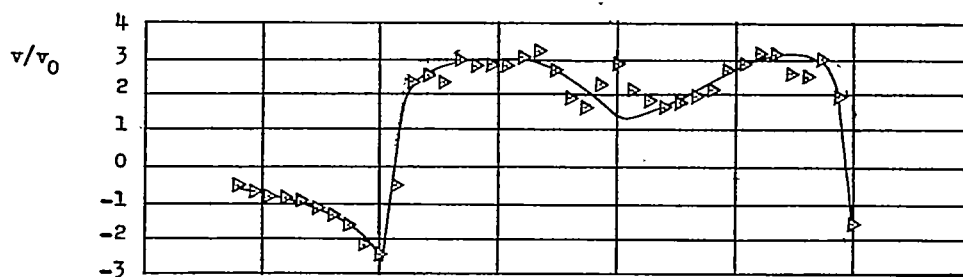
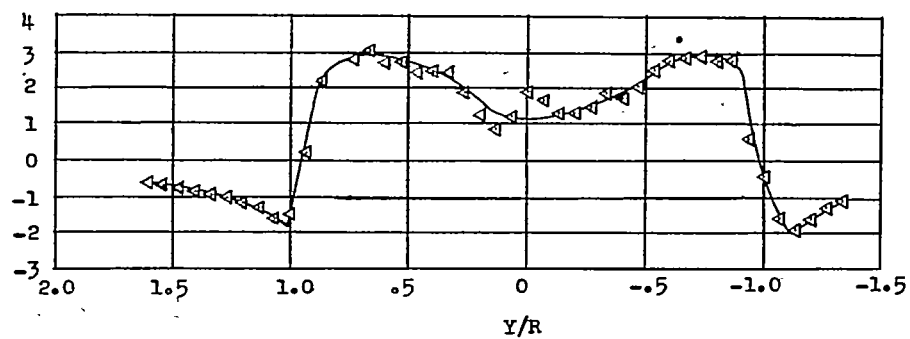
(e) $Z/R = -0.03$.(f) $Z/R = -0.10$.(g) $Z/R = -0.17$.

Figure 20.- Continued.

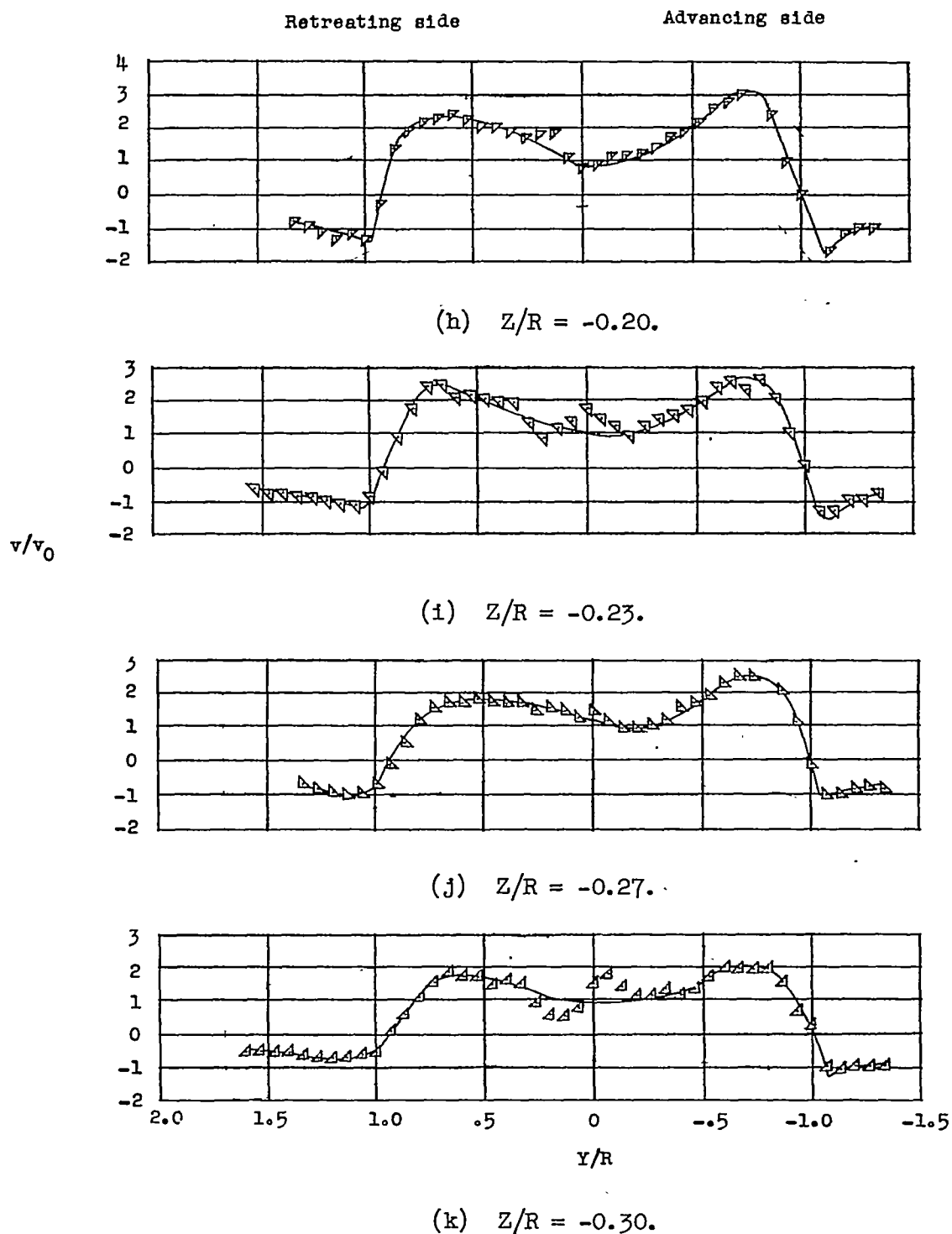


Figure 20.- Continued.

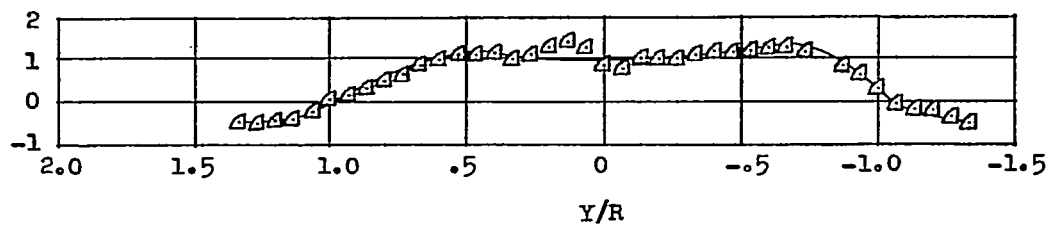
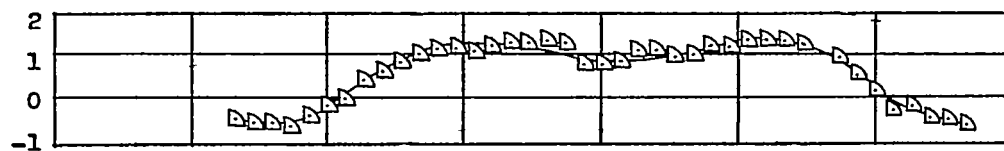
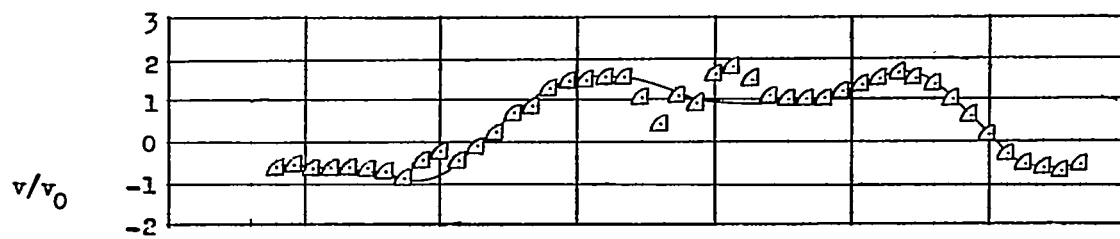
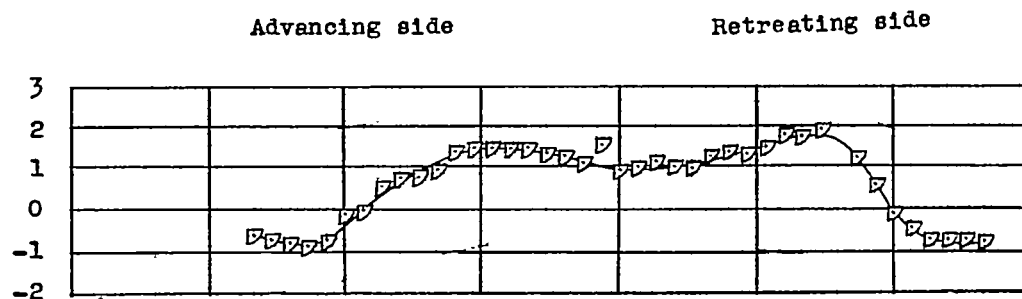


Figure 20.- Continued.

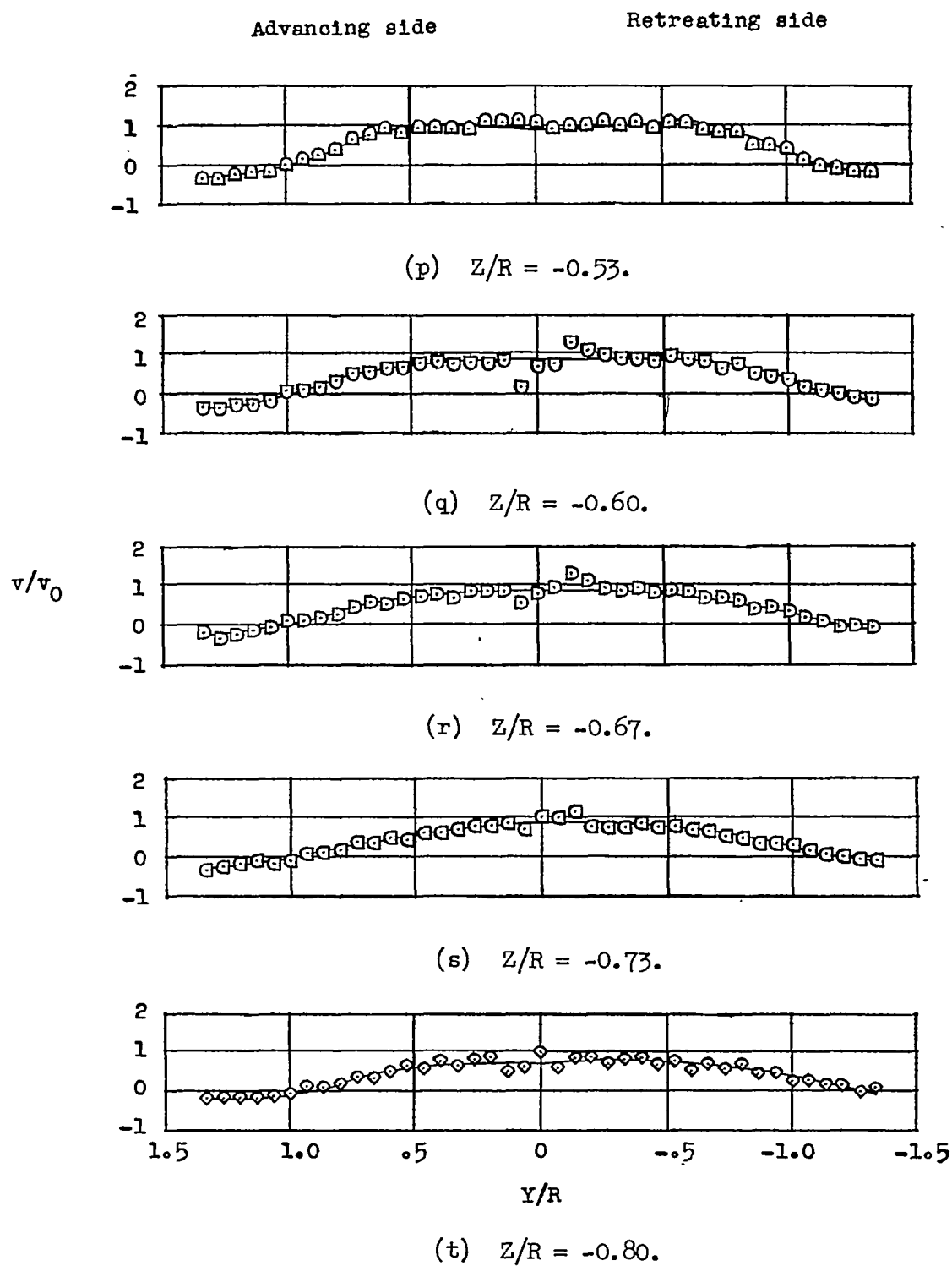


Figure 20.- Concluded.

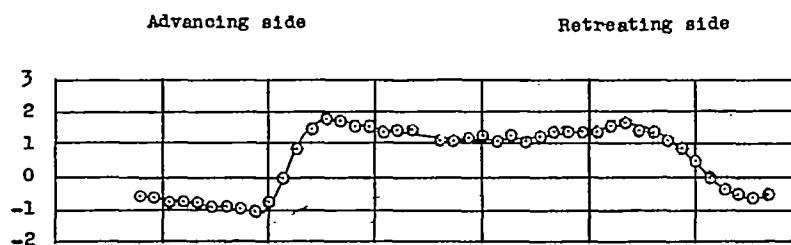
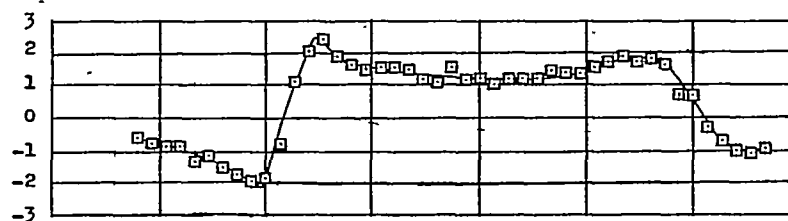
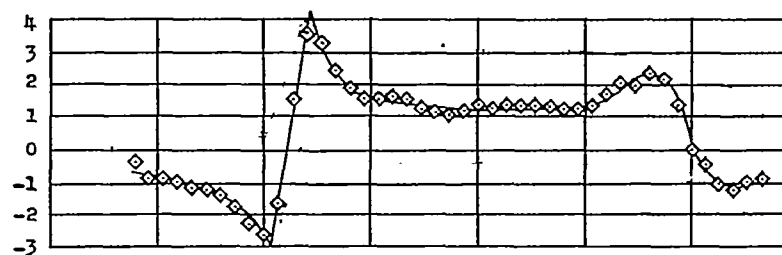
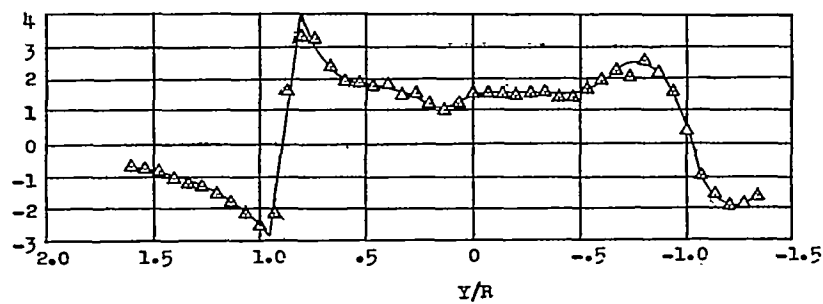
(a) $Z/R = 0.07$.(b) $Z/R = 0$. v/v_0 (c) $Z/R = -0.07$.(d) $Z/R = -0.13$.

Figure 21.- Measured values of induced-velocity ratio v/v_0 . $X/R = 2.07$;
 $\chi = 82.3^\circ$; $\mu = 0.140$.

Advancing side

Retreating side

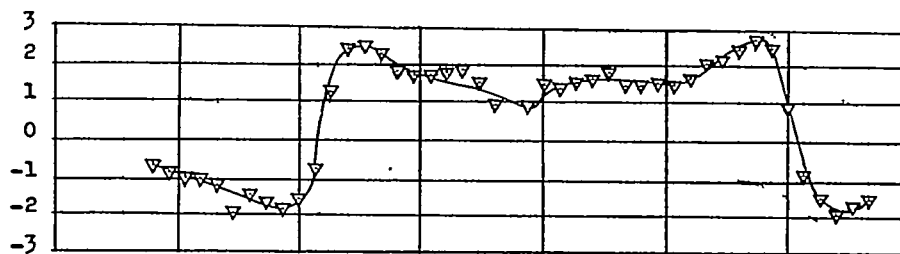
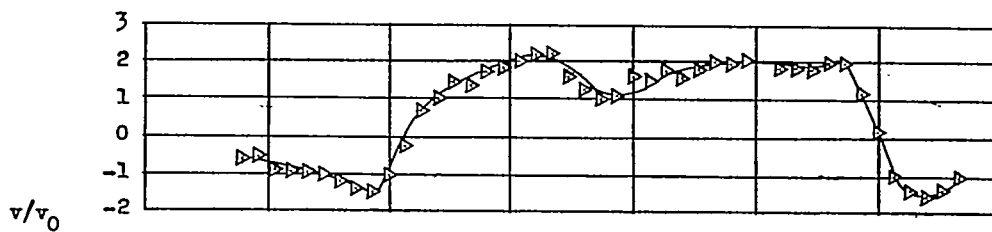
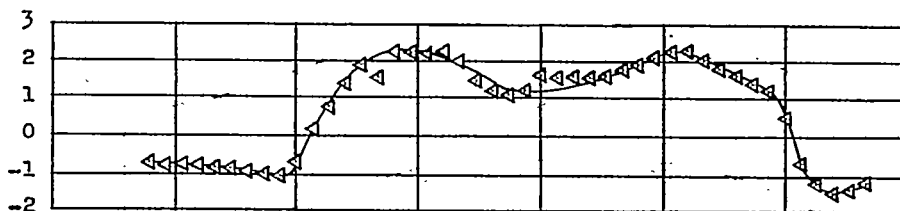
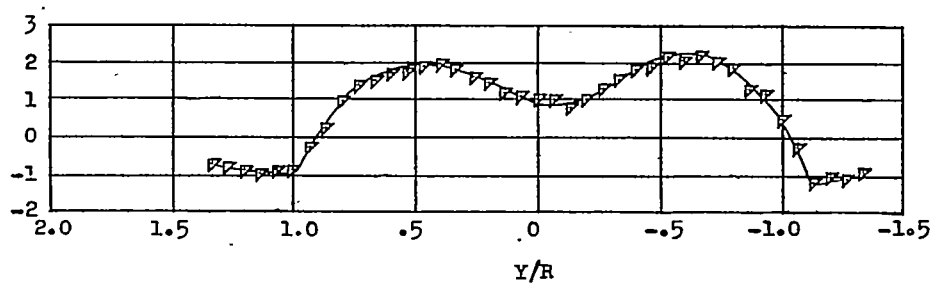
(e) $Z/R = -0.20$.(f) $Z/R = -0.27$.(g) $Z/R = -0.33$.(h) $Z/R = -0.37$.

Figure 21.- Continued.

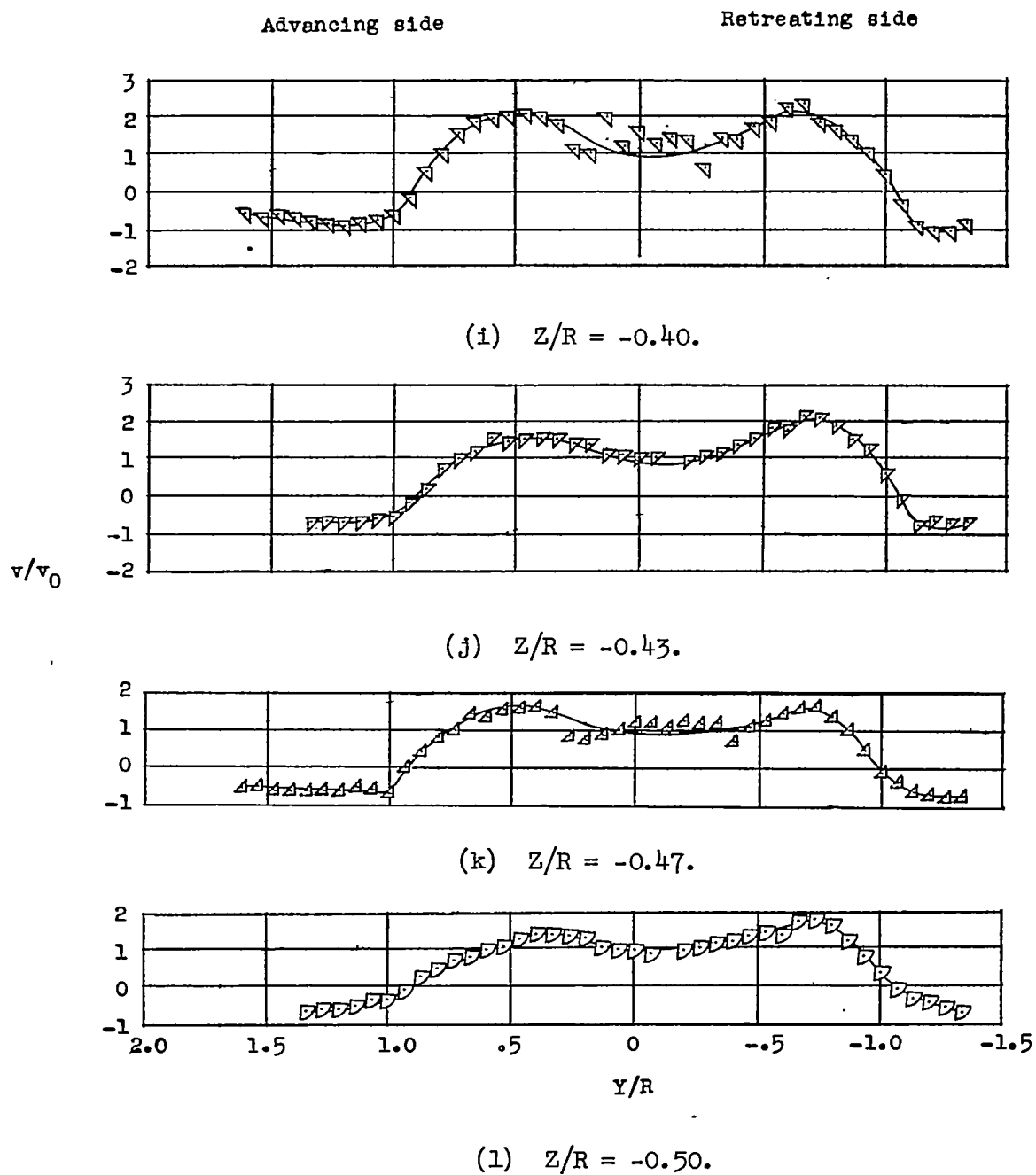
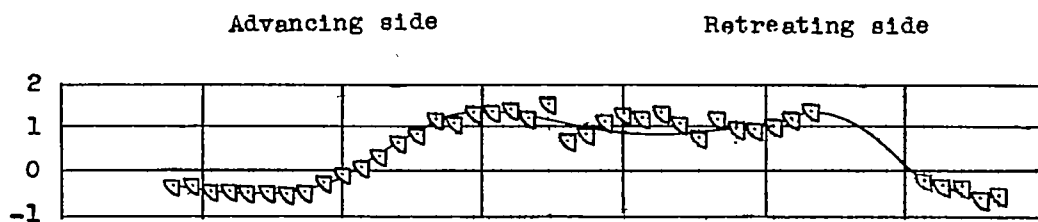


Figure 21.- Continued.

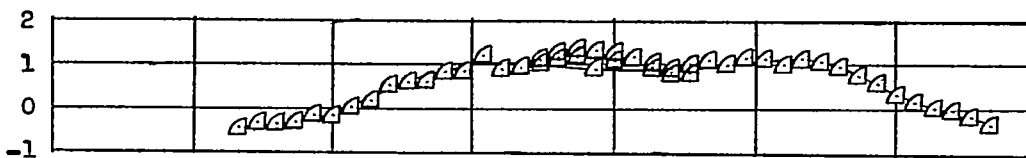


(m) $Z/R = -0.53$.

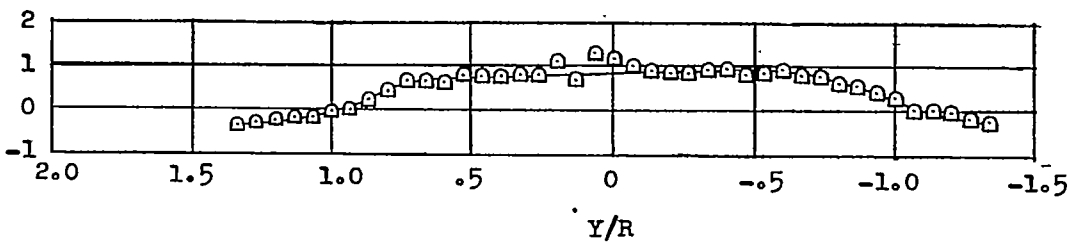


(n) $Z/R = -0.57$.

v/v_0

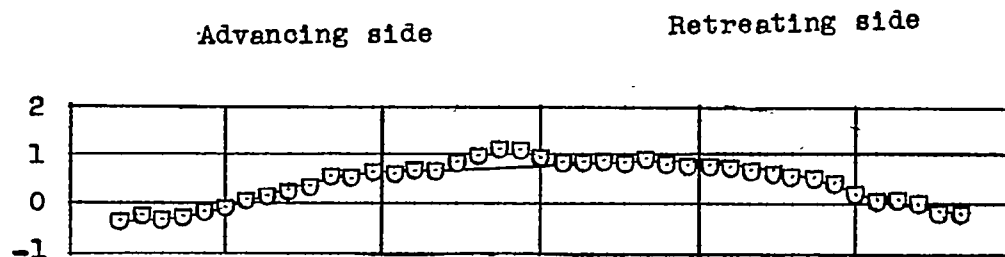


(o) $Z/R = -0.63$.

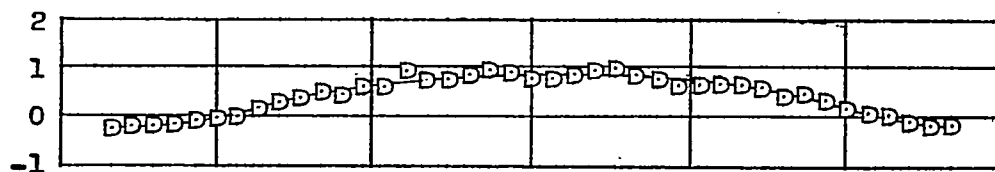


(p) $Z/R = -0.70$.

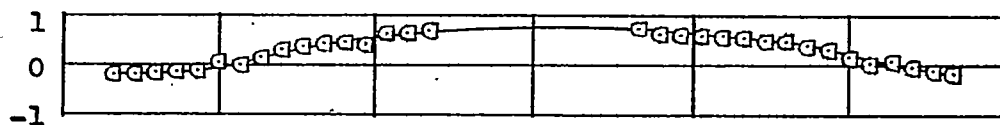
Figure 21.- Continued.



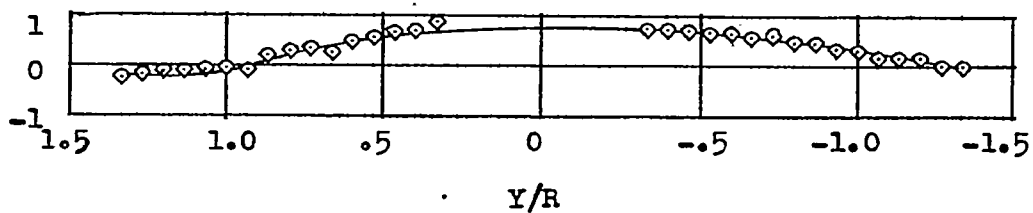
(q) $Z/R = -0.77.$



(r) $Z/R = -0.83.$



(s) $Z/R = -0.90.$



(t) $Z/R = -0.97.$

Figure 21.- Concluded.

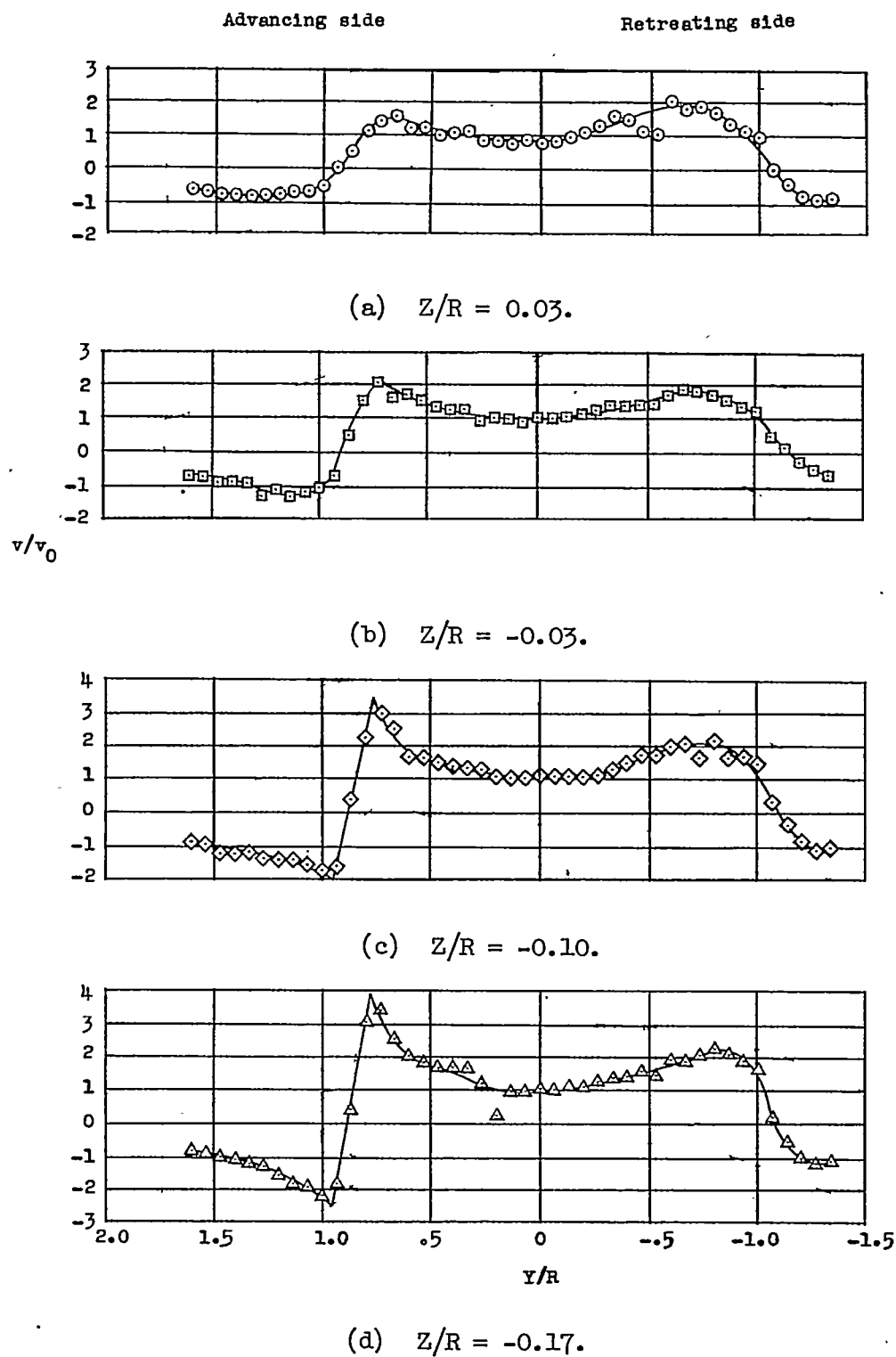


Figure 22.- Measured values of induced-velocity ratio v/v_0 . $X/R = 3.14$;
 $\alpha = 82.3^\circ$; $\mu = 0.140$.

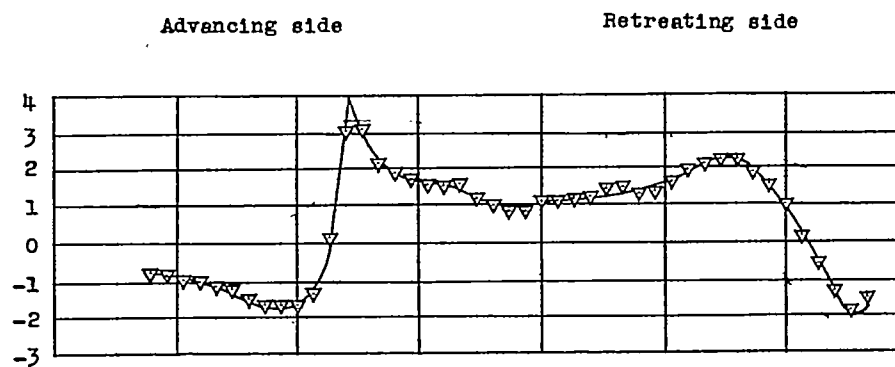
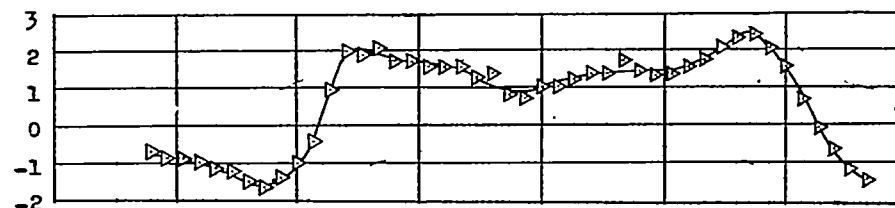
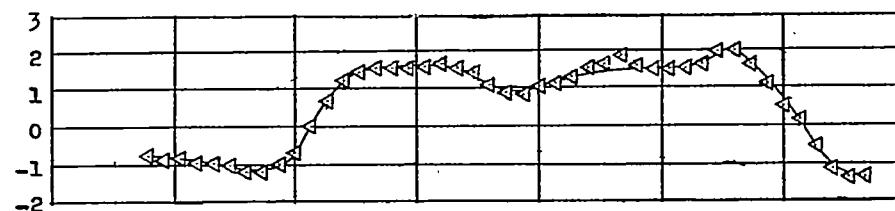
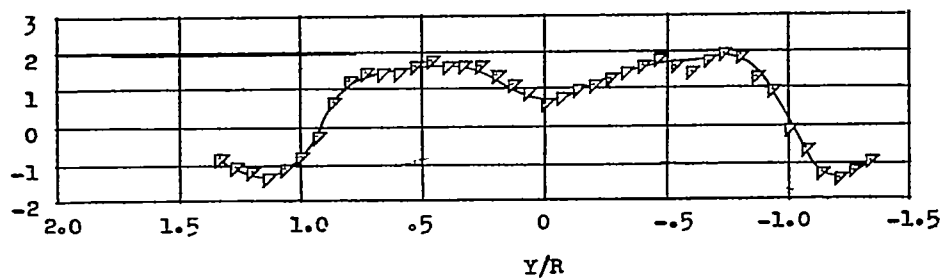
(e) $Z/R = -0.23$.(f) $Z/R = -0.30$. v/v_0 (g) $Z/R = -0.37$.(h) $Z/R = -0.40$.

Figure 22.- Continued.

Advancing side

Retreating side

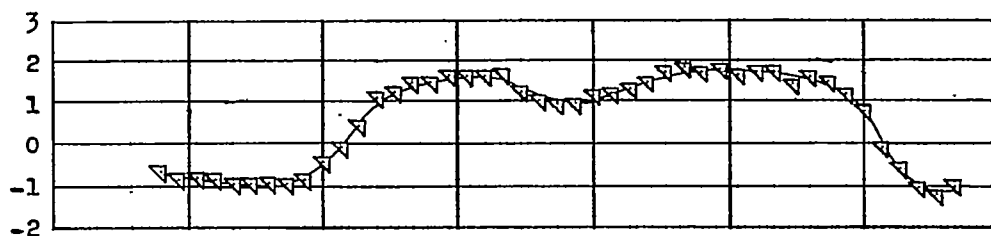
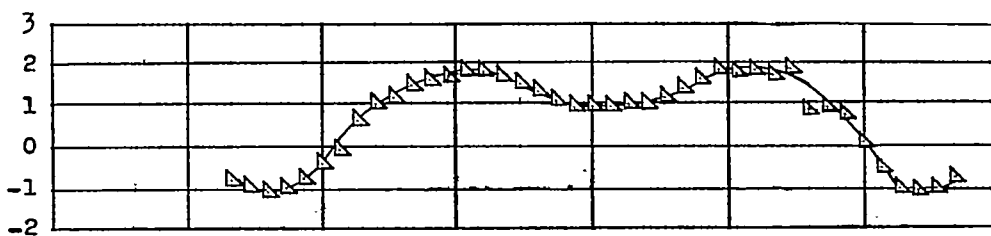
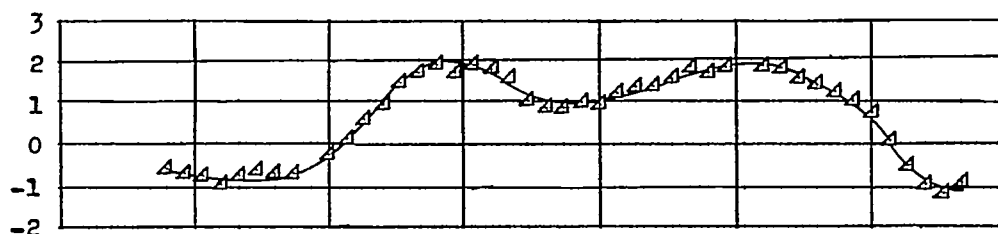
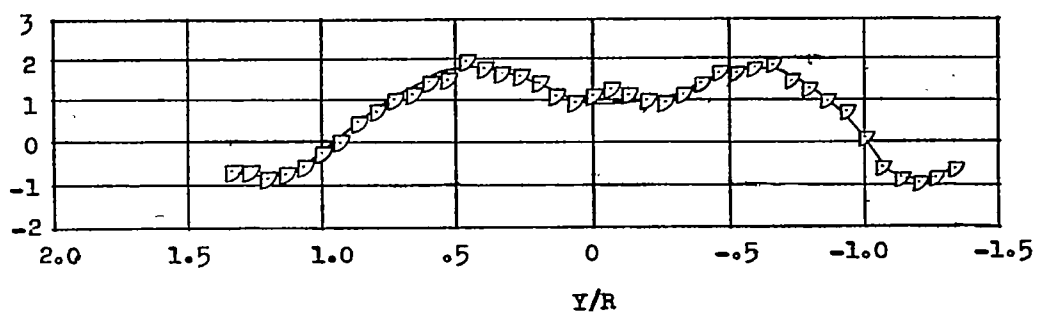
(i) $Z/R = -0.43$.(j) $Z/R = -0.47$. v/v_0 (k) $Z/R = -0.50$.(l) $Z/R = -0.53$.

Figure 22.- Continued.

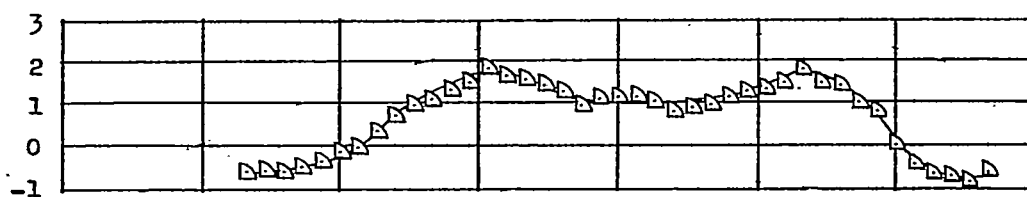
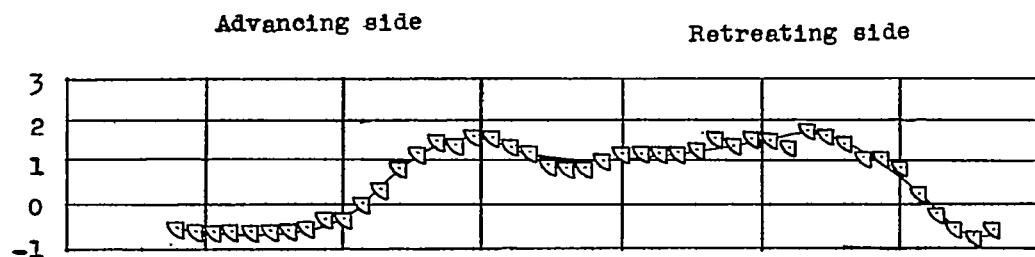
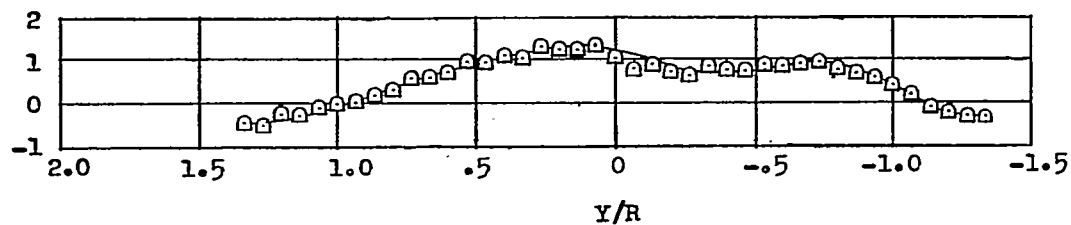
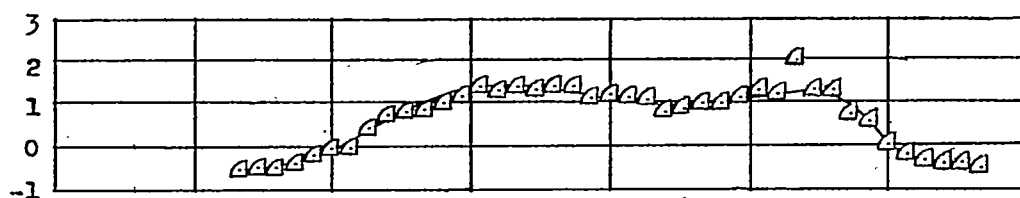

 v/v_0


Figure 22.- Continued.

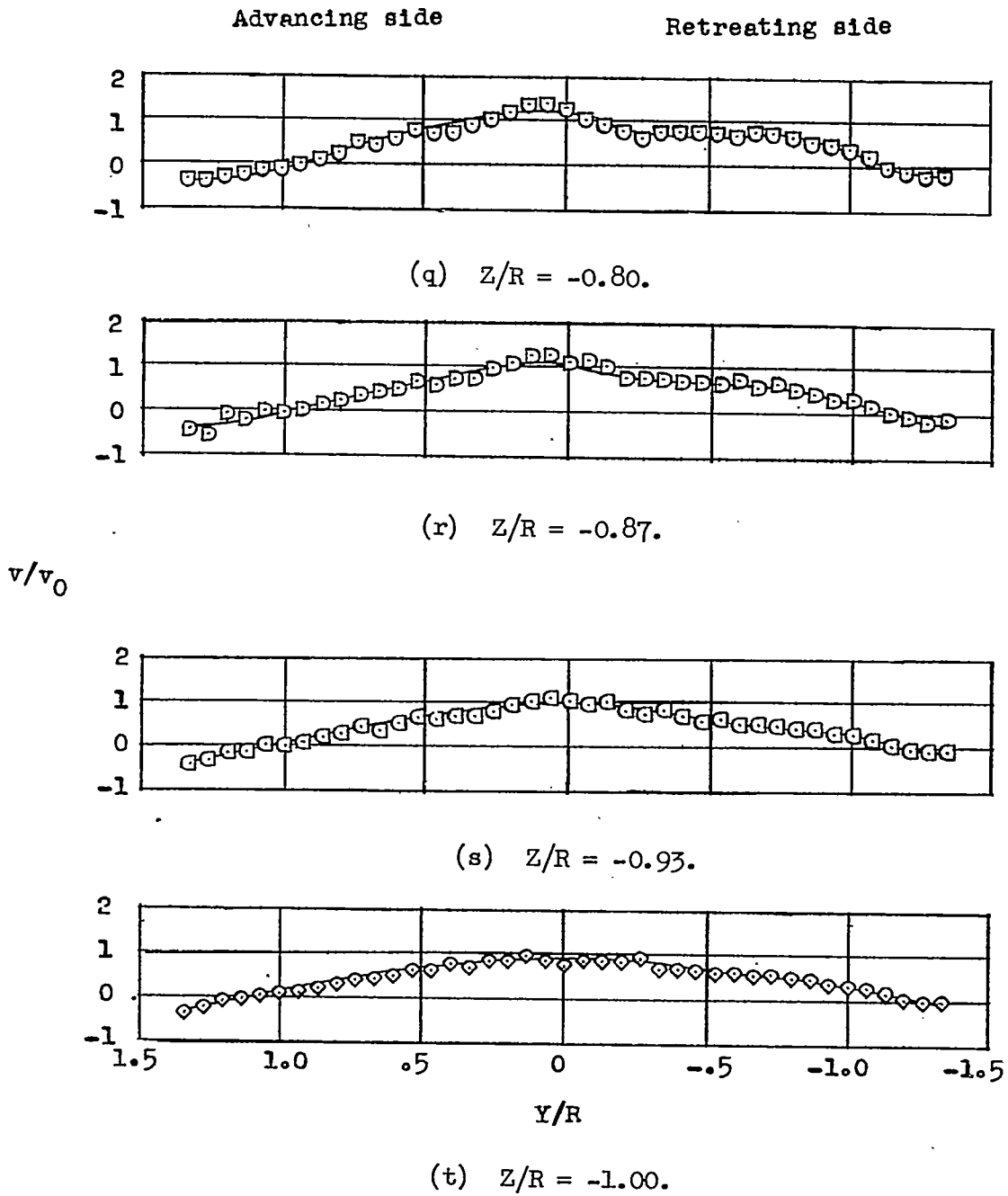


Figure 22.- Concluded.

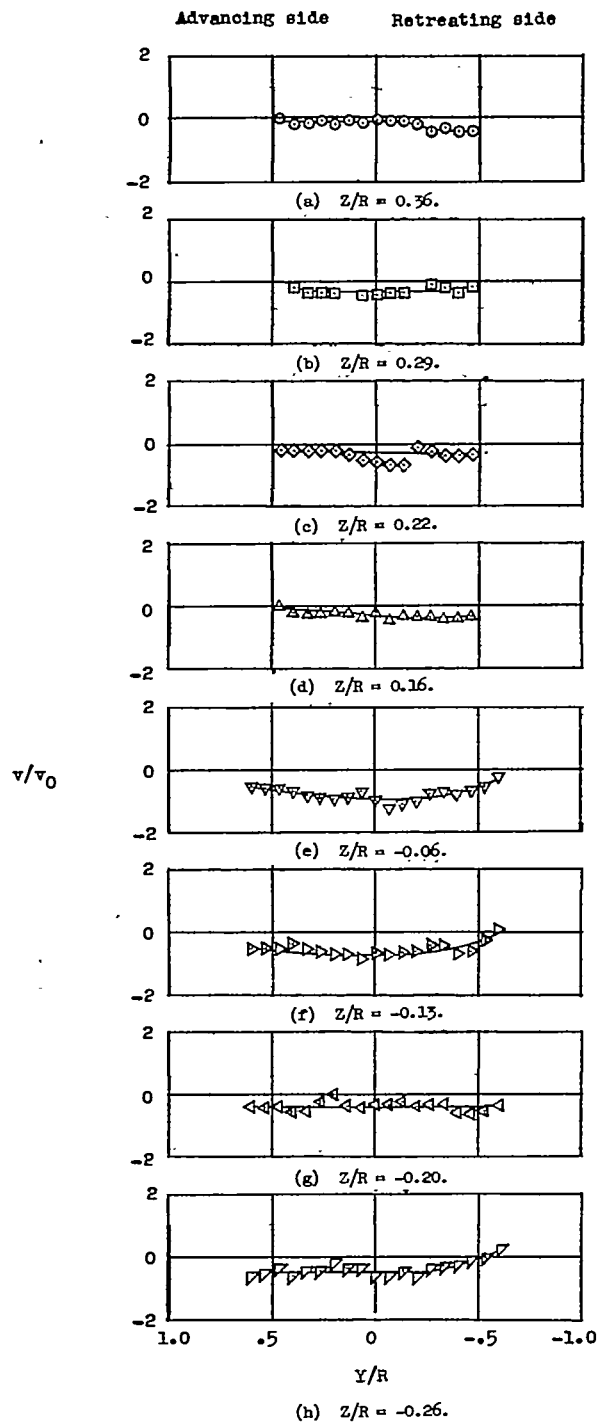


Figure 23.- Measured values of induced-velocity ratio v/v_0 . $X/R = -1.0$;
 $\chi = 83.9^\circ$; $\mu = 0.232$.

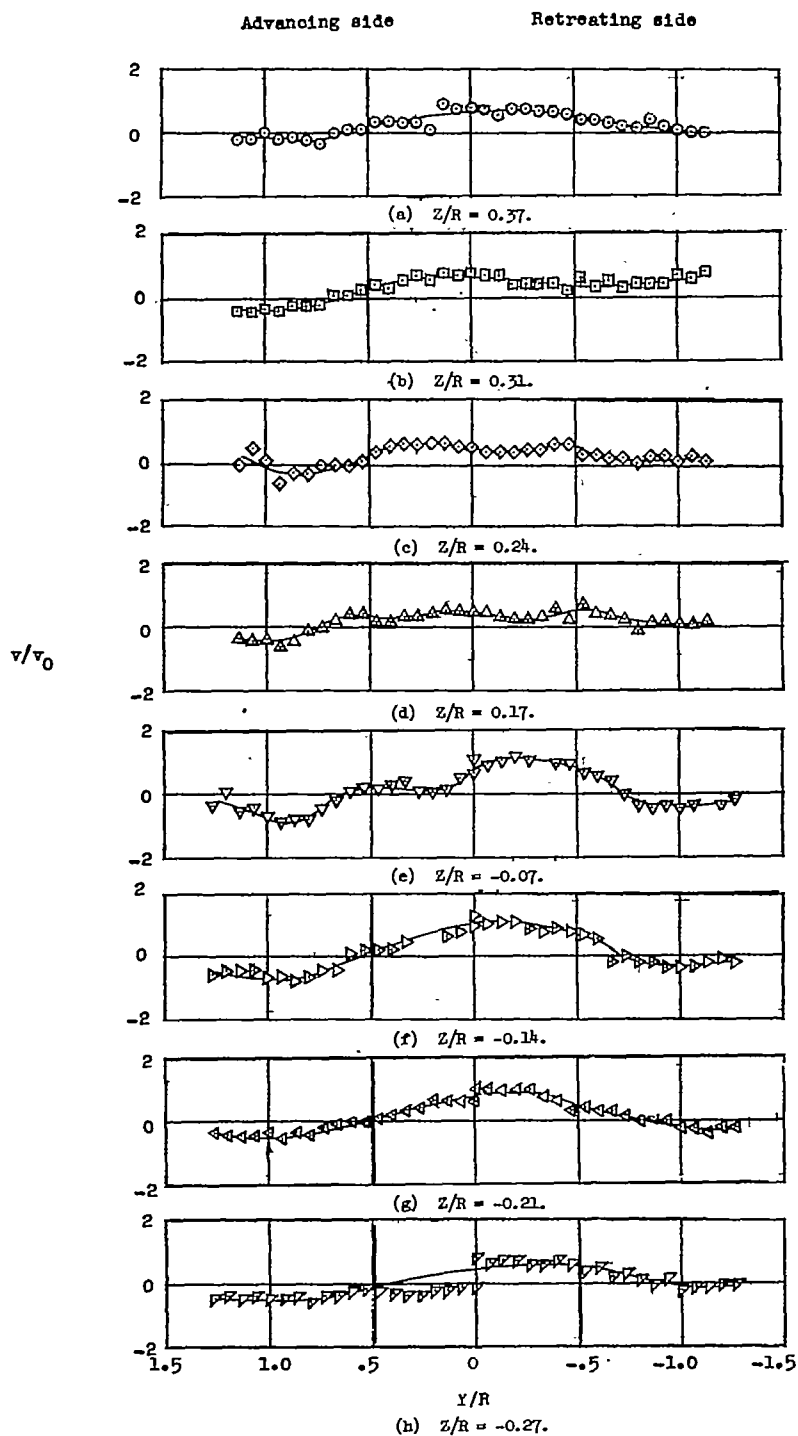


Figure 24.- Measured values of induced-velocity ratio v/v_0 . $X/R = -0.5$;
 $\chi = 83.9^\circ$; $\mu = 0.232$.

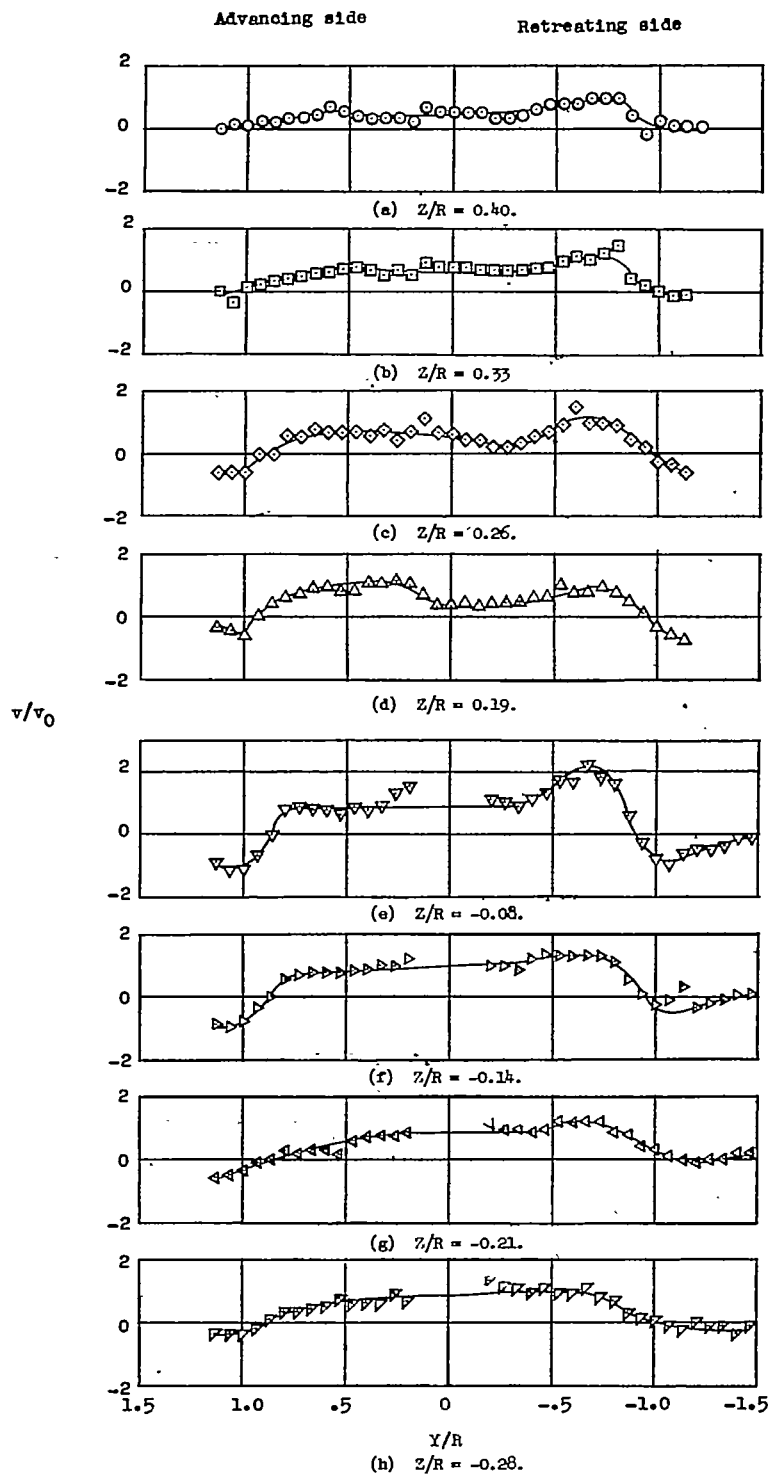


Figure 25.- Measured values of induced-velocity ratio v/v_0 . $X/R = 0$;
 $\alpha = 83.9^\circ$; $\mu = 0.232$.

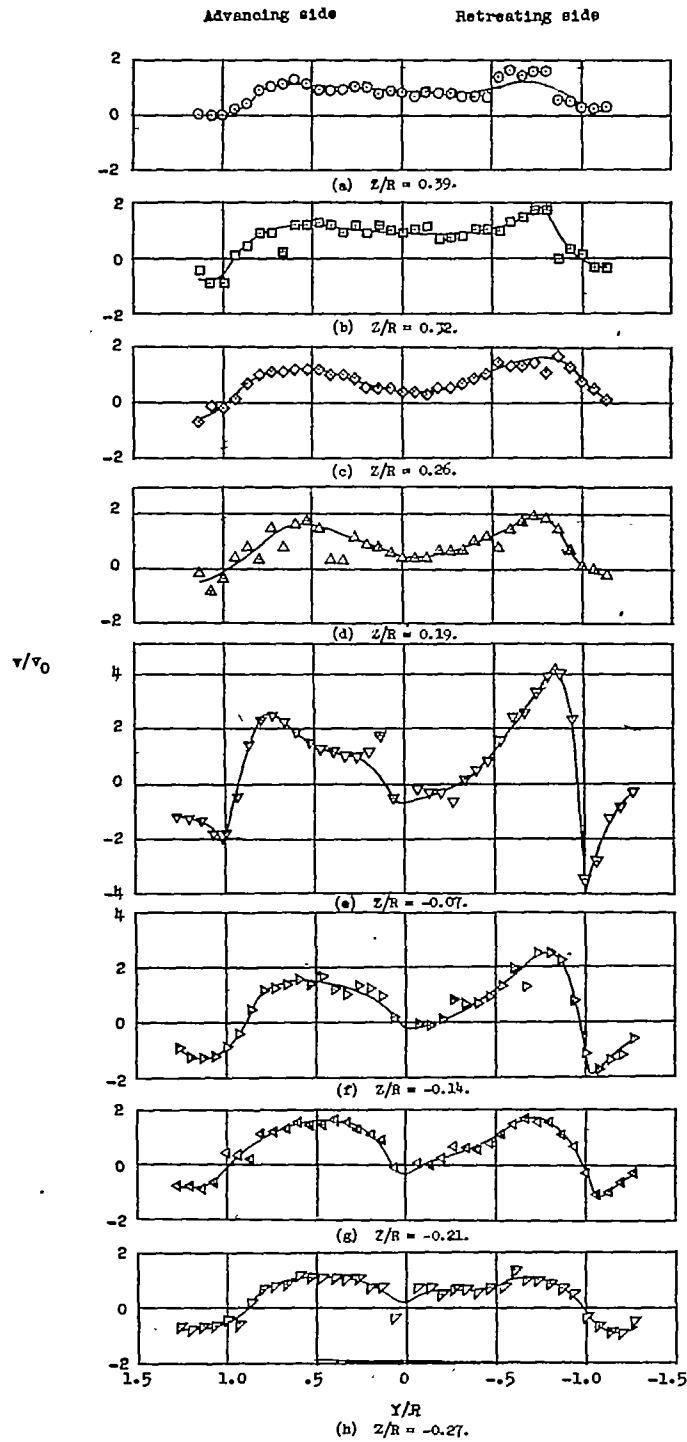


Figure 26.- Measured values of induced-velocity ratio v/v_0 . $X/R = 0.5$;
 $\chi = 83.9^\circ$; $\mu = 0.232$.

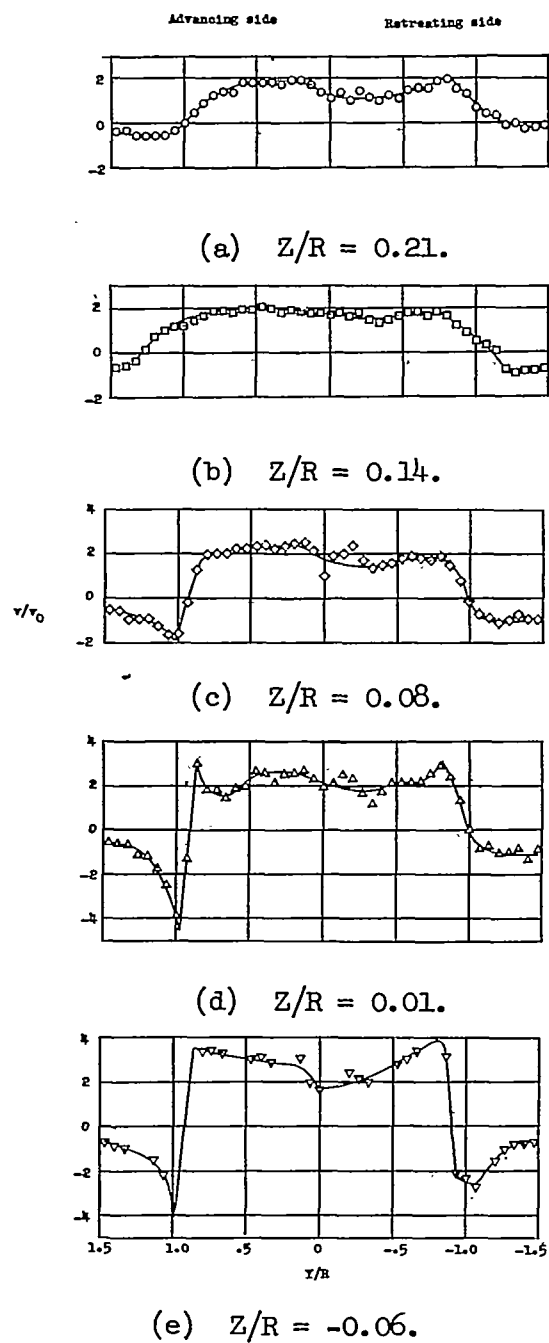
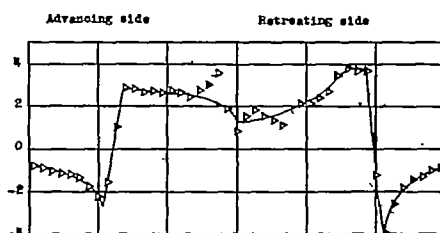
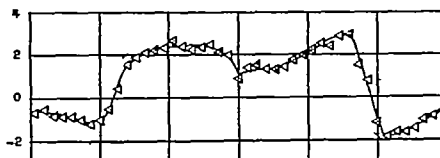


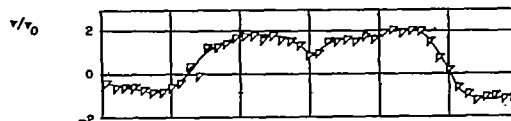
Figure 27.- Measured values of induced velocity ratio v/v_0 . $X/R = 1.07$;
 $\alpha = 83.9^\circ$; $\mu = 0.232$.



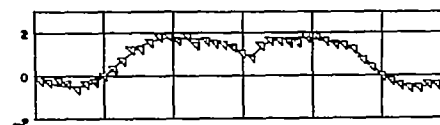
(f) $Z/R = -0.12$.



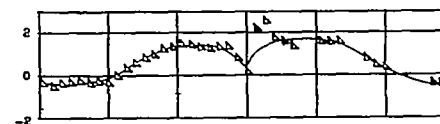
(g) $Z/R = -0.19$.



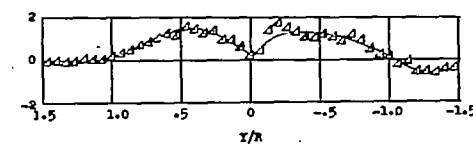
(h) $Z/R = -0.26$.



(i) $Z/R = -0.32$.



(j) $Z/R = -0.39$.



(k) $Z/R = -0.46$.

Figure 27.- Concluded.

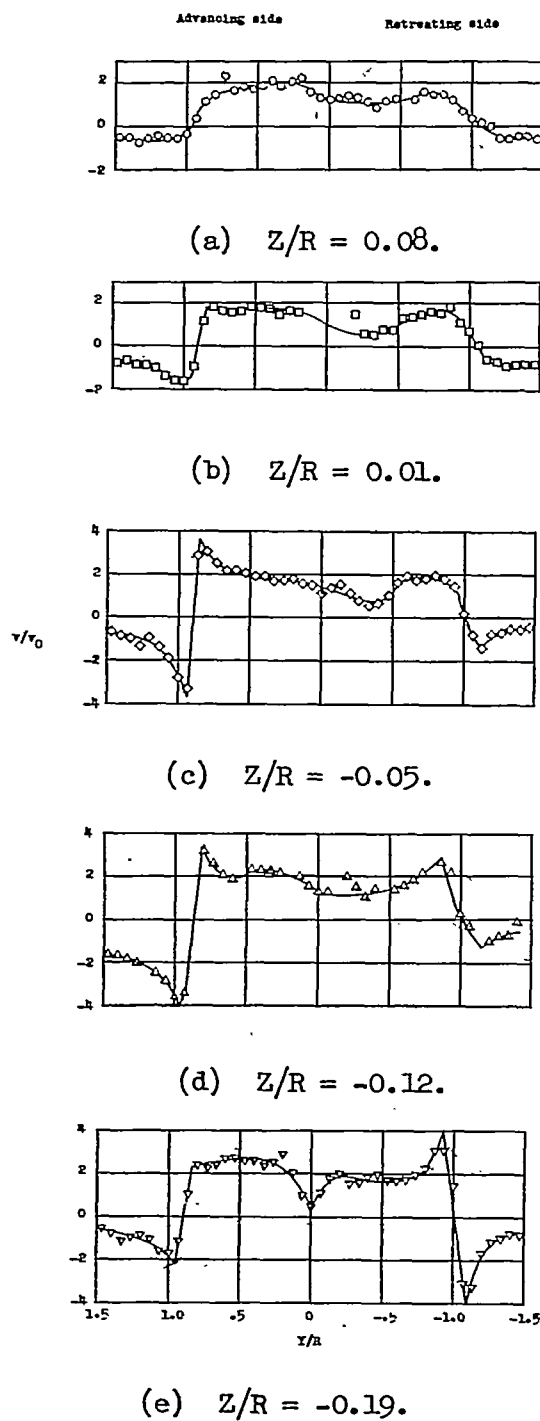
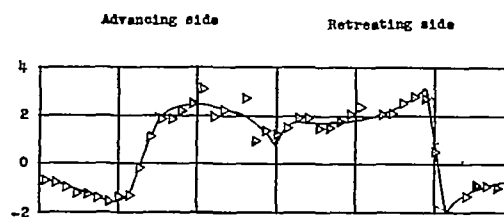


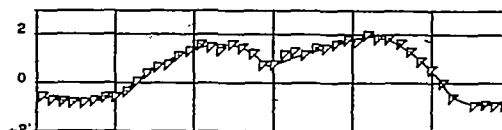
Figure 28.- Measured values of induced-velocity ratio v/v_0 . $X/R = 2.07$;
 $\chi = 83.9^\circ$; $\mu = 0.232$.



(f) $Z/R = -0.25.$

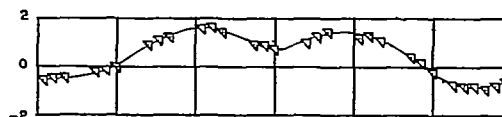


(g) $Z/R = -0.32.$

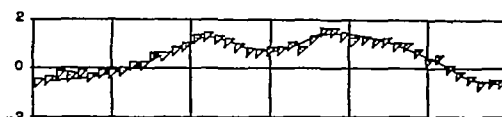


v/v_0

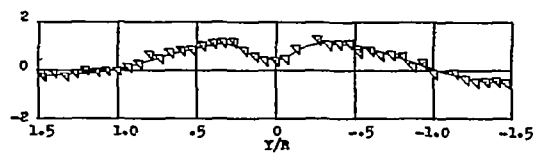
(h) $Z/R = -0.39.$



(i) $Z/R = -0.45.$



(j) $Z/R = -0.52.$



(k) $Z/R = -0.59.$

Figure 28.- Concluded.

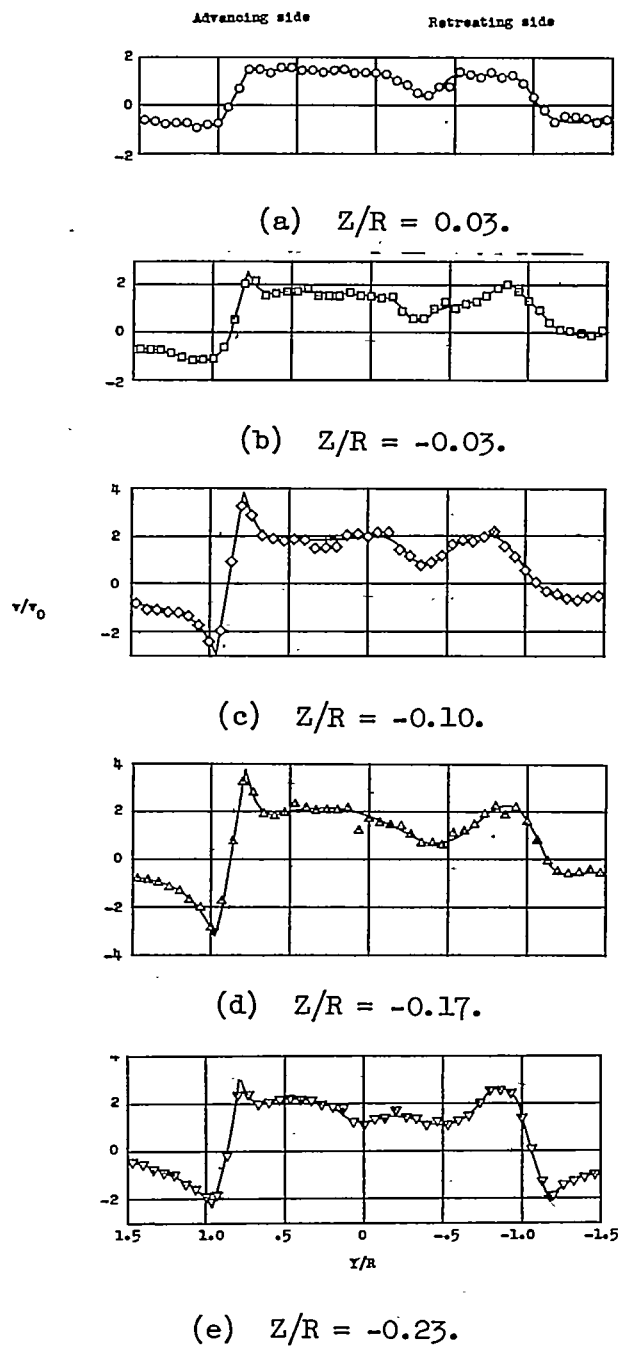


Figure 29.- Measured values of induced-velocity ratio v/v_0 . $X/R = 3.14$;
 $\alpha = 83.9^\circ$; $\mu = 0.232$.

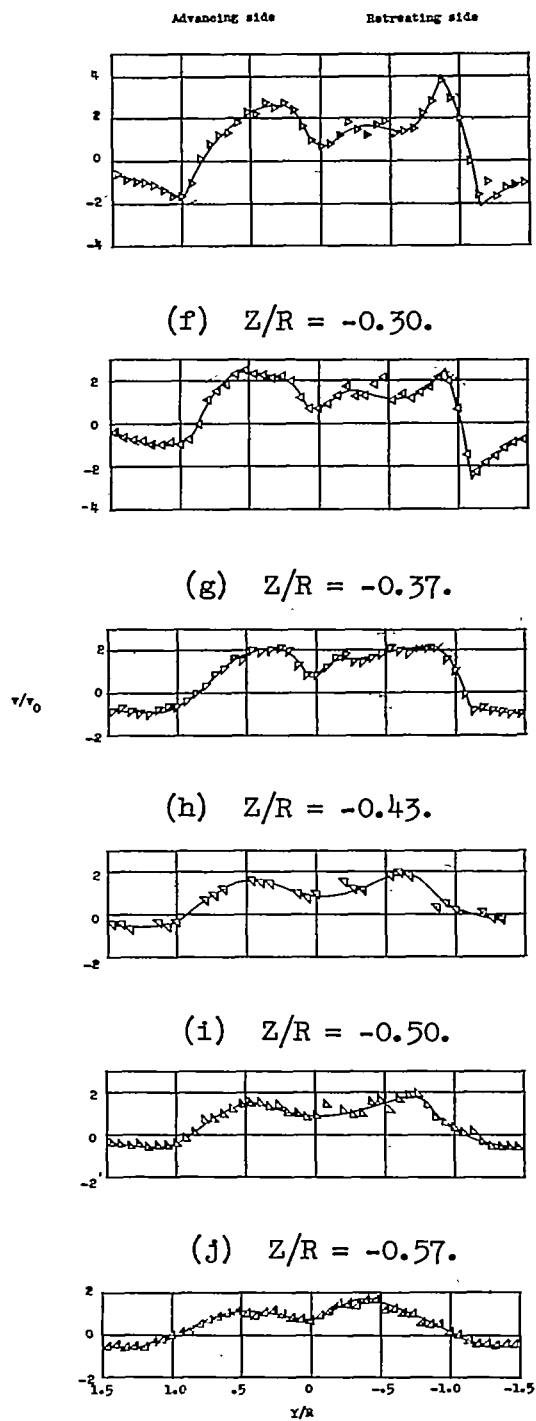


Figure 29.- Concluded.

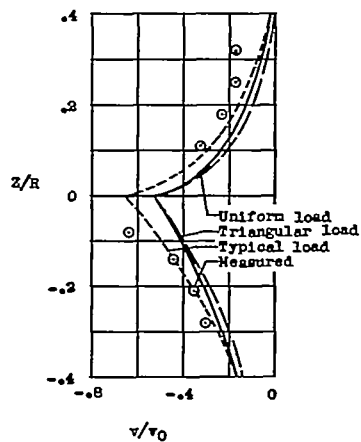
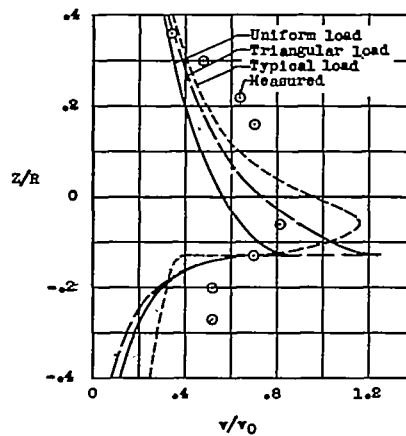
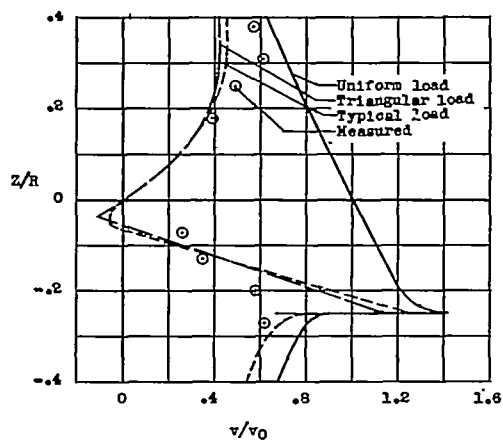
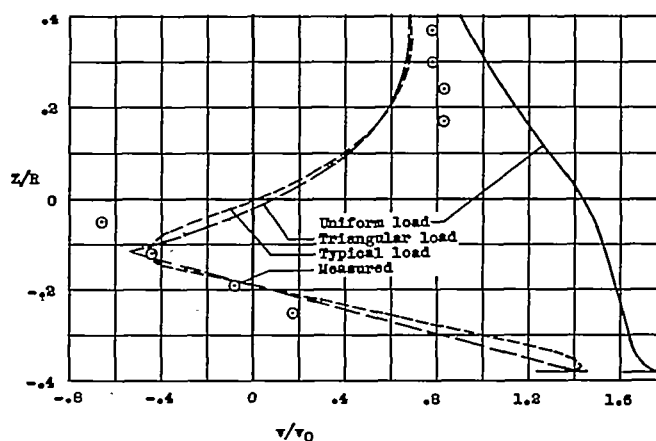
(a) $X/R = -1.0$.(b) $X/R = -0.5$.(c) $X/R = 0$.(d) $X/R = 0.5$.

Figure 30.- Comparison of measured and theoretical values of induced-velocity ratio v/v_0 in longitudinal plane of symmetry. $\chi = 75.0^\circ$; $\mu = 0.095$.

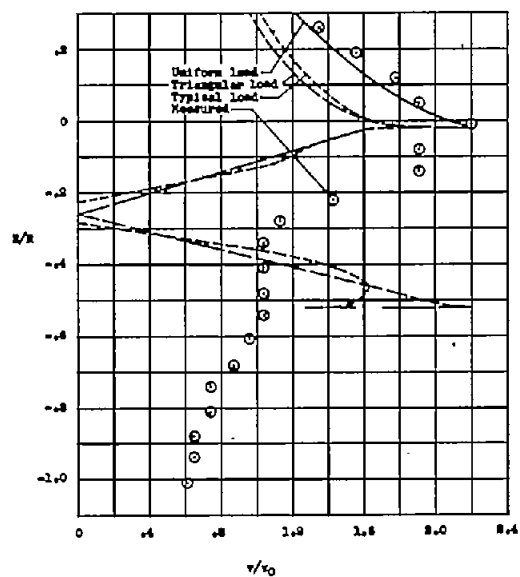
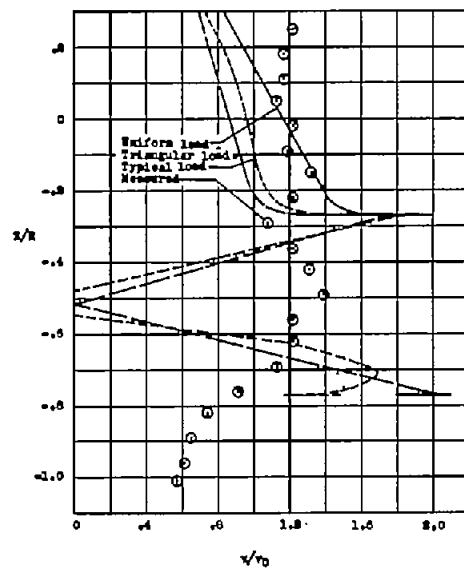
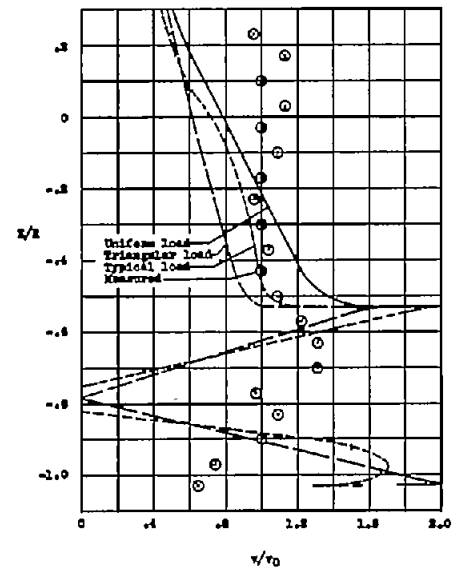
(e) $X/R = 1.07$.(f) $X/R = 2.07$.(g) $X/R = 3.14$.

Figure 30.- Concluded.

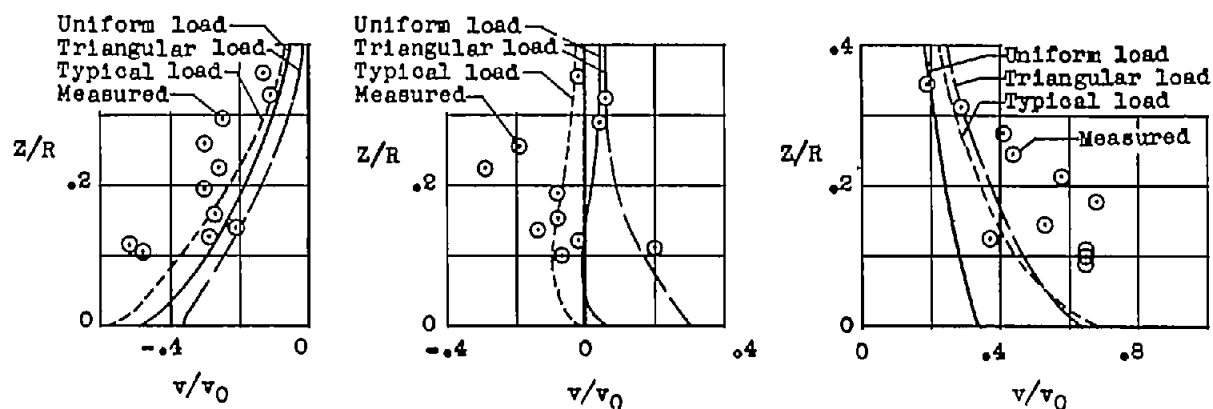
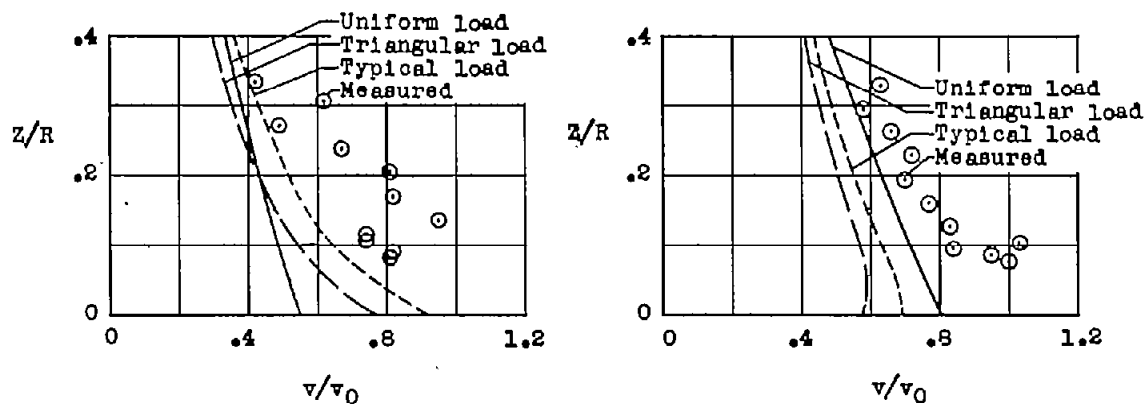
(a) $X/R = -0.95$.(b) $X/R = -0.8$.(c) $X/R = -0.6$.(d) $X/R = -0.4$.(e) $X/R = -0.2$.

Figure 31.- Comparison of measured and theoretical values of induced-velocity ratio v/v_0 in longitudinal plane of symmetry. $\alpha = 85.8^\circ$; $\mu = 0.139$.

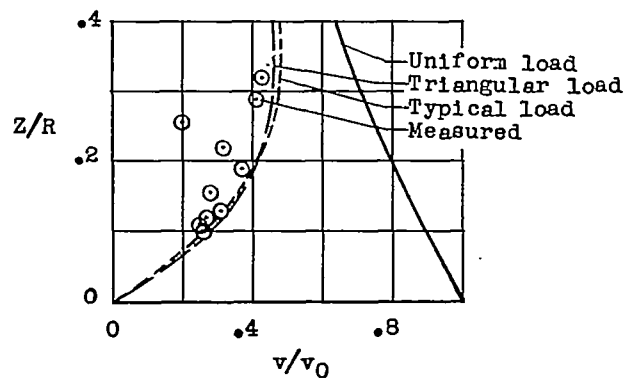
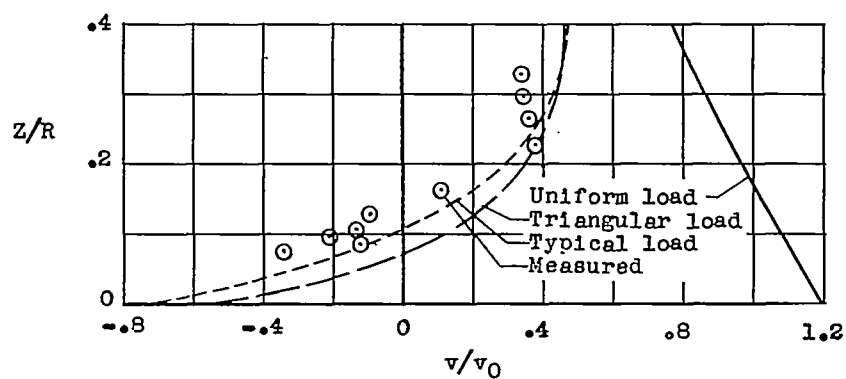
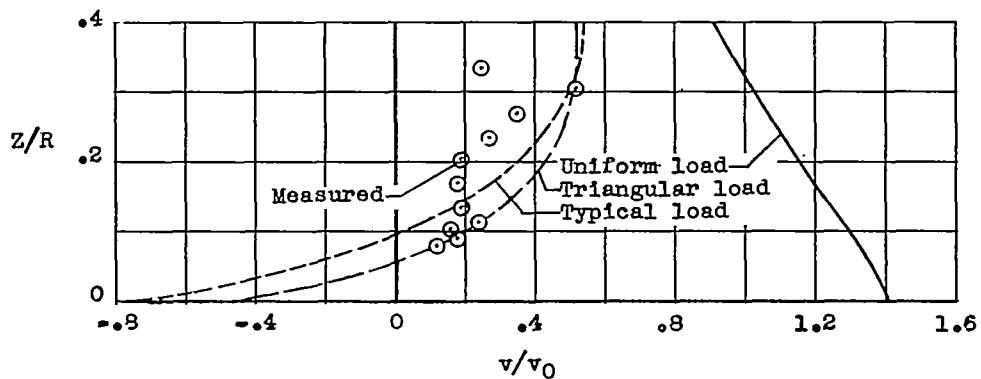
(f) $X/R = 0$.(g) $X/R = 0.2$.(h) $X/R = 0.4$.

Figure 31.- Continued.

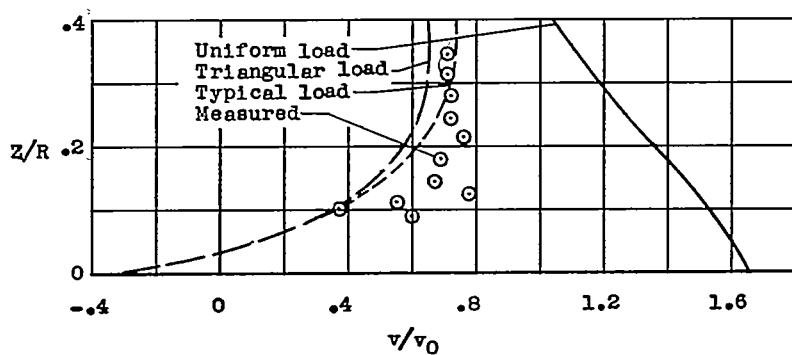
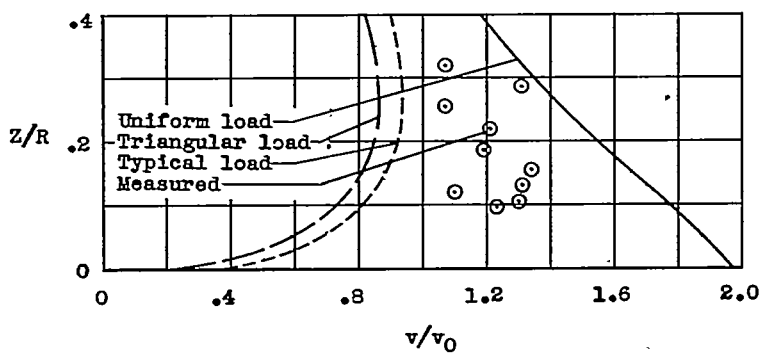
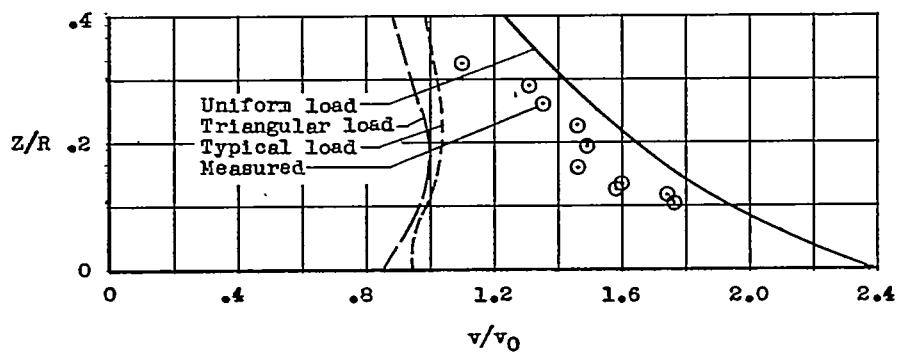
(i) $X/R = 0.6$.(j) $X/R = 0.8$.(k) $X/R = 0.95$.

Figure 31.- Concluded.

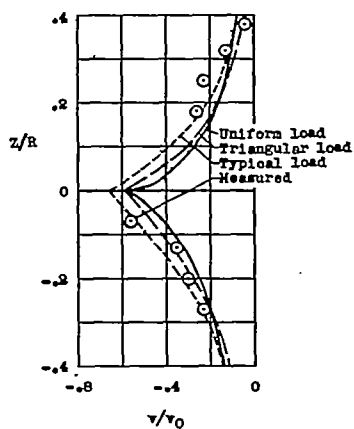
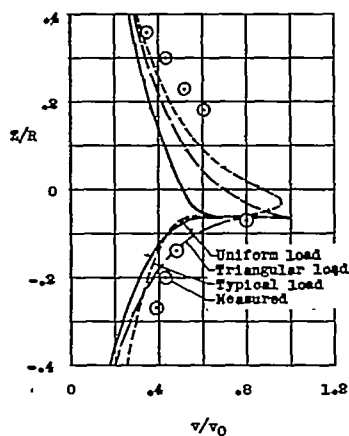
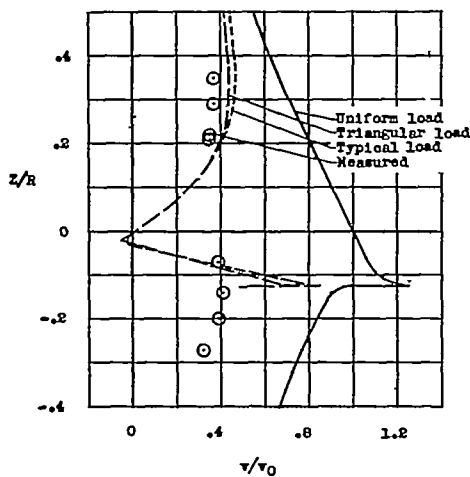
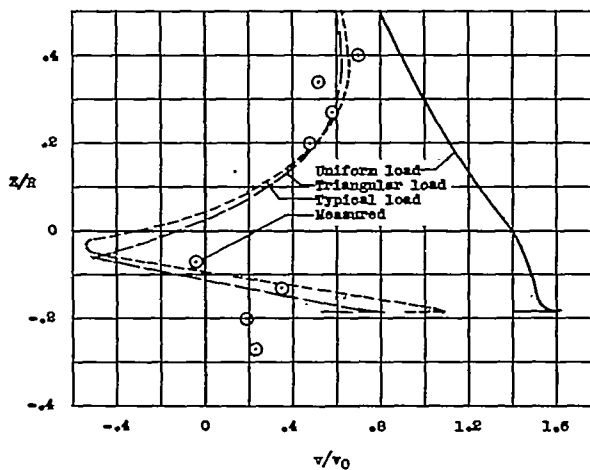
(a) $X/R = -1.0$.(b) $X/R = -0.5$.(c) $X/R = 0$.(d) $X/R = 0.5$.

Figure 32.- Comparison of measured and theoretical values of induced-velocity ratio v/v_0 in longitudinal plane of symmetry. $\chi = 82.3^\circ$; $\mu = 0.140$.

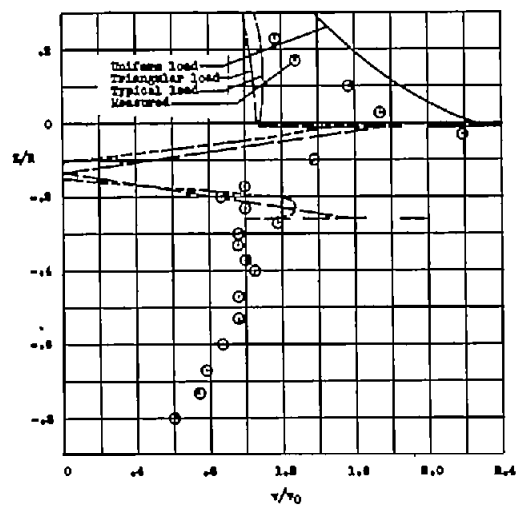
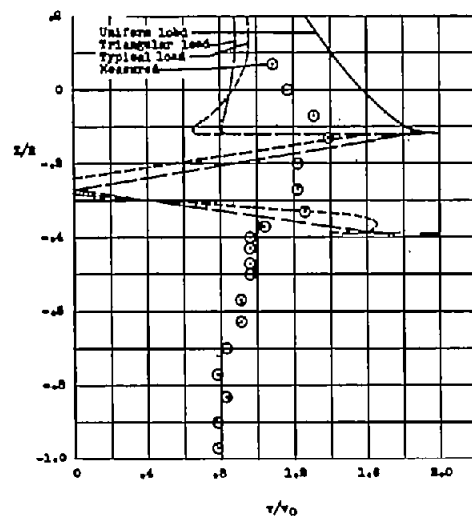
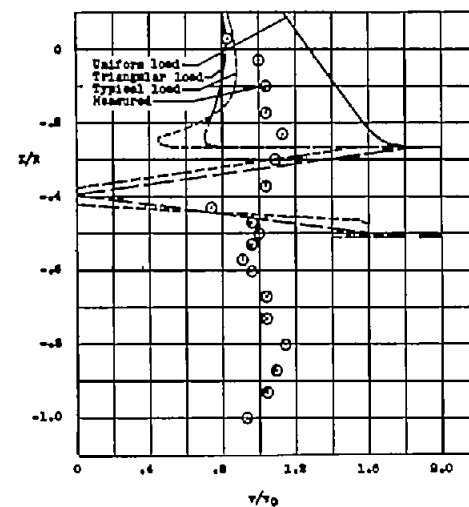
(e) $X/R = 1.07$.(f) $X/R = 2.07$.(g) $X/R = 3.14$.

Figure 32.- Concluded.

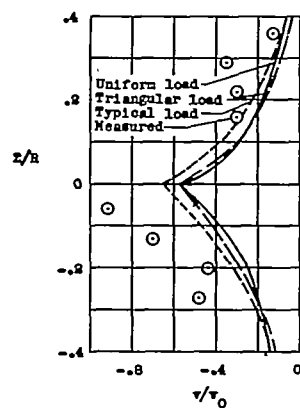
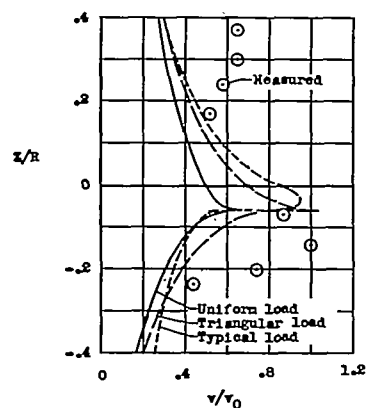
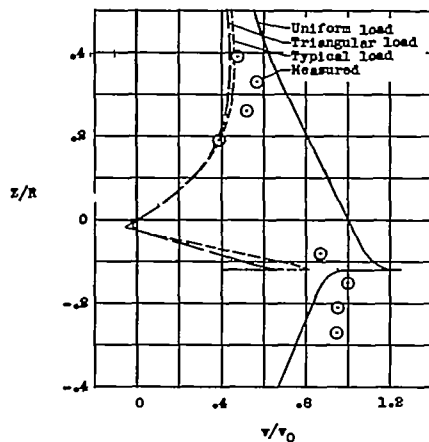
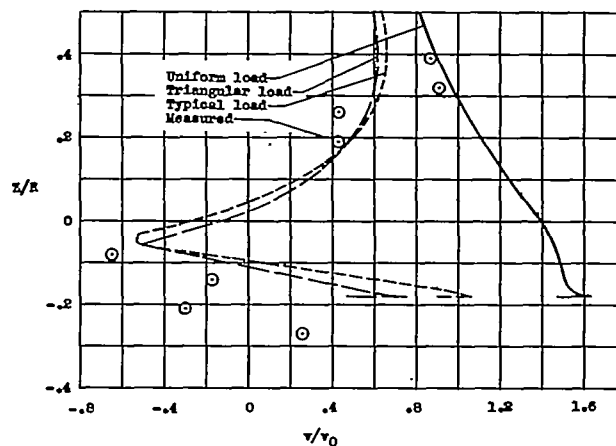
(a) $X/R = -1.0$.(b) $X/R = -0.5$.(c) $X/R = 0$.(d) $X/R = 0.5$.

Figure 33.- Comparison of measured and theoretical values of induced-velocity ratio v/v_0 in longitudinal plane of symmetry. $\alpha = 83.9^\circ$; $\mu = 0.232$.

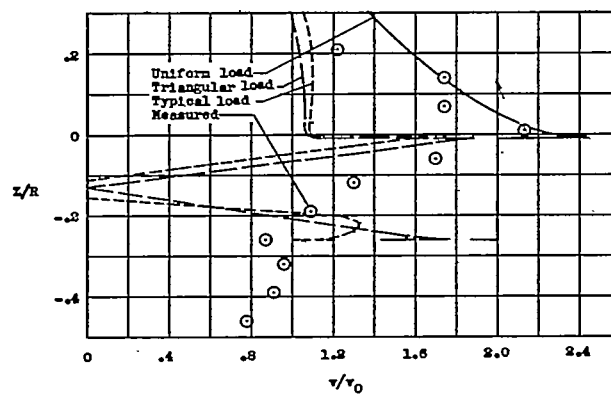
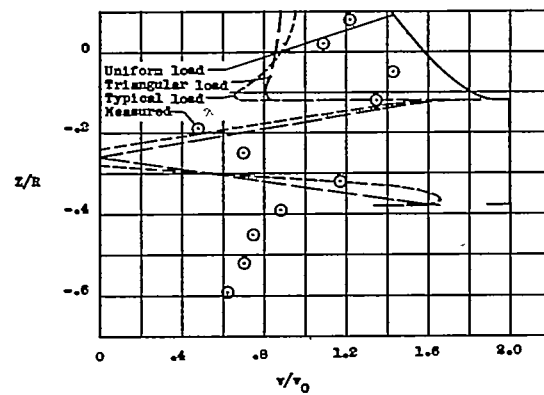
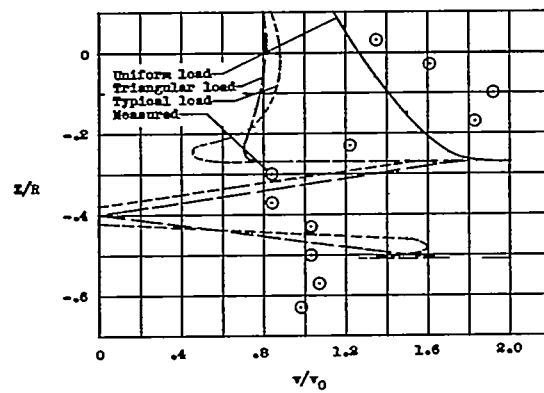
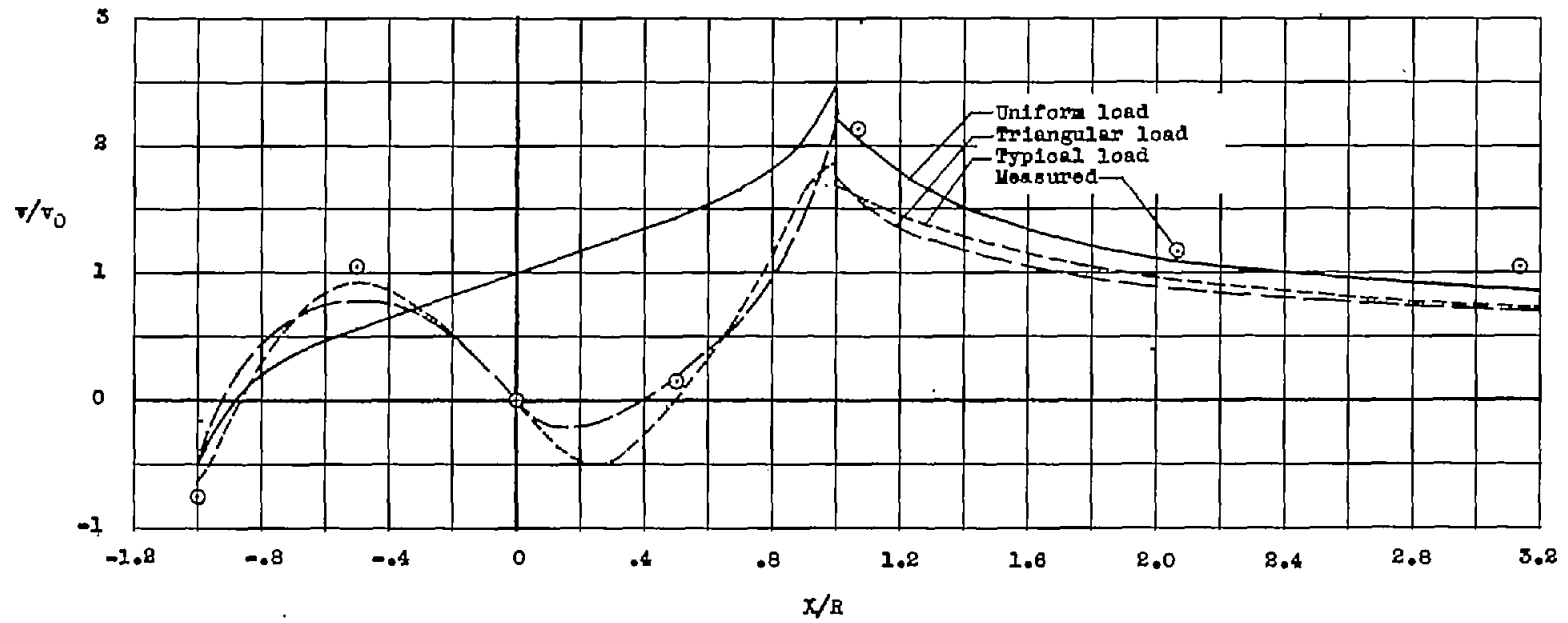
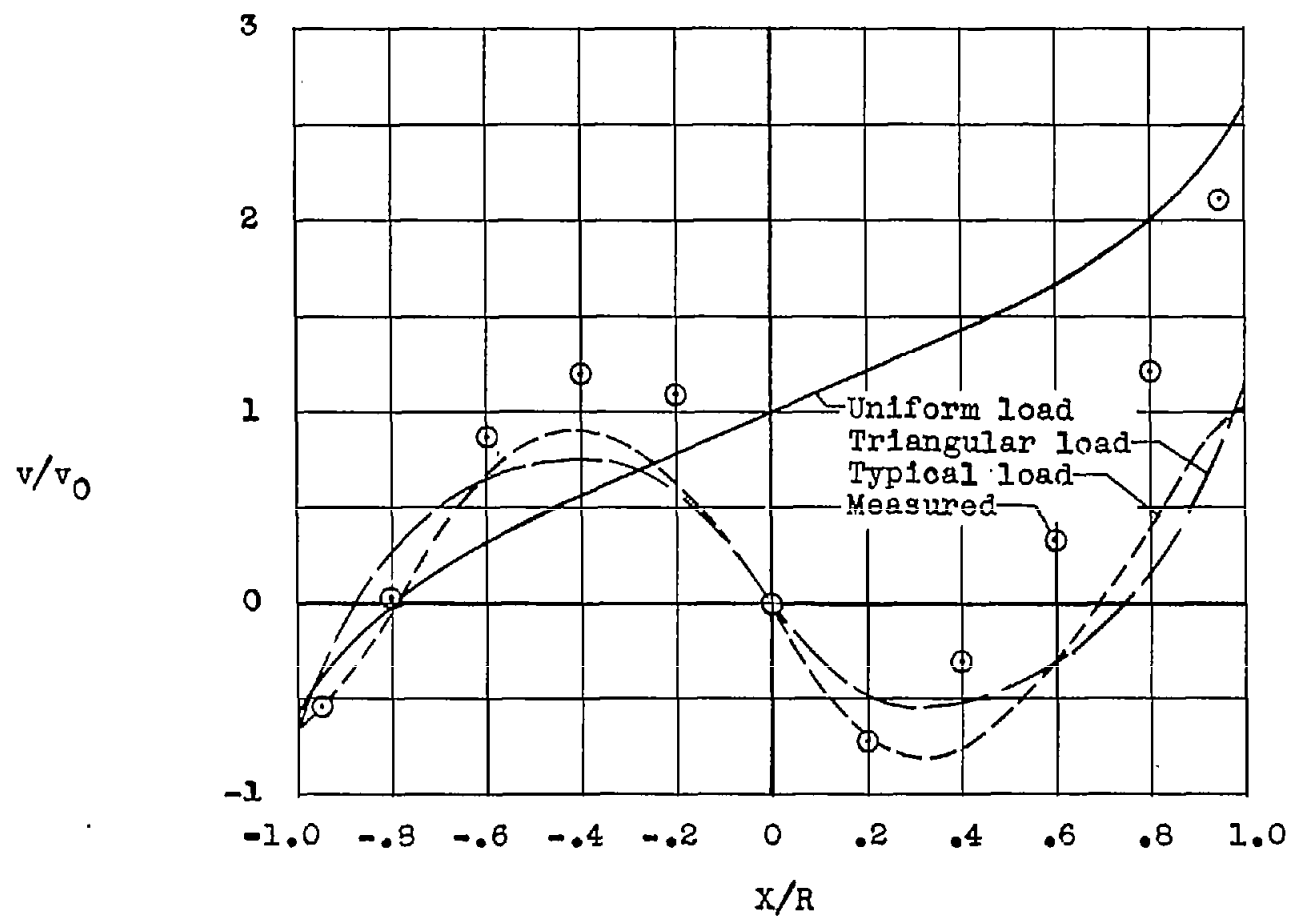
(e) $X/R = 1.07$.(f) $X/R = 2.07$.(g) $X/R = 3.14$.

Figure 33.- Concluded.



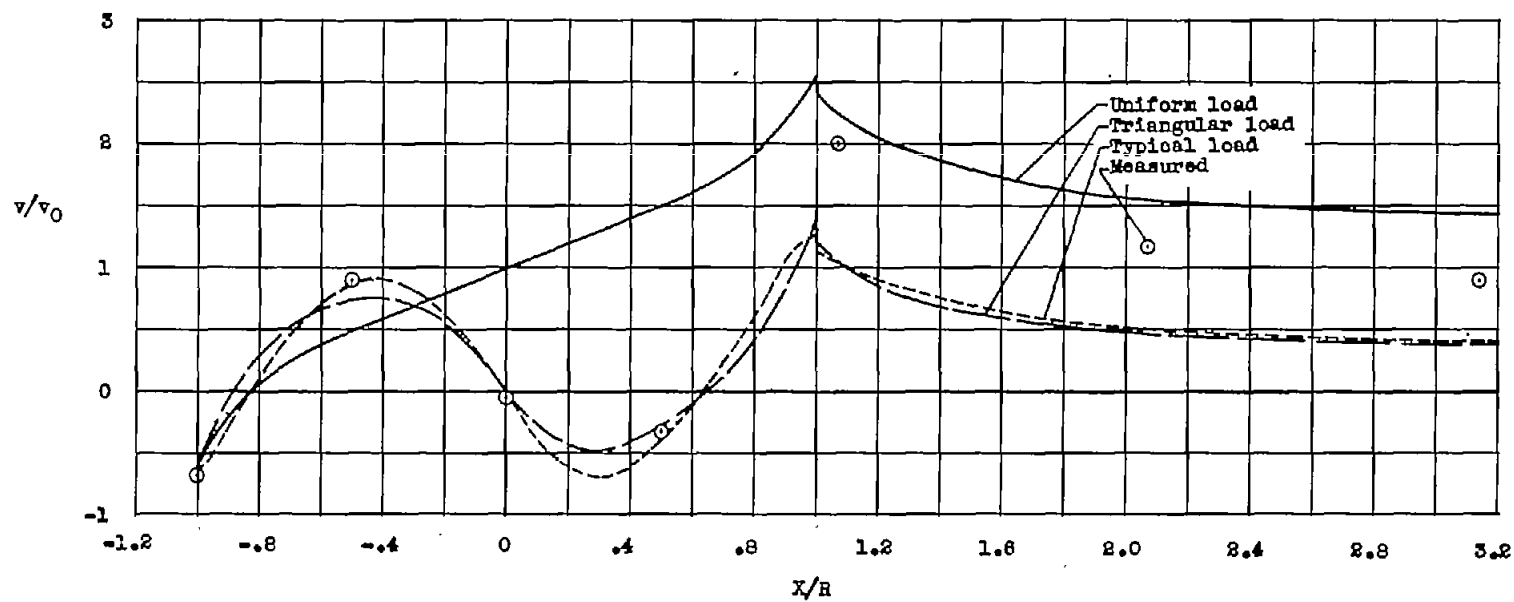
(a) $\alpha = 75.0^\circ$; $\mu = 0.095$.

Figure 34.- Comparison of measured and theoretical values of induced-velocity ratio v/v_0 along longitudinal center line.



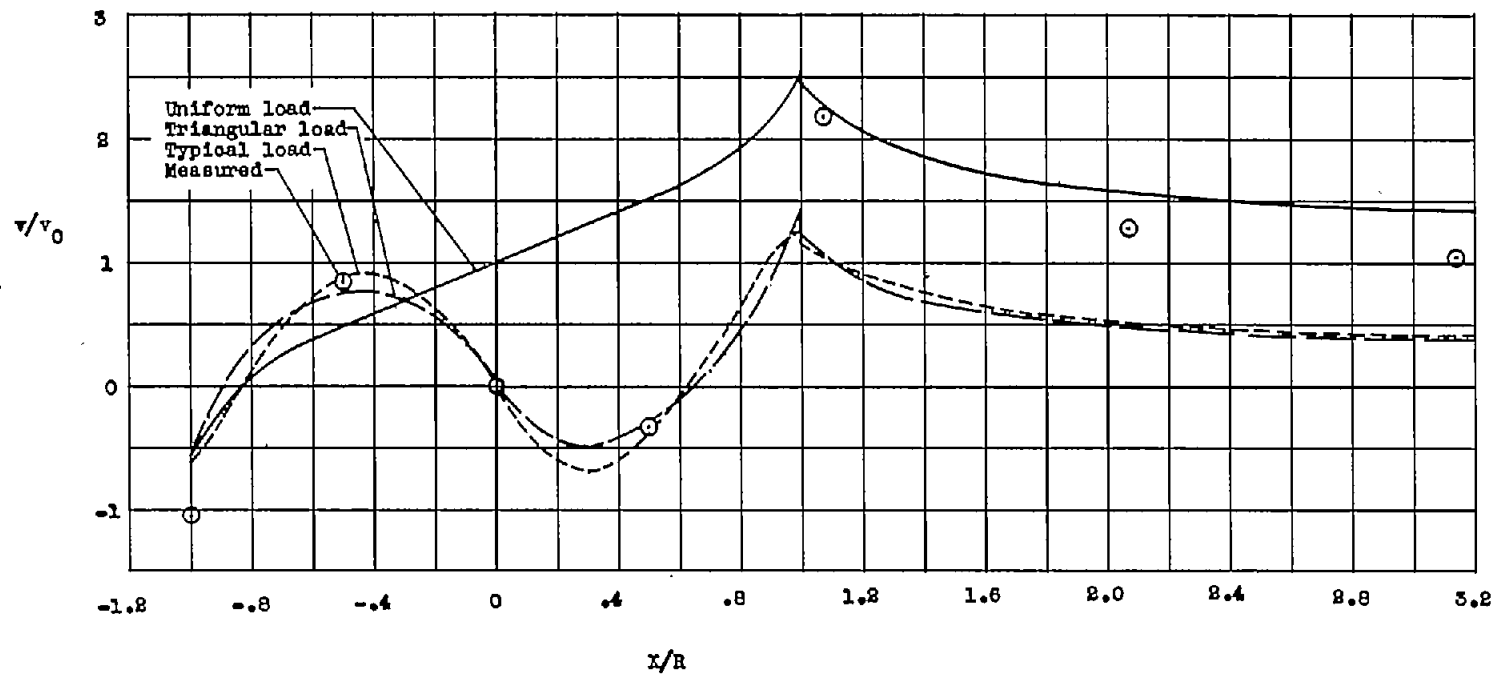
(b) $x = 85.8^\circ$; $\mu = 0.139$.

Figure 34.- Continued.



(c) $\gamma = 82.3^\circ$; $\mu = 0.140$.

Figure 34.- Continued.



(d) $\chi = 83.9^\circ$; $\mu = 0.232$.

Figure 34.- Concluded.

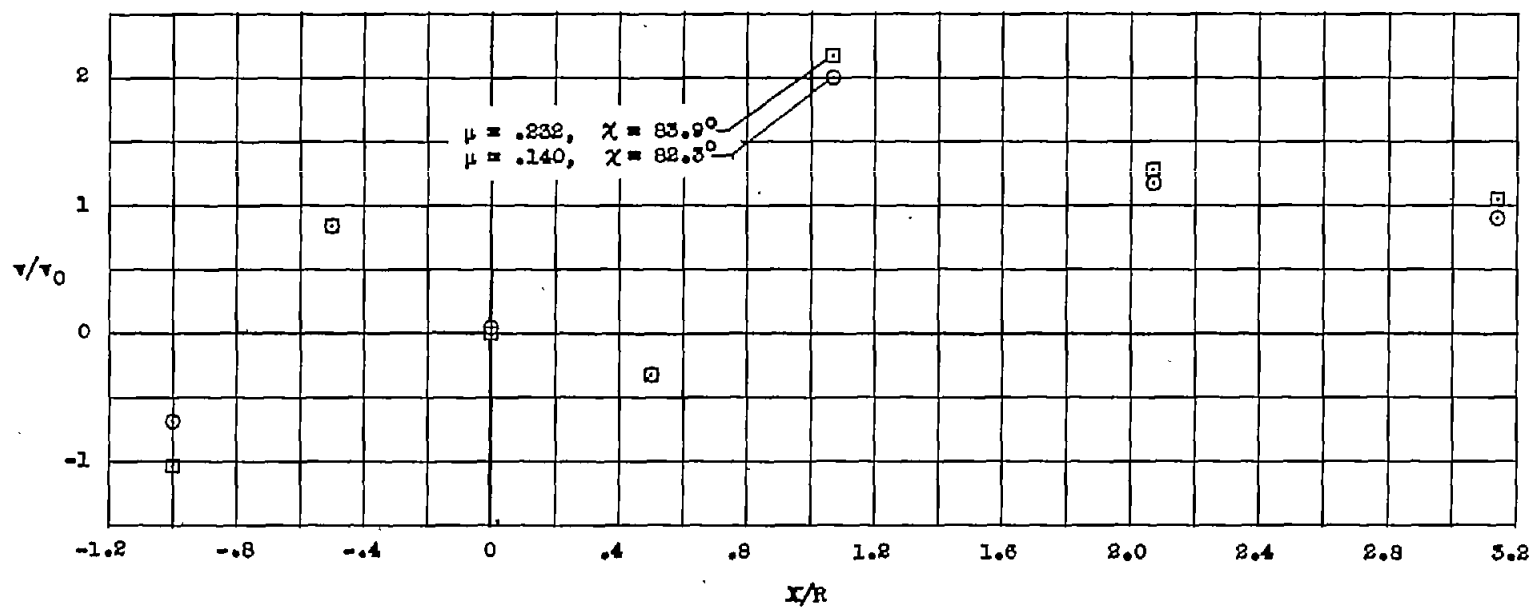
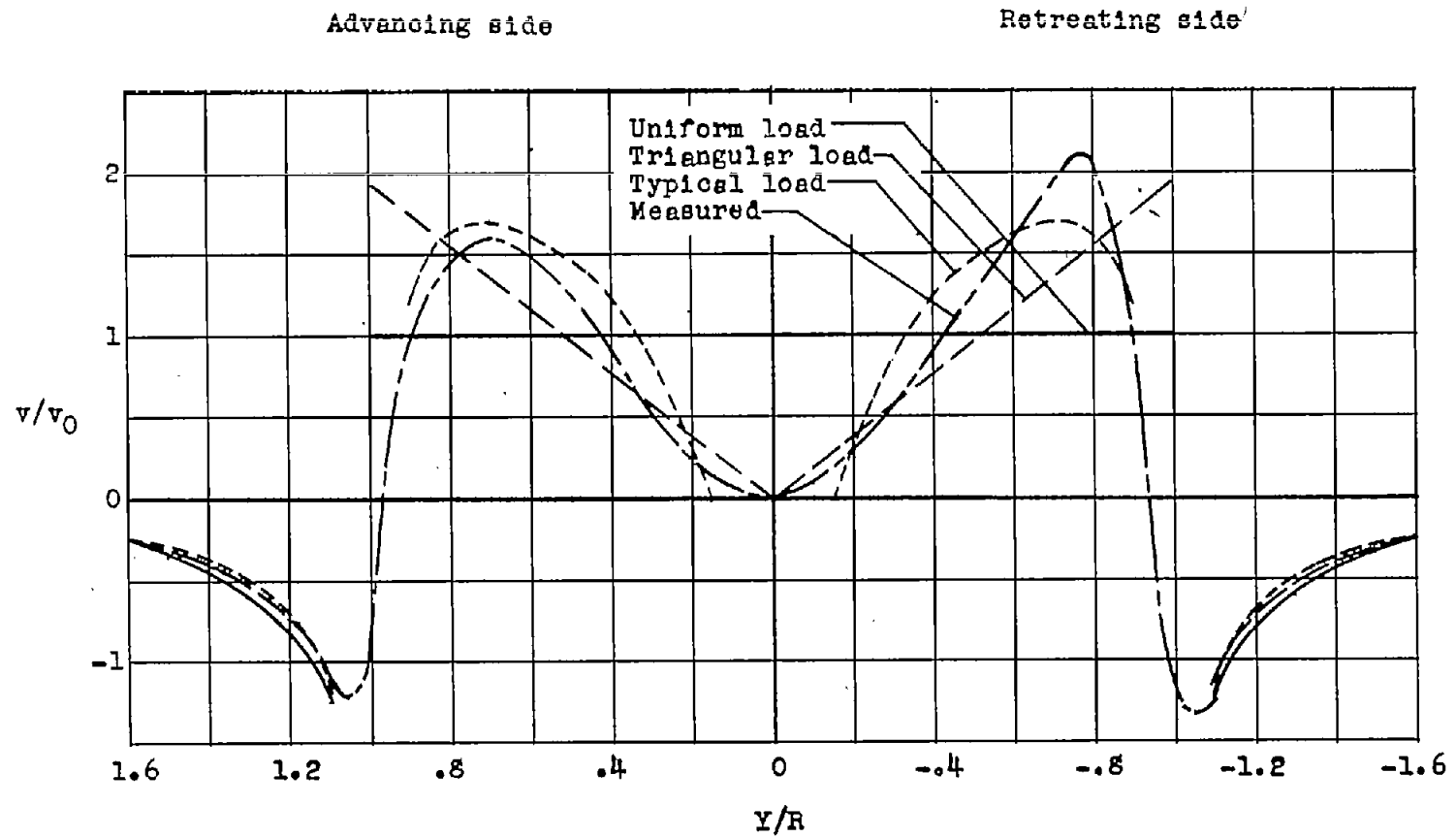
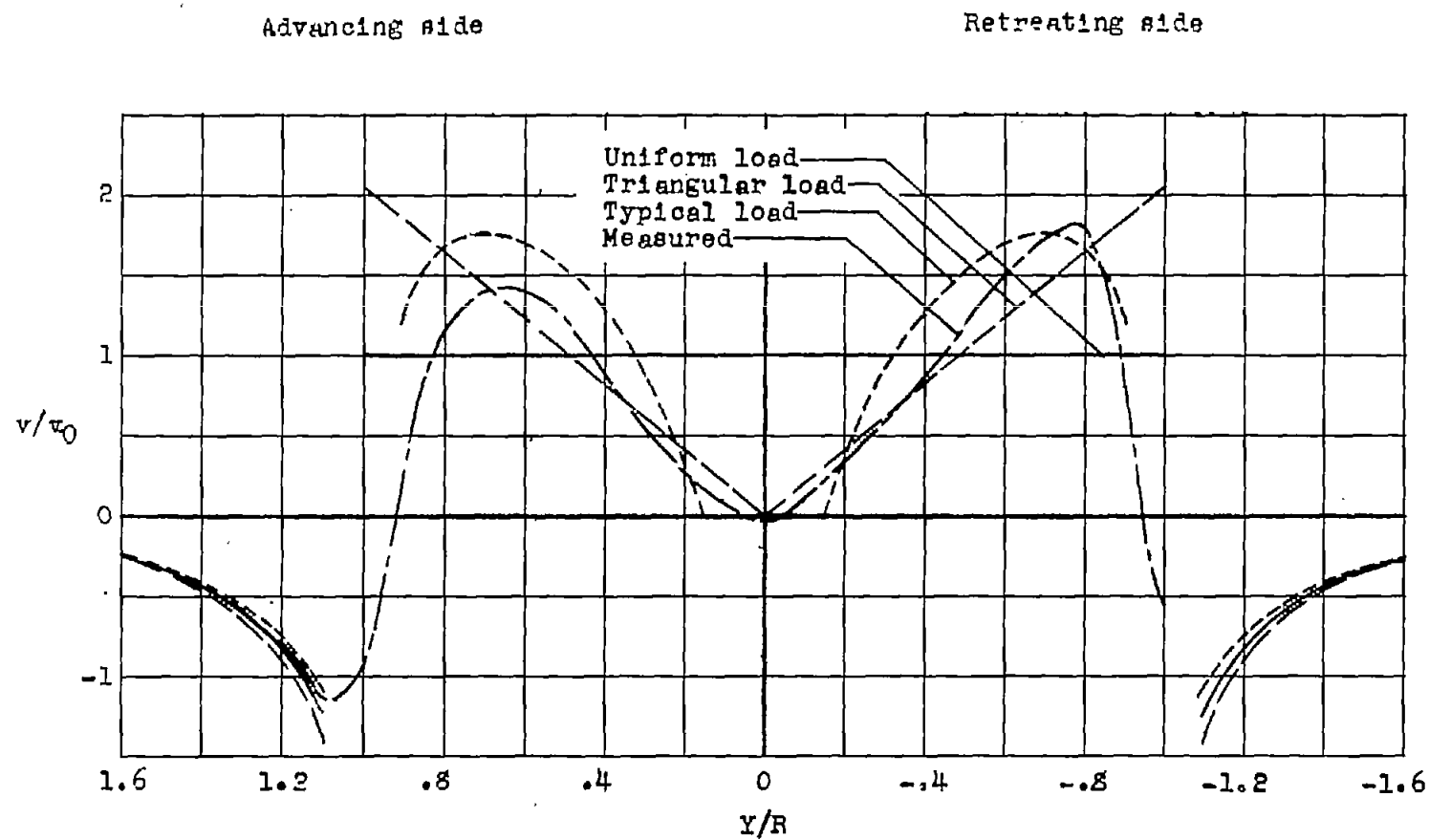


Figure 35.- Effect of tip-speed ratio on distribution of induced-velocity ratio v/v_0 along longitudinal center line.



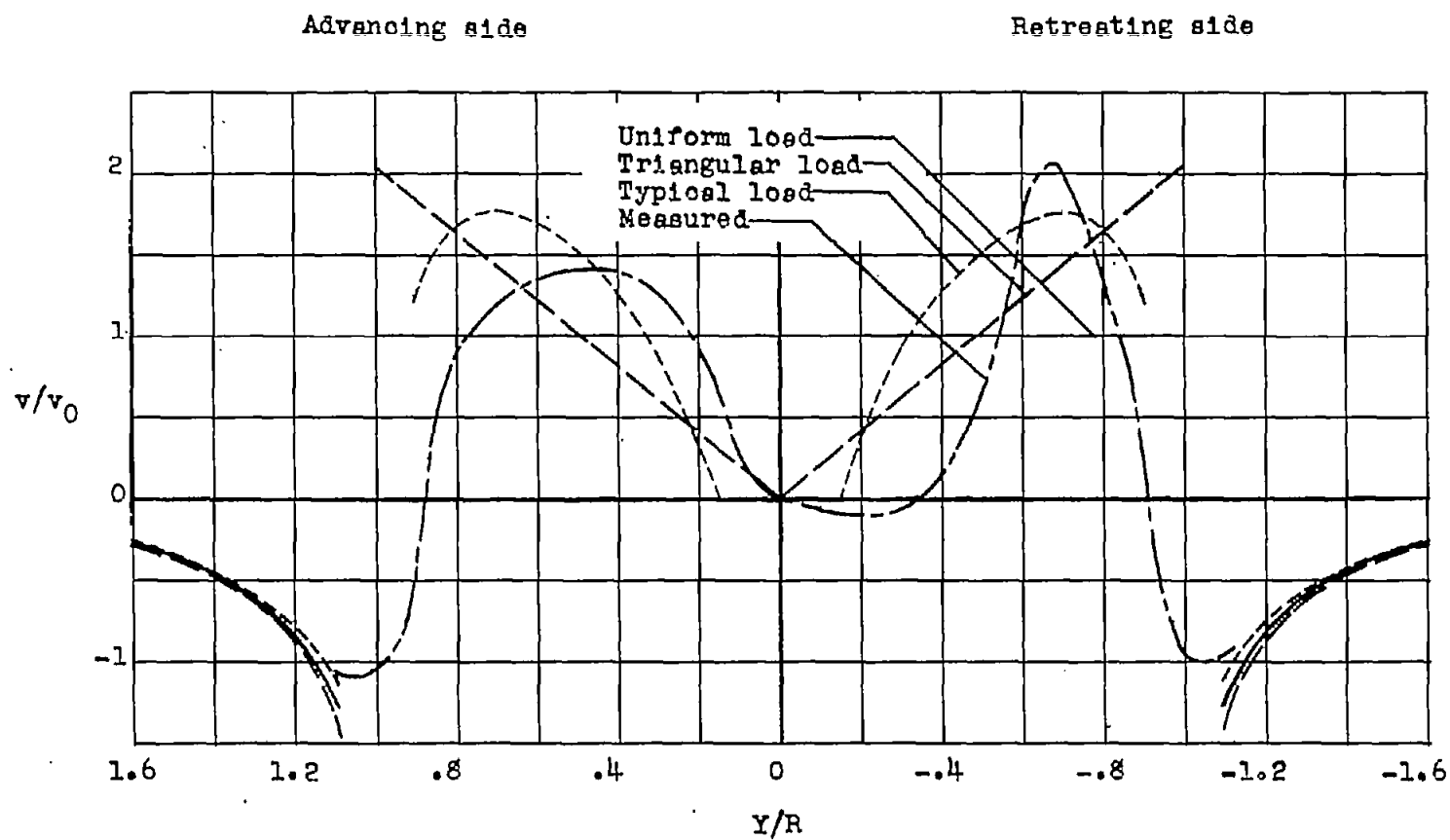
(a) $\alpha = 75.0^\circ$; $\mu = 0.095$.

Figure 36.- Comparison of measured and theoretical values of induced-velocity ratio v/v_0 along lateral center line.



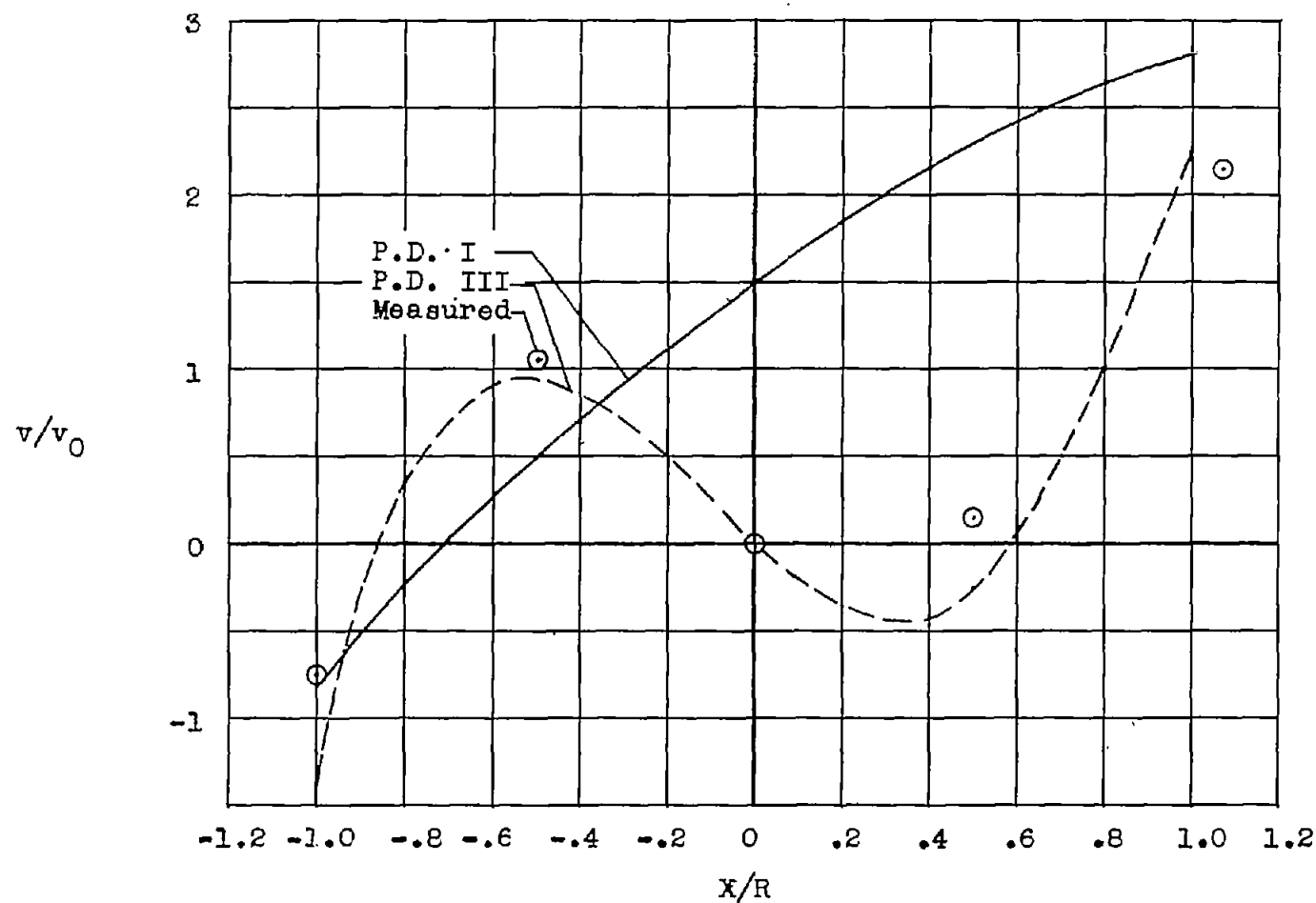
(b) $\alpha = 82.3^\circ$; $\mu = 0.140$.

Figure 36.- Continued.



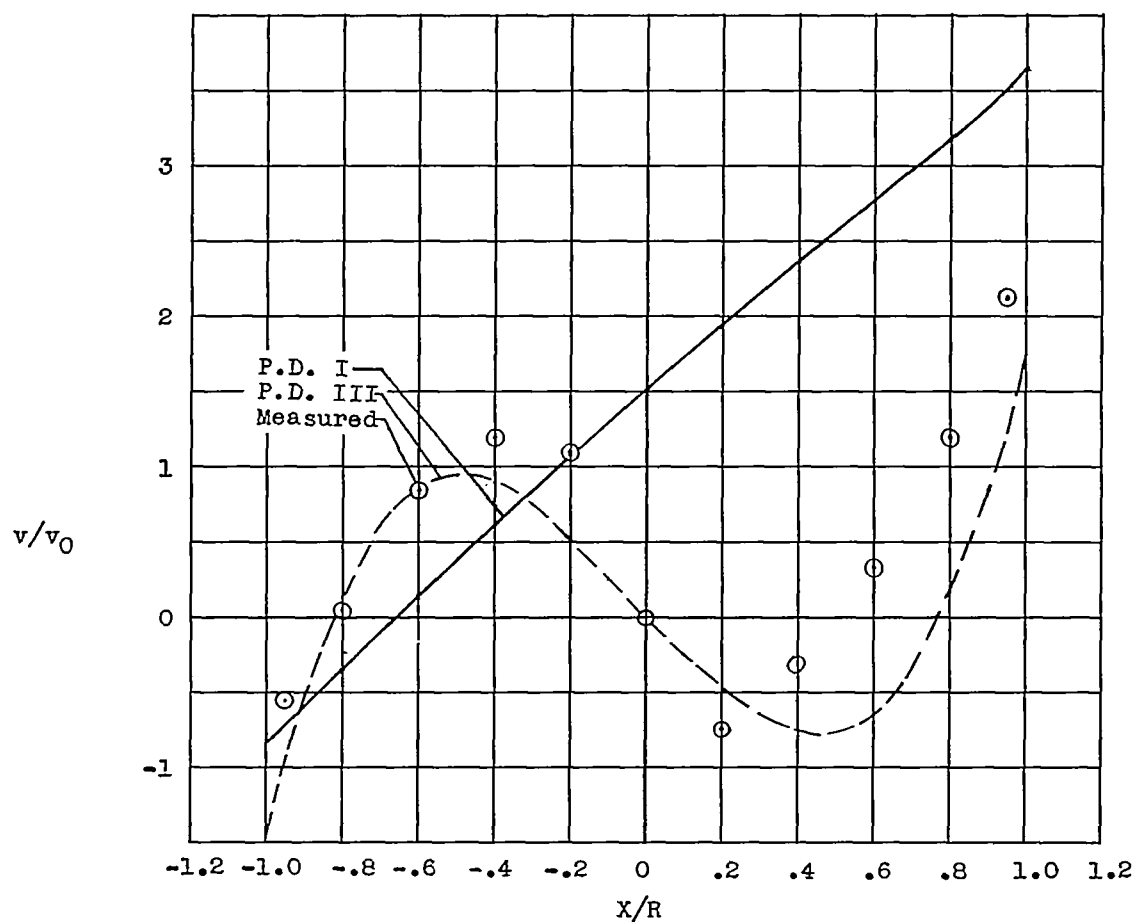
(c) $\chi = 83.9^\circ$; $\mu = 0.232$.

Figure 36.- Concluded.



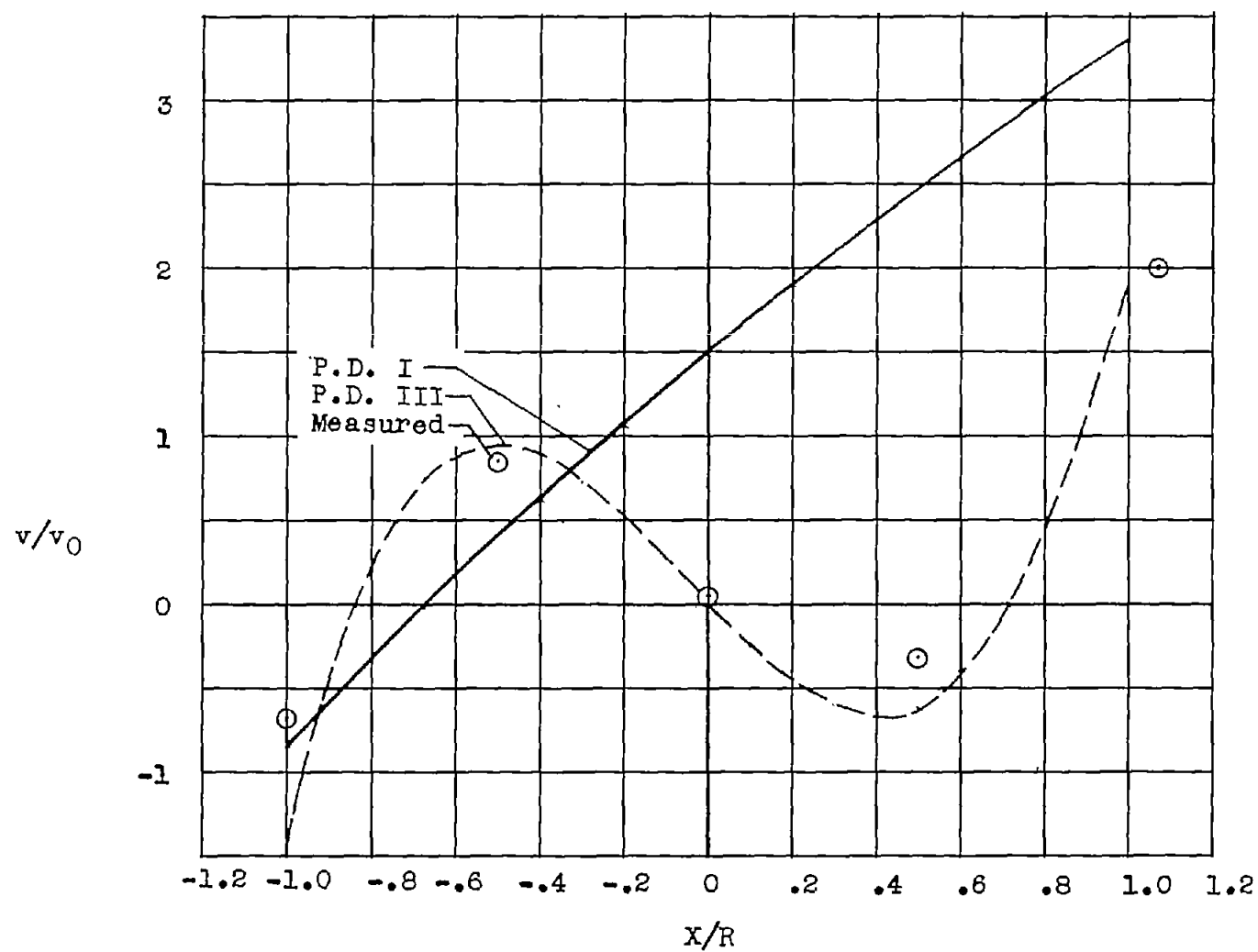
(a) $\alpha = 75.0^\circ$; $\mu = 0.095$.

Figure 37.- Comparison of measured values of induced-velocity ratio v/v_0 on longitudinal center line with theory of reference 4 modified. Pressure distributions I and III denoted by P.D. I and P.D. III.



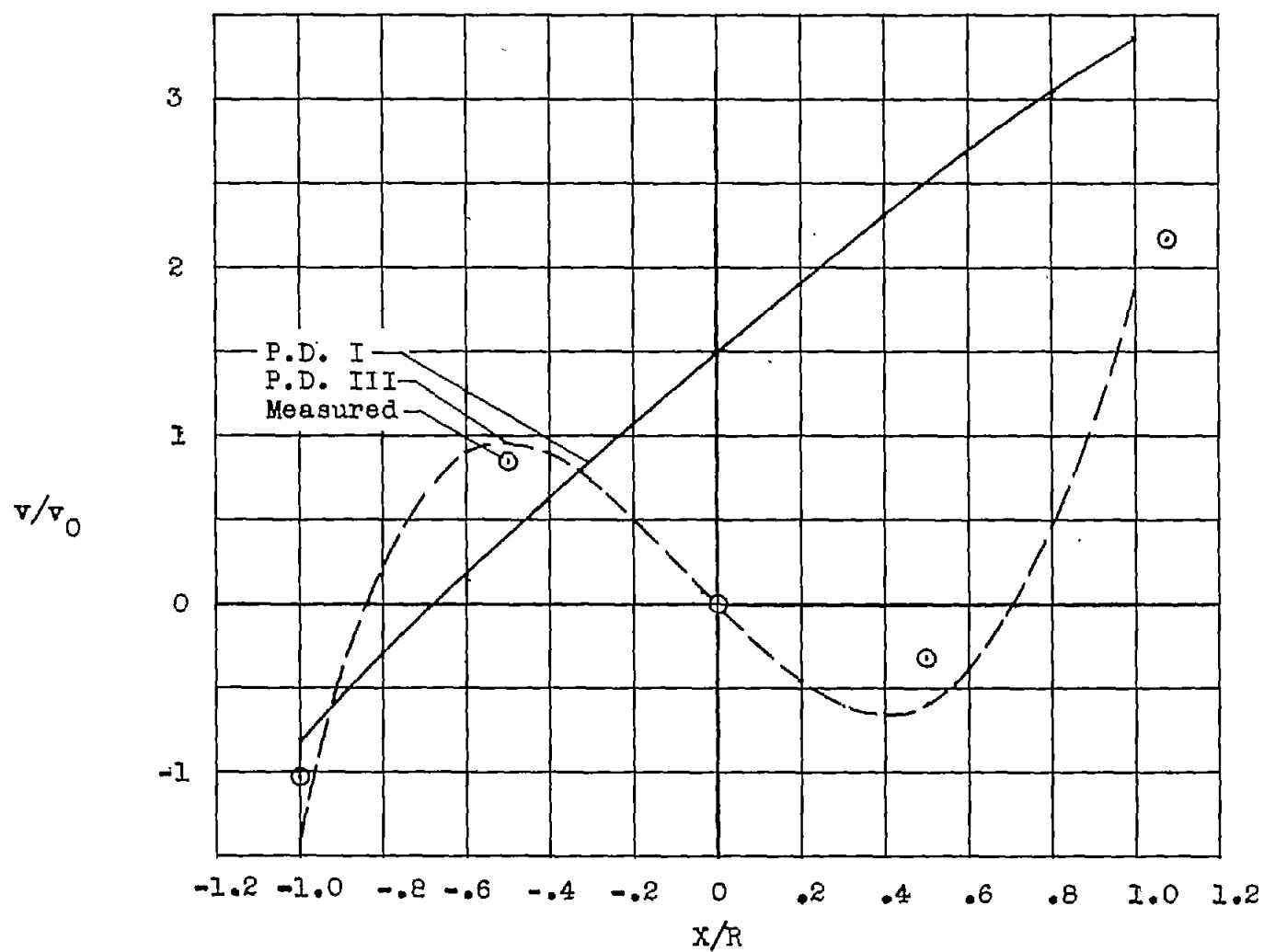
(b) $\alpha = 85.8^\circ$; $\mu = 0.139$.

Figure 37.- Continued.



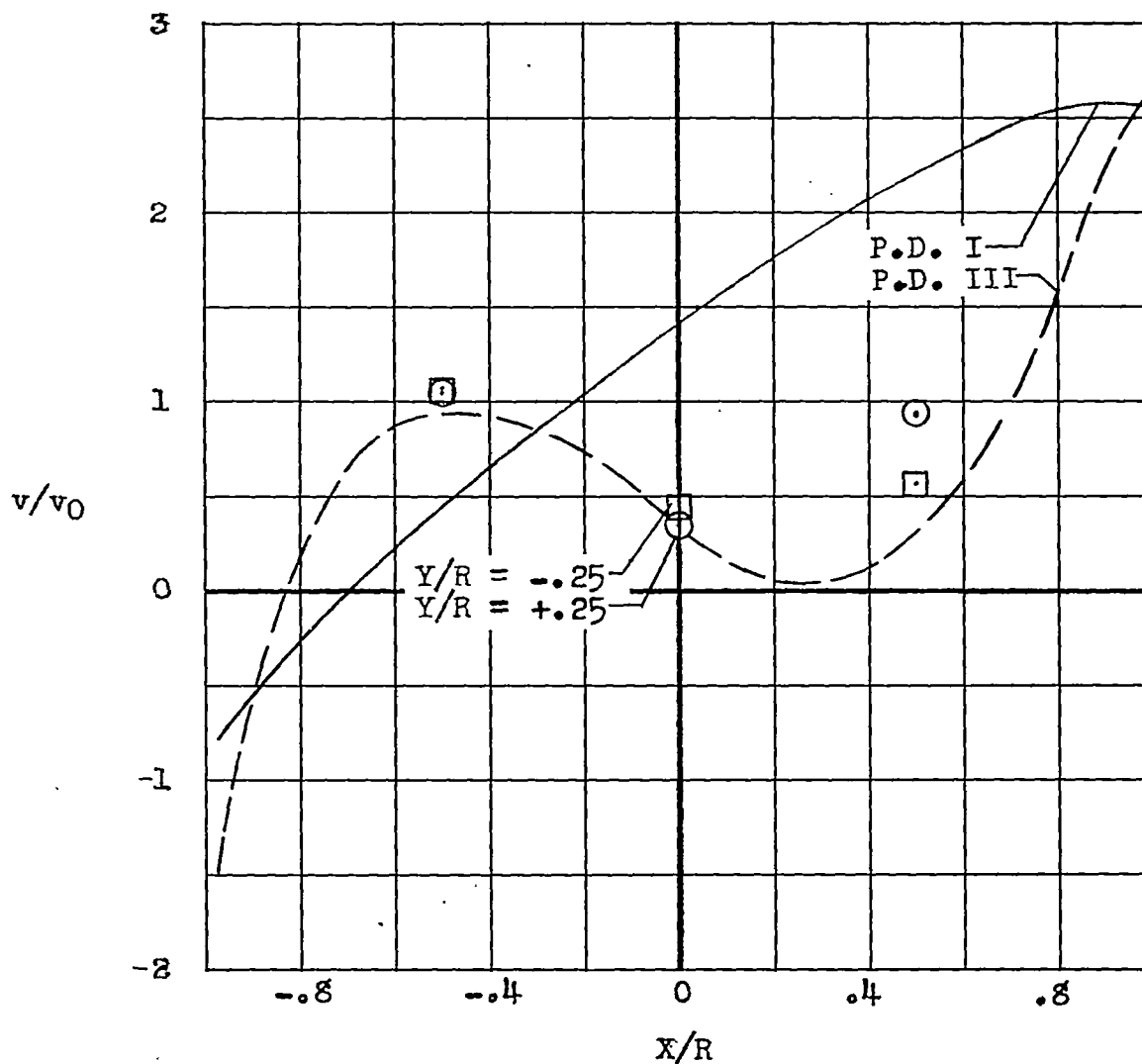
(c) $\chi = 82.5^\circ$; $\mu = 0.140$.

Figure 37.- Continued.



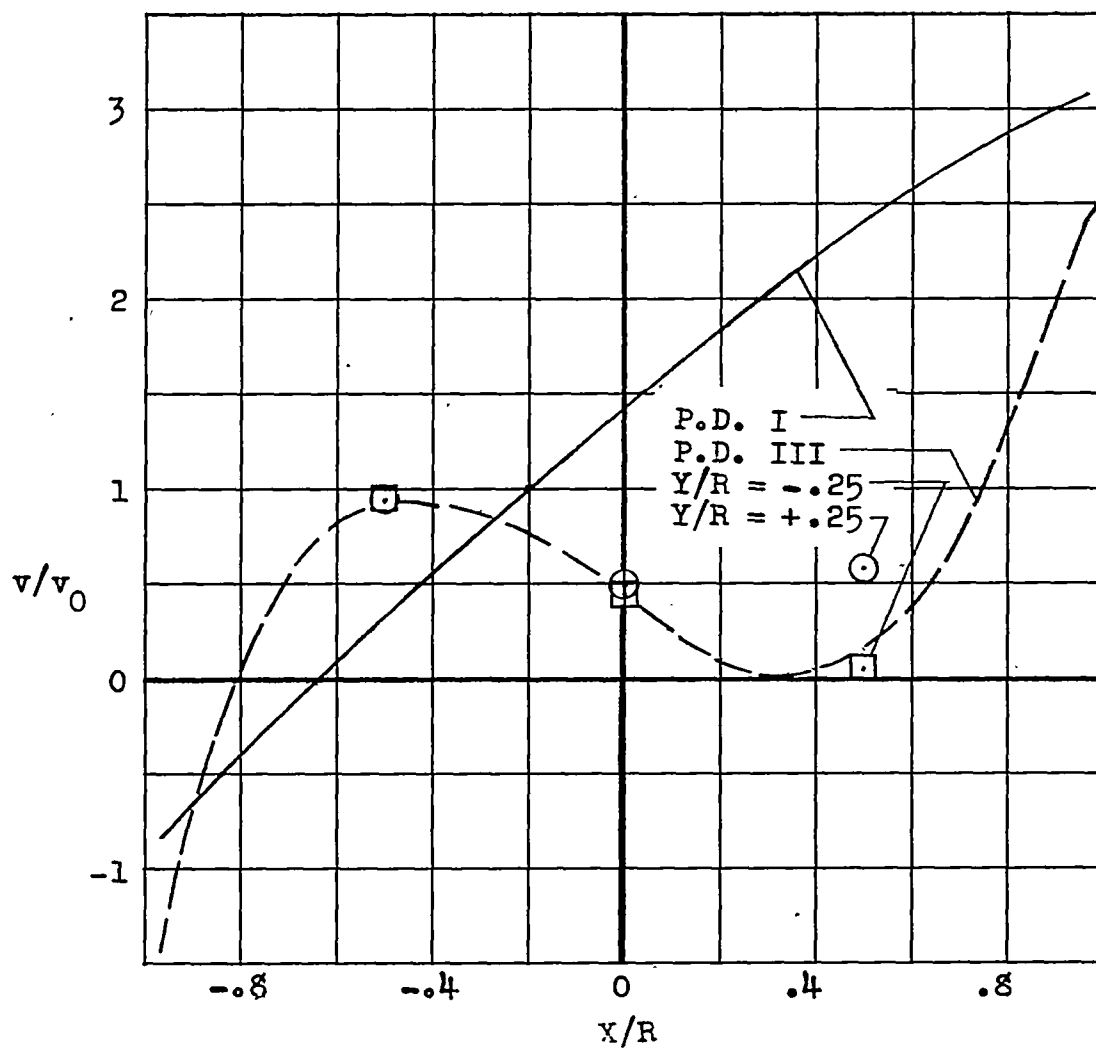
(a) $\alpha = 83.9^\circ$; $\mu = 0.232$.

Figure 37.- Concluded.



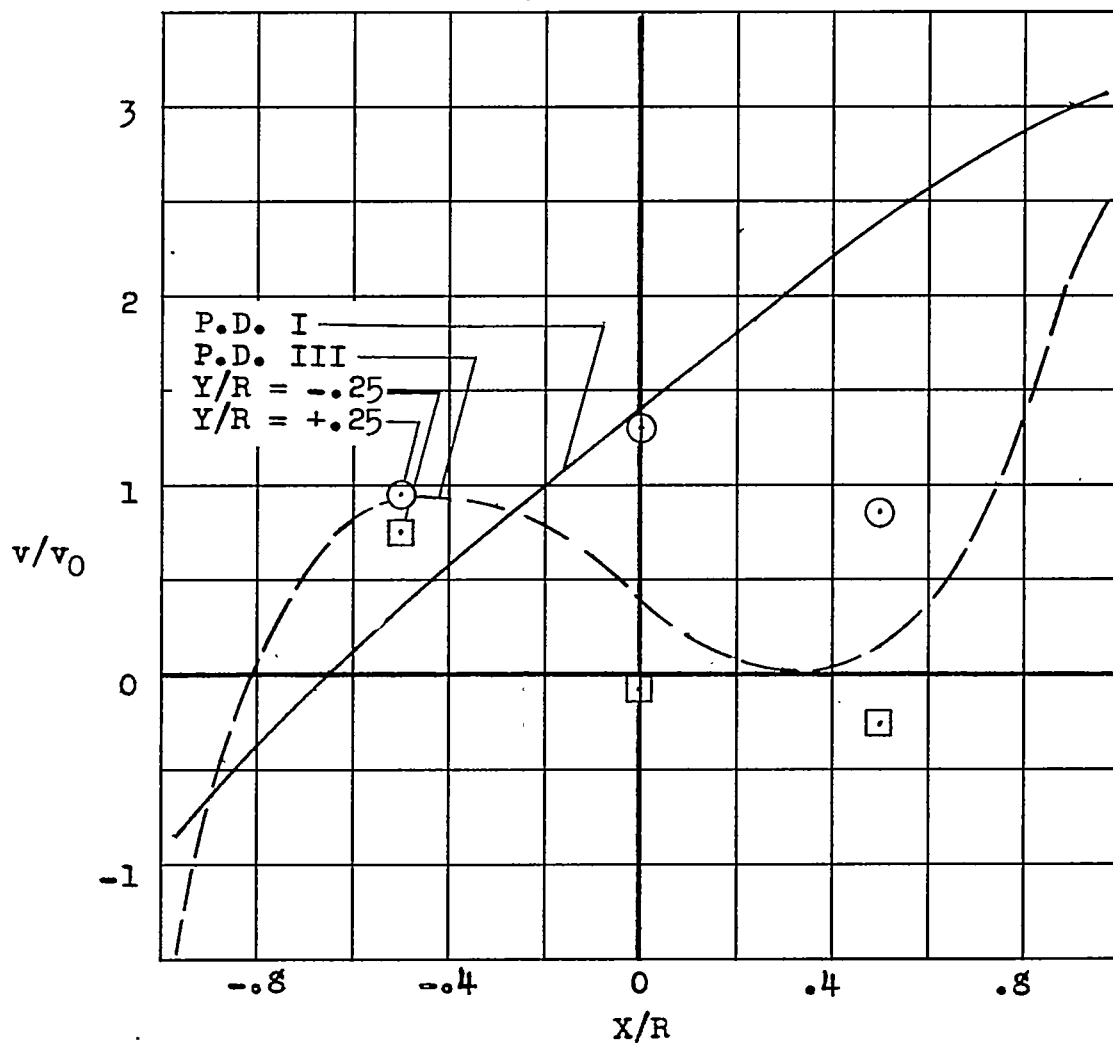
(a) $\chi = 75.0^\circ$; $\mu = 0.095$.

Figure 38.- Comparison of measured values of induced-velocity ratio v/v_0 at $Y/R = \pm 0.25$ with theory of reference 4 modified. Pressure distributions I and III are denoted by P.D. I and P.D. III.



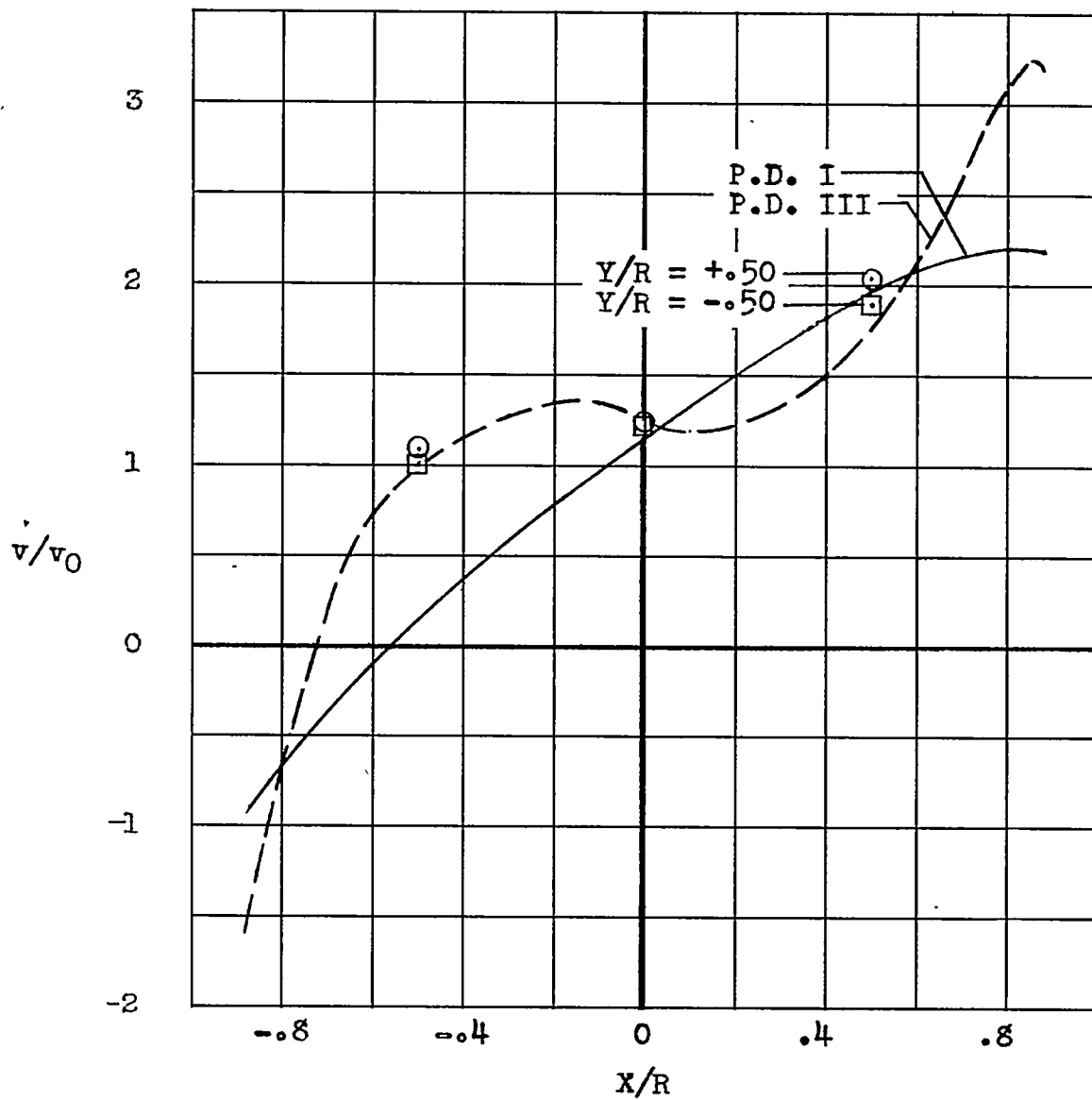
(b) $\alpha = 82.3^\circ$; $\mu = 0.140$.

Figure 38.- Continued.



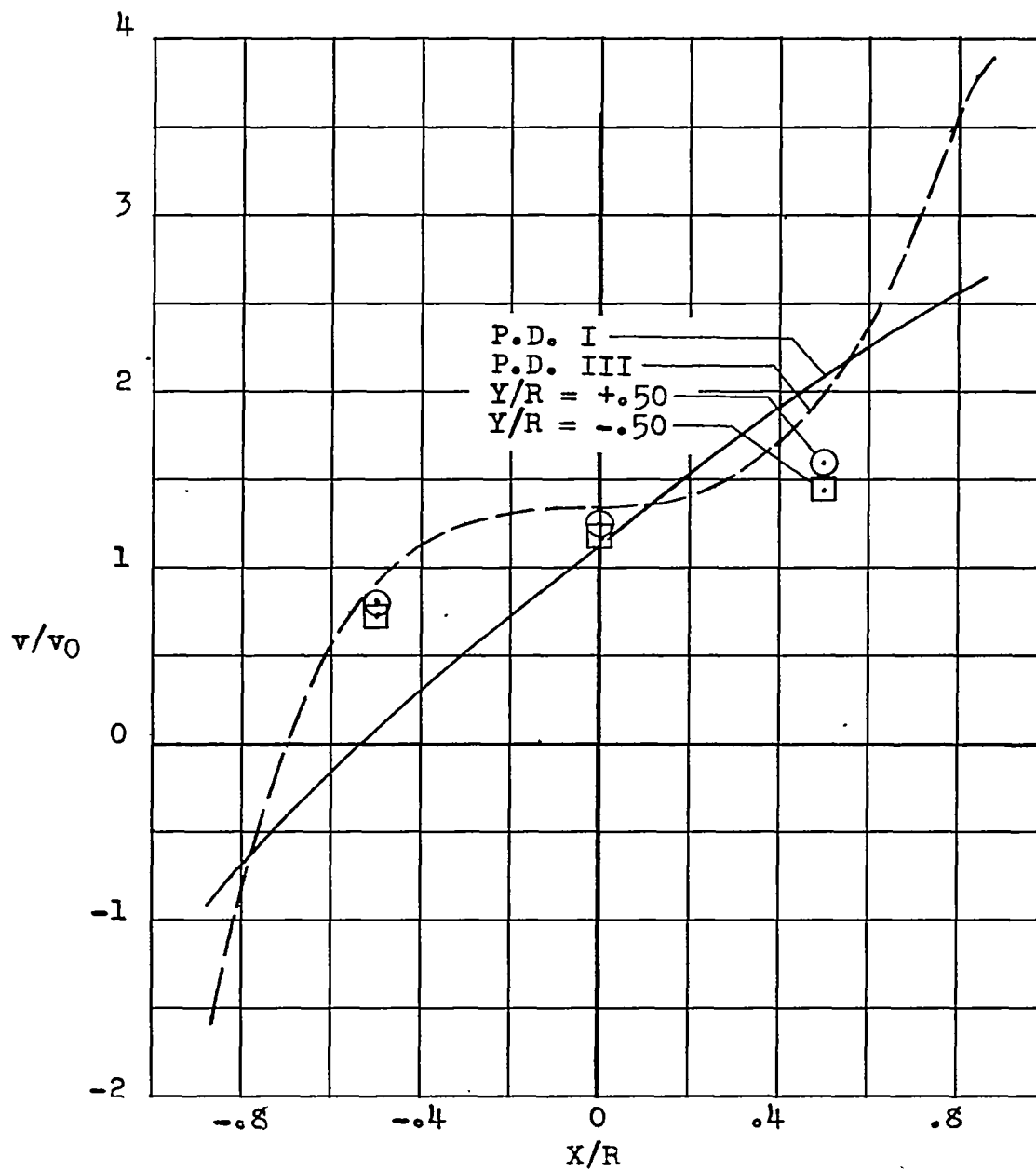
(c) $\chi = 83.9^\circ$; $\mu = 0.232$.

Figure 38.- Concluded.



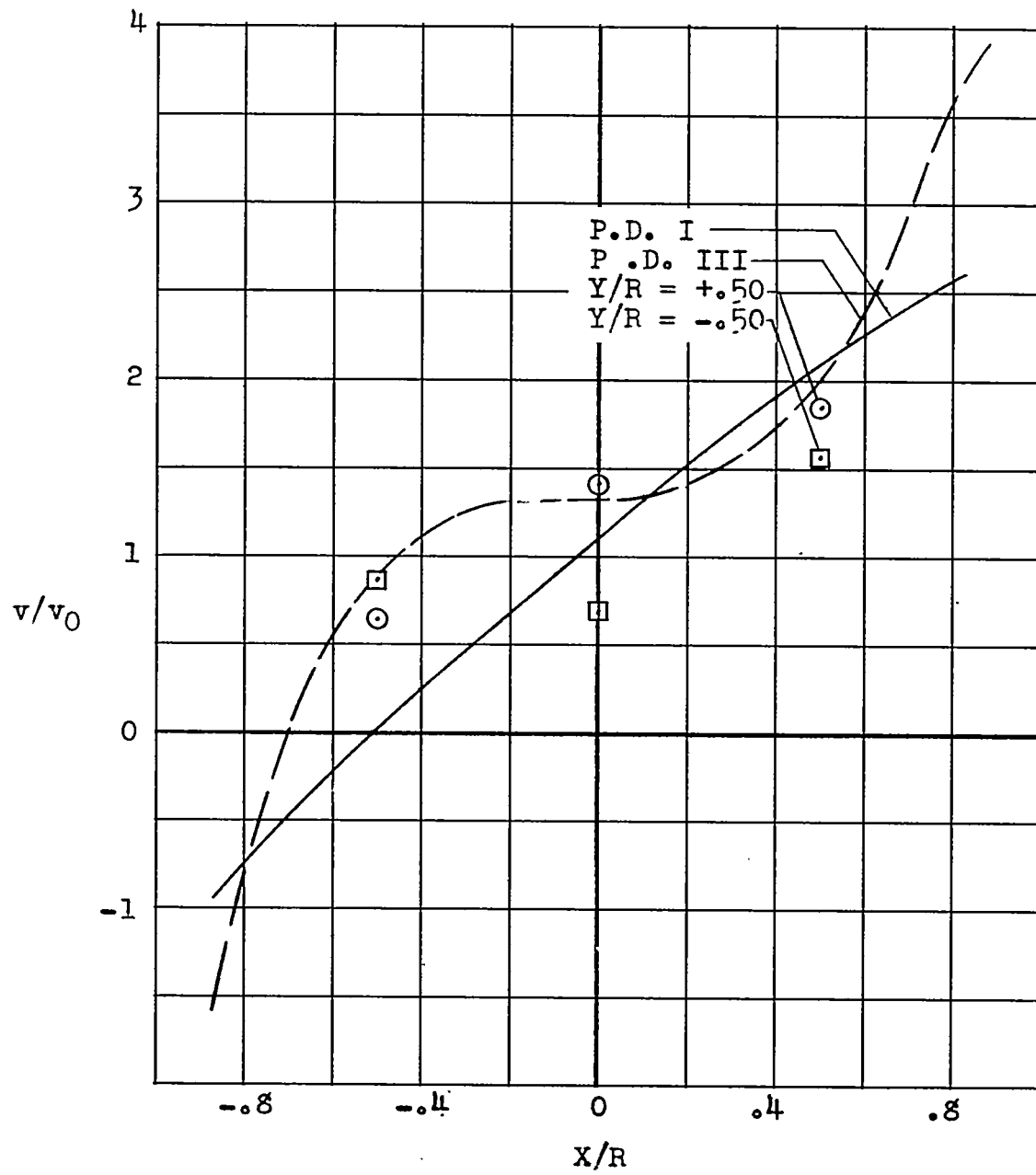
(a) $\chi = 75.0^\circ$; $\mu = 0.095$.

Figure 39.- Comparison of measured values of induced-velocity ratio \dot{v}/v_0 at $Y/R = \pm 0.50$ with theory of reference 4 modified. Pressure distributions I and III denoted by P.D. I and P.D. III.



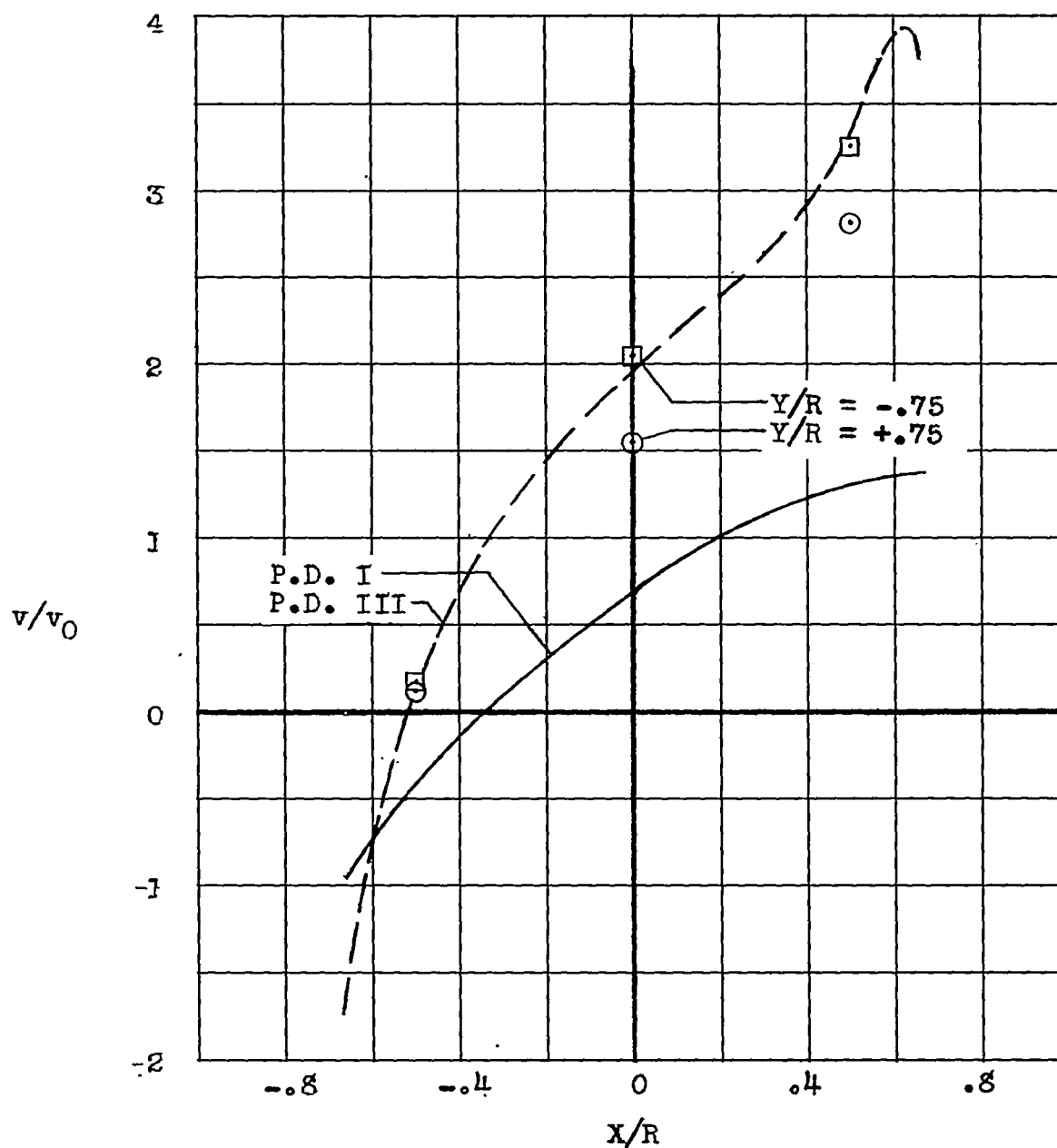
(b) $\alpha = 82.3^\circ$; $\mu = 0.140$.

Figure 39.- Continued.



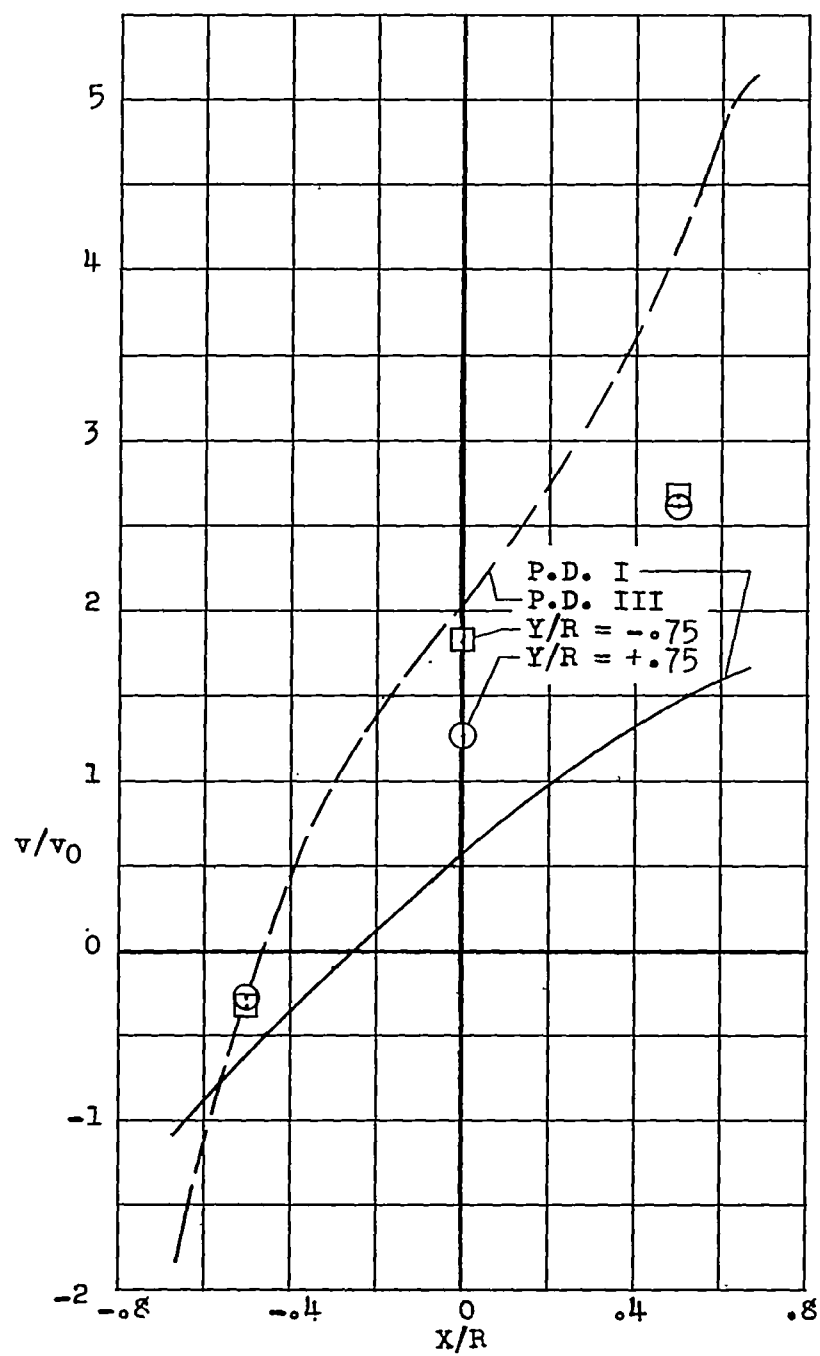
(c) $\alpha = 83.9^\circ$; $\mu = 0.232$.

Figure 39.- Concluded.



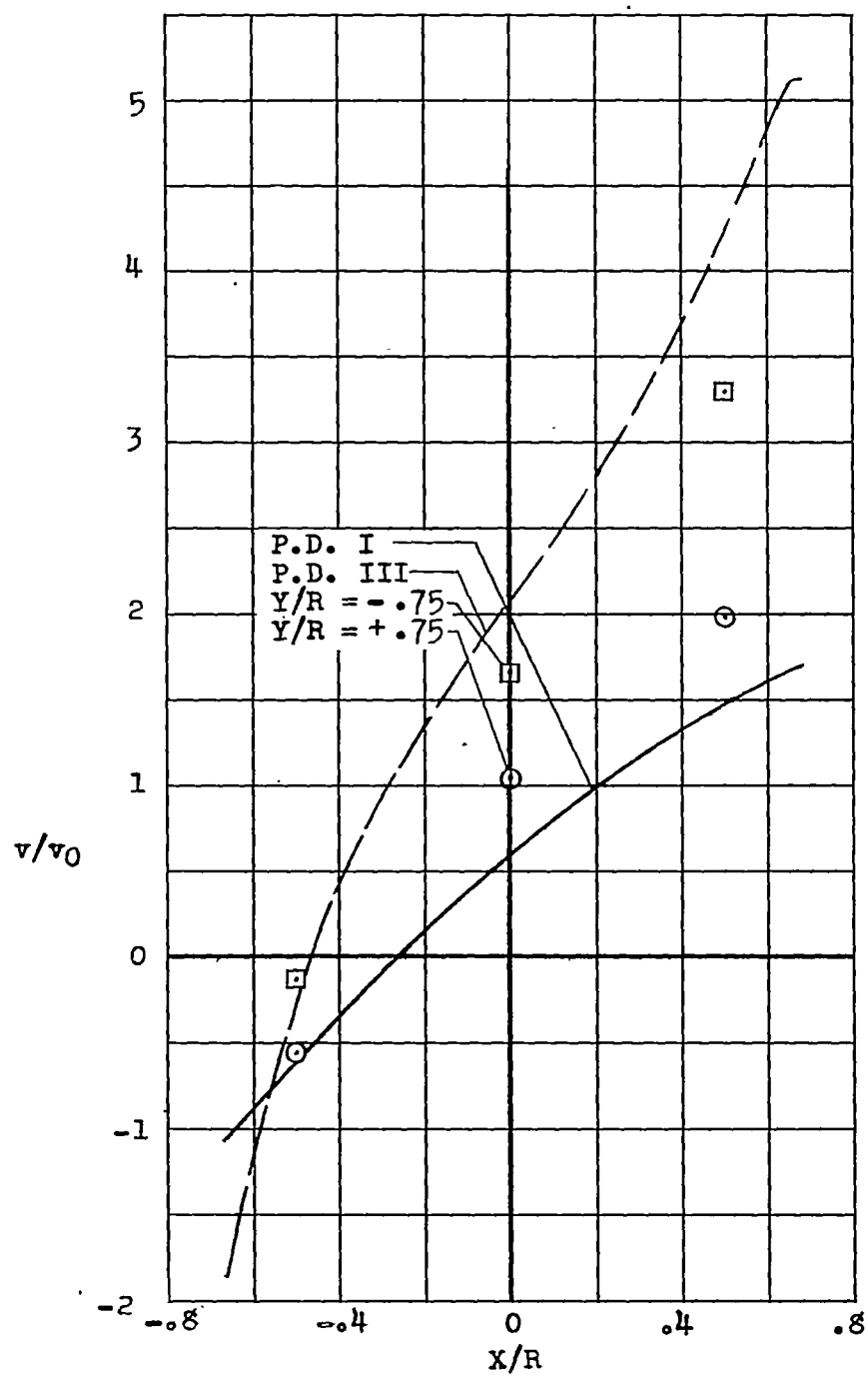
(a) $\chi = 75.00^\circ$; $\mu = 0.095$.

Figure 40.- Comparison of measured values of induced-velocity ratio v/v_0 at $Y/R = \pm 0.75$ with theory of reference 4 modified. Pressure distributions I and III are denoted by P.D. I and P.D. III.



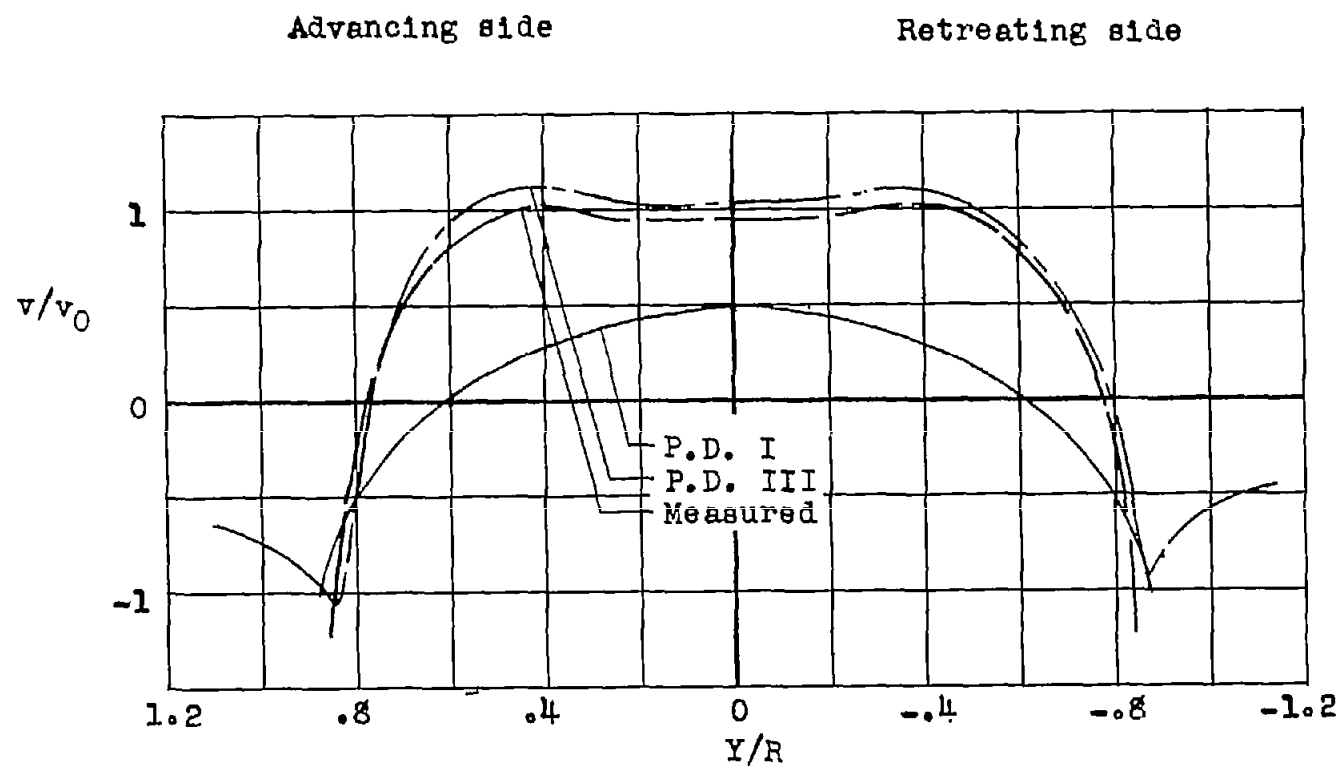
(b) $\chi = 82.3^\circ$; $\mu = 0.140$.

Figure 40.- Continued.



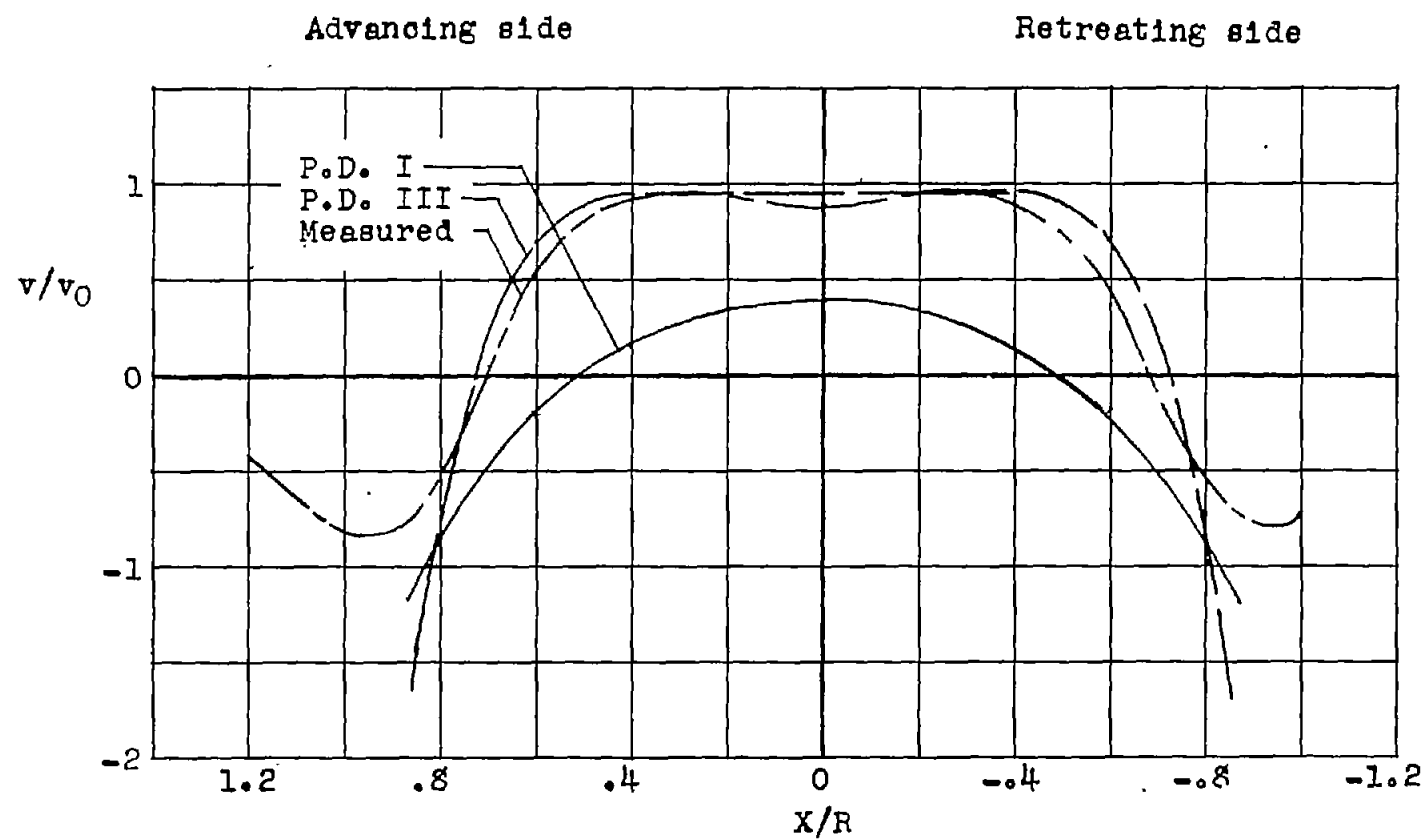
(c) $\chi = 83.9^\circ$; $\mu = 0.232$.

Figure 40.- Concluded.



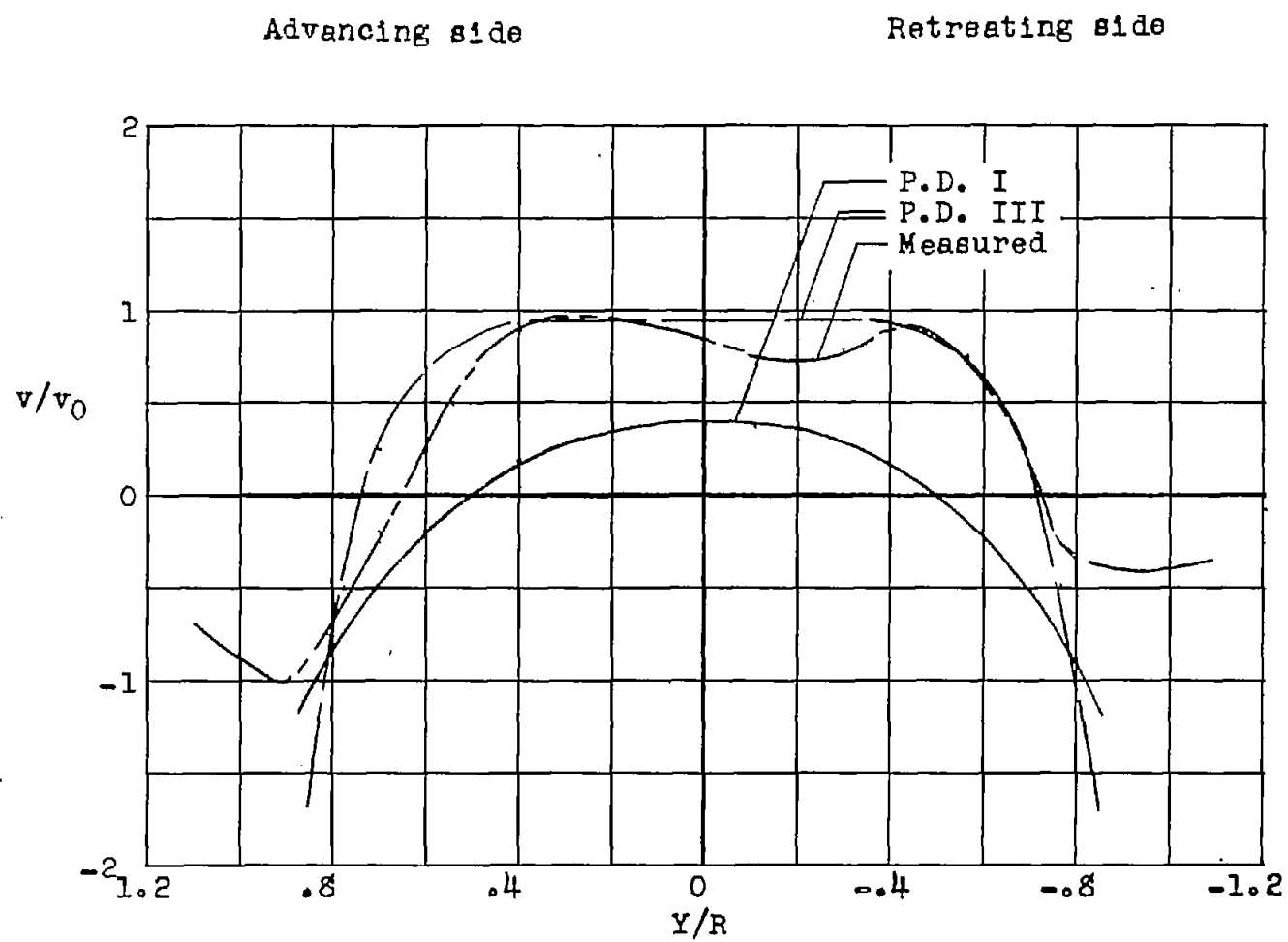
(a) $\alpha = 75.0^\circ$; $\mu = 0.095$.

Figure 41.- Comparison of measured values of induced-velocity ratio v/v_0 at $X/R = -0.5$ with theory of reference 4 modified. Pressure distributions I and III are denoted by P.D. I and P.D. III.



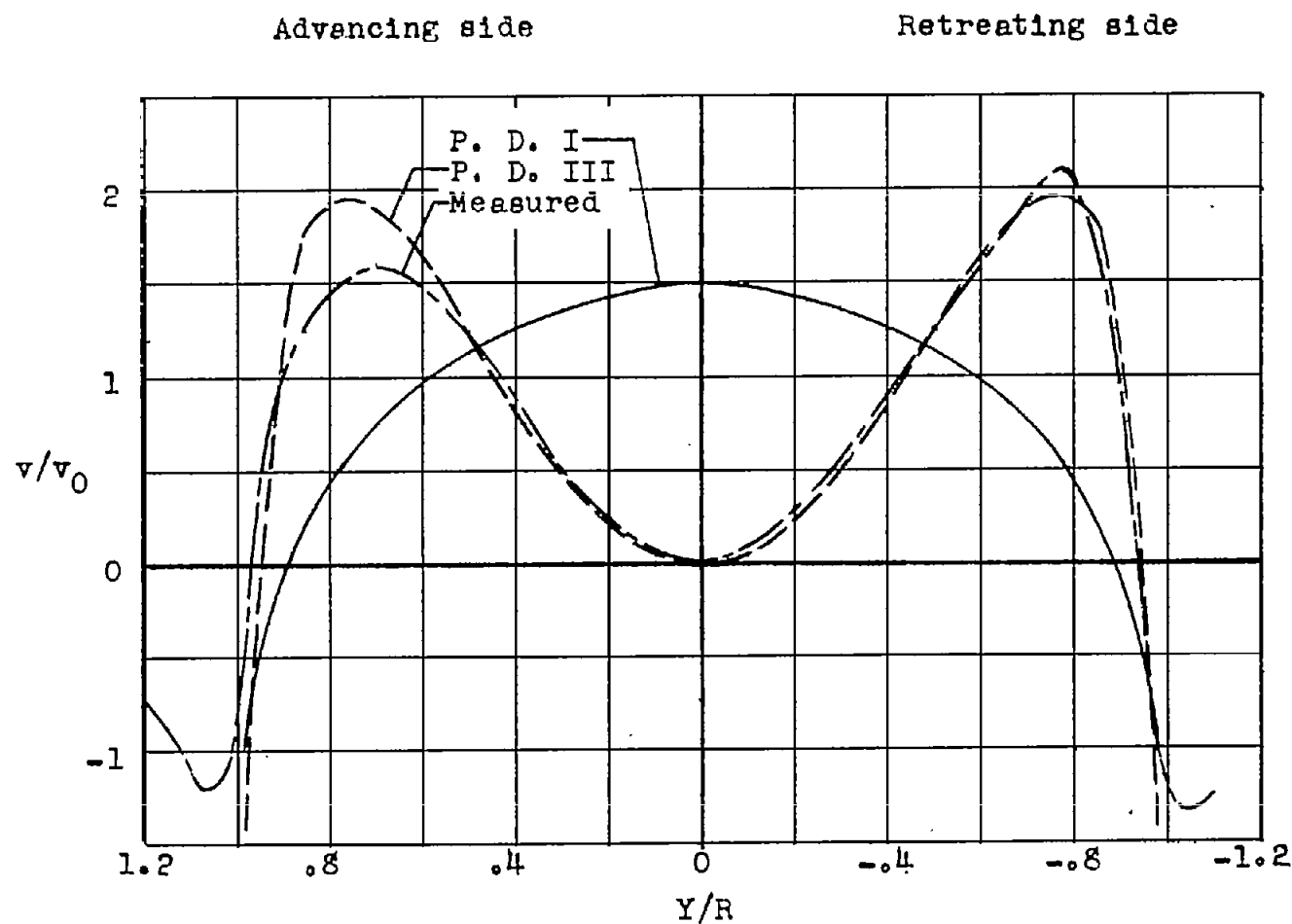
(b) $\alpha = 82.3^\circ$; $\mu = 0.140$.

Figure 41.- Continued.



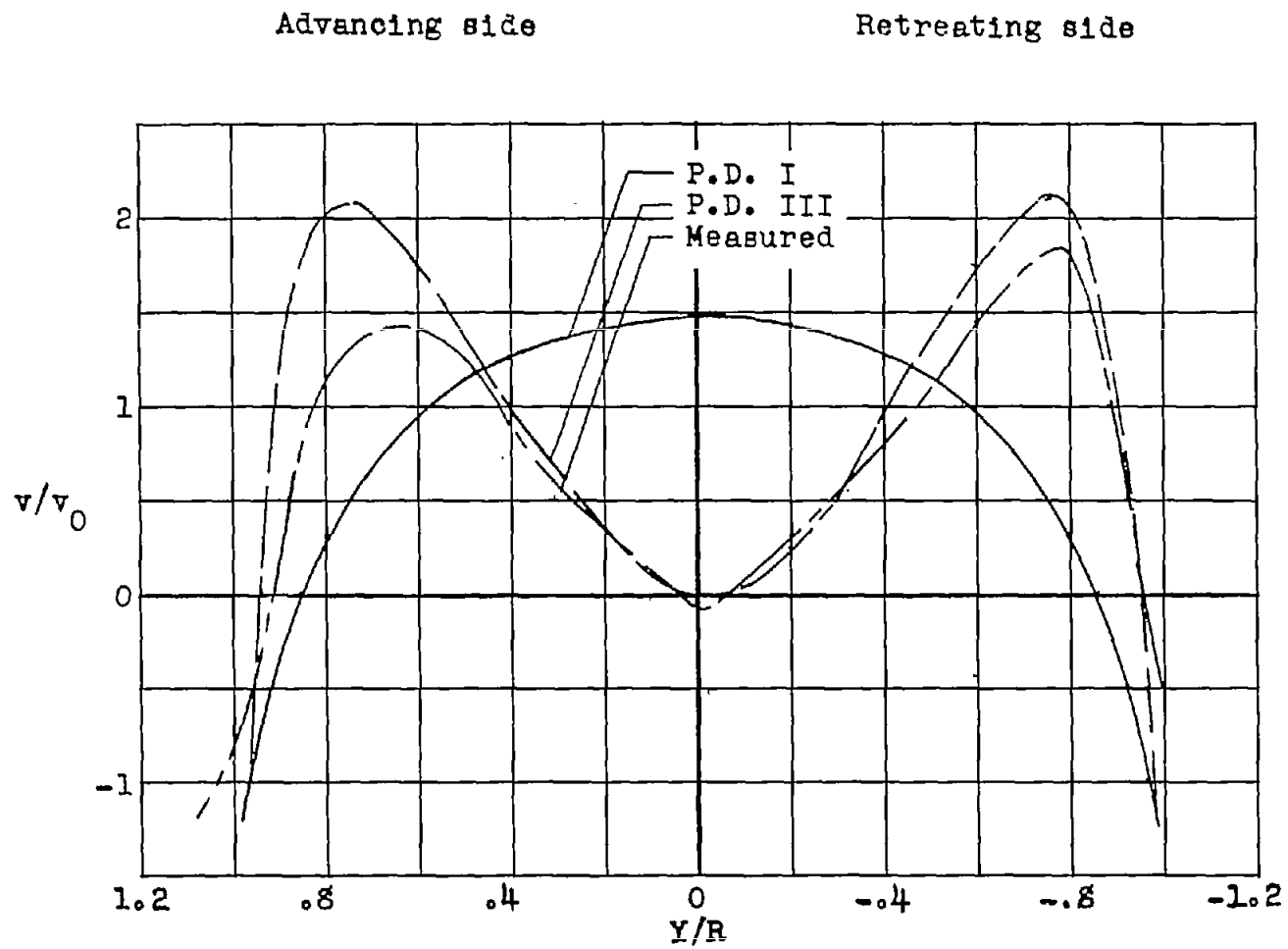
(c) $\alpha = 85.9^\circ$; $\mu = 0.232$.

Figure 41.- Concluded.



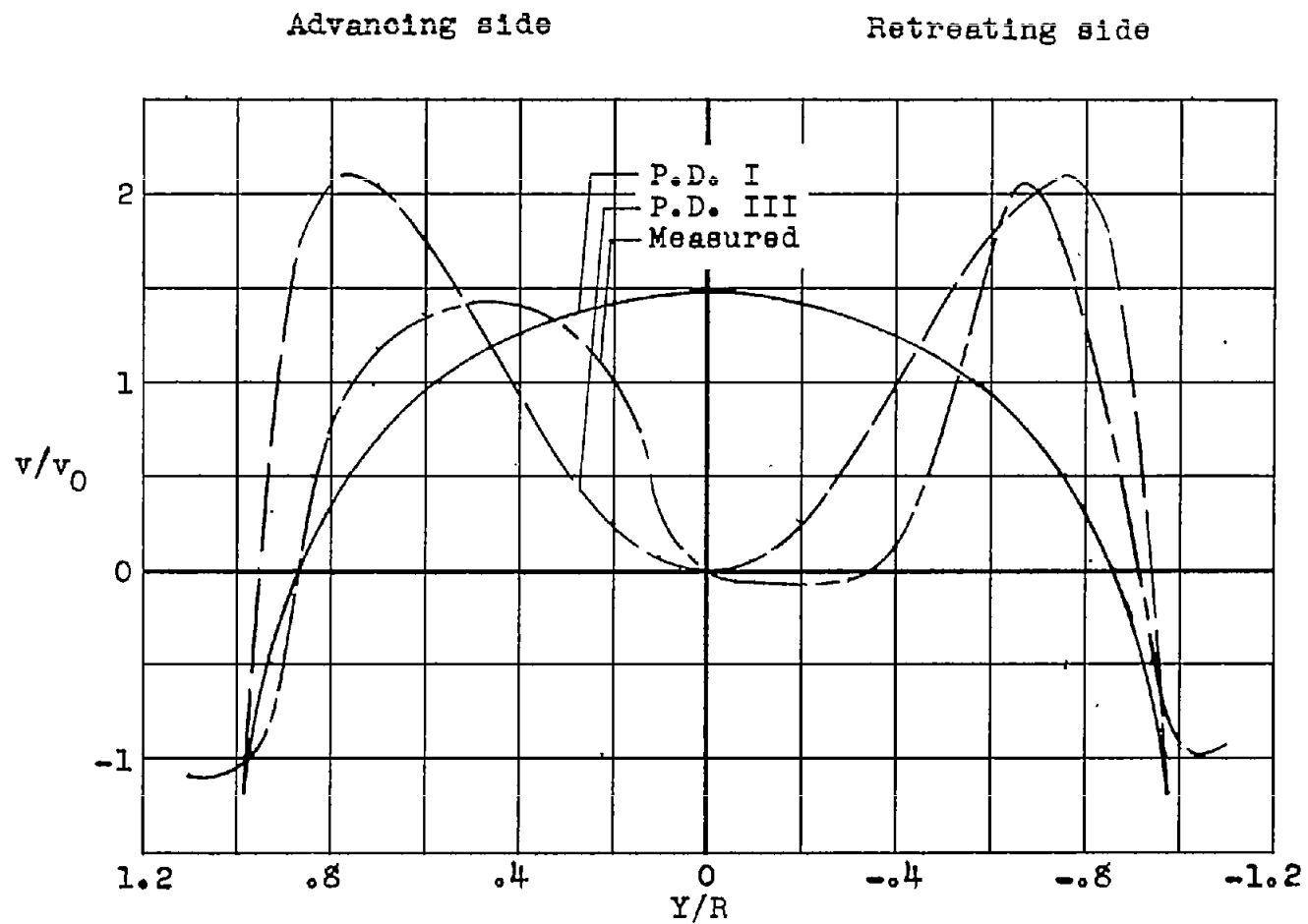
(a) $\alpha = 75.0^\circ$; $\mu = 0.095$.

Figure 42.- Comparison of measured values of induced velocity ratio v/v_0 on lateral center line with theory of reference 4 modified. Pressure distributions I and III are denoted by P.D. I and P.D. III.



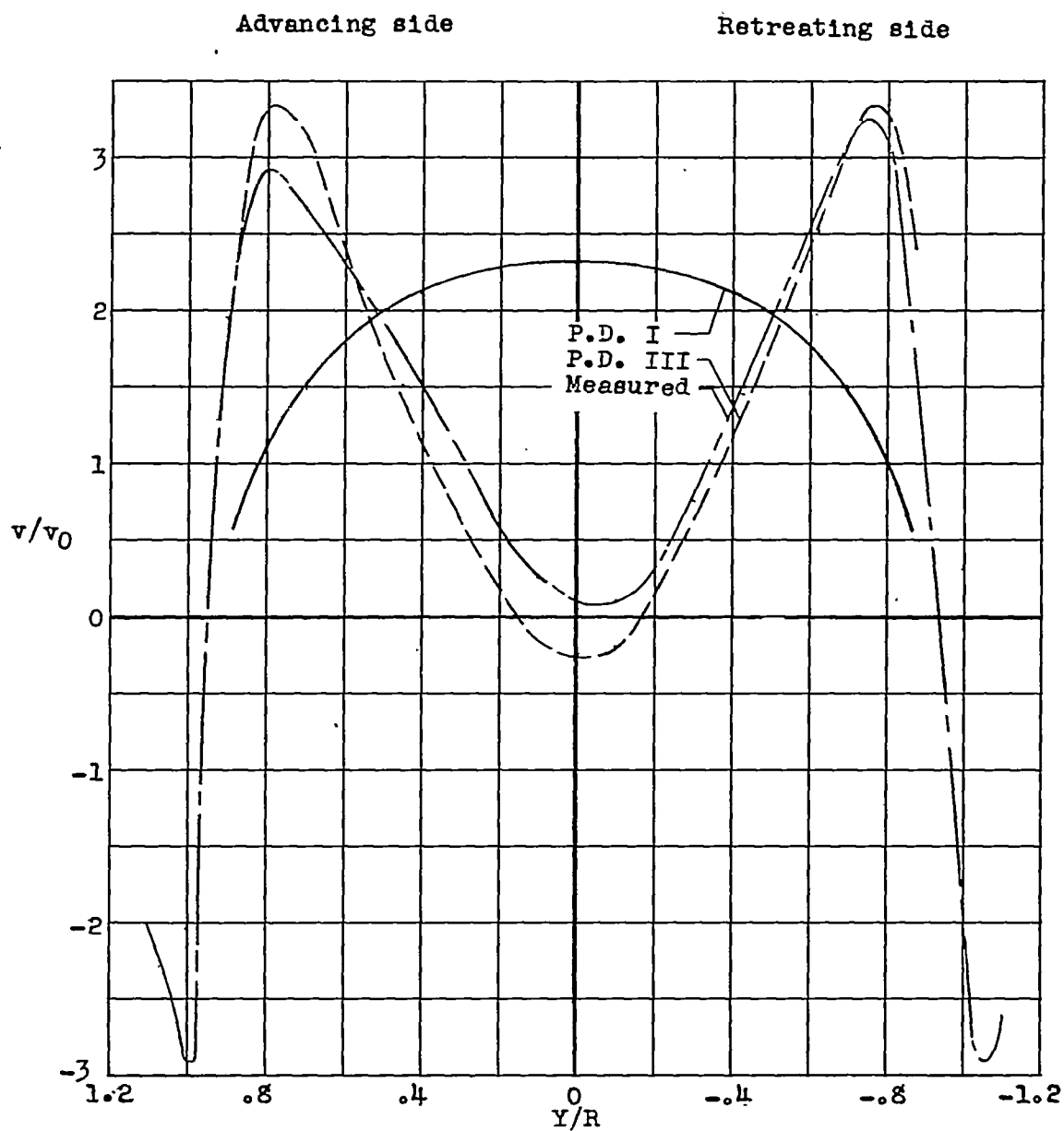
(b) $\alpha = 82.3^\circ$, $\mu = 0.140$.

Figure 42.- Continued.



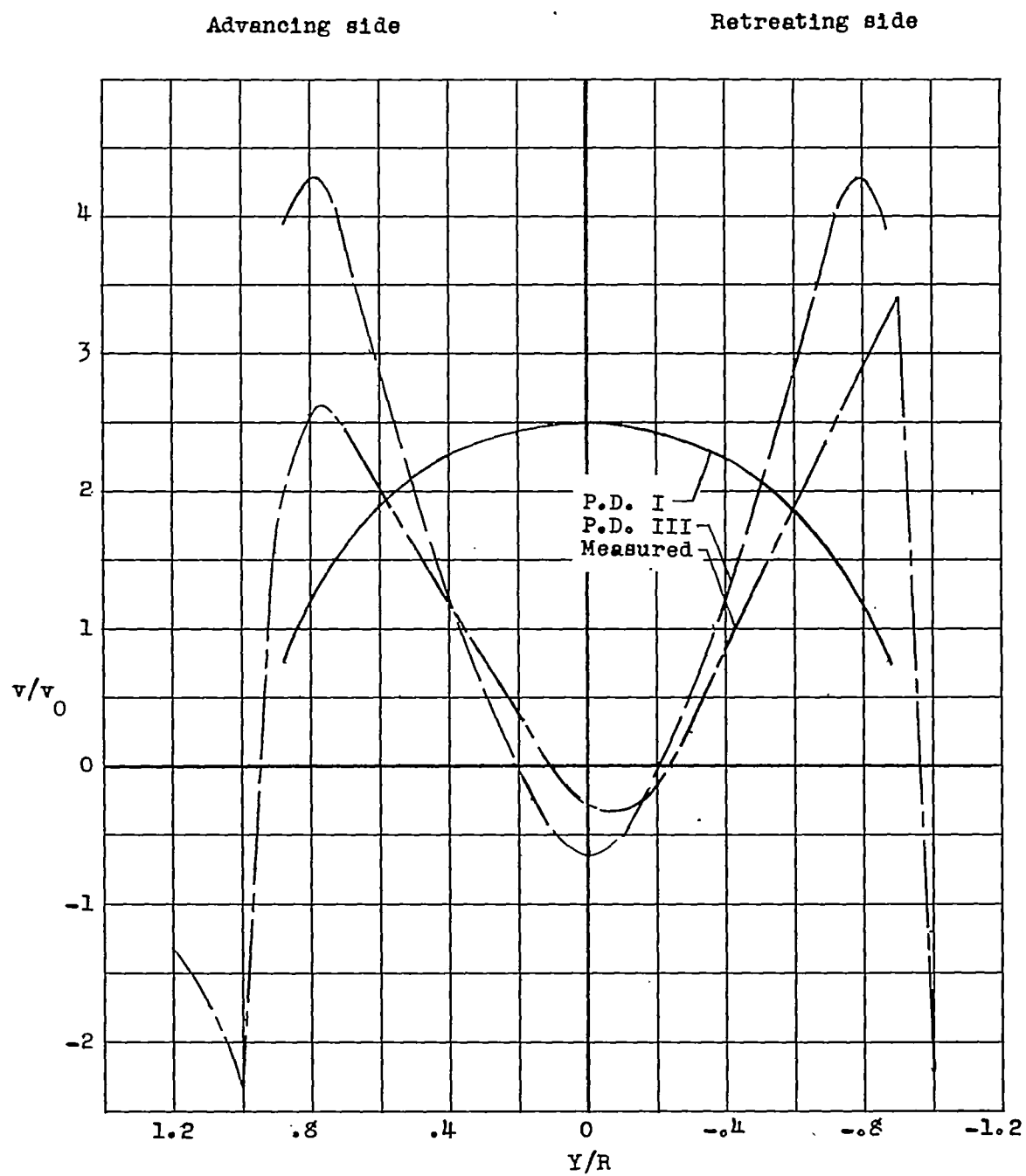
(c) $\alpha = 83.9^\circ$; $\mu = 0.232$.

Figure 42.- Concluded.



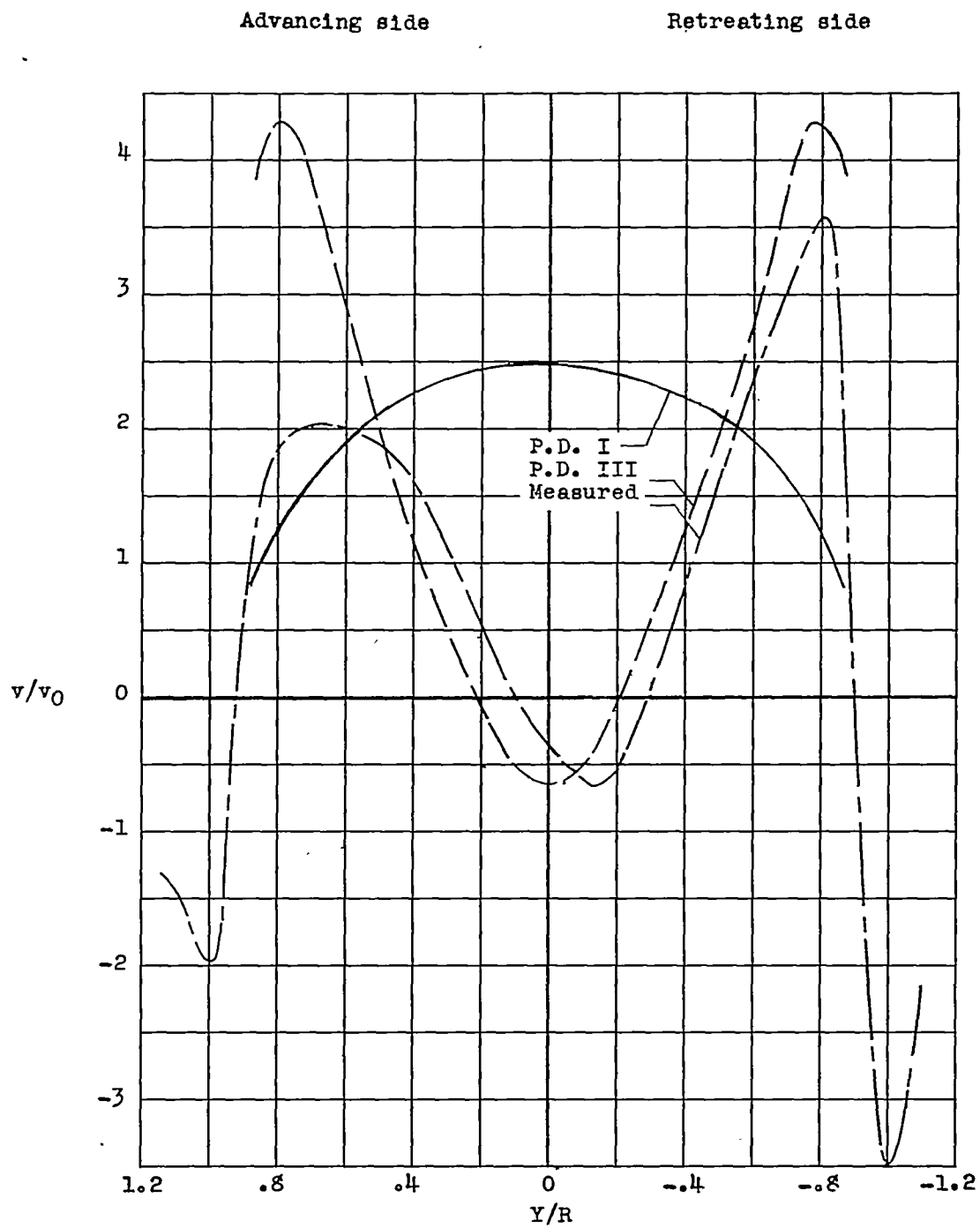
(a) $\alpha = 75.0^\circ$; $\mu = 0.095$.

Figure 43.- Comparison of measured values of induced-velocity ratio v/v_0 at $X/R = 0.5$ with theory of reference 4 modified. Pressure distributions I and III denoted by P.D. I and P.D. III.



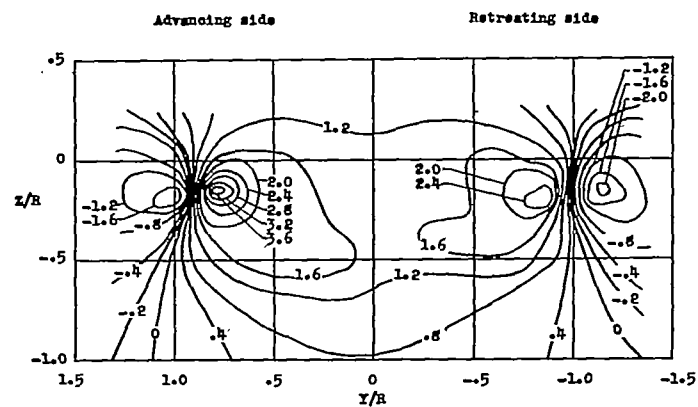
(b) $\alpha = 82.3^\circ$; $\mu = 0.140$.

Figure 43.- Continued.

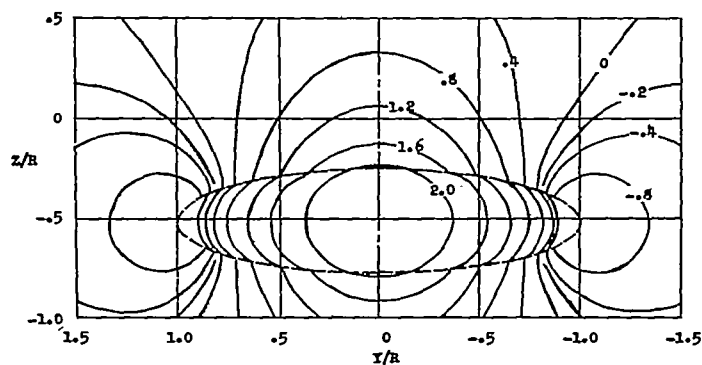


(c) $\alpha = 83.9^\circ$; $\mu = 0.232$.

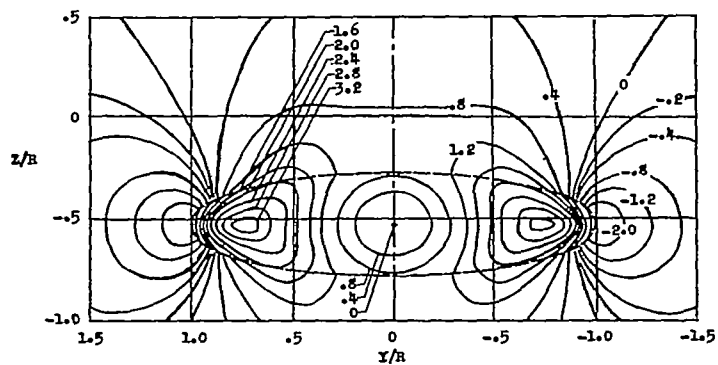
Figure 43.- Concluded.



(a) Measured data.

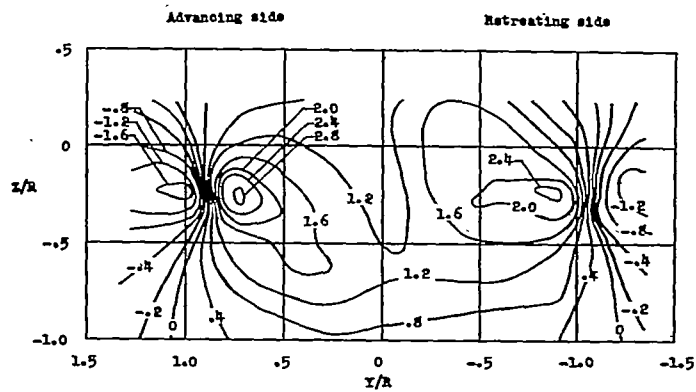


(b) Theoretical, pressure distribution I.

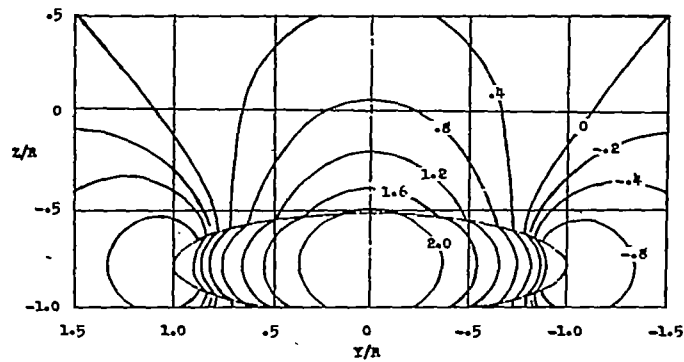


(c) Theoretical, pressure distribution III.

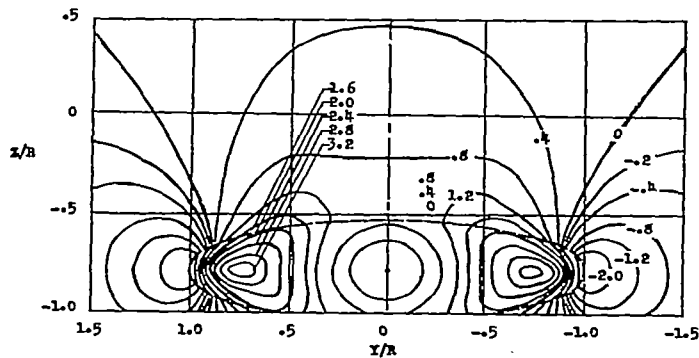
Figure 44.- Comparison of measured values of induced-velocity ratio v/v_0 at $X/R = 2.07$ with theory of reference 4 modified. $\chi = 75.0^\circ$; $\mu = 0.095$.



(a) Measured data.

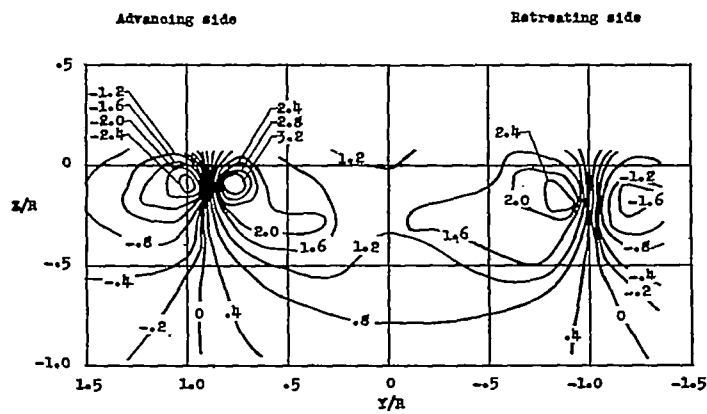


(b) Theoretical, pressure distribution I.

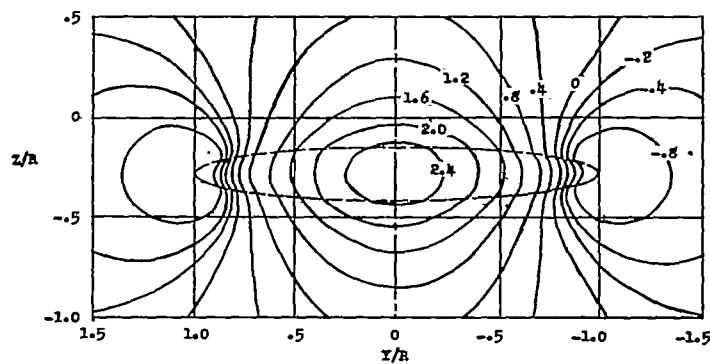


(c) Theoretical, pressure distribution III.

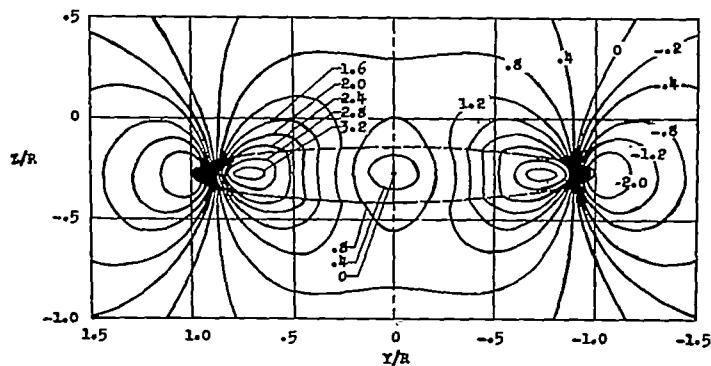
Figure 45.- Comparison of measured values of induced-velocity ratio v/v_0 at $X/R = 3.14$ with theory of reference 4 modified. $\chi = 75.0^\circ$; $\mu = 0.095$.



(a) Measured data.

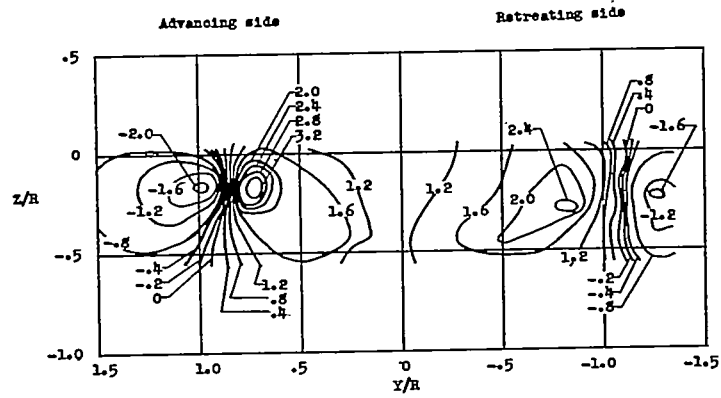


(b) Theoretical, pressure distribution I.

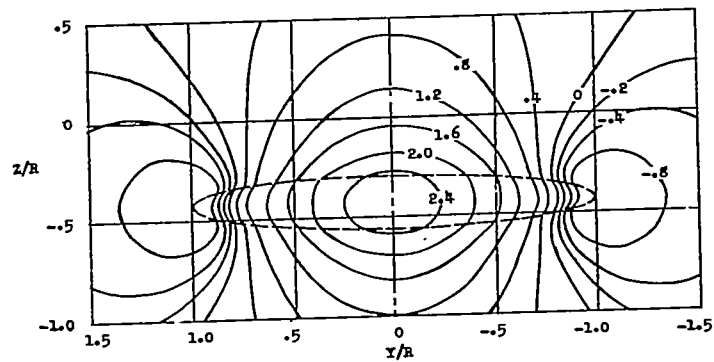


(c) Theoretical, pressure distribution III.

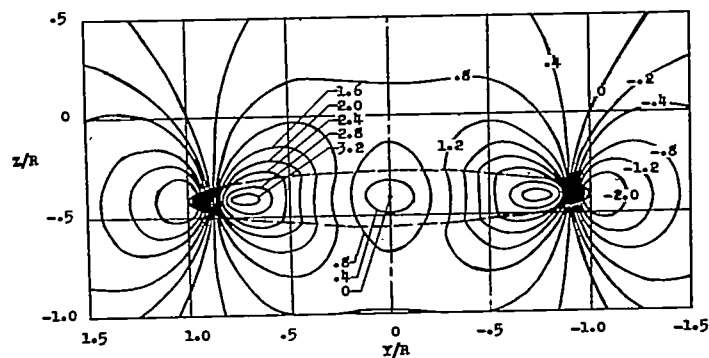
Figure 46.- Comparison of measured values of induced-velocity ratio v/v_0 at $X/R = 2.07$ with theory of reference 4 modified. $\alpha = 82.3^\circ$; $\mu = 0.140$.



(a) Measured data.

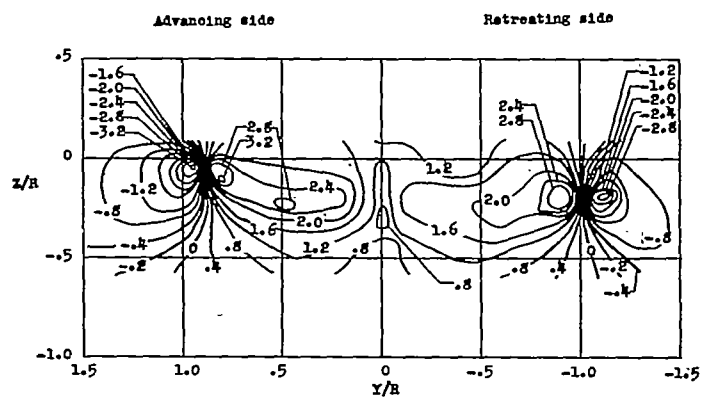


(b) Theoretical, pressure distribution I.

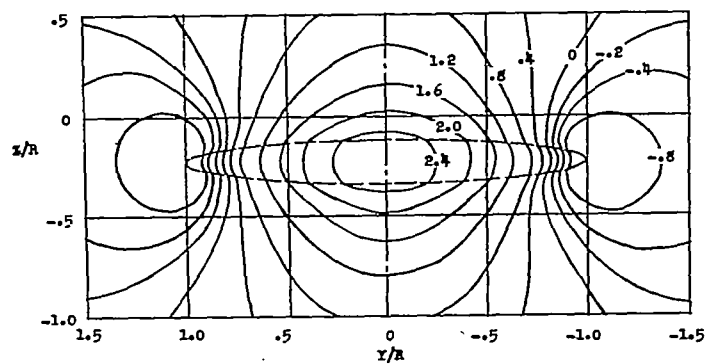


(c) Theoretical, pressure distribution III.

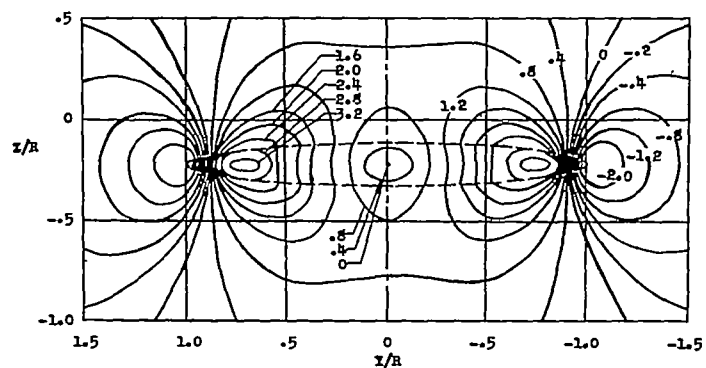
Figure 47.- Comparison of measured values of induced-velocity ratio v/v_0 at $X/R = 3.14$ with theory of reference 4 modified. $\chi = 82.3^\circ$; $\mu = 0.140$.



(a) Measured data.



(b) Theoretical, pressure distribution I.



(c) Theoretical, pressure distribution III.

Figure 48.- Comparison of measured values of induced-velocity ratio v/v_0 at $X/R = 2.07$ with theory of reference 4 modified. $\alpha = 83.9^\circ$; $\mu = 0.232$.

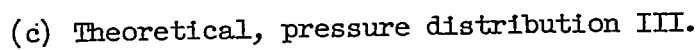
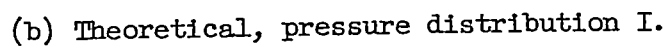
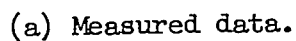


Figure 49.- Comparison of measured values of induced-velocity ratio v/v_0 at $X/R = 3.14$ with theory of reference 4 modified. $\alpha = 83.9^\circ$; $\mu = 0.232$.

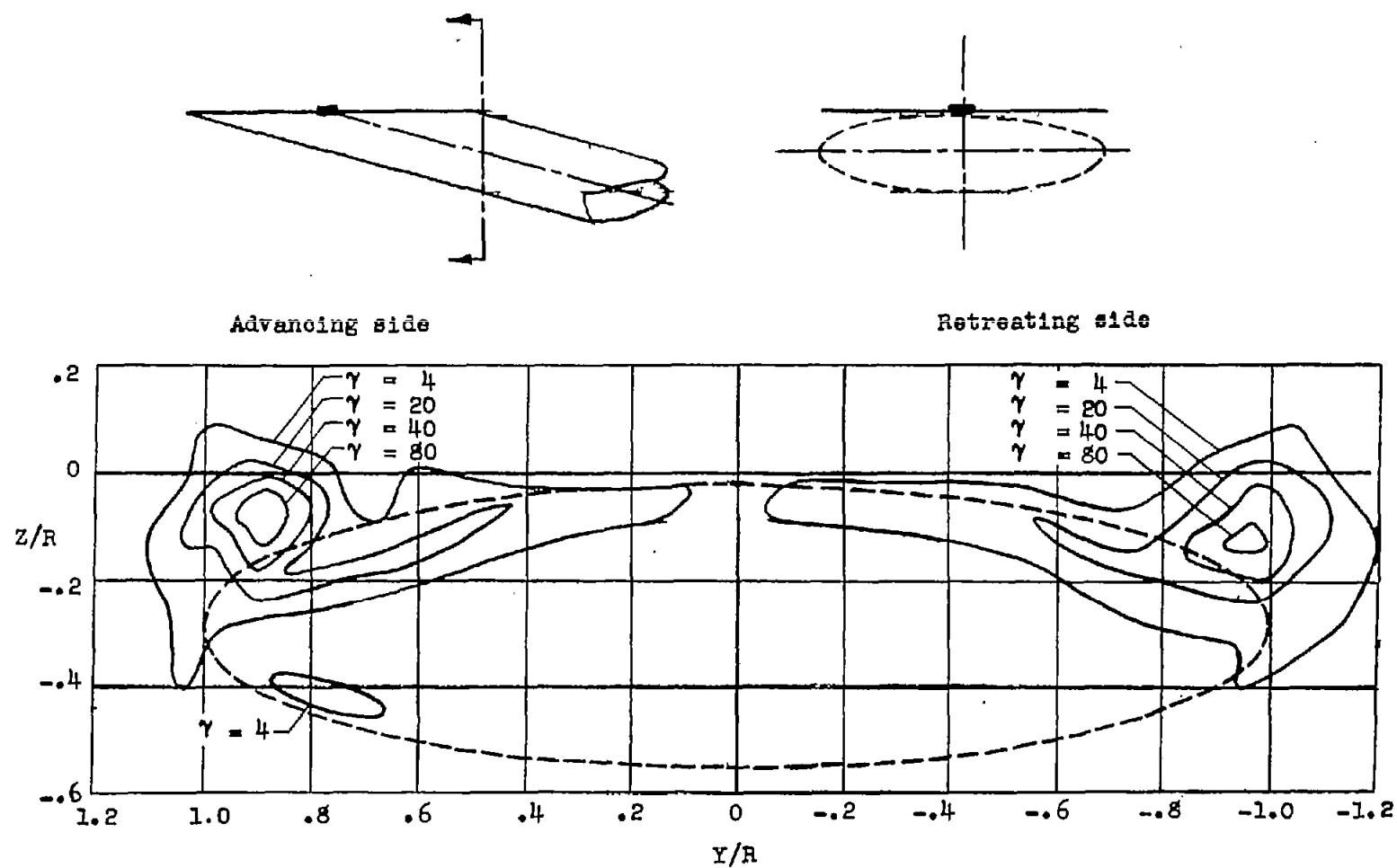
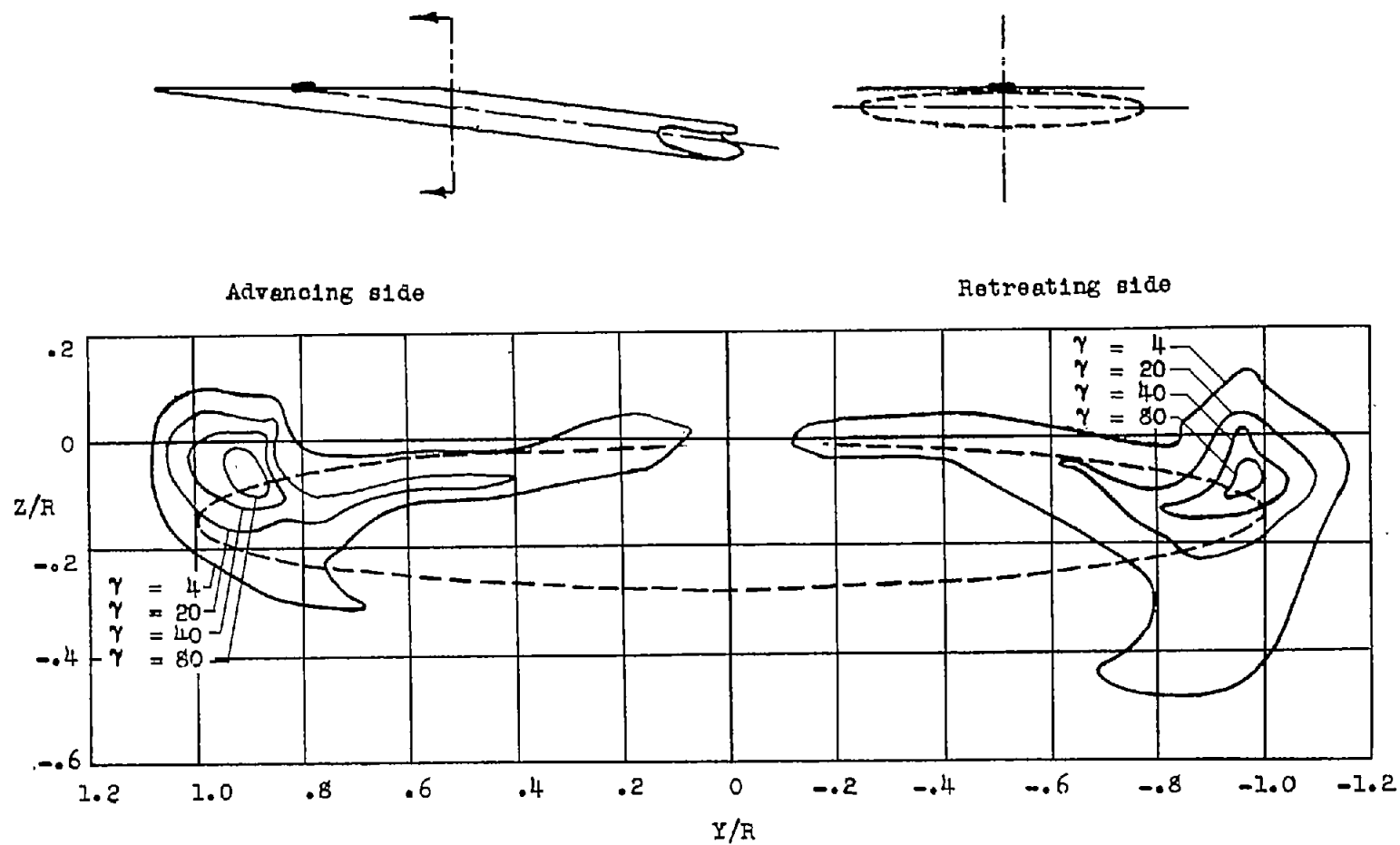
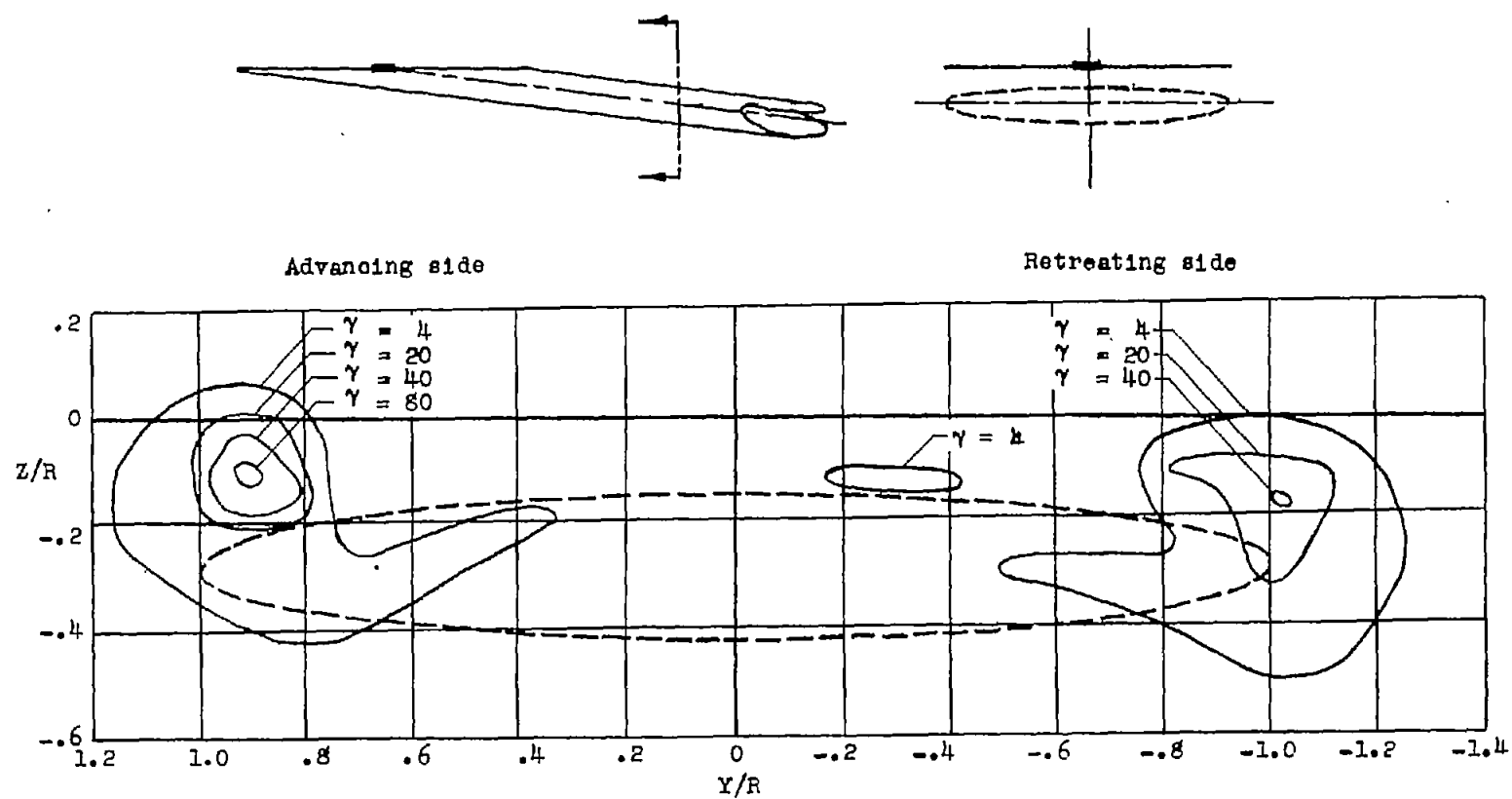


Figure 50.- Distribution of vorticity. $X/R = 1.07$; $\alpha = 75.0^\circ$; $\mu = 0.095$.



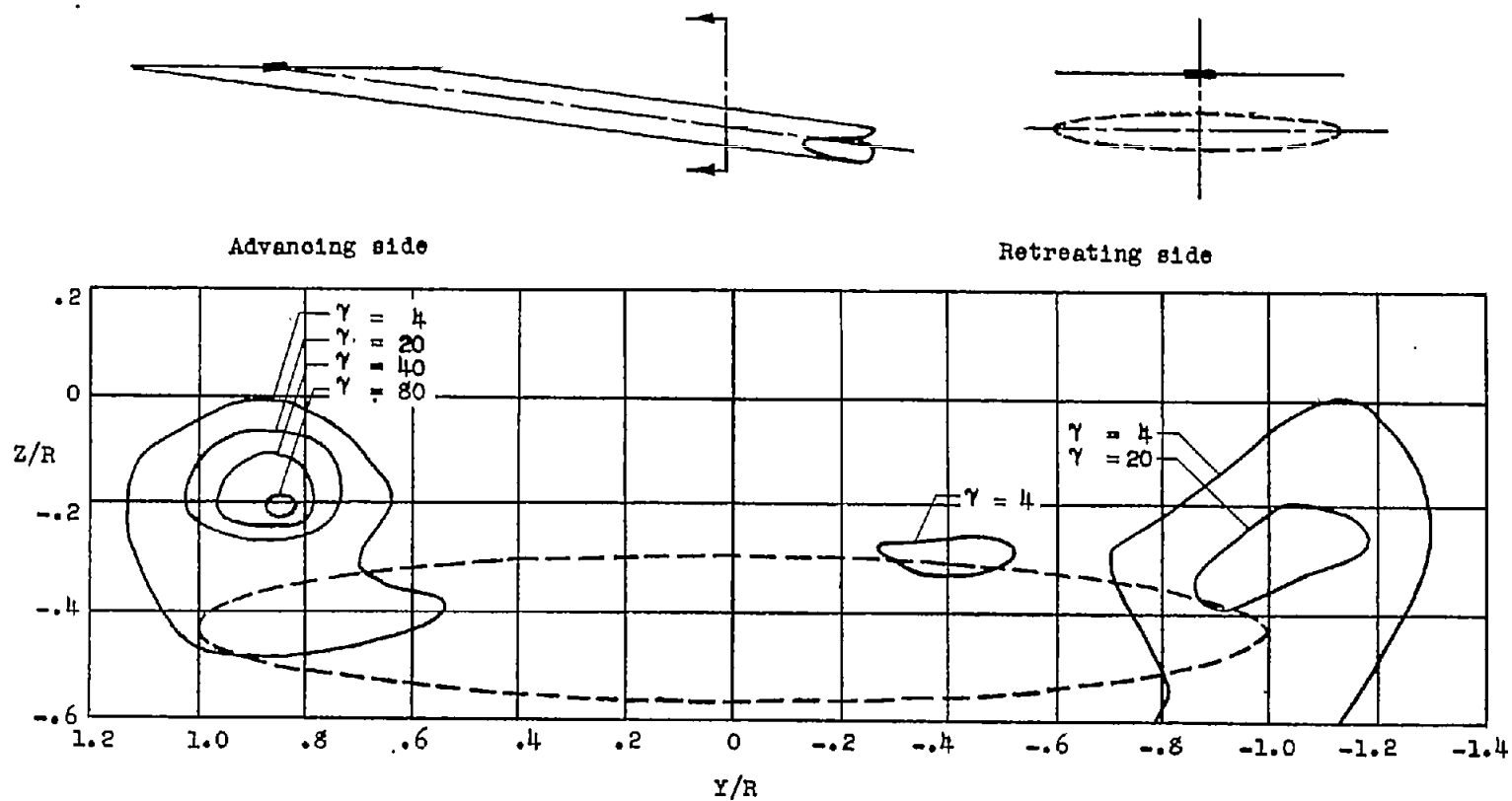
(a) $X/R = 1.07$.

Figure 51.- Distribution of vorticity behind rotor. $\alpha = 82.3^\circ$; $\mu = 0.140$.



(b) $X/R = 2.07$.

Figure 51.- Continued.



(c) $X/R = 3.14$.

Figure 51.- Concluded.

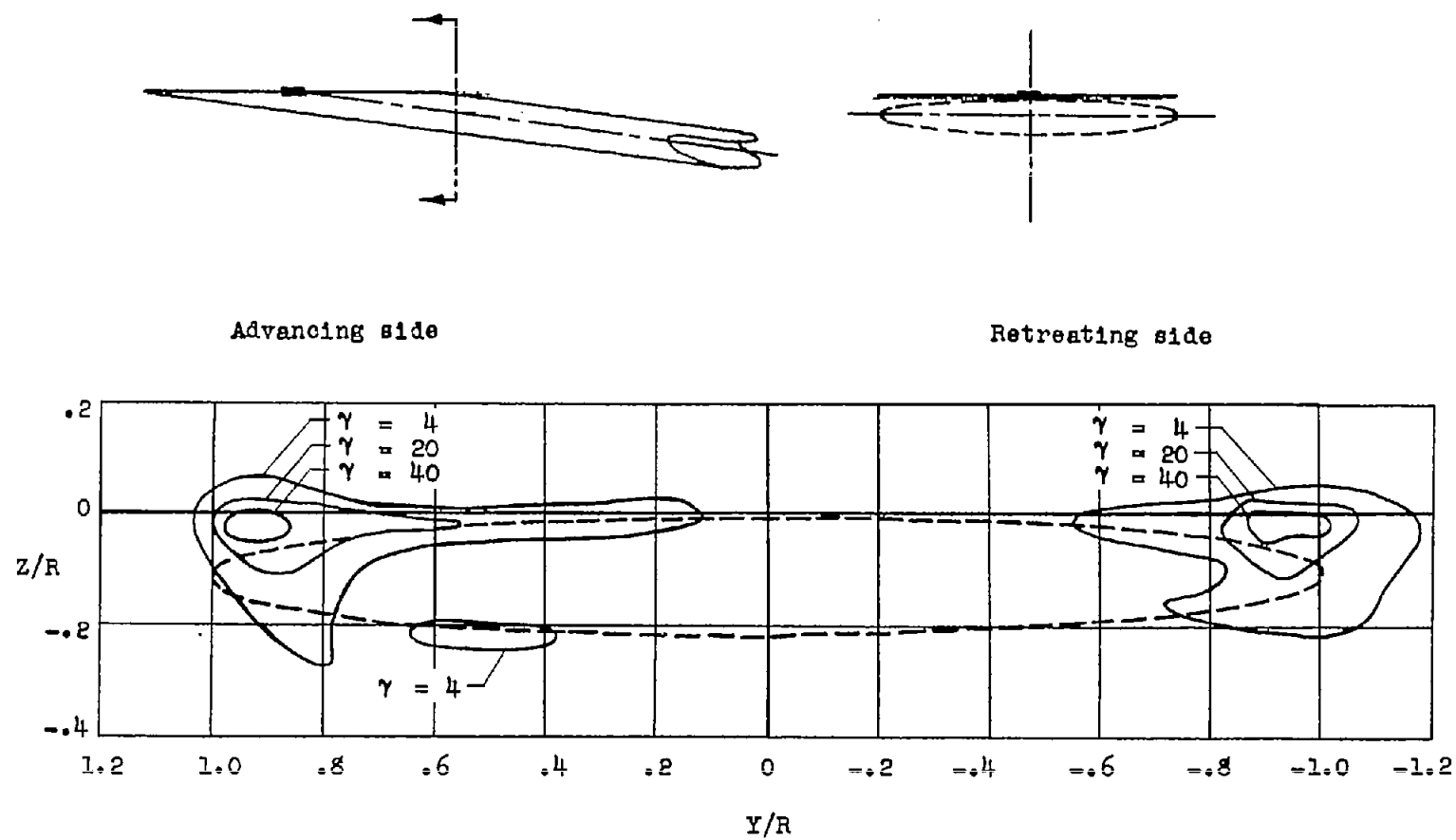


Figure 52.- Distribution of vorticity. $X/R = 1.07$; $\alpha = 83.9^\circ$; $\mu = 0.232$.

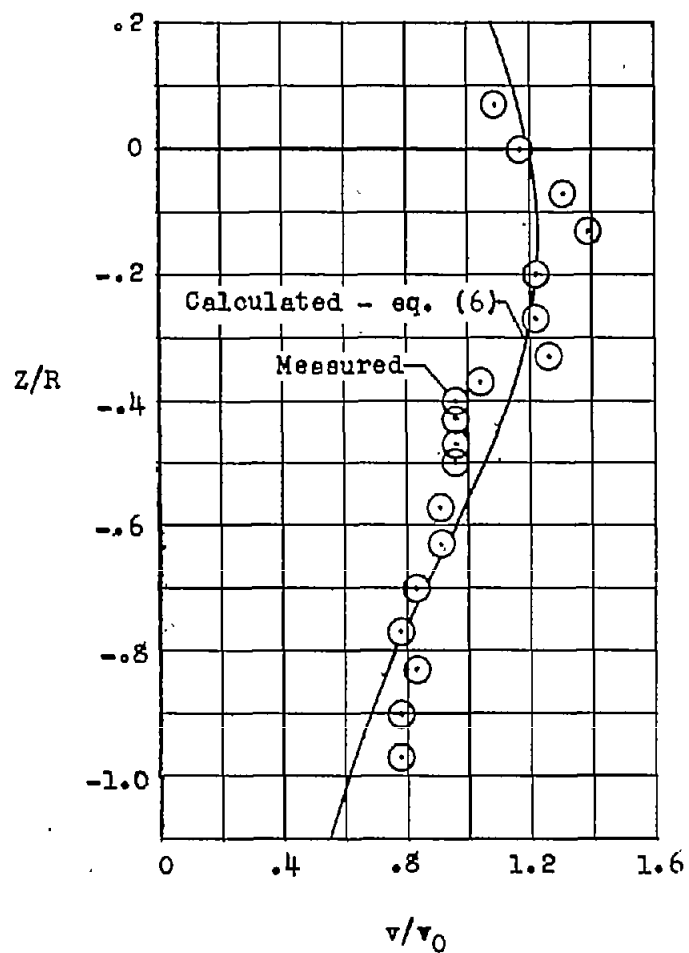
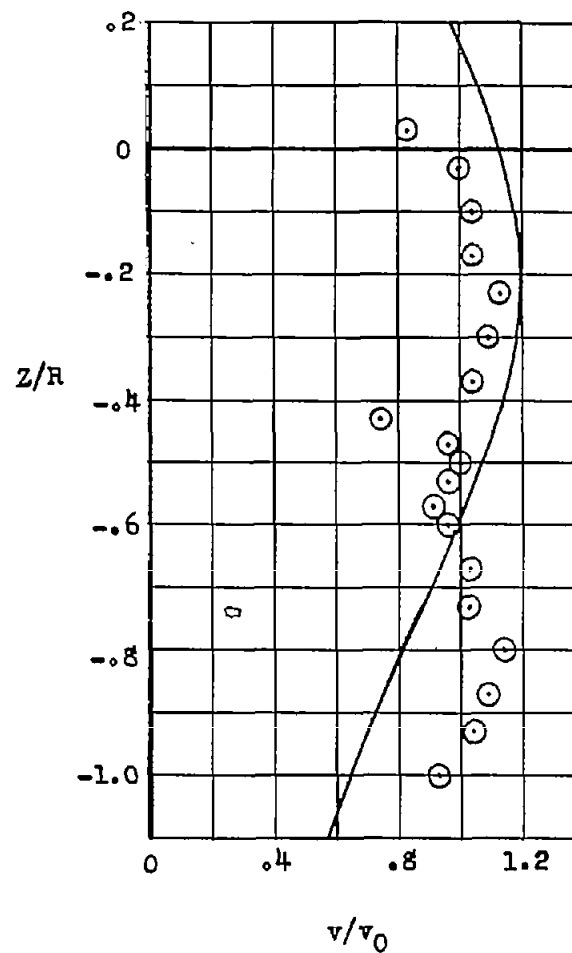
(a) $X/R = 2.07$.(b) $X/R = 3.14$.

Figure 53.- Comparison in the plane of symmetry of measured values of induced-velocity ratio v/v_0 with those calculated for an equivalent wing. $\alpha = 82.3^\circ$; $\mu = 0.140$.